UNIVERSIDAD AUTÓNOMA DE SAN LUÍS POTOSÍ

Doctorado Instituto de Física

RARE AND PRECIOUS METAL RECOVERY AT A LOW CONCENTRATION VIA CHEMISORPTION AND ELECTROSORPTION COUPLING PROCESS

PARA OBTENER EL GRADO DE

DOCTORADO POSGRADO EN CIENCIAS INTERDISCIPLINARIAS

QUE PRESENTA

Weiquan Zhan

DIRECTORES

Dr. Bernardo José Luis Arauz Lara

Dr. Shaoxian Song

PATROCINADO POR CONACyT Beca número 813934

San Luis Potosí, S.L.P. Julio 2025

UNIVERSIDAD AUTÓNOMA DE SAN LUÍS POTOSÍ

Doctorado Instituto de Física

RARE AND PRECIOUS METAL RECOVERY AT A LOW CONCENTRATION VIA CHEMISORPTION AND ELECTROSORPTION COUPLING PROCESS

PARA OBTENER EL GRADO DE

DOCTORADO POSGRADO EN CIENCIAS INTERDISCIPLINARIAS

QUE PRESENTA

Weiquan Zhan

Sinodales

Dr. Bernardo José Luis Arauz Lara_____

Dr. Francisco Alarcón Oseguera_____

Dr. Juan Rodrigo Vélez Cordero_____

Dr. Said Eduardo Aranda Espinoza_____

Dr. Guillermo Iván Guerrero García_____

San Luis Potosí, S.L.P. Julio 2025

Acknowledgement

Time filies like a fleeing show, and my studies have come to an end. This thesis marks the conclusion of a long and memorable Journey that I could not have completed without the dedicated support of my supervisors and fellow colleagues.

My sincere appreciation goes first and foremost to my supervisors, Prof. Shaoxian Song and Prof. Bernardo José Luis Arauz Lara, for their continuous inspiration and guidance.

Prof. Shaoxian Song has supported me since my master's studies. Without his consistent and enlightening instruction, this thesis would not have been possible. I'm deeply grateful for his patience, help, empathy, and academic professions. He provided me with excellent chances and valuable advice, and spent considerable time reviewing my papers and providing me with constructive feedback to improve my work.

I am especially thankful to Prof. Bernardo José Luis Arauz Lara. His thoughtful discussions helped me identify and correct many issues in my writing. He encouraged me to pursue my academic interests, and during my time in Mexico, he assisted me with housing, residency, shopping, internet access, and scholarship procedures.

I am also grateful to Dr. Alejandro Lopez Valdivieso, Dr. Feifei Jia, Dr. Juan Rodrigo Vélez Cordero, Dr. Moctezuma Martinon Rosario Esperanza, Dr. Said Aranda Espinoza, Dr. Viridiana, Ms. Maricela Cano, Ms. Rong An, Ms. Monica Anzaldo Montoya, and Emiliano for their help with both my work and daily life.

My heartfelt thanks go to my friends who supported me, especially Dr. María de Jesus Martínez-López, Dr. Noe Zamora Romero, Dr. Beni, Mr. Avilés Sánchez Juan Carlos, and Mr. Orlando. Their kindness and companionship helped me stay focused on my research and introduced me to the richness of Mexican culture. I also extend my thanks to everyone at LAMCC.

I am deeply grateful to my beloved families in China and Mexico, especially "Martinez" family from Oaxaca (Karen, Melissa, Irving, Chayo, Aide, Conchis, Daniela, and parents), who have supported me unconditionally and helped me overcome many difficulties. Thanks to them, I proudly feel like an "Oaxaqueño".

Finally, I would like to thank everyone who has directly or indirectly supported me in completing this thesis. I sincerely wish you all the best and may everything go smoothly in your life.

The work was supported by the scholarship from the Consejo Nacional de Humanidades Ciencias y Tecnologías (CONAHCYT) of Mexico (No. 813934).

Abstract

The recovery of rare earth elements (REEs) and precious metals at low concentrations from solutions has become an increasingly vital in hydrometallurgy, water treatment, and energy-related fields owing to their genotoxicity and unique physicochemical properties. Although various technologies have been developed, many remain difficult to apply in industry. In this work, an alternative approach is proposed, which regulates chemisorption and electrosorption activities using molybdenum disulfide (MoS_2) and carbon-based electrodes to achieve efficient recovery low-concentration REEs and precious metals.

Firstly, the recovery of REEs from dilute aqueous solutions was achieved using oxygen-doped MoS_2 electrodes. A Chemisorption and electrosorption coupling (CEC) process enhanced nearly 100% REE recovery at a specific initial concentration. Desorption efficiency also reached ~100% within 120 minutes, and the electrodes demonstrated excellent stability. This high performance is attributed to the strong interaction of REEs with sulfur and oxygen atoms on MoS_2 surface, its high electric double layer capacity (EDLC), and low charge transfer resistance. Building on this, defect-rich MoS_2 electrodes containing unsaturated Mo or S atoms were designed for selective separation and recovery of gadolinium (Gd(III)) based on its unique extranuclear electron configuration. These electrodes achieved ~100% recovery of Gd(III) with an adsorption capacity of 299.32 mg/(g·dm^2), together with high separation with La(III) and Y(III).

To further advance the CEC method, carbon materials functionalized with oxygen-containing groups were employed as coatings on electrodes for REEs and gold (Au) recovery. Under optimized conditions, REE recovery again reached nearly 100%. The enhanced performance is attributed to a combination of strong EDLC, electrostatic interactions from the applied voltage, and chemisorption through oxygen-containing groups. Recovery efficiency was strongly influenced by pore structure and surface functionality. Notably, Au(I) recovery from thiosulfate solutions exceeded 90%, with gold recovered in its metallic form, thereby simplifying conventional processing steps.

Finally, to enable cost-effective application, biochar electrodes derived from inexpensive walnut shell precursors were used to recover Au(I) from thiosulfate solutions. Through traditional carbonization and activation processes, porous walnut shell charcoal (WSC) was synthesized. Compared to non-activated samples, WSC exhibited superior Au(I) recovery (~100%) due to its hierarchical porous structure,

which facilitated efficient ion adsorption and charge storage. Again, metallic gold was the main recovered product. Experimental data, supported by theoretical calculations, demonstrated the critical role of pore architecture during the reduction-recovery process. Au(I) adsorption was governed by contact and diffusion steps, which depended on water molecule interactions and ion migration…… …… …… …… …… Ultimately, the developed CEC method achieved 100% Au(I) recovery from thiosulfate leachates of e-waste and gold ores, even in the presence of interfering ions.

This study highlights a novel approach to improve the recovery of low-concentration REEs and Au(I) from leaching solutions by modulating chemisorption and electrosorption behaviors. The findings offer valuable insights that may inspire future strategies for metal ion recovery using CEC-based techniques.

Keywords: Rare earth elements; Au(I); Low-concentration; Chemisorption and electrosorption coupling; MoS_2; Porous carbon materials

Resume

La recuperación de elementos de tierras raras (REEs) y metales preciosos en bajas concentraciones a partir de soluciones se ha vuelto cada vez más vital en los campos de la hidrometalurgia, el tratamiento de aguas y la energía, debido a su genotoxicidad y sus propiedades fisicoquímicas únicas. Aunque se han desarrollado diversas tecnologías, muchas siguen siendo difíciles de aplicar a nivel industrial. En este trabajo, se propone un enfoque alternativo que regula las actividades de quimiosorción y electrosorción mediante el uso de electrodos basados en disulfuro de molibdeno (MoS_2) y materiales carbonosos, con el fin de lograr una recuperación eficiente de REEs y metales preciosos en bajas concentraciones.

En primer lugar, se logró la recuperación de REEs a partir de soluciones acuosas diluidas utilizando electrodos de MoS_2 dopados con oxígeno. El proceso acoplado de quimiosorción y electrosorción (CEC) permitió una recuperación de REEs cercana al 100% a una concentración inicial específica. La eficiencia de desorción también alcanzó aproximadamente el 100% en 120 minutos, y los electrodos mostraron una excelente estabilidad. Este rendimiento sobresaliente se atribuye a la fuerte interacción de los REEs con átomos de azufre y oxígeno en la superficie del MoS_2, a su alta capacidad de doble capa eléctrica (EDLC) y a su baja resistencia a la transferencia de carga. Con base en esto, se diseñaron electrodos de MoS_2 ricos en defectos, que contienen átomos de Mo o S insaturados, para la separación selectiva y recuperación de gadolinio (Gd(III)), aprovechando su configuración electrónica extranuclear única. Estos electrodos lograron una recuperación de Gd(III) de aproximadamente el 100%, con una capacidad de adsorción de 299.32 $mg/(g \cdot dm^2)$, así como una alta selectividad frente a La(III) y Y(III).

Para avanzar en la aplicación del método CEC, se emplearon materiales carbonosos funcionalizados con grupos oxigenados como recubrimientos de electrodos para la recuperación de REEs y oro (Au). Bajo condiciones optimizadas, la recuperación de REEs volvió a alcanzar cerca del 100%. Este rendimiento mejorado se atribuye a la combinación de una fuerte EDLC, interacciones electrostáticas generadas por el voltaje aplicado y quimiosorción a través de grupos oxigenados. La eficiencia de recuperación estuvo fuertemente influenciada por la estructura porosa y la funcionalización superficial. Es notable que la recuperación de Au(I) a partir de soluciones de tiosulfato superó el 90%, y el oro se recuperó en forma metálica, lo que simplifica los procedimientos tradicionales.

Finalmente, con el objetivo de desarrollar una aplicación rentable, se utilizaron electrodos de biocarbón derivados de cáscaras de nuez económicas para la recuperación de Au(I) a partir de soluciones de tiosulfato. Mediante procesos tradicionales de carbonización y activación, se sintetizó carbón poroso de cáscara de nuez (WSC). En comparación con las muestras no activadas, el WSC mostró una recuperación superior de Au(I) (~100%) debido a su estructura porosa jerárquica, que facilitó una adsorción eficiente de iones y el almacenamiento de carga. Nuevamente, el oro metálico fue el principal producto recuperado. Los datos experimentales, respaldados por cálculos teóricos, demostraron el papel crítico de la arquitectura porosa durante el proceso de reducción y recuperación. La adsorción de Au(I) estuvo gobernada por pasos de contacto y difusión, dependientes de las interacciones con moléculas de agua y la migración
iónica…… Finalmente, el método CEC desarrollado logró una recuperación del 100% de Au(I) a partir de lixiviados de tiosulfato provenientes de residuos electrónicos y minerales auríferos, incluso en presencia de iones interferentes.

Este estudio destaca un enfoque novedoso para mejorar la recuperación de REEs y Au(I) en bajas concentraciones a partir de soluciones de lixiviación, mediante la regulación de los comportamientos de quimiosorción y electrosorción. Los hallazgos ofrecen ideas valiosas que pueden inspirar futuras estrategias para la recuperación de iones metálicos mediante técnicas basadas en CEC.

Palabras clave: Elementos de tierras raras; Au(I); Baja concentración; Acoplamiento de quimiosorción y electrosorción; MoS_2; Materiales carbonosos porosos

Extended abstract

Recovery of rare earth elements (REEs) and precious metals at low concentrations from aqueous solutions is becoming increasingly vital for hydrometallurgy, water treatment, and energy-related fields, due to their genotoxicity and unique physicochemical properties. Although various technologies have been developed, many of them face challenges in practical and industrial applications. In this study, a novel strategy is proposed to efficiently recover low-concentration REEs and precious metals by regulating chemisorption and electrosorption activities using molybdenum disulfide (MoS_2) and carbon-based electrodes.

Firstly, oxygen-doped MoS_2 electrodes were designed for REEs recovery from dilute aqueous solutions. The chemisorption and electrosorption coupling (CEC) process using these electrodes achieved nearly 100% recovery of REEs at specific initial concentrations. A maximum adsorption capacity of 365.71 mg/(g·dm²) was obtained, and desorption efficiency also reached ~100% within 120 minutes. The high performance is attributed to the strong interaction between REEs and sulfur/oxygen atoms on the MoS_2 surface, the large electric double layer capacitance (EDLC), and the low charge transfer resistance. Furthermore, the enhanced chemical interaction resulting from oxygen doping significantly influenced the binding strength between REEs and the MoS_2 surface.

Secondly, taking advantage of the special electron configuration of gadolinium (Gd), defect-rich MoS_2 electrodes with unsaturated molybdenum or sulfur atoms were developed to selectively separate and recover Gd(III) from other REEs. In competitive adsorption experiments, Gd(III) was effectively separated from La(III) and Y(III), due to the specific interaction between Gd(III) f-orbitals and the p-orbitals of unsaturated sulfur atoms. The Gd(III) recovery rate and adsorption capacity reached nearly 100% and 299.32 mg/(g·dm^2), respectively. Additionally, the superior sorption ability enhanced the EDLC and reduced charge transfer resistance, improving the overall electrochemical performance. Notably, the strong binding of La(III) to unsaturated Mo atoms also enabled its selective recovery by tuning the chemisorption activity.

To further promote the applicability of the CEC method, functionalized carbon materials were used to fabricate electrodes for REEs and gold (Au) recovery. Under specific conditions, REEs recovery reached 100%, primarily due to the synergistic effects of strong EDLC, electrostatic interactions from applied voltage, and chemisorption via oxygen-containing functional groups. HCl and NH_4Cl were

employed for REEs desorption, achieving over 90% desorption efficiency within 20 minutes (HCl), and nearly complete desorption with NH_4Cl, while preserving the electrode structure. After four cycles, a decline in recovery was observed due to material loss. Interestingly, Au(I) was also recovered from thiosulfate solutions at over 90%, with gold metal directly formed on the electrode surface, thereby simplifying the downstream recovery process.

Subsequently, to develop cost-effective electrodes, biochar derived from walnut shells (WSC) was synthesized for Au(I) recovery. Using traditional carbonization and activation techniques, porous WSC electrodes with varied pore distributions were prepared. At low initial concentrations, WSC achieved over 85% Au(I) recovery, with a maximum of 95% and an adsorption capacity of 42.9 mg/g. Multi-porous WSC electrodes exhibited even better performance (~100% recovery), attributed to the enhanced ion adsorption and storage facilitated by the porous structure. The recovered Au(I) was also found in metallic form on the WSC surface.

……
……
……
……
……
……
……
……
……..

In conclusion, this study demonstrates a novel and effective approach for recovering low-concentration REEs and Au(I) by modulating chemisorption and electrosorption properties of electrode materials. These findings provide valuable insights and offer a potential pathway for the efficient recovery of other valuable metal ions via the CEC method.

Keywords: Rare earth elements; Au(I); Low-concentration; Chemisorption and electrosorption coupling; MoS_2; Porous carbon materials

Contents

Index of figures

Index of tables

Chapter I. Introduction

1.1. Justification

Rare earth elements (REEs) and precious metals play an important role toward electric devices[1,2], catalysis[3,4], semiconductors[5], and medicine[6] because of their special properties. Hydrometallurgy is the main method to extract limited resources, which contains three procedures: leaching target elements from solid resources (leaching process), separating target elements from leaching solutions (enriching process), and reducing enriched target elements into particles for product (reduction process). Nevertheless, during enriching process, it usually comes as a technical limitation in industry.

Referring to REEs and precious metals recovery, plenty of researches have been proposed, such as, solvent extraction[7,8], ion exchange[9,10], chemical precipitation[11,12], and sorption[13,14]. However, most of these approaches are hard for actual application because of large consumption of reagents, or high cost, or poor selectivity. Moreover, they focus on the recovery under high concentration condition, while rare studies are carried within low concentration. There still exists the challenges to efficiently recover REEs and precious metals within low concentration range from aqueous solutions.

Gold (Au)[15,16] as a kind of typical precious metal is widely used not only owing to its value, but also conductivity, sustainability and stability. Cyanide leaching[17,18], the classical leaching method, starts from 100 years ago, being used as the main technique to leach gold due to its economy and simply operation. However, cyanide leaching possesses the dangerous drawbacks of well-known toxicity and explosive. As the progress of world, sustainable and green development of gold mining is a vital topic. Among non-cyanide leaching method, thiosulfate leaching[19–21] owns the advantage of quick leaching rate, cheap waste treatment, and nontoxic process. Whereas, recovery of gold from thiosulfate leaching solution is the primary limitation for thiosulfate leaching application in industries. Herein, the work aims to solve the problem of REEs recovery from aqueous solutions and Au(I) recovery thiosulfate leaching solutions.

Electrosorption[22,23] known as a kind of promising way is used to absorb low-concentration target ions in solutions since the target ions are induced to overcome the electrostatic repulsion and towards the adsorbent under the electric field. Materials as the working electrode are vital for the interaction between electrolyte and electrode. Then, the migration process can be dominated by electric field force and attraction from

applied material. Therefore, the interaction between electrolyte and electrode belongs to chemisorption and electrosorption coupling (CEC) process, which is beneficial for the recovery of REEs and precious metals from solutions.

CEC process strongly relies on the materials with its surficial properties for efficient adsorption, and it can realize highly recovery and selectivity with specific ions. Benefited from its rich sulfur atoms in the structure, molybdenum disulfide (MoS_2) has long been recognized as an outperformer in the sorption of acid metal ions based on the theory of hard and soft acids and bases[24,25]. Motivated by the electric performances of MoS_2 as electrodes as well as its earth abundance and nontoxic, it is timely to investigate whether it could be used as electrodes in the recovery of REEs and precious metals from aqueous solutions.

What's more, according to the ion storage equation in electric double layers (EDL) capacitance, $C = \frac{\varepsilon A}{d}$, capacitance is related with surface area. The target ions are captured *via* physical interaction into the pores formed in EDL. Porous electrodes are beneficial for the recovery of low-concentration REEs and precious metals as well. Carbon materials[26–28], for instance, activated carbon (AC), graphite, graphene, carbon nanotubes, with their super porous structure, low cost, and high specific surface area properties have been found as common adsorbents for metal ions adsorption. Few previous works demonstrated that activated carbon electrode could bind with REEs and precious metals, but focusing on the modification of AC and interaction with metals. During the electro-adsorption process, the function of pores is indispensable. The adsorption process of metals and role of pores on carbons electrode need to be further investigated.

Herein, we explored the recovery of REEs, especially La(III), Gd(III), and Y(III), as represented REEs, in low concentration range from aqueous solutions. Besides, gold, as typical precious metals, in low concentration range was recovered by CEC process. More insights were provided the above-mentioned issues on MoS_2 and porous AC electrodes for adsorption and recovery of target ions. The aim is to provide the insights into recovering low-concentration REEs and Au with MoS_2 and porous carbon-based electrode in environmental application. The study was firstly carried out to deeply evaluate the recovery of low-concentration REEs and Au(I) in the EDL capacitance by MoS_2 and porous structure of carbon-based electrodes.

1.2. Hypothesis

Previous researches[29,30] verified that target ions in aqueous solutions can be efficiently immigrated under the external field. If materials coated on the surface of electrode reacts only one type of components in the electrolyte, the interaction between electrolyte and electrode belongs to CEC process. Under the interaction, target ions will be efficiently and selectivity recovered on the electrodes. Moreover, the redox potential of Au(I) to Au^0 in thiosulfate solutions is about 0.15 eV, which is low enough to be reduced into gold particles on the electrodes with applied voltage. It is promising that the Au(I) is recovered and reduced at the same time, shortening the recovery procedures.

1.3. Objectives

1.3.1. General objective

The objective is to efficient recover low-concentration REEs from aqueous solutions and Au(I) from thiosulfate leaching solutions by CEC process. Based on regulating the chemisorption and electrosorption activities of MoS_2 and porous AC materials, enhanced selective REEs and Au(I) recovery are realized. This study deepens our understanding on the immigration, interaction, and mechanism of REEs and Au(I) on transition metal sulfides, and helps to guide a thought for recovering REEs and precious metal in low concentration range over green and recyclable uses.

1.3.2. Goal

a. Study the regulation of chemisorption and electrosorption activity for REEs uptake in low concentration on oxygen-doped MoS_2 electrodes.
b. Propose the chemisorption modulation activity for trace gadolinium (III) separation and recovery via defects-rich molybdenum disulfide electrodes.
c. Investigate the low-concentration REEs adsorption behaviors on carbon-based electrodes.
e. Explore the electroreduction way to realize efficient Au(I) recovery from thiosulfate solutions via carbon-based electrodes.
f. Analyze the efficient Au(I) recovery from thiosulfate solutions by self-made walnut shell charcoal electrodes.
g. Manipulate porous structure of electrodes for direct, rapid, and selective electro reduction-recovery of Au(I) from thiosulfate leaching solutions.

1.4. References

(1) Zeng, Z.; Xu, Y.; Zhang, Z.; Gao, Z.; Luo, M.; Yin, Z.; Zhang, C.; Xu, J.; Huang, B.; Luo, F.; Du, Y.; Yan, C. Rare-Earth-Containing Perovskite Nanomaterials: Design, Synthesis, Properties and Applications. *Chem Soc Rev* **2020**, *49* (4), 1109–1143. https://doi.org/10.1039/C9CS00330D.

(2) Guo, X.; Zhang, G.; Li, Q.; Xue, H.; Pang, H. Non-Noble Metal-Transition Metal Oxide Materials for Electrochemical Energy Storage. *Energy Storage Mater* **2018**, *15*, 171–201. https://doi.org/10.1016/j.ensm.2018.04.002.

(3) Ryoo, R.; Kim, J.; Jo, C.; Han, S. W.; Kim, J. C.; Park, H.; Han, J.; Shin, H. S.; Shin, J. W. Rare-Earth–Platinum Alloy Nanoparticles in Mesoporous Zeolite for Catalysis. *Nature 2020 585:7824* **2020**, *585* (7824), 221–224. https://doi.org/10.1038/s41586-020-2671-4.

(4) Yuwen, L.; Xu, F.; Xue, B.; Luo, Z.; Zhang, Q.; Bao, B.; Su, S.; Weng, L.; Huang, W.; Wang, L. General Synthesis of Noble Metal (Au, Ag, Pd, Pt) Nanocrystal Modified MoS2 Nanosheets and the Enhanced Catalytic Activity of Pd-MoS_2 for Methanol Oxidation. *Nanoscale* **2014**, *6* (11), 5762–5769. https://doi.org/10.1039/c3nr06084e.

(5) Zhou, L.; Gu, H.; Wang, C.; Zhang, J.; Lv, M.; He, R. Study on the Synthesis and Surface Enhanced Raman Spectroscopy of Graphene-Based Nanocomposites Decorated with Noble Metal Nanoparticles. *Colloids Surf A Physicochem Eng Asp* **2013**, *430*, 103–109. https://doi.org/10.1016/j.colsurfa.2013.04.012.

(6) Zheng, B.; Fan, J.; Chen, B.; Qin, X.; Wang, J.; Wang, F.; Deng, R.; Liu, X. Rare-Earth Doping in Nanostructured Inorganic Materials. *Chem Rev* **2022**, *122* (6), 5519–5603. https://doi.org/10.1021/ACS.CHEMREV.1C00644.

(7) Tang, Z.; Wei, Q.; Guo, B. A Generic Solvent Exchange Method to Disperse MoS_2 in Organic Solvents to Ease the Solution Process. *Chemical Communications* **2014**, *50* (31), 3934–3937. https://doi.org/10.1039/c4cc00425f.

(8) Kim, E.; Lee, J.; Kim, D.; Lee, K. E.; Han, S. S.; Lim, N.; Kang, J.; Park, C. G.; Kim, K. Solvent-Responsive Polymernanocapsules with Controlled Permeability: Encapsulation and Release of a Fluorescent Dye by Swelling and Deswelling. *Chemical Communications* **2009**, No. 12, 1472–1474. https://doi.org/10.1039/B823110A.

(9) Xie, F.; Zhang, T. A.; Dreisinger, D.; Doyle, F. A Critical Review on Solvent Extraction of Rare Earths from Aqueous Solutions. *Miner Eng* **2014**, *56*, 10–28. https://doi.org/10.1016/J.MINENG.2013.10.021.

(10) Naushad, M.; Mittal, A.; Rathore, M.; Gupta, V. Ion-Exchange Kinetic Studies for Cd(II), Co(II), Cu(II), and Pb(II) Metal Ions over a Composite Cation Exchanger. *Desalination Water Treat* **2015**, *54* (10), 2883–2890. https://doi.org/10.1080/19443994.2014.904823.

(11) Zupanc, A.; Install, J.; Jereb, M.; Repo, T. Sustainable and Selective Modern Methods of Noble

Metal Recycling. *Angewandte Chemie International Edition* **2023**, *62* (5). https://doi.org/10.1002/anie.202214453.

(12) Trinh, H. B.; Lee, J. C.; Kim, S.; Kim, J. Recovery of Cerium from Spent Autocatalyst by Sulfatizing-Leaching-Precipitation Process. *ACS Sustain Chem Eng* **2020**, *8* (41), 15630–15639. https://doi.org/10.1021/ACSSUSCHEMENG.0C05136.

(13) Li, Z.; Li, X.; Raiguel, S.; Binnemans, K. Separation of Transition Metals from Rare Earths by Non-Aqueous Solvent Extraction from Ethylene Glycol Solutions Using Aliquat 336. *Sep Purif Technol* **2018**, *201*, 318–326. https://doi.org/10.1016/J.SEPPUR.2018.03.022.

(14) Wang, L.; Gao, Y.; Chai, Y.; Sun, X. Recovery of Rare Earth by Electro-Sorption with Sodium Diphenylamine Sulfonate Modified Activated Carbon Electrode. *Sep Purif Technol* **2022**, *292*, 121005. https://doi.org/10.1016/J.SEPPUR.2022.121005.

(15) Campeau, D.; León Rayo, D. F.; Mansour, A.; Muratov, K.; Gagosz, F. Gold-Catalyzed Reactions of Specially Activated Alkynes, Allenes, and Alkenes. *Chem Rev* **2021**, *121* (14), 8756–8867. https://doi.org/10.1021/ACS.CHEMREV.0C00788.

(16) Hutchings, G. A Golden Future. *Nat Chem* **2009**, *1* (7), 584. https://doi.org/10.1038/nchem.388.

(17) Schuppe, A. W.; Borrajo-Calleja, G. M.; Buchwald, S. L. Enantioselective Olefin Hydrocyanation without Cyanide. *J Am Chem Soc* **2019**, *141* (47), 18668–18672. https://doi.org/10.1021/jacs.9b10875.

(18) Korolev, I.; Altınkaya, P.; Halli, P.; Hannula, P. M.; Yliniemi, K.; Lundström, M. Electrochemical Recovery of Minor Concentrations of Gold from Cyanide-Free Cupric Chloride Leaching Solutions. *J Clean Prod* **2018**, *186*, 840–850. https://doi.org/10.1016/j.jclepro.2018.03.177.

(19) Hung Ha, V.; Lee, J.; Jeong, J.; Trung Hai, H.; Jha, M. K.; Co Viet, -Dai; Nam, V. Thiosulfate Leaching of Gold from Waste Mobile Phones. *J Hazard Mater* **2010**, *178*, 1115–1119. https://doi.org/10.1016/j.jhazmat.2010.01.099.

(20) Tamayo, J. A.; Gómez, S.; Calderón, J. A. Selective Electrochemical Gold Recovery from Leaching Solutions of Thiosulfate. *J Electrochem Soc* **2017**, *164* (7), D363–D370. https://doi.org/10.1149/2.0341707JES/XML.

(21) McNeice, J.; Mahandra, H.; Ghahreman, A. Application of Biogenic Thiosulfate Produced by Methylophaga Sulfidovorans for Sustainable Gold Extraction. *ACS Sustain Chem Eng* **2022**, *10* (30), 10034–10046. https://doi.org/10.1021/acssuschemeng.2c02872.

(22) Li, P.; Gui, Y.; Blackwood, D. J. Development of a Nanostructured α-MnO_2/Carbon Paper Composite for Removal of Ni^{2+}/Mn^{2+} Ions by Electrosorption. *ACS Appl Mater Interfaces* **2018**, *10* (23), 19615–19625. https://doi.org/10.1021/ACSAMI.8B02471.

(23) Mao, M.; Yan, T.; Shen, J.; Zhang, J.; Zhang, D. Capacitive Removal of Heavy Metal Ions

from Wastewater via an Electro-Adsorption and Electro-Reaction Coupling Process. *Environ Sci Technol* **2021**, *55* (5), 3333–3340. https://doi.org/10.1021/ACS.EST.0C07849.

(24) Wang, W.; Yang, P.; Jian, Z.; Li, H.; Xing, Y.; Zhang, S. Rational Design of a 3D MoS_2/Dual-Channel Graphene Framework Hybrid as a Free-Standing Electrode for Enhanced Lithium Storage. *J Mater Chem A Mater* **2018**, *6* (28), 13797–13805. https://doi.org/10.1039/c8ta03272f.

(25) Radisavljevic, B.; Radenovic, A.; Brivio, J.; Giacometti, V.; Kis, A. Single-Layer MoS2transistors. *Nat Nanotechnol* **2011**, *6* (3), 147–150. https://doi.org/10.1038/nnano.2010.279.

(26) Wu, X.; Chen, Y.; Xing, Z.; Lam, C. W. K.; Pang, S.; Zhang, W.; Ju, Z. Advanced Carbon-Based Anodes for Potassium-Ion Batteries. *Adv Energy Mater* **2019**, *9* (21). https://doi.org/10.1002/aenm.201900343.

(27) Huijgen, W. J. J.; Witkamp, G. J.; Comans, R. N. J. Mineral CO_2 Sequestration by Steel Slag Carbonation. *Environ Sci Technol* **2005**, *39* (24), 9676–9682. https://doi.org/10.1021/ES050795F.

(28) Li, A.; Dong, C.; Dong, W.; Atinafu, D. G.; Gao, H.; Chen, X.; Wang, G. Hierarchical 3D Reduced Graphene Porous-Carbon-Based PCMs for Superior Thermal Energy Storage Performance. *ACS Appl Mater Interfaces* **2018**, *10* (38), 32093–32101.

(29) Li, P.; Schott, J. A.; Zhang, J.; Mahurin, S. M.; Sheng, Y.; Qiao, Z. A.; Hu, X.; Cui, G.; Yao, D.; Brown, S.; Zheng, Y.; Dai, S. Electrostatic-Assisted Liquefaction of Porous Carbons. *Angewandte Chemie International Edition* **2017**, *56* (47), 14958–14962. https://doi.org/10.1002/ANIE.201708843.

(30) Tiras, E.; Ardali, S.; Tiras, T.; Arslan, E.; Cakmakyapan, S.; Kazar, O.; Hassan, J.; Janzén, E.; Ozbay, E. Effective Mass of Electron in Monolayer Graphene: Electron-Phonon Interaction. *J Appl Phys* **2013**, *113* (4), 043708. https://doi.org/10.1063/1.4789385.

Chapter II. Antecedents

2.1. Introduction

Recently, MoS_2, as a typical layered transition-metal dichalcogenide with unique crystal structures and unusual properties, has attracted increasing interest[1]. In the structures of MoS_2 (Figure 2-1a), strong covalent bonds exist between the Mo and S atoms and weak Van der Waals forces connect the layers. The interval distance between adjacent layers is 0.65 nm[2,3]. The Mo-S bond length, crystal lattice constant and distance between the upper and lower sulfur atoms are 0.24, 0.32 and 0.31 nm, respectively. To date, MoS_2 has been found to possess three crystal structures, namely, 1T (tetragonal symmetry, each repeat unit with one layer), 2H (hexagonal symmetry, each repeat unit with two layers) and 3R (rhombohedral, each repeat unit with three layers), according to the coordination mode between the Mo and S atoms and the stacking order between layers, as shown in Figure 2-1b. Among these structures, 2H-MoS_2 is the most stable under normal conditions.

Because of its unique physical, chemical and electrical properties, MoS_2 has been researched in various fields, including desalination, energy storage and conversion, lithium and sodium batteries, biology, optoelectronics and nanodevices. So far, many works have been carried out to regulate the structure of MoS_2 for the enhancement of its performance based on different dimensional morphologies[4]. However, owing to the drawbacks of MoS_2, which include a lack of active sites, hydrophobicity and a slow transfer of photoelectrons, it must be modified with regards to its surface, structural and semiconducting properties for enhanced applications. In this review, we introduce the methods for the preparation and structural engineering of zero-, two- and three-dimensional (0D, 2D and 3D) MoS_2. Simultaneously, the perspectives of 0D, 2D and 3D MoS_2 are proposed in different application fields to provide vital guidance for researchers.

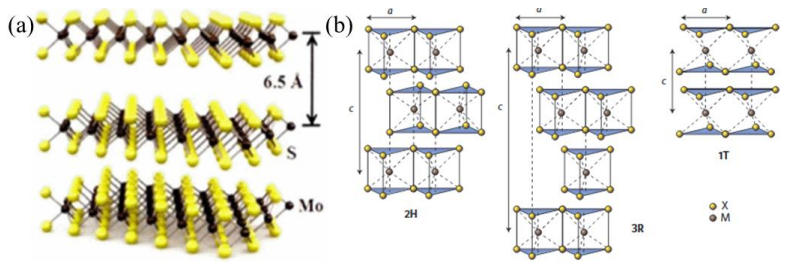

Figure 2-1. Layered structure of (a)[5] bulk MoS_2 and (b)[6] its three crystal structures: 2H; 3R; 1T.

2.2. Structural properties

2.2.1. 0D MoS_2

MoS_2 has a layered S-Mo-S structure and weak Van der Waals forces between the layers and can therefore form a 0D structure. The size of 0D MoS_2 is less than 10 nm and is very small in three dimensions, similar to a point. Due to the quantum limitation and small size effects, 0D MoS_2 exhibits a direct band gap, which endows it with high quantum efficiency, in contrast to bulk MoS_2 with an indirect band gap. 0D MoS_2 is considered a promising new material with low toxicity and good biocompatibility that can be used as a cell penetration probe and in vitro imaging and fluorescence sensing.

Photoluminescence

Compared with the quenching properties of MoS_2[7], one of the most promising properties of 0D MoS_2 is photoluminescence (PL). The PL emission spectra of 0D MoS_2 are at different excitation wavelengths (320–520 nm) compared with that of bulk MoS_2[8]. With a change in excitation wavelength, the emission wavelength also changes, exhibiting an excitation wavelength-dependent effect. Fluorescence microscopy images of dried 0D MoS_2 at 405, 488 and 552 nm show that 0D MoS_2 emits blue, green and red light, respectively.

In addition, there exist some relationships between the PL intensity of 0D MoS_2 and pH. For example, 0D MoS_2 synthesized by Wang et al.[9] showed that its PL is almost unaffected by pH. However, the PL of 0D MoS_2 synthesized by Dai et al.[10] was basically influenced by pH. At pH of 2–6, the PL of 0D MoS_2 increases with increasing pH. However, the PL decreases with increasing pH without the movement of the peak at pH of 10–12. Interestingly, Siddiqui et al.[11] prepared 0D MoS_2 with excitation wavelength independence. When the excitation wavelength varied from 260 to 350 nm, the emission wavelength was 448 nm.

Anti-Stokes luminescence

Anti-Stokes luminescence is a short wavelength and high frequency light excited from long wavelength, low frequency excitation light. Dong et al.[12] reported the anti-Stokes luminescence properties of 0D MoS_2 in the wavelength range of 775–900 nm. When the excitation wavelength changed from 775 to 900 nm, the corresponding emission peak moved from 525 to 610 nm.

Cytotoxicity

Since 0D MoS_2 can be easily dispersed in water and exhibits strong fluorescence properties, concerns have been raised regarding its cytotoxicity. For instance, Xu et al.[13]

used the MTT method to detect the cytotoxicity of 0D MoS_2 and HEK 293T and HeLa cells with different concentrations of 0D MoS_2 were incubated for 24 h to conduct cell survival experiments. The results showed that the survival rate of the HEK 293T and HeLa cells decreased by ~1% and ~11%, respectively, when the concentration of 0D MoS_2 was 250 μg/mL. When the concentration of 0D MoS_2 was increased to 2000 μg/mL, the cell survival rate of HEK 293T cells decreased by ~12% and that of HeLa cells by ~30%, revealing that 0D MoS_2 was harmless to the cells. The results showed better biocompatibility compared to the cytotoxicity of MoS_2 reported by Wang et al.[14] and also indicated the potential application value of 0D MoS_2 in the field of bioimaging.

Electrochemical activity

Recently, researchers have attempted to explore the high catalytic behavior of 0D MoS_2 in the hydrogen evolution reaction. Qiao et al.[15] synthesized 0D MoS_2 via multiple lithium intercalation and stripping and then tested its electrocatalytic activity using 0.5 M H_2SO_4 as an electrolyte in a typical three-electrode system. The results showed that 0D MoS_2 prepared with more stripping cycles had a lower overpotential, higher cathode current and lower Tafel slope. The reason for this was the existence of the rich active edge of 0D MoS_2 that endows it with excellent catalytic performance, thereby representing a new method for the application of 0D MoS_2 in electrochemistry.

2.2.2. 2D MoS_2

2D layered materials refer to planar materials at the nanoscale in only one direction. These materials have transverse dimensions larger than 100 nm and can be several microns or more but are only one or a few atomic layers thick[16]. 2D MoS_2 is a representative transition metal sulfide and has attracted extensive attention from researchers. Single- or few-layer crystals of MoS_2 can be obtained by interlayer stripping because of the weak Van der Waals forces between adjacent layers. Like graphene, the transformation of MoS_2 from the bulk phase to a 2D layered structure produces some special physicochemical properties, such as unique mechanical and electrical properties and band gap tunable fluorescence luminescence properties. It has been widely used in dry lubrication, catalysis, photovoltaic equipment and energy applications.

Electronic structure

MoS_2 is a unique layered transition metal sulfide and its band gap varies with the number of layers. The direct band gap of bulk MoS_2 is ~1.29 eV[17]. Due to its ultrathin 2D crystal structure, the band structure and band gap of MoS_2 are affected by the

quantum local effect[18]. The highest valence band (VB) is at the Γ point and the lowest conduction band (CB) is about half of the Γ-K direction, which causes the transition from an indirect to direct band gap[19]. As the number of layers decreases, the lowest band in the CB rises, thereby increasing the overall bandwidth. The K point in the Brillouin region is mainly due to the fact that the d orbital of the Mo atom is not affected by the interlayer interaction. The direct band gap only increases by ~0.05–0.10 eV at the K point in the Brillouin region[20]. The CB state near the Γ point is caused by the interlayer interaction between the P_z orbital of the S atom and the d orbital of the Mo atom. Therefore, the band gap is more susceptible to the layer number change at the Γ point[21]. When the number of layers becomes one (i.e., a single layer), the indirect conversion band gap is larger than the direct conversion band gap and the minimum direct band gap is ~1.9 eV at the K point. This special transition from indirect to direct band gap originates from the interlayer influence and quantum local and long-range Coulombic effects[22].

Optical properties

Photoexcited optical studies show that monolayer MoS_2 has a very high quantum yield with a photoconversion band gap of ~1.9 eV. Compared with bulk MoS_2, the quantum yield of 2D MoS_2 is very high at 4×10^{-3} [19]. Thus, photoemission and Raman spectroscopy can be used to characterize the quality and crystallinity of 2D MoS_2[23]. The photoemission spectrum of 2D MoS_2 has two exciton peaks at the K point, namely, the exciton A peak and exciton B peak, which may be caused by the spin orbit splitting of VB. VB splitting occurs at the K point, the highest point in the VB. Therefore, two conversions from excitons to the double degenerate CB are possible[24]. 2D MoS_2 possesses higher mechanical strength and Young's modulus than steel[25]. The distortion of 2D MoS_2 can reach 11% without rupture[26]. In addition, 2D MoS_2 exhibits piezoelectricity and can be used in sensitive sensors[27]. Theoretical calculations have shown that the effective electron mass of 2D MoS_2 at the K point is 0.48 m_e, much larger than the value of 0.012 m_e for graphene[28]. Feng et al.[29] created a broadband optical funnel by adjusting the tension of 2D MoS_2.

2.2.3. 3D MoS_2

2D MoS_2 can easily aggregate and stack during use, owing to its large surface energy and small particle size. During the aggregation process, the dispersion stability and effective specific surface area are reduced. Moreover, its solid-liquid separation and recycling performance are poor. The 3D structure is an effective method to improve

the performance of 2D MoS_2 and can effectively reduce its inherent stacking and aggregation characteristics, thereby enhancing its specific surface area, reducing its ion diffusion resistance and increasing its number of active sites[19]. Gelation is the most common method to achieve the 3D structure of MoS_2. Through crosslinking polymerization between 2D MoS_2 and polymers, a spatial network structure with numerous pore structures and strong mechanical stability can be formed. In order to achieve the 3D structure of MoS_2, various functional groups, including carboxyl, hydroxyl and mercaptan groups and alkyl chains, can be introduced on the surface of 2D MoS_2 by organic modification[30]. A crosslinking agent is then added to make the modified 2D MoS_2 crosslinked and polymerized to form MoS_2 gel.

Characterization

Researchers have designed and constructed a series of 3D MoS_2-based materials with various frameworks (e.g., aerogels, sponges and foams). These 3D MoS_2-based materials not only retain the intrinsic properties of MoS_2 but also possess some new collective physiochemical properties, including high porosity, low density, large specific surface area, strong mechanical strength and unique electrochemical performance. Furthermore, 3D MoS_2-based materials obtain multi-level pore structures (micropores, mesopores and macropores) and internal connection frameworks, which endow them with improved surface accessibility and better mass transport.

Zhang et al.[30] prepared a MoS_2/graphene foam using nickel foam as a template. Nickel foam itself is a porous, microporous structure and the MoS_2/graphene obtained by this method has a large specific surface area with a Tafel slope of only 42.8 mV/decade. The existence of the 3D structure not only promotes the electron transfer process but also effectively avoids the volume change of the electrode for long periods in electrocatalytic hydrogen evolution, thereby enhancing the stability of the electrode. Liu et al.[31] synthesized a MoS_2/graphene hydrogel via a one-step hydrothermal method, which confirmed the existence of a microporous structure by scanning electron microscope (SEM) and specific surface area test, and directly used the prepared material as the electrode for an electrocatalytic hydrogen evolution reaction. The electrochemical experiments showed that MoS_2 has a lower initial potential and Tafel slope and its current density reached 52.4 A/g at a potential of 400 mV.

2.3. Preparation of 0D, 2D, and 3D MoS_2

2.3.1. Synthesis of 0D MoS_2

0D MoS_2 has received extensive attention because of its unique optical properties and broad application prospects[32]. So far, the mainstream synthesis techniques of 0D MoS_2 have developed into liquid exfoliation, electrochemical, Li^+ intercalation and hydrothermal synthesis.

Liquid exfoliation method

The liquid exfoliation method uses ultrasonication to disperse bulk MoS_2 in an organic solvent and ultrasonically treat the suspension. During the ultrasonication process, MoS_2 is damaged and sheared into small sizes by mechanical force[33]. The choice of solvent is particularly important because the solubility and surface tension index of the solvent are related to the good monodispersity[34]. Gopalakrishnan et al.[35] subjected a MoS_2 powder to bath sonication and probe sonication in sequence for 3.5 h in a 1-methyl-2-pyrrolidone (NMP) solution and then centrifuged it to obtain heterodimensional nanostructures on the upper layer of the solvent, as shown in Figure 2-2. In bath sonication, the hydrodynamic forces generated by the increase in pressure and temperature promoted the cleavage of bulk MoS_2 into small particles. Probe sonication broke most of the nanosheets into ultrathin sheets with 0D MoS_2 interspersed. The presence of NMP maintains the stability of the exfoliated MoS_2 dispersion the highest. This method yielded ~2 nm single-layer 0D MoS_2, which slightly agglomerated over time and could become 10 nm after 7 d. Another commonly used solvent is N,N-dimethylformamide (DMF). Wang et al.[36] placed bulk MoS_2 powder in DMF and successfully prepared 0D MoS_2 of 1.47 ± 0.16 nm by a combination of ultrasonic exfoliation for 4 h and gradient centrifugation. Dong et al. used TBA to insert the interlayer and ultrasonic treatment to assist in the preparation of bulk MoS_2 flakes with a lateral size of ~13 nm[12]. The flakes were uniformly distributed with 0D MoS_2 in a honeycomb lattice atomic structure, a uniform crystal form and a height of 1–2 nm.

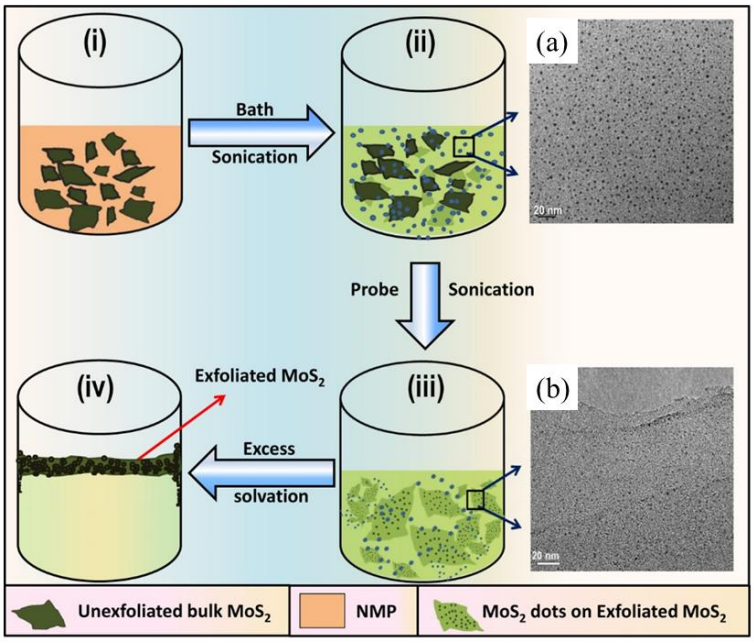

Figure 2-2. Schematic diagram of 0D MoS_2 synthesized by liquid exfoliation method (insets (a,b): TEM images of 0D MoS_2)[37].

Electrochemical method

The electrochemical method is an environmental-friendly, efficient and condition-controllable method for preparing 0D MoS_2[38]. A direct current (DC) voltage is applied to the electrolyte and free radicals are generated in the solution. The radicals etch MoS_2, thereby triggering its cleavage, leading to further exfoliation of the bulk material that results in monolayer or multilayer 0D MoS_2[39]. Shrivastava et al.[40] placed MoS_2 microspheres in a two-electrode system of an electrochemical cell with a 1 mol% lithium bis-trifluoromethylsulphonylimide ionic liquid as the electrolyte. A constant DC voltage of 5 V was applied to the electrode pair and the reaction continued for 3 h. 0D MoS_2 was separated from the supernatant after centrifugation, washed with acetone and dried at room temperature to obtain 0D MoS_2 in powder form. Li et al.[41] used the electro-Fenton reaction to generate a large number of hydroxyl radicals, which acted on the preparation of 0D MoS_2, as shown in Figure 2-3. The nanosheets could be completely converted into uniformly distributed single 0D MoS_2 by continuously applying a potential of -0.5 V and bubbling O_2 to the mixed solution containing MoS_2 nanosheets and $FeSO_4$ for 60 min. The electro-Fenton reaction can be used to easily obtain nanosheets with different nanopores, as well as 0D MoS_2, by controlling the time.

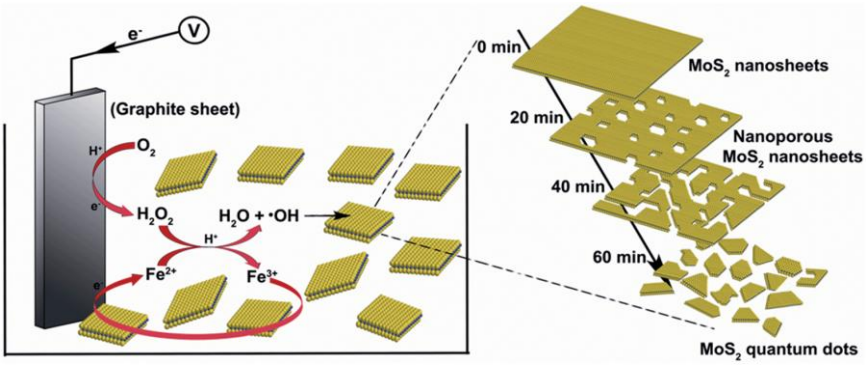

Figure 2-3. Schematic diagram of 0D MoS_2 synthesized by electrochemical method[41].

Intercalation method

Intercalation is the most suitable route for the large-scale production of monolayer MoS_2 and 0D MoS_2. By controlling the number of repeated exfoliation steps on the sample by lithium intercalation, monolayer MoS_2 nanosheets with different lateral dimensions can be generated until a large number of 0D MoS_2 monolayers with sufficiently small size can be obtained[42]. Three important mechanisms contribute to the exfoliation of MoS_2 and the preparation of 0D MoS_2: (1) the intercalation agent intercalates between the layers of the material, which weakens the interlayer force; (2) the intercalation agent reacts violently with water to generate H_2, which further increases the interlayer spacing; (3) Coulombic repulsion exists between the layers[43]. Lithium-containing compounds and some alkali metal compounds can be used as intercalation agents, among which n-butyllithium (n-BuLi) is widely used for the exfoliation of layered materials. Qiao et al.[42] soaked MoS_2 powder in an n-BuLi solution for a long period, followed by stripping, filtration, washing, sonication and drying. The above process was repeated three times and single-layer 0D MoS_2 was finally prepared. n-BuLi easily leads to the transformation of MoS_2 from the semiconducting 2H phase to the metallic 1T phase during the intercalation process. An et al. proposed the addition of laser radiation-assisted stripping on the basis of Li^+ intercalation to induce the 1T phase transition to 5–10 nm 2H phase 0D MoS_2[44], as shown in Figure 2-4. It is noteworthy that part of the MoS_2 oxidized spontaneously due to laser ablation.

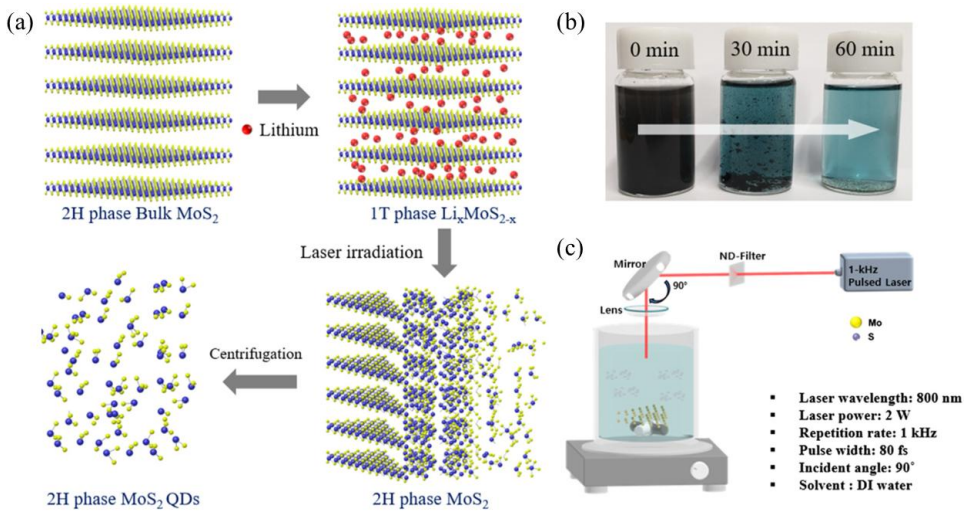

Figure 2-4. Schematic diagram of 0D MoS_2 synthesized by (a) intercalation method. (b) Digital images of solution change during exfoliation. (c) Schematic diagram of experimental setup[44].

Hydrothermal method

Under the premise of using water as the solvent, by placing the precursor solution in a closed reactor and controlling the reaction time, temperature, pressure and other conditions, 0D MoS_2 with different structures and morphologies can be prepared. Wang et al.[9] used sodium molybdate and L-cysteine as precursors and reacted them in an autoclave at 200 °C for 36 h to obtain 0D MoS_2 of ~2.5 nm in solution. Ren et al.[45] converted the sulfur source into dibenzyl disulfide and reacted it with $Na_2MoO_4 \cdot 2H_2O$ at 220 °C for 18 h to obtain 0D MoS_2 with a uniform distribution and an average size of 3.6 nm, as shown in Figure 2-5. Mohanty et al.[47] used ammonium tetrathiomolybdate ($(NH_4)_2MoS_4$) as the single precursor and hydrazine hydrate ($N_2H_4 \cdot 4H_2O$) as the reducing agent and reacted them at 200 °C for 24 h to obtain 0D MoS_2 with an average size of 2.8 nm. This one-step hydrothermal synthesis avoids the inhibition of the performance of 0D MoS_2 by carbon that may be generated in the presence of organic solvents.

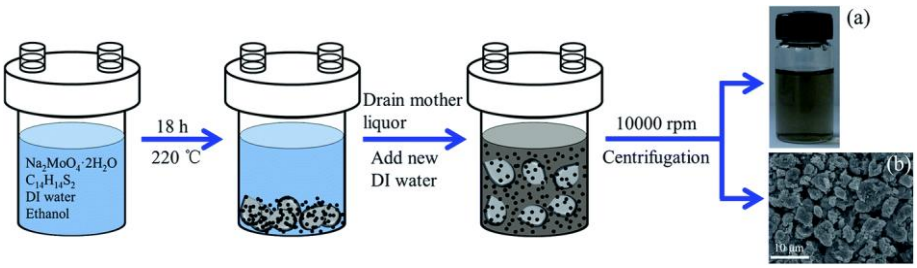

Figure 2-5. Schematic diagram of 0D MoS_2 synthesized by hydrothermal method. (a) Digital image of 0D MoS_2 suspension. (b) SEM image of μm-sized 0D MoS_2[45].

2.3.2. Synthesis of 2D MoS_2

Based on its excellent properties, significant research work has been carried out to prepare high-quality 2D MoS_2. At present, the preparation strategies for 2D MoS_2 can mainly be divided into top-down and bottom-up methods (Figure 2-6)[48]. The basic principle of the top-down method is to reduce the interlayer force of massive MoS_2 and then prepare high-quality materials by stripping. The bottom-up method mainly uses Mo and S precursors to prepare 2D MoS_2 through chemical synthesis.

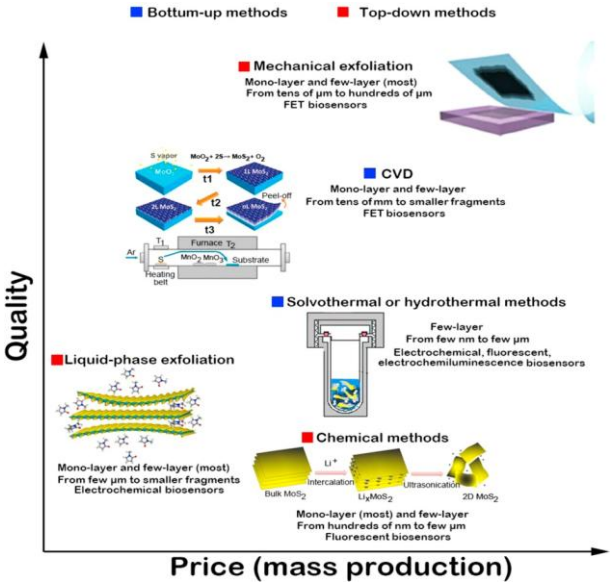

Figure 2-6. Preparation methods of 2D MoS_2[46].

Top-down methods

Micromechanical cleavage method. Micromechanical cleavage is a traditional top-down method for preparing 2D materials. According to the Van der Waals forces between the material layers, suitable adhesive tapes can be selected for artificial stripping to prepare single- or few-layer 2D materials, including the preparation of 2D MoS_2. Li et al.[47] exfoliated suitable MoS_2 from bulk crystals using Scotch tape and then contacted these newly peeled flakes on the tape with the target substrate and rubbed them with tools, such as plastic tweezers, to further cut them. After removing the Scotch tape, the obtained optical microscopy and AFM images of single- or few-layer 2D MoS_2 on the substrate are shown in Figure 2-7a_{1-8}. The height of monolayer MoS_2 is ~0.8 nm, which is consistent with the theoretical value[48]. Similarly, Ghatak et al.[49] obtained different layers of 2D MoS_2 by tape stripping, in which schematics of optical microscopy and field-effect transistors are exhibited in Figure 7b_{1-2}. It is obvious that the separation of the E_{2g}^1 and A_{1g} peaks for three-, two- and single-layer 2D MoS_2 are 23, 21 and 16–18 cm^{-1}, respectively, as characterized by Raman spectroscopy (Figure

2-7b$_{3-4}$). 2D MoS_2 obtained from Scotch tape has nearly perfect surfaces and high crystallinity and is usually used as a material for optoelectronic devices in fundamental research. Simultaneously, the high crystallinity of 2D MoS_2, which leads to its low chemical activity, reduces its application prospects in other aspects, such as photocatalysis and adsorption. In addition, the micromechanical cleavage method faces the limitations of small yield and low production efficiency. These problems limit the application of this method to fundamental research at present, and it is difficult to realize the actual production of 2D MoS_2 using this method.

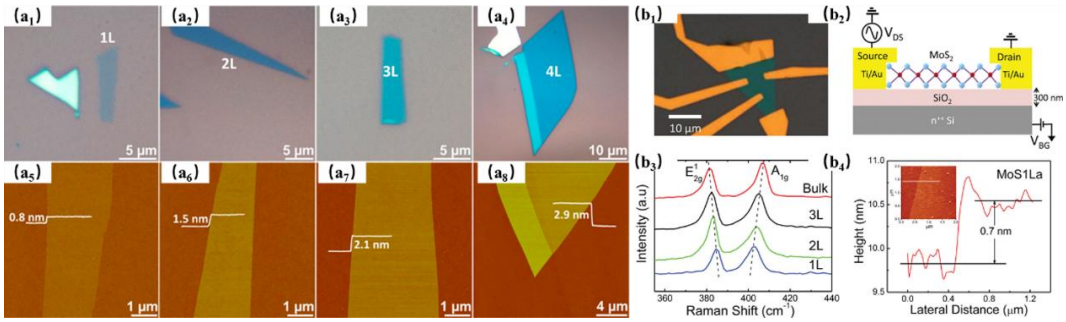

Figure 2-7. (a_{1-4}) Mechanically exfoliated 2D MoS_2 on 300 nm SiO_2/Si: optical microscopy. (a_{5-8}) AFM images[47]. (b_1) Optical micrograph of a typical MoS_2 device. (b_2) Schematic of a single-layer MoS_2 field-effect transistor. (b_3) Raman spectrum. (b_4) Thickness scan of single-layer MoS_2 (inset: AFM image) [49].

Liquid exfoliation. The basic strategy of liquid exfoliation, similar to chemical mechanical exfoliation, is to disperse the bulk crystals in the liquid phase to reduce the interlayer force and then peel the 2D materials from the bulk and disperse them stably in the solvent by assisted shear or ultrasound. In this method, reducing the interlayer force of MoS_2 is pivotal to preparing high-quality 2D MoS_2. Therefore, significant research has been conducted on the method for effectively reducing the interlayer force of MoS_2 in recent years. According to the different methods to reduce the interlayer force, the liquid exfoliation technology of MoS_2 can be mainly divided into solvent-assisted stripping, surfactant-assisted stripping and ion intercalation stripping.

Solvent-assisted stripping, as one of the most direct methods for stripping layered materials, involves dispersing MoS_2 in an organic solvent and then performing ultrasonic stripping to finally obtain 2D MoS_2 by centrifugation. It has been shown that the energy required for stripping layered minerals is strongly related to the difference between the surface energy of layered minerals and the surface tension of the organic solvents[50]. In addition, a suitable solvent can stabilize the dispersion of 2D MoS_2 by inhibiting the agglomeration and restacking between nanosheets. In summary, the type

of dispersing solvent plays a decisive role in the stripping efficiency of MoS_2 and the commonly used solvents include NMP, dimethyl sulfoxide and DMF[53]. Li et al.[51] successfully dispersed massive MoS_2 in an NMP solvent. The high-speed shear effect of the homogenizer was used to overcome the weak Van der Waals forces between the MoS_2 layers in NMP, which reduced the size of the sheet (Figure 2-8a). From AFM images of 2D MoS_2 in the supernatant (MoS_2-p) and the histogram of layer number (Figure 2-8b_{1-2}), the statistical data suggested that the thickness distribution of 2D MoS_2 was wide, while the average layer number was around six. By adding sodium citrate to the NMP suspension, the concentration of 2D MoS_2 in the supernatant (MoS_2-sc) was greatly increased and the dispersion stability was also significantly improved. More importantly, the thickness of the obtained 2D MoS_2 was thinner and the distribution narrower. The average layer number of 2D MoS_2 was about four, of which ~9% were single layers, as shown in Figure 2-8b_{3-4}. Although the effective stripping of MoS_2 can be achieved by using NMP as a solvent, it is difficult to be popularized due to the toxicity of NMP. Furthermore, the removal of NMP (and other solvents) from 2D MoS_2 is also challenging.

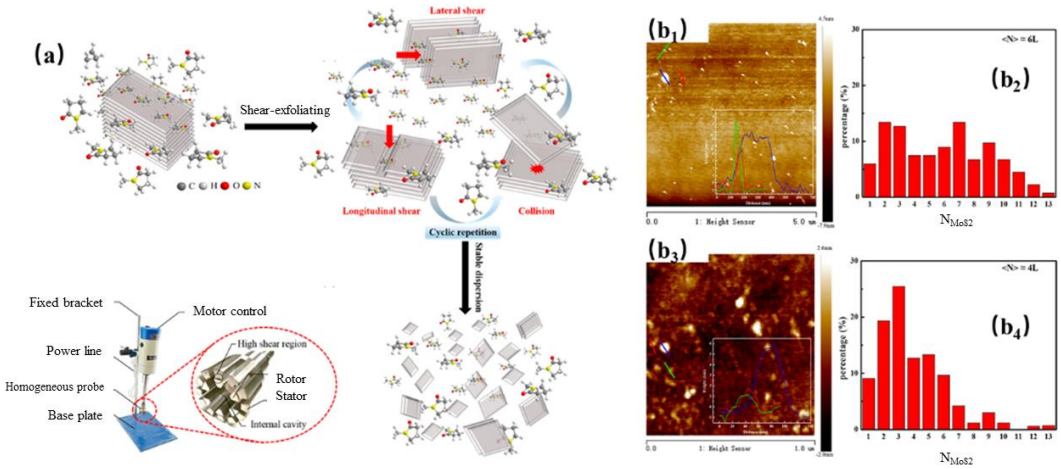

Figure 2-8. (a) Schematic diagram of liquid-phase shear exfoliation of 2D MoS_2 by a high-speed dispersive homogenizer. Typical AFM images (left) and histogram of layer number of 2D MoS_2 calculated from height measurements of AFM images of above 100 flakes (right): (b_{1-2}) MoS_2-p; (b_{3-4}) MoS_2-sc[51].

Surfactant-assisted stripping is the other liquid exfoliation method. Small molecular organics, surfactants and polymers have high adsorption energy on the molybdenite surface, which greatly promotes its separation. The surfactants can be divided into ionic and nonionic depending on their structure. Gupta et al.[52] obtained stable water dispersions of 2D MoS_2 by ultrasonic treatment in the presence of cationic surfactant cetyltrimethylammonium bromide (CTAB) or anionic surfactant sodium

dodecyl sulfate (SDS). Observation of the micromorphology of 2D MoS_2 stripped by CTAB revealed that it was highly dispersed and exhibited a defect-free structure and a hexagonal honeycomb shape (Figure 2-9a_{3-5}). As shown by the AFM analysis in Figure 9a_2, the thickness of 2D MoS_2 was ~1.2 nm, indicating that the nanosheets in the MoS_2 dispersion were composed of one or two layers, irrespective of the surfactant used for exfoliation. Interestingly, the magnitude and distribution of the potential energy of the two dispersions (Figure 2-9a_1) were similar, but their signs were opposite (CTAB was positive and SDS was negative). These charges must have been generated by the interaction between 2D MoS_2 and the surfactant because there were no ionizable groups on the 2D MoS_2. Guardia et al.[53] used a series of nonionic surfactants, including polyoxyethylene sorbitol monooleate (Tween 80), polyoxyethylene sorbitol trioleate (Tween 85), PVP, polyoxyethylene (4) dodecyl ether (Brij 30) and so on, to effectively produce h-BN (Figure 2-9$b_{1,4}$), 2D MoS_2 and WS_2 (Figure 2-9$b_{3,6}$) suspensions with long-term stability (several months). It was clear through AFM analysis that the produced 2D MoS_2 consisted of platelets with lateral dimensions from fifty to several hundred nanometers and thicknesses in several nanometers (Figure 2-9$b_{2,5}$). Unfortunately, the 2D MoS_2 dispersion obtained by this method exhibited anti-aggregation properties and its inherent characteristics were degraded to a certain extent due to the loading and modification of the surfactant.

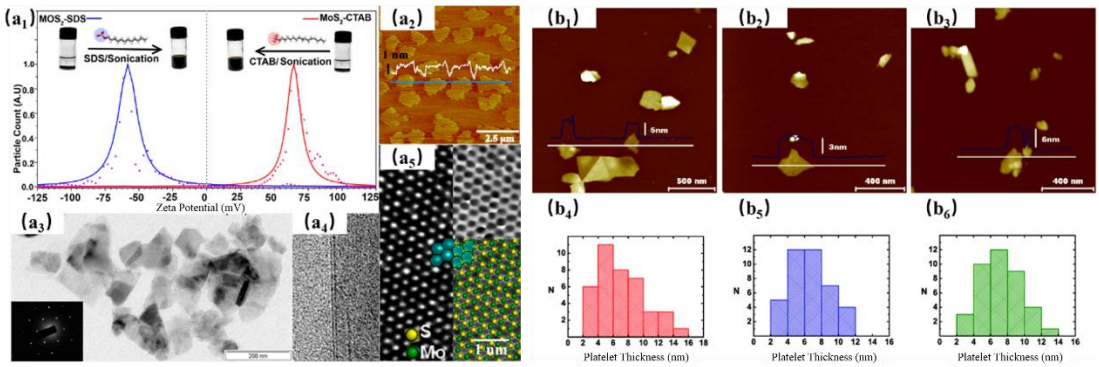

Figure 2-9. Digital image of MoS_2, surfactant solutions before and after sonication and the zeta potential distribution of (a_1) as-prepared MoS_2-CTAB and MoS_2-SDS dispersions. (a_{2-5}) Tapping-mode AFM images (the height profiles of the sheets along the blue line marked on the images are indicated in white), electron microscope images (inset: selected area diffraction pattern) and TEM and HRTEM images of MoS_2-CTAB[52]. AFM images of platelets exfoliated in water with Tween 80 and deposited onto mica substrates: (b_1) h-BN; (b_2) MoS_2; (b_3) WS_2. Histogram of thickness distribution of the sample in the corresponding AFM image: (b_4) h-BN; (b_5) MoS_2; (b_6) WS_2[53].

The ions inserted between the layers can significantly reduce the Van der Waals

forces between the layers of a layered material, and then the slices can be easily separated by a simple mechanical external force. Therefore, ion intercalation is considered an excellent liquid exfoliation method to improve the exfoliation efficiency of layered materials. For MoS_2, because its layer spacing is small (~0.65 nm), only Lewis or alkali metal bases with a small ionic radius can be inserted into the interlayers. At present, Li^+ intercalation stripping is the most versatile and effective method for molybdenite exfoliation, as schematically depicted in Figure 2-10a[54]. The method mainly includes three steps. Firstly, MoS_2 is immersed in an inert solvent containing n-butyl lithium to promote the insertion of lithium ions into the interlayer of MoS_2. The intercalated MoS_2 is then immersed in pure water and Li_xMoS_2 is hydrolyzed rapidly to produce a large amount of hydrogen, which causes the interlayer expansion of MoS_2. Finally, 2D MoS_2 is produced by ultrasonic-assisted stripping[55]. This method is low-cost and scalable. However, n-butyl lithium is highly reductive and reacts violently with water, resulting in serious deformation of the 2D MoS_2 structure. In addition, the intercalation reaction time is particularly long, and the insertion amount of Li^+ in molybdenite cannot be effectively controlled.

Later, Yeon et al.[56] introduced a new strategy for exfoliating nanosheets in an environmentally-friendly and inexpensive aqueous solution using Na^+ instead of Li^+. The morphology and thickness of 2D MoS_2 exfoliated with 0.1 M Na^+ are characterized in Figure 2-10b_{1-2}. The 2D MoS_2 slices are thin enough to clearly observe film holes through them, with most being monolayer or bilayer MoS_2, according to the AFM statistics. The bulk MoS_2 does not show any identifiable emission owing to its indirect band gap. In contrast, the exfoliated 2D MoS_2 has a PL peak near 650 nm, which is similar to that obtained by stripping bulk MoS_2 with Scotch tape. In addition, a strong PL peak is observed at 565 nm (Figure 2-10b_3), which is considered to originate from MoS_2 quantum dots, similar to 0D MoS_2 observed by TEM in Figure 2-10b_4. Similarly, the electrochemically assisted Li^+ intercalation method has been used to achieve the effective stripping of MoS_2, as described in detail in the later electrochemical stripping section.

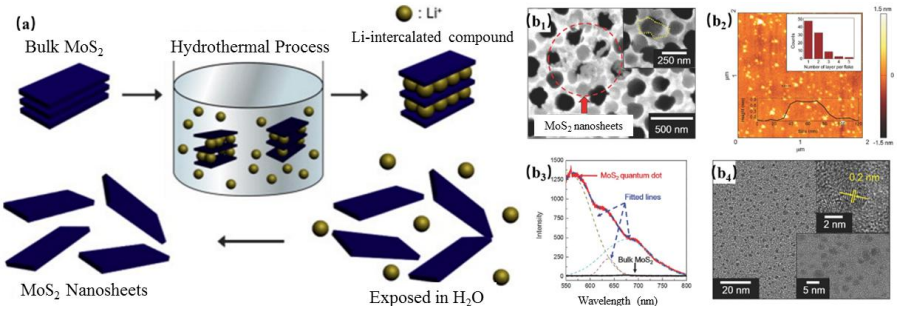

Figure 2-10. (a) Schematic representation of the formation of 2D MoS_2[54]. (b_{1-2}) SEM images (flakes were vacuum filtered on an aluminum oxide membrane) and AFM image of 2D MoS_2 (inset: histogram of the number of layers of 2D MoS_2 measured from AFM images). (b_3) PL spectra of bulk MoS_2 and 2D MoS_2. (b_4) TEM images of MoS_2 quantum dots[56].

In order to achieve green and efficient liquid exfoliation, external forces have also been developed to prepare 2D MoS_2. Usually, grinding and shearing can be used to separate layers from bulk MoS_2, thereby increasing the exfoliation yield of MoS_2 (Figure 2-11a). Yu et al.[57] used pure water as a solvent, separated bulk MoS_2 through the mechanical force between sandpapers in a mechanical sanding machine and dispersed 2D MoS_2 in water by a cell grinder, thereby realizing this stripping process. It is found by SEM in Figure 2-11b_{1-3} that the exfoliated 2D MoS_2 is randomly stacked and the thickness of the sheet is several nanometers. Its transverse size is found to be in the range of 500 nm to 5 μm by TEM (Figure 2-11b_{4-6}), which is consistent with the SEM results. Lee et al.[58] dispersed a MoS_2 powder using ultrasound in a water/ethanol system and obtained a 2D MoS_2 supernatant by two-step centrifugation. It was shown that almost the smallest size of MoS_2 sheet could be obtained at high centrifugal speed, with a primary height of 3–4 nm and an average height of ~7 nm through characterizing the 2D MoS_2 deposited on a Si/SiO_2 substrate by AFM. Although the stability of the obtained dispersions may not be as stable as in organic solvents, these methods can realize on-site production and avoid the use of organic solvents.

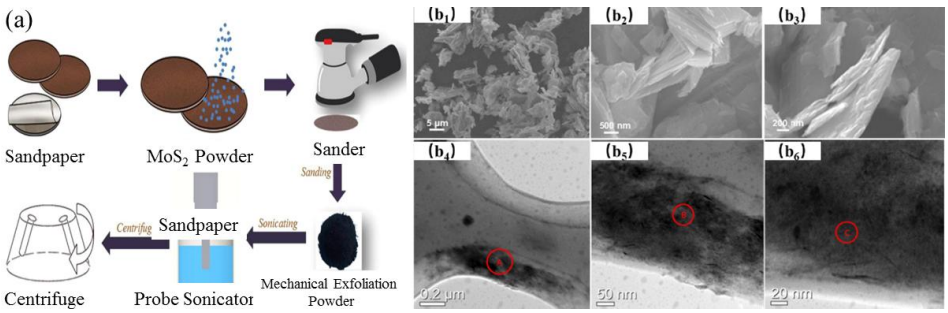

Figure 2-11. (a) Typical green exfoliation process of 2D MoS_2. (b_{1-3}) SEM and (b_{4-6}) TEM Images of 2D MoS_2[57].

Electrochemical exfoliation. Since MoS_2 has certain semiconducting properties,

2D MoS_2 can be prepared by electrochemical expansion. You et al.[59] reported an environmentally-friendly electrochemical stripping method for the rapid and large-scale production of 2D MoS_2 at low cost for the first time. Schematic diagrams of the electrochemically expanded MoS_2 device are shown in Figure 2-12a_{1-2}, where the bulk natural MoS_2 and platinum foil are connected to the two electrodes, respectively, and immersed in a 0.5 M H_2SO_4 aqueous solution. A potentiostat was used to apply a bias potential between MoS_2 and Pt. In the initial stage, a static bias of +1 V was applied to MoS_2 for 10 min, which was then increased to +10 V and kept constant for 30 min to complete the exfoliation process. Finally, 2D MoS_2 could be obtained by placing the expanded MoS_2 in a DMF solution and then stripping the expanded MoS_2 under ultrasonic assistance. As shown in Figure 2-12b_{1-2}, the average morphology height of exfoliated MoS_2 on the Si/SiO_2 substrate measured by AFM was ~1.8 nm and the transverse size was ~10 μm. In addition, EDS scans showed only Mo, S and other four elements, indicating pure MoS_2 on the Si/SiO_2 substrate. The sharp, obvious vibration peaks in the Raman spectrum indicate that it has high crystallinity (Figure 2-12b_{3-4}). By this method, the obtained MoS_2 maintains its semiconducting properties, but its large-scale production remains difficult.

In order to improve the yield of 2D MoS_2, Zeng et al. developed a method based on Li^+-assisted electrochemical exfoliation[60], which could promote the effective stripping of MoS_2. From the flow chart shown in Figure 2-12c, it could be seen that lithium foil replaced the platinum electrode to become a new anode. When the current was released, Li^+ was inserted into the interlayer to reduce the Van der Waals forces between the layers of MoS_2. Subsequently, the MoS_2 after Li^+ intercalation was gradually stripped into highly dispersed 2D MoS_2 under ultrasonic action. Figure 2-12d_1 shows the TEM image of 2D MoS_2, illustrating its high dispersion in the aqueous solution. The electron diffraction pattern in the flat region of the nanosheets (Figure 2-12d_2) and the corresponding HRTEM image (Figure 2-12d_3) show the hexagonal lattice structure with a lattice spacing of 2.7 Å distributed to the (100) crystal plane. The AFM measurement of 2D MoS_2 showed that its thickness was ~1.0 nm, thereby confirming the existence of 2D MoS_2. In addition, the slices of prepared 2D MoS_2 were detected by AFM, with 92% of them found to be monolayers (Figure 2-12e_{1-4}). The most obvious advantage of this method is that it cannot only control Li^+ insertion by controlling the working voltage, but that it also regulates the crystal phase of MoS_2 by adjusting the discharge process of the device.

Bottom-up methods

Vapor deposition. Both physical vapor deposition (PVD) and chemical vapor deposition (CVD) have been used to prepare 2D MoS_2. In PVD, the material source (solid or liquid) is vaporized into gaseous atoms or molecules or partially ionized into ions under vacuum conditions. Thin films are then deposited on the substrate surface through a low-pressure gas (or plasma) process, which is one of the main surface treatment technologies. Importantly, PVD is based on magnetron sputtering, meaning that extremely thin 2D films can be grown on very large areas of various substrate materials. Moreover, PVD has significant advantages in precisely defining the atomic scale, thickness control and interface cleanliness when processed in an ultra-high vacuum environment.

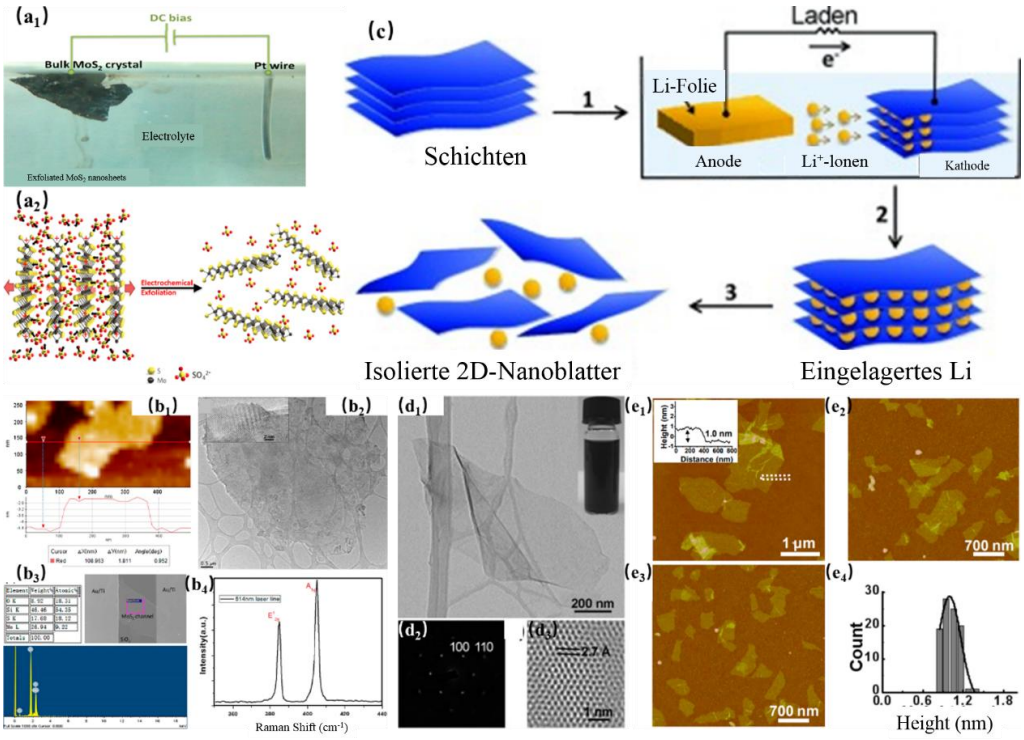

Figure 2-12. (a_1) Stereogram and (a_2) schematic illustration of 2D MoS_2 electrochemical exfoliation experiment setup. (b_1) AFM image, (b_2) TEM image (inset: higher resolution TEM image) [59], (b_3) SEM-EDS and (b_4) Raman spectroscopy of 2D MoS_2. (c) Electrochemical lithiation process for 2D MoS_2. (d_1) TEM image, (d_2) SAED pattern and (d_3) HRTEM image of 2D MoS_2 and (e_{1-3}) AFM images and (e_4) height distribution of 2D MoS_2[60].

Nevertheless, the demands for controllable size, thickness, morphology and scalability have led to the dominant usage of CVD. CVD has been recognized as one of the preferred methods for preparing large-sized 2D MoS_2 with high crystal quality and uniform thickness. The main process is summarized as follows. The precursor containing Mo and S is decomposed into corresponding gaseous molecules under high

temperature and specific atmospheric conditions, and then the reaction deposition is carried out on the substrate to generate 2D MoS_2. Among them, the most common is atmospheric pressure CVD (APCVD) with MoO_3 as the precursor. Of course, in addition to MoO_3, the molybdenum source mainly includes $MoCl_5$ and elemental Mo[61], while the sulfur source is mainly sulfuring powder. Generally, MoO_3 and sulfur powder are placed in a single-zone tube furnace to effectively CVD grow MoS_2 on the substrate in an inert gas atmosphere (Figure 2-13a). The reaction proceeds as a step-by-step vulcanization process described by three intermediate reactions[62]:

$$2MoO_3 + S \rightarrow 2MoO_2 + SO_2 \quad (1)$$

$$2MoO_2 + 5S \rightarrow 2MoOS_2 + SO_2 \quad (2)$$

$$2MoOS_2 + S \rightarrow 2MoS_2 + SO_2 \quad (3)$$

Perkgoz et al.[63] used APCVD to grow monolayer 2D MoS_2 and the deposition duration and temperature effect were systematically changed to better understand MoS_2 deposition and the influence of these parameters on the quality of the monolayer sheets. Figure 2-13b_{1-4} displays the TEM/HRTEM and SAED images of 2D MoS_2 to further understand its growth structure under better conditions. It can be seen that 2D MoS_2 with triangular and "chip" shapes were successfully grown, corresponding to the periodic atomic arrangement shown in Figure 2-13b_3. The symmetry of the diffraction spots, as shown in Figure 2-13b_4, indicates that the monolayer sheets were continuous single crystals with no rotational boundary, illustrating the high crystallinity of 2D MoS_2. Although the use of APCVD can achieve grain sizes of up to hundreds of microns of all-round growth, the process is seriously affected by many restrictions, such as overall thickness control, coverage uniformity and repeatability of operation. The variation in the characteristic morphology is related to the relative content of the precursor loaded into the reactor, leading to the consistency of the coverage and feature size remaining a challenge.

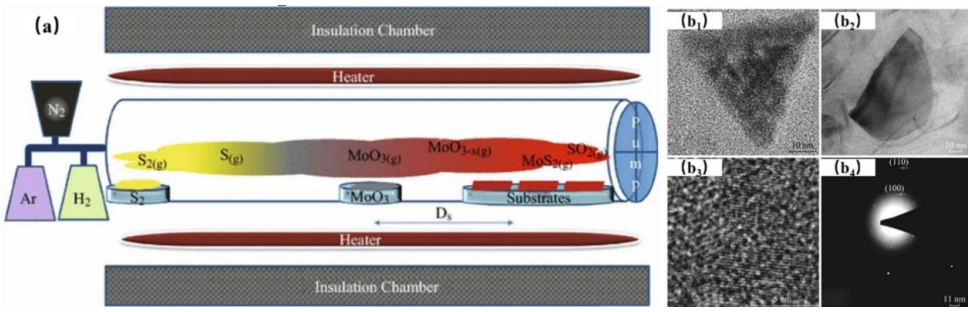

Figure 2-13. (a) CVD system for deposition of 2D MoS_2. (b_{1-2}) TEM images, (b_3) periodic atomic arrangement and (b_4) SAED pattern of 2D MoS_2[63].

Metal-organic/organometallic chemical vapor deposition (MOCVD/OMCVD) is

a new technology in which the gas molecules of organometallic compounds are sent to the reaction chamber with a carrier gas and undergo thermal decomposition reactions to form the compound. The first two letters, “MO” or “OM”, refer to metal-organic or organometallic as the precursor for the growth of sheet. Chowdhury et al.[64] used $Mo(CO)_6$, a metal-organic compound, and $(C_2H_5)_2S$ as precursors, which were kept in bubblers in APs at 45 °C and room temperature, respectively (Figure 2-14a). A large area of 2D MoS_2 was then deposited in a furnace at 850 °C for 1 min through a needle valve, which was uniformly covered and non-polluting on the whole substrate. The Raman spectrum in Figure 2-14b$_1$ exhibits that there are two different peaks at ~386 and ~406 cm^{-1}, which are consistent with the vibrations of the Mo-S phonon mode E_{2g}^1 (in-plane) and A_{1g} (out-plane), respectively, thereby proving the existence of MoS_2. After vulcanization (Figure 2-14b$_2$), most of the defect-induced peaks in the growth samples disappeared, indicating that the defect density decreased and the crystal quality improved.

Liu et al.[65] designed a bifunctional precursor, molybdenum dimethyldithiocarbamate (Mo-DMDTC), which is a metal-organic compound. The CVD diagram is displayed in Figure 14c. It is clear that Mo-DMDTC decomposes at elevated temperatures, providing a Mo source for the CVD growth of MoS_2. Importantly, the presence of organic compounds reduces the free energy of MoS_2 nucleation on the substrate, namely, organic promoters, which also greatly promote the growth of MoS_2 (Figure 2-14d$_1$). The UV-vis spectra (Figure 2-14d$_2$) show that when the molar ratio of DMDTC and Mo^{5+} reached five, the absorbance was close to saturation, indicating that the coordination number of Mo was close to five. A large area of triangular 2D MoS_2 with a length of 20–30 μm, was obtained on a sapphire substrate based on CVD, as shown in Figure 2-14d$_3$. The thickness scan analysis of AFM suggested that the thickness of triangular MoS_2 was ~0.65 nm, corresponding to monolayer MoS_2 (Figure 2-14d$_4$).

In order to prepare large-sized and uniform 2D MoS_2 with excellent electrical properties, researchers have subsequently proposed the thermal decomposition of precursors containing both molybdenum and sulfur atoms. Compared with MoO_3 and $MoCl_5$, the method based on the pyrolysis of $(NH_4)_2MoS_4$ to grow 2D MoS_2 has the advantages of a single precursor source and large growth window and therefore the potential for large-scale production. Fei et al.[66] in-situ observed the thermal decomposition of $(NH_4)_2MoS_4$ and subsequent 2D MoS_2 crystallization behavior by TEM (Figure 2-15a). The pattern evolution with increasing temperature, as exhibited

in Figure 2-15b$_{1-4}$, was clearly observed by SAED. From room temperature (25°C) to 400, 780 and then 900 °C, the pattern displays no diffraction ring, a fuzzy diffraction ring, a sharper bright diffraction ring and then a discrete diffraction ring, respectively. In summary, the crystallization of MoS_2 occurs at 400–900 °C in the vacuum, the crystal size of MoS_2 increases rapidly after 800 °C and MoS_2 finally decomposes at high temperature. The reaction equation of $(NH_4)_2MoS_4$ pyrolysis to MoS_2 in a N_2 environment is shown as follows:

$$(NH_4)_2MoS_4 \rightarrow 2NH_3 + H_2S + MoS_3\ (120 - 360\ °C) \quad (4)$$

$$MoS_3 \rightarrow MoS_2 + S\ (> 800\ °C) \quad (5)$$

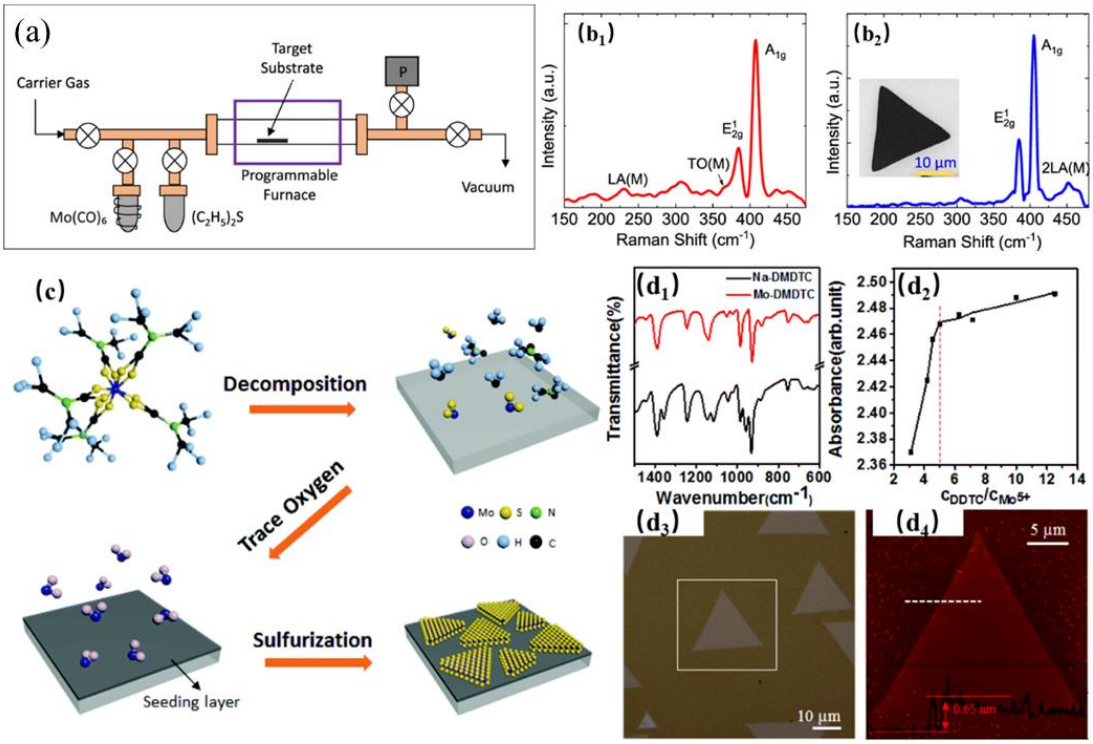

Figure 2-14. (a) Schematic of MOCVD growth system[64]. Raman spectrum of MoS_2 films (b$_1$) before and (b$_2$) after sulfurization at 850°C for 30 min (inset: SEM image of a triangular MoS_2 domain following sulfurization). (c) Schematic of 2D MoS_2 synthesis. FTIR spectra of Na-DMDTC and (d$_1$) Mo-DMDTC. UV-vis absorbance (at 210 nm) of the mixture of Na-DMDTC and (d$_2$) $MoCl_5$ with varied molar ratios. (d$_3$) Optical image of 2D MoS_2. (d$_4$) AFM image of 2D MoS_2 marked with a square box[65].

The average grain size of MoS_2 increases with increasing temperature (820–850°C), i.e., it is 3.2 nm at 820°C, 6.5 nm at 840°C and 18.5 nm at 850°C (Figure 2-15d$_1$). The same test result can also be observed in the in-situ TEM images of Figure 2-15c$_{1-4}$. Figure 2-15d$_2$ exhibits the in-situ Raman spectra of the fresh chips, including the $(NH_4)_2MoS_4$ precursor and the grown MoS_2 (annealed at 850 °C for 30 min). Notice

that the peak intensity of E^1_{2g} is over 50% of the A_{2g} peak, suggesting the horizontal growth of MoS_2. The distance between the two Raman peaks is ~25.5 cm^{-1}, corresponding to four to five layers of MoS_2. Compared with other preparation methods, the vapor deposition method can be used to prepare single- or few-layer MoS_2 with a large diameter, and the synthesized 2D MoS_2 has the advantage of high crystallinity. However, the operation process of this method is extremely complex and the energy consumption is very high, so it is still unable to realize the mass production of 2D MoS_2.

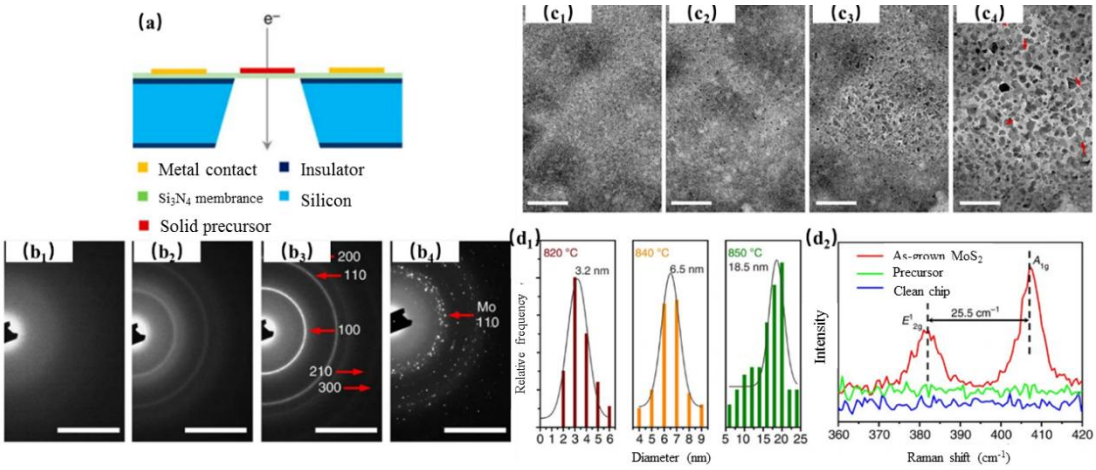

Figure 2-15. (a) Schematic side view of experimental setup of in-situ TEM heating stage. (b_{1-4}) Evolution of SAED patterns across a wide temperature range: (b_1) 25°C; (b_2) 400°C; (b_3) 780°C; (b_4) 900°C. (c_{1-4}) TEM images showing the size of 2D MoS_2 increasing with increasing temperatures: (c_1) 800°C; (c_2) 820°C; (c_3) 840°C; (c_4) 850°C. (d_1) Statistical distribution of 2D MoS_2 size as a function of heating temperature from c_{1-4}. (d_2) Raman spectra of silicone chip, $(NH_4)_2MoS_4$ precursor and as-grown MoS_2[66].

Hydrothermal/solvothermal method. Hydrothermal/solvothermal syntheses are typical bottom-up methods that are widely used in the synthesis of 2D MoS_2, owing to their simplicity, high efficiency and strong adaptability. Generally, the Mo source (e.g., MoO_3, ammonium molybdate or sodium molybdate) and S source (e.g., sulfur powder, KSCN or thiourea) are dissolved in an aqueous solution/organic solvent at a certain ratio. The solution is then transferred to a sealed reactor and kept at ~200 °C for a certain period (several to more than ten hours), with 2D MoS_2 then obtained after the reaction. According to the different precursor or preparation conditions (temperature, solution pH, and so on), a variety of nanostructured MoS_2 can be easily obtained, including granular, flakes, flower-like microspheres and so on. 2D MoS_2 can be obtained by the hydrothermal treatment of ammonium tetrathiomolybdate at 350°C in different solution pH values and the SEM images are shown in Figure 2-16a_{1-3}[67]. The samples prepared at pH of 4.5 are composed of aggregates that are irregularly shaped and interconnected

(Figure 2-16a$_1$), while the samples prepared at pH 7 are composed of particles with different shapes, rather than aggregates (Figure 2-16a$_2$). In contrast, the samples prepared at pH of 9.5 are flower-like, consisting of petals with a thickness of 10 nm and lengths of 100–200 nm (Figure 2-16a$_3$). These petals aggregate to form microspheres of 300–400 nm, with an increase in pH from 4.5 to 9.5, leading to the aggregation of thin nanosheets into flower-like MoS_2.

Furthermore, 2D MoS_2 can also be grown on carbon felt using phosphomolybdic acid and thiourea at different temperatures, as shown by the macroscopic SEM images in Figure 2-16b$_{1-3}$ and the corresponding microscopic SEM images in Figure 2-16b$_{4-6}$[68]. The structure of MoS_2-180°C is a well-assembled multi-faceted nanoflower with a diameter of 200–300 nm, which is composed of crosslinked nanosheets. As the temperature rises to 240 °C, 2D MoS_2 aggregates into larger particles and forms clusters on the surface of the carbon fibers. The three samples all have a 2D layered structure and the stacking structure becomes more obvious with increasing synthesis temperature. In addition, Wu et al.[69] used CTAB as a surfactant to assist in the preparation of 2D MoS_2 with various shapes under different growth conditions, including hollow, nanosheets and flower-like (Figure 2-16c$_{1-3}$). Figure 2-16c$_4$ shows that the nanomaterials are composed of Mo and S with a stoichiometric ratio (Mo:S) of 1:2, with no other elements detected by EDS, indicating pure MoS_2.

Interestingly, 2D MoS_2 with a special shape was obtained by the hydrothermal treatment of sodium molybdate dihydrate and thioacetamide at 200°C for 36 h, as indicated by the SEM and TEM measurements in Figure 2-16d$_{1-2}$, which reveal the morphology of the product[70]. Finally, 2D MoS_2 with a diameter of ~200 nm and an edge thickness of ~10 nm is observed, which is similar to morphology of radar. Furthermore, the solvothermal method is also a simple and efficient method to synthesize 2D MoS_2. Chen et al.[71] synthesized ultrathin 2D MoS_2 with ammonium molybdate tetrahydrate and thiourea assisted by polyethylene glycol (PEG). 2D MoS_2 prepared with PEG and pure water, as solvents, was labeled as MWP-MoS_2, pure water was PW-MoS_2 and pure PEG was PP-MoS_2. The prepared PW-MoS_2 was clustered and composed of densely stacked nanosheets. MWP-MoS_2 showed a highly folded surface and layered structure. For PP-MoS_2, the agglomeration of nanoparticles was observed and was obviously composed of randomly oriented layers rather than regular stacked layers (Figure 2-16e$_{1-3}$).

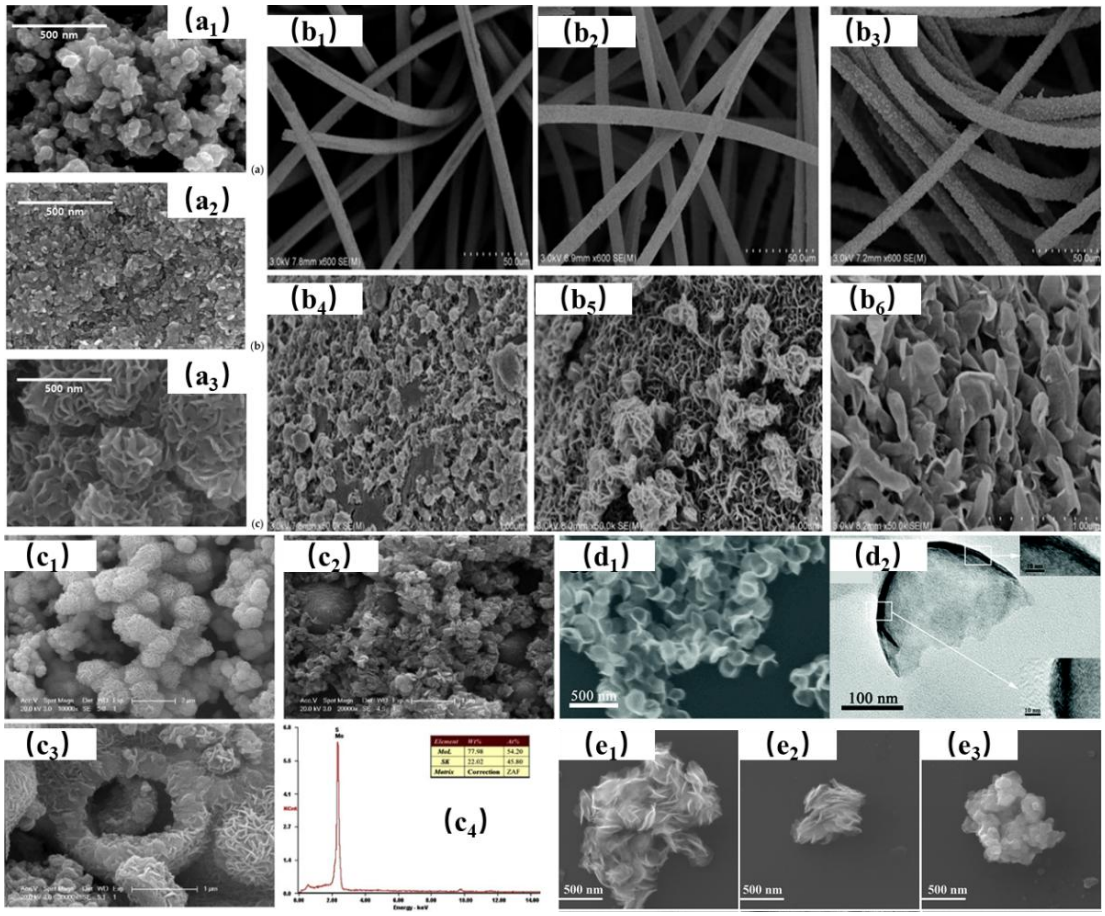

Figure 2-16. (a_{1-3}) SEM images[67] of 2D MoS_2 prepared at pH (a_1) 4.5, (a_2) pH 7.0 and (a_3) pH 9.5. (b_{1-6}) SEM images of ($b_{1,4}$) MoS_2-160°C, ($b_{2,5}$) MoS_2-180°C and ($b_{3,6}$) MoS_2-240°C before inoculation[68]. (c_{1-3}) SEM and (c_4) EDS spectrum of as-prepared MoS_2[69]: (c_1) flowerlike; (c_2) nanosheet; (c_3) hollow MoS_2. (d_1) SEM image of MoS_2 RNPs. (d_2) TEM image of an MoS_2 RNP (the inset images reveal that the edge thickness was ~10 nm)[70]. (e_{1-3}) SEM images of (e_1) PW-MoS_2, (e_2) MWP-MoS_2 and (e_3) PP-MoS_2[71].

2.3.3. 3D MoS_2-based materials

Despite a large number of approaches for the synthesis of 3D MoS_2-based materials having been developed, a clear classification has not yet been established. Here, the synthetic strategies for 3D MoS_2-based materials are briefly outlined and divided into three types, namely, template-based, self-assembly and sol-gel methods.

Template-based method

2D MoS_2 can be anchored on the surfaces of some templates (including sponge, aerogel and carbon matrix) that possess a 3D architecture via the hydrothermal method, CVD or impregnation method[72,73]. Benefitting from the facile preparation process, the structural and physical properties of 3D MoS_2-based materials can be easily modified

by changing the template. Zhu et al.[74] prepared a 3D-MoS_2 sponge by anchoring MoS_2 nanosheets and graphene oxide (GO) on the skeleton of a sandwich-structured sponge via a simple two-step impregnation method. A blank melamine sponge was dipped into MoS_2 and GO alcohol solutions in sequence to obtain a 3D sponge@MoS_2@GO after a simple heat treatment at 200 °C in an oven for 6 h (Figure 2-17a). This material could adsorb organic molecules and provide multidimensional electron transport pathways, as well as exhibit excellent performance in the degradation of aromatic organics. A 3D porous MoS_2/chitosan aerogel with excellent mechanical strength and stability was constructed by anchoring MoS_2 to the surface of the chitosan aerogel[75]. Benefitting from the superior photocatalytic performance and porous networks, which promote the mass transfer and shorten the diffusion pathway of the substances, the MoS_2/chitosan aerogel can effectively recover gold from a thiosulfate solution via the direct in-situ reduction of Au(I) to Au^0 under sunlight.

In order to improve the application performance of MoS_2 nanosheets in lithium-ion battery anodes and water electrolysis, 2D MoS_2 can be anchored on the skeleton of a conductive 3D matrix, such as 3D porous carbon aerogels (CAs)[76], carbonized cellulose aerogels[77], 3D nickel and CAs[78], graphene foam[79] and carbon cloth[80], which avoids the aggregation and restacking of 2D MoS_2 and ensures the fast transport of both electrons and ions during the electrochemical process. A CA was synthesized by Zhang et al. through the combination of a sol-gel process and high-temperature carbonization and 2D MoS_2 was subsequently decorated on its skeleton via a solvothermal treatment to obtain a MoS_2/CA aerogel (Figure 2-17b-e)[76]. The resulting composite was carbonized at 900°C to obtain a lightweight MoS_2/CNF aerogel with a hierarchical structure (Figure 2-17f-h)[81]. A novel 2D spatial confinement strategy to in-situ fabricates 2D MoS_2 anchored on 3D porous carbon nanosheet networks was demonstrated by Zhou et al., in which highly crystalline MoS_2 nanosheets with five or fewer layers very homogeneously and tightly lie on the surface of carbon nanosheet walls (with thickness a $\geqslant$3 nm)[82]. The novel 3D architecture composite exhibited an outstanding long-life cycling capability at high rates, i.e., a specific capacity as large as 709 $mAh \cdot g^{-1}$ was delivered at 2 $A \cdot g^{-1}$ and maintained at ~95.2% even after 520 deep charge/discharge cycles.

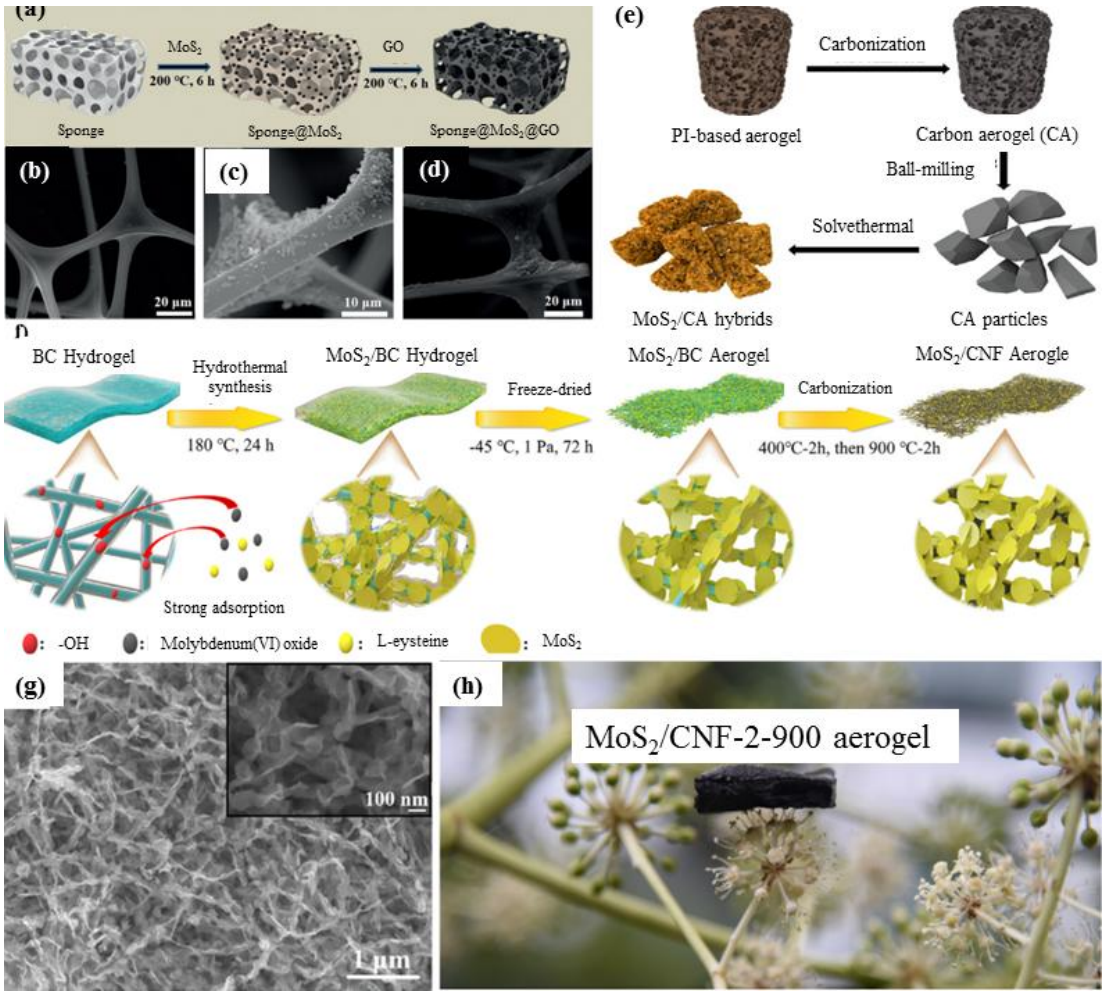

Figure 2-17. Synthetic pathway of (a) sponge@MoS_2@GO and (b) SEM images of sponge, (c) sponge@MoS_2 and (d) sponge@MoS_2@GO[74]. (e) Schematic of MoS_2/CA hybrid preparation[76]. Schematic of (f) MoS_2/CNF aerogel fabrication and (g) SEM image and (h) physical appearance of MoS_2/CNF-2-900 aerogel[81].

Self-assembly

3D MoS_2-based materials have been frequently fabricated with the assistance of GO, owing to its self-assembly feature during the reduction process. When a MoS_2 suspension is mixed with a GO suspension, 2D MoS_2 is prone to deposit on the surface of GO. With a decrease in the oxygen-containing group content on GO during thermal or chemical reduction, the hydrophobicity and internal π-π interactions between GO nanosheets are enhanced, resulting in the aggregation and formation of a MoS_2-graphene hydrogel[83]. Finally, MoS_2-graphene aerogels can be obtained after freeze-drying. 3D MoS_2/graphene aerogels are mainly applied in supercapacitors and lithium/sodium-ion batteries because the constructed 3D architecture facilitates electrolyte ion transport and improves the electrochemical performance through electric double-layer and faradaic pseudo-capacitance[84–86].

3D hybrid aerogels of MoS_2 nanosheet/nitrogen-doped graphene (3D MoS_2/N-GAs) with a large surface area and high electrical conductivity were fabricated by Liu et al. using urea as a reductant (Figure 2-18a)[87]. A 3D free-standing cylinder was obtained after the reaction, in which the MoS_2 nanosheets were uniformly anchored onto graphene sheets with interconnected pores ranging from several nanometers to several micrometers (Figure 2-18b, 2-18c, and 2-18d). When used as a supercapacitor electrode material, this hybrid aerogel exhibited an excellent specific capacitance of 532 F/g at a current density of 1 A/g and superior cycling stability of 93.6% capacitance retention after 10000 cycles at 10 A/g, which was significantly higher than those of 2D MoS_2 and nitrogen-doped graphene aerogels alone.

To reduce the reliance on polymeric binders, conductive additives and metallic current collectors during the electrode preparation process, as well as to assess the true performance of lithium-ion battery anodes, a MoS_2-anchored graphene aerogel paper (MGAP) was synthesized by Lee et al. via a self-assembly and compression process (Figure 18e)[88]. The fabricated MGAP, with a density of 0.47 g cm^{-3} and a surface area of 5.5 m^2 g^{-1}, was able to undergo 180° bending (Figure 2-18f) and MoS_2 was successfully incorporated into the aerogel paper (Figure 2-18g). Another method of one-pot freeze-drying self-assembly combined with in-situ thermal decomposition-reduction for 3D MoS_2/graphene aerogel preparation was proposed by Wang et al.[89], with significant potential for scale-up. A precursor aerogel was first constructed via the self-assembly of $(NH_4)_6Mo_7O_{24}$ and CH_4N_2S-loaded GO nanosheets. Upon the subsequent in-situ thermal decomposition-reduction treatment process, $(NH_4)_6Mo_7O_{24}$ and CH_4N_2S were decomposed to MoO_3/NH_3 and NH_3/H_2S, respectively (Figure 2-18h). MoO_3 was subsequently in-situ reduced to MoS_2 by reacting with H_2S and GO was reduced to graphene nanosheets (GSs), giving rise to the final MoS_2/GS aerogels.

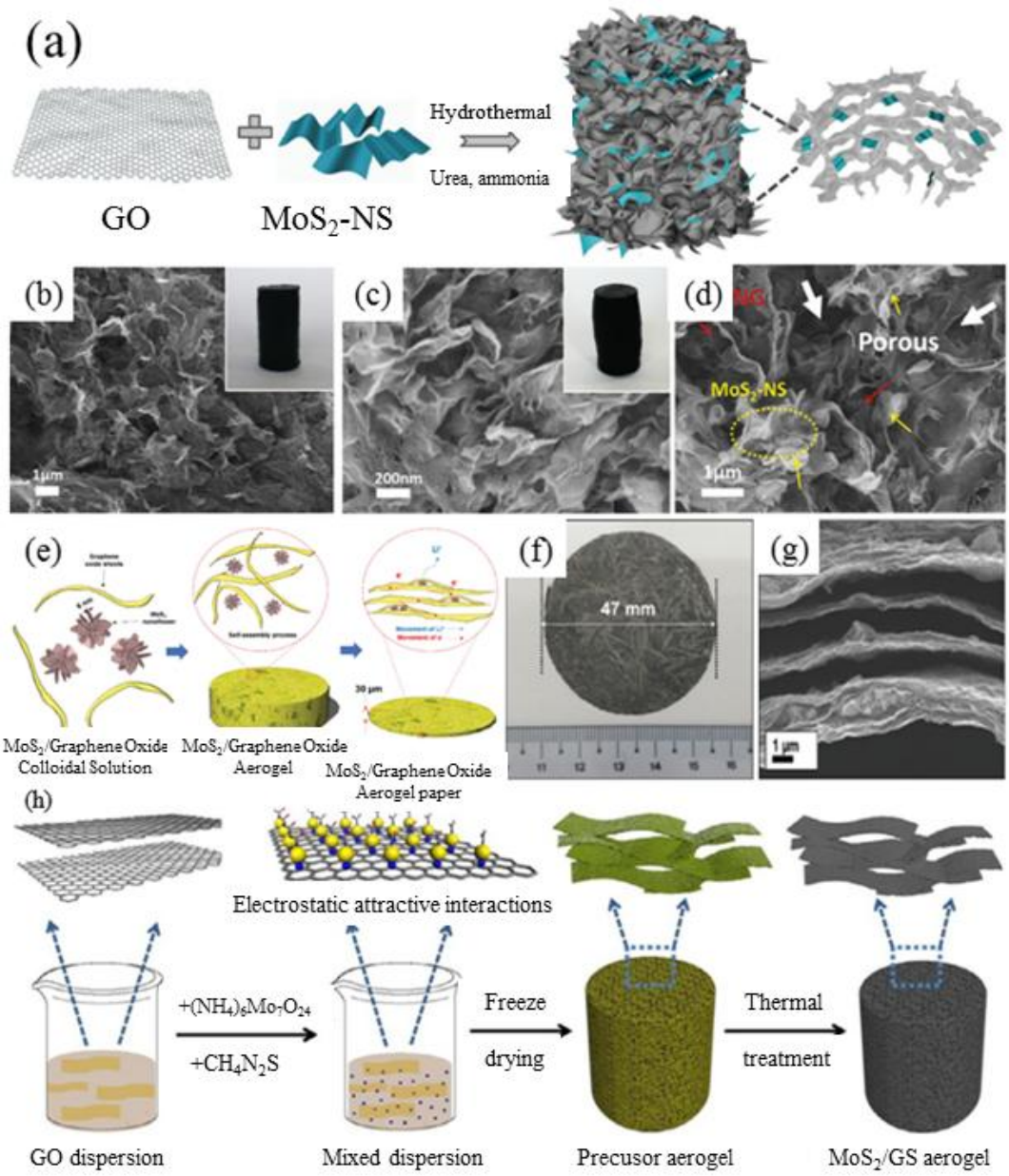

Figure 2-18. (a) Schematic of the synthesis process of 3D MoS_2/N-GA porous aerogel hybrids. SEM images of (b) N-doped graphene aerogel (c-d) and 3D MoS_2/N-GAs[87]. (e) Schematic of MGAP fabrication process and (f-g) photographic and SEM images of MGAP[88]. (h) Schematic of the fabrication process of MoS_2/GS hybrid aerogels[89].

Sol-gel method

3D MoS_2-based materials can also be fabricated via a sol-gel process and subsequent drying to remove the solvent. During the typical process of gelation, the sol-gel transition of MoS_2 nanosheets creates a 3D network by polymeric binders through physical or chemical crosslinking[90,91]. A method of vacancy-driven gelation to obtain chemically crosslinked hydrogels from defect-rich MoS_2 nanoassemblies and polymeric binder was reported by Jaiswal et al.[92]. The defects of MoS_2 nanoassemblies

acted as active centers for vacancy-driven gelation with a thiol-activated terminal, such as four-arm poly(ethylene glycol)–thiol(PEG-SH) via chemisorption, forming an elastomeric and robust gel (Figure 2-19a). The MoS_2 nanoassemblies were completely encapsulated by PEG-SH, endowing a remarkable mechanical resilience for the PEG–SH/2%MoS_2 hydrogel that could be stretched, bended and twisted easily (Figure 2-19b). Furthermore, the hydrogel had an interconnected porous network with a pore size of ~10 μm (Figure 2-19c and 2-19d).

The lack of connecting/bonding sites in the part of functional groups greatly limits the construction of high-quality MoS_2 aerogels. The functionalization of 2D MoS_2 was achieved by Wang et al. via the self-polymerization of dopamine monomers, rendering MoS_2 nanosheets rich in functional groups, such as catechol, amine and imine[93]. A 3D MoS_2 aerogel could then be facilely constructed under the crosslink of the functionalized MoS_2 nanosheets and chitosan (Figure 2-19e). The resulting MoS_2 aerogel could stand on a flexible cedar leaf without changing its original shape, revealing the high porosity and ultralight properties of 3D MoS_2. Furthermore, Mo^{4+} was presented in metallic MoS_2, which links with carboxyl (–COOH) and hydroxyl (–OH) groups in the cellulose chains to form crosslinked metal–carboxylate complexes. These complexes allowed the 2D MoS_2 to effectively encapsulate the cellulose nanofiber (CNF) at the nanoscale, based on which Yang et al. synthesized an ultralight, highly porous CNF/MoS_2 aerogel with good mechanical strength via a combined sol-gel and freeze-drying process (Figure 2-19f)[94].

Due to the encapsulation of 2D MoS_2 by polymeric binders, the catalytic activity and conductivity of 3D MoS_2 prepared by the sol-gel method may be weakened, thereby restricting its application in the fields of supercapacitors, lithium-/sodium-ion batteries and electrochemical hydrogen production. Therefore, these 3D MoS_2 aerogels are primarily applied in the field of solar desalination, fire retardants and microwave adsorption[95] with the utilization of their physical properties.

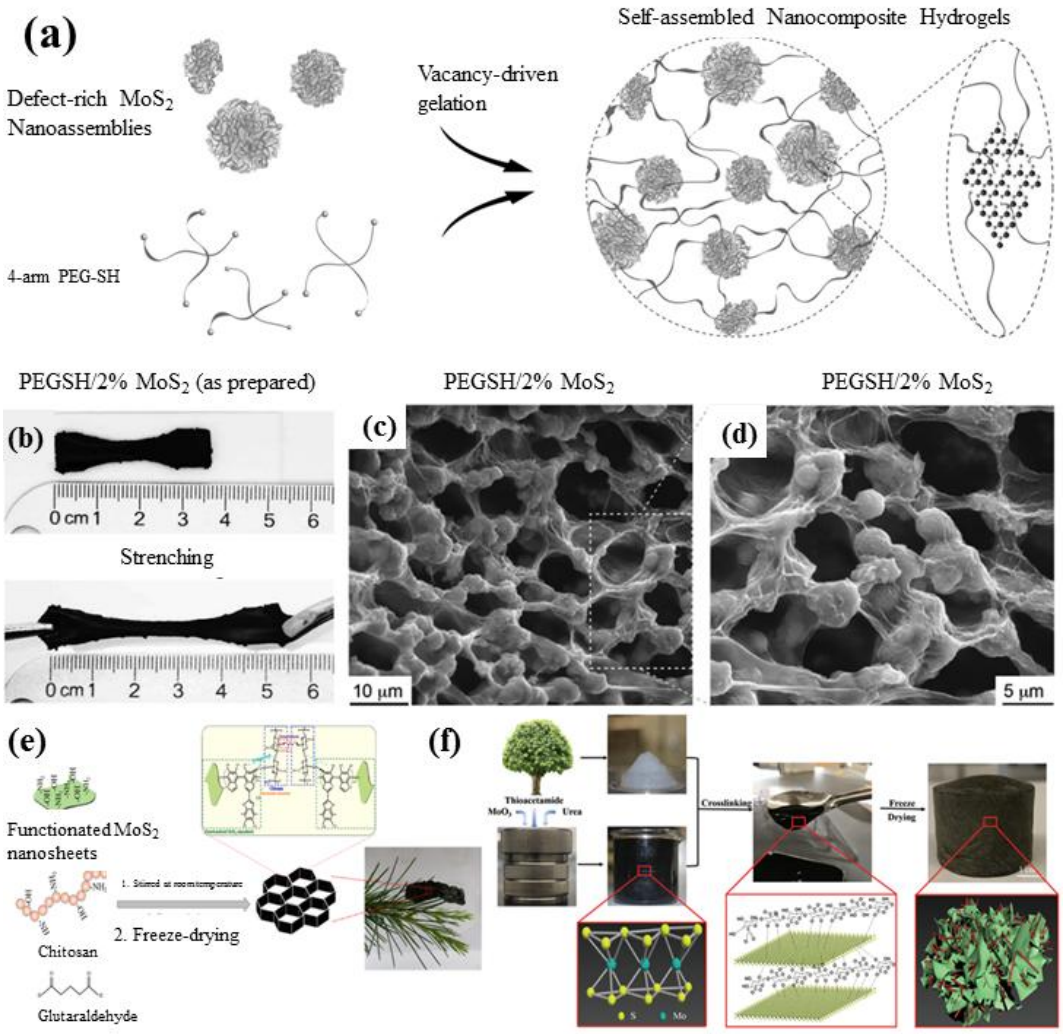

Figure 2-19. Schematic of (a) PEG–SH/MoS_2 hydrogel synthesis mechanism and (b) photographs and (c, d) SEM images of PEG–SH/MoS_2 hydrogel[92]. (e) Schematic of preparation strategy of 3D MoS_2 aerogel[93]. (f) Schematic of the growth process of CNF/MoS_2 aerogel[94].

2.4. Modification

2.4.1. Modification for surface defects

The crystal anisotropy of MoS_2 makes it exhibit discrepant properties between "surface" and "edge" sites. In particular, the "edge" sites show more active chemical reactivity, such as adsorption[96], photocatalysis[97] and electrochemistry[98], which is beneficial for their applications in relevant fields. Based on this characteristic of the MoS_2 structure, executing defect engineering on "surface" sites to induce more neonatal "edge" sites represents an effective method for the optimization of chemical performance. In the past few decades, numerous studies regarding defect-modified

MoS_2 have been reported, thereby illustrating the importance of defect engineering in current MoS_2 research. According to the dimensionality, the defect types in MoS_2 can be mainly classified into two categories: (1) point-like defects and (2) plane-like defects.

Point-like defects. Point-like defects in MoS_2 include anionic, cationic and hybrid vacancies, which are generated from the movement of lattice atoms from their original sites, i.e., internal defects. The existence of point-like defects destroys the crystal lattice of MoS_2, leading to the regulation of its chemical properties and electrical configuration[99]. So far, numerous studies have attempted to produce point-like defects in MoS_2.

Point-like defects in MoS_2 can be induced by the irradiation of particles, i.e., irradiation-induced defects. Normally, particle irradiation is produced from special equipment, such as a tandem accelerator. As illustrated in Figure 2-20a, when particles with high energy are shot at the MoS_2 surface, the lattice atoms passively release from their original sites to leave point-like defects in the crystal structure[100]. Importantly, the density of the point-like defects is accurately regulated by controlling the irradiation strength. As shown from the high angle annular dark-field (HAADF) images in Figure 2-20b, with increasing Ca^+ irradiation strength, it can be seen that the quantity of point-like defects (the black holes in the images) gradually increases[101]. Various sources of radiation, including heavy ions, electrons, protons, X-rays, gamma rays, ultraviolet light and infrared irradiation, have been carried out with this technique[102].

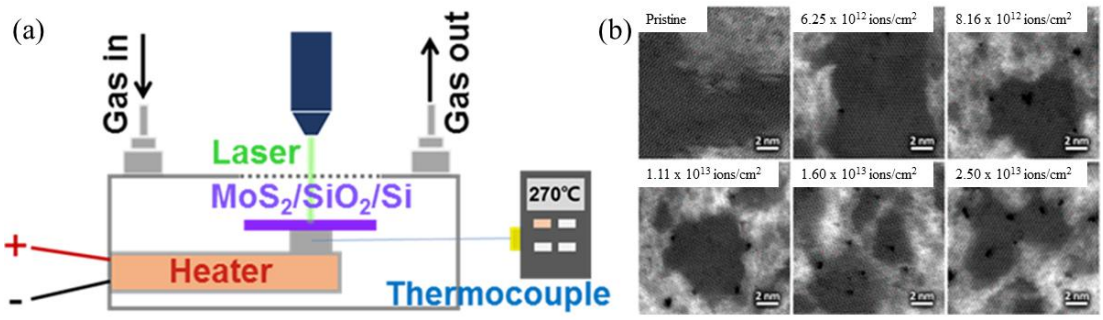

Figure 2-20. (a) Schematic of inducing defects in MoS_2 by irradiation[100]. (b) HAADF images of MoS_2 after Ga^+ irradiation under various strengths[101].

Heavy ions with high energies are generally accelerated by particle accelerators. Mishra et al.[103] used a Ga flux beam under ultrahigh vacuum conditions to irradiate MoS_2. As a result, the Raman signals and XPS spectra of the Mo-3d orbital exhibited an obvious shift, revealing that the original atoms in MoS_2 were replaced by Ga atoms. Furthermore, other heavy metals, including uranium[104], xenon[105], bismuth[106] and manganese[107], have also been adapted to irradiate MoS_2 and successfully induce point-

like defects on its surface. In addition, similar procedures to induce point-like defects have been carried out by using other irradiation particles. In conclusion, although the generation of point-like defects in MoS_2 by particle irradiation is a mature technique, it requires specialistic equipment, which limits its popularization.

In addition, the hydrothermal method is another technique to prepare MoS_2 with point-like defects. During the synthetic procedure, the precursors of Mo and S are firstly dissolved in water and transferred into a closed container. Subsequently, MoS_2 crystals form and gradually grow under an environment of high temperature and pressure. It is noteworthy that the microstructure of synthesized MoS_2 can be regulated by adding different molar ratios of the Mo and S precursors. Normally, when the molar ratio of Mo and S atoms breaks the balance of 1:2, point-like defects will form in the MoS_2 structure. MoS_2 samples with different concentrations of point-like defects were synthesized via a hydrothermal method by Chen et al.[108] and the majorization of the piezoelectric response for gold recovery was realized. Furthermore, according to the report of Jayabal et al.[109], 1T-MoS_2 samples with point-like defects were prepared using a hydrothermal strategy and exhibited excellent performance in the hydrogen evolution reaction. As a consequence, point-like defects produced by the hydrothermal technique were executed by only using a Teflon-lined stainless-steel autoclave, making it a facile method for wide research applications.

Plane-like defects. Compared to the formation of point-like defects, the generation of plane-like defects in MoS_2 requires more energy from the environment to destroy the crystal structure, thus to form a large area of vacancies. As a common method, thermal annealing is an effective method of inducing large-scale edges through the etching of the MoS_2 crystal. By simply undergoing heating, plane-like defects could be induced in MoS_2. Importantly, the degree of defects can be regulated through the selection of reaction atmosphere and temperature. Jia et al. studied the formation rule and mechanism of edge defects in MoS_2 through thermal treatment[110]. As shown from the AFM images in Figure 21, MoS_2 displays different areas of plane-like defects after thermal treatments under various conditions. A larger etched area is induced at higher temperature and oxygen content in order to achieve good control of plane-like defects in MoS_2. Meanwhile, the shape of the defects oriented to equilateral triangular pits, which was ascribed to the trigonal prismatic 2H phase of MoS_2[111]. Relevant research has been reported for further understanding the technique mechanism and a similar conclusion was reached[112,113]. Using this thermal treatment method, numerous properties of MoS_2 have been improved and widely applied in desalination[114] and

adsorption[96].

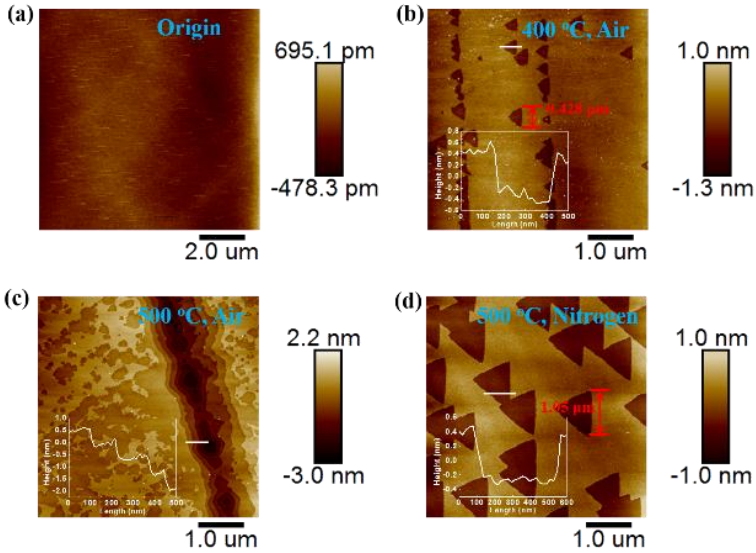

Figure 2-21. AFM images of MoS_2 after thermal treatments under different conditions ((a) Origin MoS_2; (b) 400°C for 2h in air; (c) 500°C for 2h in air; (d) 500°C for 3h in N_2[110].

2.4.2. Heteroatom doping

Heteroatom doping is an effective method to tune both the chemical and physical properties of MoS_2. Dopants in MoS_2 can substitute at either the Mo or S site. Furthermore, they can exist at the surface or as adatoms on the basal plane or an edge on an MoS_2 sheet. Dopants occur in some high symmetry sites, for example, atop S, atop Mo and at the center of a hexagonal hollow[2].

Doping atoms affect the local structure, lattice parameters and even the overall crystal structure of MoS_2. For instance, the intercalation of Li atom changes the crystal structure type from 2H to 1T, and the substitution of Mo by Nb changes it from 3R to 2H. Furthermore, the crystal and morphology are influenced by dopants through kinetic or thermodynamic effects. Many synthetic processes occur in non-equilibrium conditions, so theoretical studies are complicated.

Dopants can generally be considered in the context of the following factors. One important factor is whether the ionic radius of the doping atoms is similar to the radii of the Mo and S atoms. Whether the doping atoms possess similar bond lengths with Mo or S compared with the corresponding bond length in MoS_2 is another vital point. Doping atoms are chosen as a 4+ oxidation state to fit the Mo site and a 2- oxidation state to fit the S site. With regard to intercalated dopants, the atoms are neutral. In synthetic conditions, the doping location can be controlled by adjusting the chemical potentials of Mo, S and the dopant; for instance, an S-rich environment will benefit the

substitution of Mo. Possible dopants include transition metals and chalcogens[115–124].

Since 2013, many researches have attempted to dope heteroatoms into MoS_2 and doping methods based on the following three strategies have been established[125]:

(i) Charge transfer doping, where the type and concentration of photoelectrons can be regulated by surface charge transfer that is realized by depositing and adsorbing small molecules and polymers on the surface of MoS_2;

(ii) Substitutional doping, where dopants are introduced to replace Mo or S atoms to regulate the band structure and transport characteristics of MoS_2 by forming in-plane covalent bonds during or after growth, and the material properties are further enriched by introducing heteroatoms;

(iii)Intercalation doping, where the structure and electrical transport characteristics can be controlled by the interlayer insertion of atoms, molecules or ions.

Charge transfer doping. Charge transfer doping is realized by either physical or chemical interactions between dopants and the supporting material, and the dopants originate from gas (O_2 and NO_2), metal or compound molecules. Dopants can attach to MoS_2 via adsorption, deposition and spin and dip coating. The doping degree can be determined by Raman spectroscopy, the PL peak position and intensity charge, the XPS peak position shift, the change in source-drain current-gate voltage response in electrical measurements, Hall measurements and so on[126]. The activity of the charge transfer direction is governed by the difference at the Fermi level (E_F). The main experimental methods to characterize the doping effect include determining the type and which created by the dopants and supporting materials (Figure 2-22a)[118]. If the E_F of the dopants is lower than that of the supporting materials, electrons will be transferred from the supporting materials to the dopants, i.e., p-type doping. In contrast, n-type doping is based on the electron transfer from dopants to supporting materials. Generally speaking, the interaction regarding charge transfer happens on the interface of any adjacent media, like particle ions, surface atoms, molecules and supporting materials[22,127–129]. The advantage of charge transfer doping is enhancing the electronic behavior of semiconductors whilst avoiding lattice distortion and high mobility transport.

The main purposes of charge transfer doping are changing the work function of the material and reducing the Schottky barrier between the material and electrode with an improvement in device performance[130]. It also regulates the type and concentration of carriers in the channel to obtain high-performance devices with electrons (n-type) or holes (p-type) as the main carriers or to construct space charge regions (p-n junction)

to provide basic structural elements[131]. Finally, charge transfer doping can be used to turn the field-effect transistor by constructing a steep in-plane tunneling junction with high heterogeneity.

Gas molecules are often adsorbed on the surface of MoS_2 and then turn the optical and electronic behavior of the supporting materials[132]. This characterization is applied in gas sensing, in which semiconductor materials are employed as the sensing channel[133]. The simplest method of gas-phase doping is to directly expose MoS_2 to a target atmosphere. The usual interaction is physical adsorption via weak van der Waals interactions, where desorption is possible. During thermal annealing in a vacuum, the exposure effect will be strengthened. This process can clean unnecessary contaminants and increase the concentration of S vacancies, which promote the adsorption of gas molecules.

Tongay et al.[134] found that after exposing MoS_2 to various atmospheres, such as O_2, H_2O, ambient and inert gases, the PL intensity in n-type MoS_2 was obviously enhanced because of the depletion of electrons and the suppression of non-radiative recombination (Figure 2-22b, and 2-22c). The PL intensity is much higher than that under a vacuum and increases by 10×, 35× and 100× after exposure to H_2O, O_2 and air, respectively, and the peak shifts from 1.84 to 1.88 eV. However, the PL intensity and peak position remain unchanged when the air is changed to Ar and N_2. When the inert gas contacts the surface of MoS_2, there is no charge transfer due to the stable electronic structure, so it is very difficult to gain and lose electrons, meaning that it cannot play a role in regulating the PL intensity and position[134]. Later, Nan et al. demonstrated the reinforced modulation of the PL emission of MoS_2 through chemically bonded O_2 in a mild plasma treatment[135]. Although physical adsorption is a reversible method for quantitatively adjusting the doping concentration through controlling the gas pressure, it cannot meet the requirements for preparing controllable and stable doping materials due to its poor adsorption ability.

Metal and metal compounds[131], like ion complexes[136] and oxides[137,138], can be applied to decorate the surface of MoS_2. In general, evaporation and solution case methods that are compatible with existing patterning techniques are applied for decorating MoS_2. It has been proved that choosing the dopant sources according to their work function can be used to predict the electrical doping behavior. Sarkar et al. studied the electrical doping of MoS_2 via various noble metals, such as Au, Ag, Pd, Pt, Sc and Y[139]. All the metals with large work functions (44.6 eV) were doped into MoS_2. Of these metals, Sc exhibited only a slight depletion effect, while Y induced electron

doping behavior with the lowest work function. This phenomenon demonstrates that the dopants with higher work functions have a tendency to act as p-type dopants.

Potassium has a strong ability to supply electrons for most surfaces due to its low electron affinity[140]. Fang et al.[131] first reported an n-type-doped thin layer of MoS_2 based on surface charge transfer by depositing potassium atoms on the surface of MoS_2 via vacuum thermal evaporation and controlling the adsorption amount (Figure 2-22d). The transfer curve before and after doping (Figure 2-22e) shows that the device has a large switching ratio (lon/off > 105) before doping. When the channel was completely evaporated of potassium atoms, the source leakage current increased by five orders of magnitude, close to milliamps. Moreover, the source-drain current was almost saturated, indicating the transfer of electrons from potassium to the surface of MoS_2. The surface change density of potassium-doped MoS_2 reached 1.0×10^{13} cm^{-2}. Although the surface charge density of MoS_2 is greatly improved after potassium doping, the current switching ratio significantly decreases. Furthermore, its poor stability limits its practical application, owing to the facile reaction between potassium and O_2 and H_2O.

In addition to potassium, other materials, such as fullerenes (C60) and molybdenum trioxide (MoO_3)[141], have been doped on the surface of MoS_2. Lin et al.[142] researched the effects of C60 and MoO_3 on the surface charge of MoS_2 via vapor methods. Since the lowest unoccupied electrons of the energy level in C60 is higher than the CB of MoS_2, the electron transfer from MoS_2 to C60 is prevented. Furthermore, the p-type doping effect is not produced and the mobility does not decrease, indicating that C60 can be used as an effective protective film. When MoO_3 is used as the covering film, the threshold voltage increases from 0 to 70 eV, indicating that MoO_3 significantly reduces the charge on the surface of MoS_2 and is a suitable p-type dopant. Cs_2CO_3, as an electron injection layer in organic light-emitting diodes, has the ability to provide electrons and produce a strong n-type doping effect on different organic semiconductor materials. Rai et al.[143] spin-coated amorphous titanium oxide in a solution-gel state on the surface of MoS_2 and found that the electron mobility was as high as 83 $cm^2\cdot V^{-1}\cdot s^{-1}$ after doping at room temperature and the intrinsic mobility at 77 K is as high as 501 $cm^2\cdot V^{-1}\cdot s^{-1}$. Simultaneously, they reported that only when titanium is in excess, amorphous titanium oxide with oxygen holes has the doping effect because the extra Ti atoms can generate additional energy levels at the bottom of the CB.

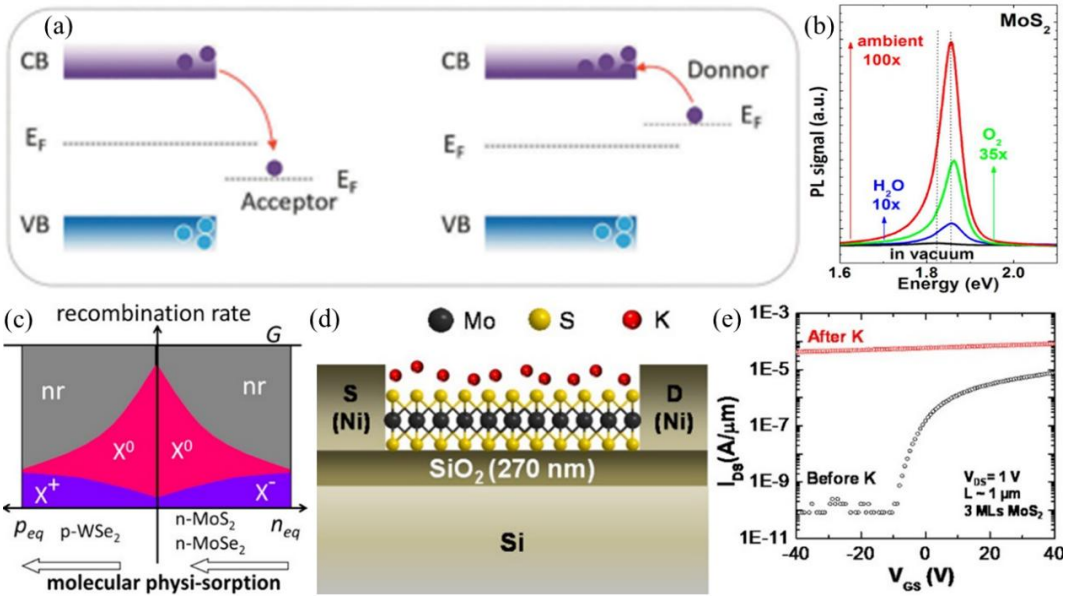

Figure 2-22. (a) Behavior of charge transfer doping[118]. (b, c) Modulation of PL property of MoS_2 via exposure to various gas atmospheres and the change in exciton and non-radiation recombination[134]. (d-e) Electrical characteristics of K-doped MoS_2[131].

In addition to the above methods for achieving surface charge transfer based on gas-phase physical adsorption, surface evaporation or spin coating, solution immersion is also a simple and effective method to achieve the adsorption of doped molecules on the surface of MoS_2[144]. Du et al.[145] soaked MoS_2 in a methanol solution containing amino-rich polyetherimide. The in-plane and contact resistance decreased from 19.99 and 5.06 kΩ·m^{-1} to 7.65 and 4.57 kΩ·m^{-1}, respectively. After doping MoS_2, it also has good air stability.

Charge transfer represents a simple and effective doping method to improve the concentration of surface carriers or change the type of carrier in MoS_2. When n-type MoS_2 is doped with an electron-donating dopant, such as an amino group, the electron concentration of the surface of MoS_2 reaches the limit of electron concentration. When patterned p-type doping is carried out with highly electronegative dopants, such as O and F, homogeneous p-n junctions can also be constructed. Compared with substitutional doping, surface adsorption does not destroy the structure of MoS_2 and only transfers the charge; thus, the structure of MoS_2 is more complete. The experimental method of charge transfer doping has also been expanded from gas physical adsorption to solution-phase adsorption, which needs to be further developed in the future to meet the requirements of large-area, controllable, air stable and other practical applications.

Substitutional doping. Substitutional doping involves the replacement of the Mo

and S atoms in MoS_2 with cationic and anionic elements of comparable radii[146,147]. After doping, the generation of n- or p-type MoS_2 depends on the number of valence electrons of the dopants. Substitutional doping requires significant energy because of the replacement of heteroatoms for Mo or S atoms and the bonding of heteroatoms with Mo and S atoms around. There are two main methods to realize substitutional doping. One is in-situ doping in the growth process. The other is the creation of vacancies by post-processing, with heteroatoms introduced to fill the vacancies.

Both the bottom-up chemical synthesis and top-down stripping of MoS_2 have S atom holes, so that MoS_2 shows n-type characteristics. If MoS_2 can be doped into a p-type semiconductor, a MoS_2 homojunction will be constructed. In the crystal lattice of MoS_2 (Figure 2-23a), the Mo atoms are sandwiched between the outer chalcogenide layers, which screens the incorporated metal atoms into the substitutional sites. Non-metal dopants tend to occupy the anionic sites at the outer layers due to the length limitation of the ionic bonds. For metal dopants, the radii of the foreign dopant atoms are vital for a favorable position. For light metals (Li and Na), which have small radii, the interlayer distance (0.615 nm) is sufficient for intercalation. However, for heavy dopants with large radii (e.g., Mn, Co, Zn, and so on), substitutional doping is preferred thermodynamically[146].

At the cation sites, many transition metal ions with similar radii to Mo atoms can achieve effective substitutional doping into the lattice of MoS_2, which enriches its functionality (Figure 2-23c and 2-23d). In theory, Nb is a very suitable electron acceptor for p-type doping in MoS_2 because it has fewer valence electrons than Mo[148]. From the perspectives of the structures of 2H MoS_2 and 2H NbS_2, the lattice parameters are similar. The covalent radii of r(Mo) (130 pm) and r(Nb) (134 pm) are similar. In terms of oxidation valence states, Mo and Nb are in the 4+ state. Based on the above factors, Nb doping does not cause obvious damage to the original structure of MoS_2. Suh et al.[119] prepared millimeter-grade MoS_2 single crystals through chemical vapor phase transport using iodine as a transport agent under a growth temperature gradient of 1050–936 °C for 500 h. Finally, monolayer Nb-doped MoS_2 was obtained by mechanical stripping. Figure 2-23b shows a schematic of the Nb-doped MoS_2 structure by chemical vapor transport. After doping, the hole concentration reached 1.8×10^{14} cm^{-2}, which is consistent with theoretical calculations that when an Nb atom absorbs an electron, 0.5% Nb atoms can produce a hole density of ~2.8×10^{14} cm^{-2}. Finally, the MoS_2 homojunction was constructed[119]. As seen in the figure of transfer characteristic, the dependence of Nb-doped MoS_2 on the gate decreases and the current increases,

presenting p-type doping characteristics (Figure 2-23e and 2-23f). Different from the above Nb-MoS_2, which was first synthesized in the bulk phase and then obtained as a monolayer by stripping, Laskar et al.[149] adopted the method for synthesizing Nb-doped MoS_2 with a thickness of 10 nm by CVD. In terms of doping concentration, the concentration of holes in the bulk phase reached 3.1×10^{20} cm^{-3} and their mobility was 8.5 $cm^2\cdot V^{-1}\cdot s^{-1}$.

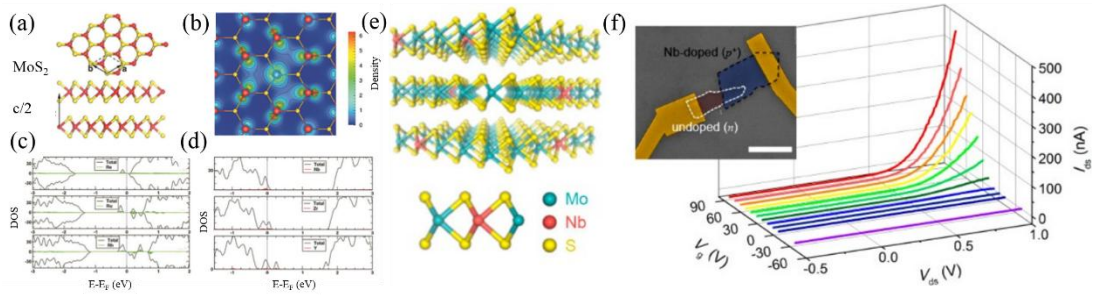

Figure 2-23. (a) Substitutional doping of MoS_2. Crystal structure of MoS_2. (b) Electron density mapping of MoS_2 with Mo substituted by Nb atom. Electronic DOS of (c) Re, Ru and Rh and(d) Nb, Zr and Y substitutionally doped MoS_2[148]. (e) Structure and (f) electrical properties of Nb-doped MoS_2[119].

In 2016, Gao et al.[150] successfully prepared Nb- and Re-doped MoS_2 with a monolayer thickness by direct growth in CVD. The obtained concentration of Re was lower than that of Nb because of the difference in formation energy. In order to make sure whether the dopants were at the substitutional site, aberration-corrected Z-contrast scanning transmission electron microscopy (STEM) was used to observe the position of Nb in the single-layer MoS_2. Furthermore, other indirect methods have been used for detecting the substitutional position. Lin et al.[151] investigated the stability of dopants by high electron beam irradiation. On the surface of MoS_2, it was found that Au migrates to the edges and vacancy sites when it possesses sufficient energy from electron irradiation, while the Nb doping results in enhanced stability. The successful substitutional doping in CVD growth enables the turning of electrical conductance. The n-type dopant (Re) greatly reduced the contact resistance in transistors.

The doping of Fe, Mn and other metal atoms may make MoS_2 magnetic, which provides conditions for the preparation of spin devices. It is predicted that the Curie temperature of MoS_2 can exceed room temperature when the Mn content reaches 10–15%[152]. The chemical bond strength between these dopants and S atoms greatly differs from that of the Mo-S bond, so doping with these atoms may produce lattice defects. Zhang et al.[122] studied the influence of the substrate on the doping of Mn atoms. When

a substrate with a flat surface was used, such as graphene, trace doping could be carried out at concentrations of <2%. Higher concentrations led to competition between MoS_2 and MnS, resulting in structural instability. When using substrates with suspended bonds on the surface, like SiO_2/Si and sapphire, doped Mn atoms caused defects in MoS_2. They used molybdenum trioxide as a molybdenum source, heated it to 725°C in the center of a tubular furnace and placed decarbonyl manganese and sulfur powder in an argon gas inlet and heated them to 70 and 300°C, respectively, for in-situ doping during growth. The morphology of MoS_2 with SiO_2/Si and sapphire substrates before and after the doping of Mn atoms showed that MoS_2 had smooth edges before doping that became serrated after doping.

Because MoS_2 is a sandwich structure, the Mo atom is located in the middle, while the S atoms are located in the upper and lower layers, so the substitution of S atoms can be achieved either by in-situ growth by mixing the doped atoms with the S source or by hole creation by post-laser doping. The substitutional anion doping tends to happen in the presence of anion vacancies exposed to the outer surface. Various doping elements that are available in the gas phase, like H, O, Cl, N and P, can be adopted to reduce the resistance.

Anion substitutional doping depends on the diffusion of dopants to the vacancy sites. Fixed point doping can be accomplished through a laser-assisted doping method. Li et al.[153] realized the Se doping of MoS_2 through a CVD method to obtain 2D $MoS_{2x}Se_{2(1-x)}$ with a tuned composition. Ma et al.[154] demonstrated that using Se sources of diselenodiphenyl at about 350°C achieved 21% selenization. Since N-doped MoS_2 can enhance its catalytic hydrogen evolution reaction ability[155], Qin et al.[156] prepared gelatinous precursors by dissolving molybdenum pentachloride and thiourea in an ethanol solution with various molar ratios and then placed the gelatinous precursors in a tube furnace. Chen et al.[157] etched MoS_2 on the surface of sulfur hexafluoride, trifluoromethane, tetrafluoromethane and O_2, thus obtaining p-type F-doped MoS_2 and constructing a MoS_2 homojunction, which is simpler in structure compared with the traditional heterojunction. The lattice constants between the interfaces were exactly the same. In 2016, Nipane et al.[158] doped both non-degenerate and degenerate p-type conductance into MoS_2 via inductively-coupled PH_3:H_2 plasma treatment. The hole mobility in P-doped MoS_2 reached 8.4 and 137 $cm \cdot V^{-1} \cdot s^{-1}$, respectively, after correcting for the contact resistance.

Substitutional doping is important for achieving control of the magnetic and optical properties of MoS_2 and enriching the diversity of its composition. Because

excessive Mo or S atoms in substituted MoS_2 will destroy the stability of its structure, substitutional doping is not the main method to control the electron concentration. The homogenous distribution of impurity atoms can be obtained by central doping in the growth process of MoS_2, while the laser-assisted method can realize the fixed-point doping of dopants. The doping concentration can be controlled by adjusting the laser intensity and exposure time. This method provides a new concept for the construction of homojunctions.

Intercalation doping. Unlike substitutional doping, the van der Waals interlayer of MoS_2 allows for foreign ion intercalation[159] and atoms[160] and also molecules to enter into the interlayer space. Intercalation is beneficial for the exfoliation of MoS_2 in solution in order to produce novel batteries and electrochemical cells[60,161]. Intercalation doping can modulate the electronic structure and crystal lattice of the supporting materials, resulting in physical or chemical phenomena, including charge density and superconductivity.

H and alkali metal ions can be very easily intercalated into the intercalation layers due to their small radii[162]. Furthermore, they induce electronic structure changes and lattice distortion due to the reductive nature by donating electrons to the lattice. At room temperature, the stable crystal structure of MoS_2 is 2H, i.e., six S atoms are coordinated around Mo atoms to form a trigonal prism coordination environment. In this coordination environment, the 4d orbital of the central Mo ion is divided into three groups and the two 4d electrons of the tetravalent Mo ions are arranged in the lowest orbital, which keeps the system with the highest stability. However, after interlayer doping with alkali metals, the coordination environment of the central Mo ion is changed into the octahedral 1T configuration for maintaining the lowest energy electron configuration. This is because the alkali metal injects more electrons into MoS_2 and the 4d orbital is separated into two groups. The newly injected electrons are arranged with the original two electrons in the lowest energy d_{xy}, d_{yz}, and d_{xz} parallel rails. Therefore, the intercalation doping of alkali metal ions brings changes in the crystal structure of MoS_2. It was seen that the injection of electrons changes the electrical properties of MoS_2 according to the distribution diagram of state density before and after doping. The Fermi level has the distribution of state density, which makes MoS_2 change from a semiconducting to a metal state[163].

Alkali metal intercalation is mainly achieved through the immersion of a butyl solution or electrochemical method. Lukowski et al.[164] synthesized petal-like multilayer MoS_2 with highly exposed edge sites on a graphene substrate by CVD, then soaked the

multilayer petal-like MoS_2 in an n-butyl lithium solution for 6–8 h and finally removed it with deionized water to remove the excess Li. Acerce et al.[165] prepared 1T MoS_2 with a size of 1-5 μm by first making MoS_2 into a single layer and then stacking it. MoS_2 powder was first soaked in an n-butyl lithium solution, filtered through argon for 48 h and the excess butyl lithium solution was washed away with hexane, before finally soaking the Li-intercalated MoS_2 in deionized water and ultrasound for 1 h to wash away the Li interlayer and obtain the single-layer MoS_2.

The zerovalent intercalation of heavy metal elements, such as Co, Cu and so on, can be intercalated into the intercalation layers[166–168]. This avoids lattice disruption without a charge interaction between the doping atoms and supporting materials. It was demonstrated that various organic molecules with different functional groups can facilitate the origination of new intercalation systems with engineered enhanced functions, including ferromagnetic moments[169], charge density waves and superconductivity[170]. Chen et al.[171] successfully synthesized the intercalation doping of Pt, Ru, Au and Pd in highly reductive 1T' Li_xMoS_2 by the in-situ reduction of metal ions. In the process, Li^+ intercalation enlarges the van der Waal gap in 1T' Li_xMoS_2, which allows the diffusion of highly charged metal ions ($PbCl_6^{2-}$, Ru^{3+}, $AuCl_4^-$ and Pb^{2+}) into the interlayer space. After in-situ reduction, the noble metal particles are precipitated in the interlayer space. Li^+ and Cl^- are leached out through ion exchange, the zerovalent intercalated MoS_2 is restored to the 2H phase. The zerovalent is kept in the stable 2H structure. The encapsulation of precious metal clusters in MoS_2 is used for stability in catalytic applications. In addition to the above-mentioned ions and elemental atoms with small sizes, large molecules can also be applied as intercalants. The organic molecules as intercalation dopants facilitate the discovery of new intercalation systems and engineering owing to their enormous functional groups.

2.5. Composites

2.5.1. Composite construction with single elements

Although its special microstructure and proper bandgap structure endow MoS_2 with excellent physical properties and chemical activity, its properties can be further optimized by constructing composites with single elements. Precious metals are the most common elements used to modify MoS_2 for superconductivity and special surface plasmon resonance. Through some techniques, noble metal nanoparticles can be anchored on MoS_2 to form composites[172]. According to Sun et al., MoS_2 decorated with

Ag^0 could be successfully prepared by reducing $AgNO_3$ on MoS_2[173]. As a result, Ag^0 dramatically facilitated the delivery of photogenerated electrons from MoS_2, leading to an improvement in the photocatalytic efficiency for Cr(VI) reduction. In another study, Ag/MoS_2 was fabricated as a Fenton catalyst. Under the irradiation of light, "hot electrons" generated by the surface plasmon resonance effect of Ag^0 can facilitate the separation of electron-hole pairs to co-catalyze Fenton reaction, thus improving the degradation of 2,4-dichlorophenol[174]. As another kind of noble metal, Au is popular in the modification on MoS_2 to regulate the surface structure. Yin et al.[175] loaded Au nanoparticles on MoS_2 to improve the photocatalytic features. After Au decoration, the photocurrent response increased from 100 to 370 $\mu A \cdot cm^{-2}$ at 0.8 V (vs. Ag/AgCl), ascribed to the local electric field generated by Au. As well as Ag and Au, other common noble metals, such as Pt and Pd, have also been used to decorate MoS_2. Luo et al.[176] adopted an electrodeposition method to import Pt on MoS_2 and it exhibited a comparable HER activity. As reported by Yuwen et al.[172], they utilized a microwave-assisted method to disperse Pd on MoS_2, leading to an enhanced catalytic activity for methanol oxidation.

Some heavy metal elements have also been adopted to construct composites with MoS_2 in the lubrication and advanced oxidation process fields. Sun et al.[177] induced Cu atoms into MoS_2 to form a turbulence-like micro-nanostructured composite (Cu/MoS_2) and utilized it as a solid lubricant. With the introduction of Cu, the composite exhibited higher hardness and a lower friction coefficient in the atmosphere than pure MoS_2. The Fenton reaction is considered a promising technique among various advanced oxidation processes. In the report of Lan et al.[178], isolated protruding Fe atoms were immobilized on MoS_2 surface through a dipping calcination method to prepare a Fenton catalyst (Fe-MoS_2). During the piezo-activation of peroxymonosulfate, the isolated Fe atomic sites play important roles in promoting the separation of e^- and h^+ of MoS_2, as well as providing Fe^{2+} for peroxymonosulfate decomposition.

2.5.2. Heterojunctions

The photoactivity of MoS_2 can be enhanced through appropriate heterojunction engineering for inhibiting the recombination of induced photoelectrons and holes. According to the contact interface, heterojunctions can be divided into six groups (Figure 2-24): traditional (types I, II and III); p-n; Z-scheme; step-scheme; Schottky and surface heterojunctions[179–181]. The diverse heterojunction structure shows different methods and mechanisms for the transfer of photogenerated carriers.

In type I heterojunction photocatalysts (Figure 2-24a), both photogenerated electrons and holes flow from the higher conduction and lower valence bands to another semiconductor. Nevertheless, type I heterojunctions cannot easily separate charge carriers, resulting in the accumulation of electrons and holes in one semiconductor[182]. Type II heterojunctions effectively avoid the accumulation problems (Figure 2-24b), as the electrons transfer to the semiconductor with a lower CB and holes transfer with a higher VB, thus decreasing the contact and recombination of electron-hole pairs[183]. Although the structure of type III heterojunctions (Figure 2-24c) is close to the type II structure, the bandgap of each does not overlap due to the extreme levels of the bands[184]. In a traditional heterojunction, only type II heterojunctions possess an ideal structure for improving the separation of electron-hole pairs.

Taking the example of CdS/MoS_2[185], a type I heterojunction, the photogenerated electrons in the CB of CdS transfer to the CB of MoS_2 due to the more positive conduction of MoS_2 than that of CdS. Therefore, photogenerated electron-hole pairs will be separated in CdS and then enhance the catalytic activity. However, simultaneously, the holes transfer from the VB of CdS to that of MoS_2. Both electrons and holes accumulate in MoS_2, resulting in the ineffective separation in the type I CdS/MoS_2 heterojunction. For a type II heterojunction, like $MoS_2/g\text{-}C_3N_4$[186], the photogenerated electrons transfer from the CB of $g\text{-}C_3N_4$ to the CB of MoS_2, while the holes move in the opposite direction. As a result, electrons and holes are separated and accumulated in MoS_2 and $g\text{-}C_3N_4$, respectively. The separation of charge carriers can significantly reduce the recombination of charges and achieve high catalytic activity.

Because of the diffusion of carriers between semiconductors, there exists an internal electric field on the interface between p- and n-type semiconductors (Figure 2-24d)[187]. In the electric field, the electrons and holes will be quickly driven to the CB of the n-type semiconductor and the VB of the p-type semiconductor, respectively. Thus, electrons and holes will be finally separated in the presence of the internal electric field in a p-n heterojunction system. For example, Meng et al.[37] synthesized a p-n heterojunction ($p\text{-}MoS_2/n\text{-}Bi_2WO_6$) through a bath sonication method. Electrons on $n\text{-}Bi_2WO_6$ transfer into the $p\text{-}MoS_2$, while holes on $p\text{-}MoS_2$ move in the opposite direction, thus resulting in a built-in electric field forming at the interface. With the illumination, electrons and holes will be separated quickly via the synergetic effect and fast charge recombination will be efficiently inhibited simultaneously. All the heterojunction catalysts show high separation efficiency of photogenerated electron-hole pairs.

There are three types (traditional, all-solid-state and direct Z-scheme) of Z-scheme

heterojunctions. In the structures, the charge transfer method is similar but with no intermediate[188,189]. In a direct Z-scheme catalyst, recombination occurs between weak electrons with less negative CB and holes from the semiconductor with less positive VB (Figure 2-24e). As a result, the high oxidation holes and reduction electrons cannot recombine and be maintained for catalytic reactions[190,191]. This method gives new insights into the enhancement of catalytic activity by consuming the excess electrons and holes for the remaining high redox potential in the system. Xiong et al.[192] prepared a Z-scheme heterojunction, $(BiO)_2CO_3/MoS_2$, for the removal of NO 44. Under irradiation, both $(BiO)_2CO_3$ and MoS_2 generated electron-hole pairs. The photogenerated electrons in the CB of $(BiO)_2CO_3$ diffused and combined with the holes in the VB of MoS_2. After that, electrons and holes will be separated and then accumulated at the CB of MoS_2 and the VB of $(BiO)_2CO_3$, respectively. In addition, ternary heterojunctions are also effective architectures for improving the catalytic activity of binary structures. Zhang et al.[193] synthesized a ternary nanocomposite, $TiO_2/g\text{-}C_3N_4/MoS_2$, which exhibited two type II heterojunctions at the interface of $TiO_2/g\text{-}C_3N_4$ and TiO_2/MoS_2. Photogenerated electrons will transfer from the CB of g-C_3N_4 (or MoS_2) to the CB of TiO_2. Furthermore, the photogenerated holes in the VB of TiO_2 shift to the VB of g-C_3N_4 (or MoS_2). Finally, TiO_2 will receive the most photogenerated electrons, which reduce the O_2 and $\bullet O^{2-}$ for degradation. In contrast, g-C_3N_4 and MoS_2 collect the main photogenerated holes. According to previous reports, $TiO_2/g\text{-}C_3N_4$ with the addition of MoS_2 has higher catalytic activity than that without MoS_2 because of the existence of a synergetic effect between $TiO_2/g\text{-}C_3N_4$ and TiO_2/MoS_2 heterojunctions. Beyond that, $TiO_2/g\text{-}C_3N_4/MoS_2$ composite not only extends the light absorption ability but also enhances the light utilization rate. Other ternary catalysts with MoS_2 possess advanced performance.

The step-scheme system is composed of two n-type semiconductors with a staggered band structure, which is similar to type II except for the path of charge migration (Figure 2-24f)[194–196]. An electric field is generated from semiconductor A with a greater work function and lower Fermi level to the one (semiconductor B) with smaller work function and higher Fermi level because of the spontaneous diffusion of electrons on the interface. In addition, electron donors will bend upward owing to electron depletion, and another conductor does the opposite with downward bending originating from the electron accumulation[197]. Therefore, the electrons in semiconductor B will combine with oxidative holes from semiconductor A, which is similar to the Z-scheme heterostructure. Schottky heterojunctions are generated with an

interaction between a semiconductor and a metal (Figure 2-24g)[198]. The electrons are transferred from metal to semiconductor, owing to their different Fermi energies. As for surface heterojunctions, they mainly consist of two different crystal facets of a single semiconductor[199,200]. The mechanism regarding separation of carriers in the surface heterojunction is similar to that in type II (Figure 2-24h)[201]. However, the redox potential in surface heterojunctions is lower than that in type II heterojunctions.

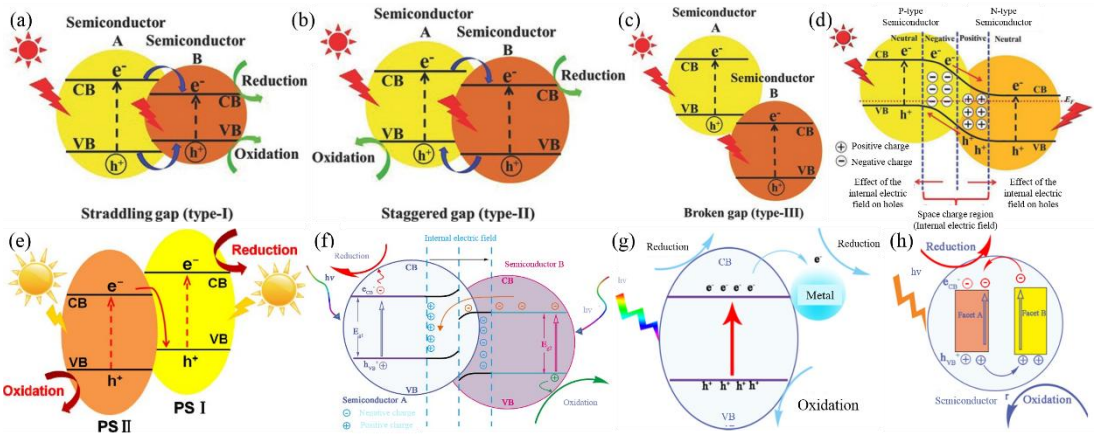

Figure 2-24. Schematic of (a-c) band structure and charge carrier transfer of traditional heterojunction systems, (d) a p-n heterojunction system[202], (e) a direct Z-scheme heterojunction system[190], (f) a step scheme heterojunction system[203], (g) a Schottky junction system[204] and (h) a surface heterojunction system[199].

2.5.3. Composite construction with other materials

With increased research, scientists have gradually recognized that pure MoS_2 nanosheets do not meet practical requirements because of their poor conductivity, difficult recovery and low chemical stability [78,112,208]. As a result, various kinds of functional materials have emerged and been researched in recent years as potential hybrids with MoS_2 to solve these challenges.

Polydopamine (PDA) can be synthesized through a self-polymerization method of dopamine by a simple surface coating in an aqueous solution. As a result of its strong surface adhesion, PDA can adhere well onto almost all inorganic and organic materials. Importantly, the stability can be improved after PDA wrapping, according to the literature[205]. For the enhancement of MoS_2 chemical stability, Wang et al.[206] coated PDA on MoS_2 to fabricate a MoS_2@PDA composite as a catalyst to recover $AuCl_4^-$. As a result, MoS_2@PDA not only exhibits extraordinary performance in catalysis but also shows strong chemical stability for practical applications.

In order to facilitate the separation of MoS_2 from water for further utilization, it is

a common strategy to magnetize MoS_2. Sun et al.[207] constructed Fe_3O_4 on MoS_2 to fabricate a core-shell structured MoS_2@Fe_3O_4 composite (Figure 2-25a). As shown in Figure 2-25b, this material shows stronger magnetism than pure Fe_3O_4 that can be easily separated from water by a magnet. Furthermore, the MoS_2 component plays the original role, such as the properties of adsorption and exhibited extraordinary effect in recovering gold. Furthermore, Wang et al.[208-210] fabricated a ternary composite of Fe_3O_4@PDA-MoS_2 nanospheres (Figure 2-25c). This material not only provides a convenient way to separate material from water by a magnet, but also possesses enough chemical stability, thereby promoting its application as an adsorbent for Pb^{2+} removal. In summary, such MoS_2-based nanocomposites combine the merits of both MoS_2 nanosheets and functional materials, promoting the applications progress of MoS_2-based nanocomposites in the relevant fields.

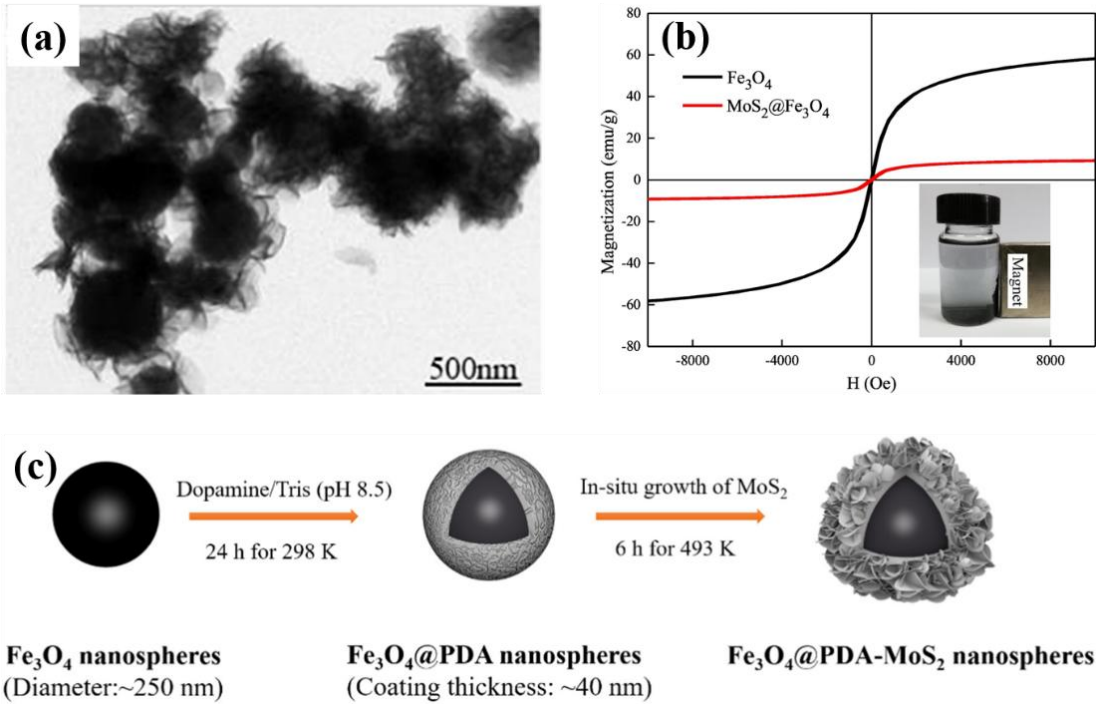

Figure 2-25. (a) TEM image of MoS_2@ Fe_3O_4 composite. (b) Magnetic hysteresis loop of Fe_3O_4 nanospheres and MoS_2@Fe_3O_4 composite. (c) Fabrication procedure of Fe_3O_4@PDA-MoS_2 nanosphere[207,208].

2.6. Conclusions

This review has provided an overview on the strategies and recent advances towards the synthesis, modification and application of 0D, 2D and 3D MoS_2. It has been

demonstrated that 0D, 2D and 3D MoS_2 are very promising for many applications in the fields of water treatment, energy storage and conversion, biology and optoelectronics because of their special properties, including non-toxicity, optical, semiconducting and layer structure properties. The methods for synthesizing 0D, 2D and 3D MoS_2, including liquid exfoliation, electrochemical, template-based, self-assembly and sol-gel and hydrothermal methods, are widely researched. However, the main challenging issue remains the usage of 0D, 2D and 3D MoS_2 is the efficient and low-cost preparation with high quality. An attempt to overcome this issue will drive force for the development of 0D, 2D and 3D MoS_2 for applications.

Furthermore, this review focuses on the modification methods, including surface defects, heteroatom doping and composites for turning the structure and improving the ability of 0D, 2D and 3D MoS_2. Until now, point-like and plane like defects engineering, charge transfer doping, substitutional doping, intercalation doping, composite with elemental, heterojunction and other materials are adopted for both the non-degenerate and degenerate modulation of MoS_2. This not only enables the realization of widely tuned physical and chemical properties but also allows the appearance of metallic behaviors and phase transition under intensive charge injection. Nevertheless, there are still challenges mainly arising from the requirements of addressing the precisely controlled properties, expensive, activation and long-term stability issues, and also the performance. Every method has its own limitations and properties, which greatly improve the development of MoS_2. Moreover, optimizing existing or finding methods is still vital for improving the performance and application of 0D, 2D and 3D MoS_2.

Hence, it is concluded that when advanced synthetic methods satisfy the applications, 0D, 2D and 3D MoS_2 would be realized in various fields, such as electronics, optoelectronics, environmental and energy technologies. In conclusion, the modification strategies of 0D, 2D and 3D MoS_2 and their potential applications have been reviewed. There is immense worth in realizing the application potential of MoS_2.

References

(1) Pető, J.; Ollár, T.; Vancsó, P.; Popov, Z. I.; Magda, G. Z.; Dobrik, G.; Hwang, C.; Sorokin, P. B.; Tapasztó, L. Spontaneous Doping of the Basal Plane of MoS_2 Single Layers through Oxygen Substitution under Ambient Conditions. *Nat. Chem.* **2018**, *10* (12), 1246–1251. doi: 10.1038/s41557-018-0136-2.

(2) Yuan, Y.; Guo, R.; Hong, L.; Ji, X.; Li, Z.; Lin, Z.; Pan, W. Recent Advances and Perspectives

of MoS_2-based Materials for Photocatalytic Dyes Degradation: A Review. *Colloids and Surfaces A: Physicochemical and Engineering Aspects*. **2021**, *611*, 125836. doi: 10.1016/j.colsurfa.2020.125836.

(3) Liu, G.; Robertson, A. W.; Li, M. M. J.; Kuo, W. C. H.; Darby, M. T.; Muhieddine, M. H.; Lin, Y. C.; Suenaga, K.; Stamatakis, M.; Warner, J. H.; et al. MoS_2 Monolayer Catalyst Doped with Isolated Co Atoms for the Hydrodeoxygenation Reaction. *Nat. Chem.* **2017**, *9* (8), 810–816. doi: 10.1038/NCHEM.2740.

(4) Yuan, Y.; Yang, B.; Jia, F.; Song, S. Reduction Mechanism of Au Metal Ions into Au Nanoparticles on Molybdenum Disulfide. *Nanoscale* **2019**, *11* (19), 9488–9497. doi: 10.1039/c8nr09420a.

(5) Xia, D.; Gong F.; Pei X.; Wang W.; Li H.; Zeng W.; Wu M.; Papavassiliou D. V. Molybdenum and Tungsten Disulfides-based Nanocomposite Films for Energy Storage and Conversion: A Review. *Chemical Engineering Journal*. **2018**, *348* (15), 908–928. doi: 10.1016/j.cej.2018.04.207.

(6) Zhang, J.; Wang, T.; Liu, P.; Liu, S.; Dong, R.; Zhuang, X.; Chen, M.; Feng, X. Engineering Water Dissociation Sites in MoS_2 Nanosheets for Accelerated Electrocatalytic Hydrogen Production. *Energy Environ. Sci.* **2016**, *9* (9), 2789–2793. doi: 10.1039/c6ee01786j.

(7) Zhu, H.; Gan, X.; McCreary, A.; Lv, R.; Lin, Z.; Terrones, M. Heteroatom Doping of Two-Dimensional Materials: From Graphene to Chalcogenides. *Nano Today* **2020**, *30*, 100829. doi: 10.1016/j.nantod.2019.100829.

(8) Ge, J.; Ou, E. C.; Yu, R. Q.; Chu, X. A Novel Aptameric Nanobiosensor Based on the Self-Assembled DNA-MoS_2 Nanosheet Architecture for Biomolecule Detection. *J. Mater. Chem. B* **2014**, *2* (6), 625–628. doi: 10.1039/c3tb21570a.

(9) Wu, J. Y.; Zhang, X. Y.; Ma, X. D.; Qiu, Y. P.; Zhang, T. High Quantum-Yield Luminescent MoS_2 Quantum Dots with Variable Light Emission Created via Direct Ultrasonic Exfoliation of MoS_2 Nanosheets. *RSC Adv.* **2015**, *5* (115), 95178–95182. doi: 10.1039/c5ra19201c.

(10) Wang, Y.; Ni, Y. Molybdenum Disulfide Quantum Dots as a Photoluminescence Sensing Platform for 2,4,6-Trinitrophenol Detection. *Anal. Chem.* **2014**, *86* (15), 7463–7470. doi: 10.1021/ac5012014.

(11) Dai, W.; Dong, H.; Fugetsu, B.; Cao, Y.; Lu, H.; Ma, X.; Zhang, X. Tunable Fabrication of Molybdenum Disulfide Quantum Dots for Intracellular Micro RNA Detection and Multiphoton Bioimaging. *Small* **2015**, *11* (33), 4158–4164. doi: 10.1002/smll.201500208.

(12) Siddiqui, G. U.; Ali, J.; Choi, K. H.; Jang, Y.; Lee, K. Fabrication of Blue Luminescent MoS_2 Quantum Dots by Wet Grinding Assisted Co-Solvent Sonication. *J. Lumin.* **2016**, *169*, 342–347. doi: 10.1016/j.jlumin.2015.09.028.

(13) Dong, H.; Tang, S.; Hao, Y.; Yu, H.; Dai, W.; Zhao, G.; Cao, Y.; Lu, H.; Zhang, X.; Ju, H. Fluorescent MoS_2 Quantum Dots: Ultrasonic Preparation, Up-Conversion and Down-Conversion

Bioimaging, and Photodynamic Therapy. *ACS Appl. Mater. Interfaces* **2016**, *8* (5), 3107–3114. doi: 10.1021/acsami.5b10459.

(14) Xu, S.; Li, D.; Wu, P. One-Pot, Facile, and Versatile Synthesis of Monolayer MoS_2/WS_2 Quantum Dots as Bioimaging Probes and Efficient Electrocatalysts for Hydrogen Evolution Reaction. *Adv. Funct. Mater.* **2015**, *25* (7), 1127–1136. doi: 10.1002/adfm.201403863.

(15) Wang, N.; Wei, F.; Qi, Y.; Li, H.; Lu, X.; Zhao, G.; Xu, Q. Synthesis of Strongly Fluorescent Molybdenum Disulfide Nanosheets for Cell-Targeted Labeling. *ACS Appl. Mater. Interfaces* **2014**, *6* (22), 19888–19894. doi: 10.1021/am505305g.

(16) Qiao, W.; Yan, S.; Song, X.; Zhang, X.; Sun, Y.; Chen, X.; Zhong, W.; Du, Y. Monolayer MoS_2 Quantum Dots as Catalysts for Efficient Hydrogen Evolution. *RSC Adv.* **2015**, *5* (118), 97696–97701. doi: 10.1039/c5ra19893c.

(17) Zhang, H. Ultrathin Two-Dimensional Nanomaterials. *ACS Nano* **2015**, *9* (10), 9451–9469. doi: 10.1021/acsnano.5b05040.

(18) Ataca, C.; Şahin, H.; Ciraci, S. Stable, Single-Layer MX_2 Transition-Metal Oxides and Dichalcogenides in a Honeycomb-like Structure. *J. Phys. Chem. C* **2012**, *116* (16), 8983–8999. doi: 10.1021/jp212558p.

(19) Eda, G.; Yamaguchi, H.; Voiry, D.; Fujita, T.; Chen, M.; Chhowalla, M. Photoluminescence from Chemically Exfoliated MoS_2. *Nano Lett.* **2011**, 5111–5116. doi: 10.1021/nl201874w.

(20) Mak, K. F.; Lee, C.; Hone, J.; Shan, J.; Heinz, T. F. Atomically Thin MoS_2: A New Direct-Gap Semiconductor. *Phys. Rev. Lett.* **2010**, *105* (13), 2–5. doi: 10.1103/PhysRevLett.105.136805.

(21) Kuc, A.; Zibouche, N.; Heine, T. Influence of Quantum Confinement on the Electronic Structure of the Transition Metal Sulfide TS_2. *Phys. Rev. B - Condens. Matter Mater. Phys.* **2011**, *83* (24), 1–4. doi: 10.1103/PhysRevB.83.245213.

(22) Splendiani, A.; Sun, L.; Zhang, Y.; Li, T.; Kim, J.; Chim, C. Y.; Galli, G.; Wang, F. Emerging Photoluminescence in Monolayer MoS_2. *Nano Lett.* **2010**, *10* (4), 1271–1275. doi: 10.1021/nl903868w.

(23) Ataca, C.; Ciraci, S. Functionalization of Single-Layer MoS_2 Honeycomb Structures. *J. Phys. Chem. C* **2011**, *115* (27), 13303–13311. doi: 10.1021/jp2000442.

(24) Mann, J.; Sun, D.; Ma, Q.; Chen, J. R.; Preciado, E.; Ohta, T.; Diaconescu, B.; Yamaguchi, K.; Tran, T.; Wurch, M.; et al. Facile Growth of Monolayer MoS_2 Film Areas on SiO_2. *Eur. Phys. J. B* **2013**, *86* (5), 2–5. doi: 10.1140/epjb/e2013-31011-y.

(25) Kadantsev, E. S.; Hawrylak, P. Electronic Structure of a Single MoS_2 Monolayer. *Solid State Commun.* **2012**, *152* (10), 909–913. doi: 10.1016/j.ssc.2012.02.005.

(26) Ramasubramaniam, A. Large Excitonic Effects in Monolayers of Molybdenum and Tungsten Dichalcogenides. *Phys. Rev. B - Condens. Matter Mater. Phys.* **2012**, *86* (11), 115409. doi:

10.1103/PhysRevB.86.115409.

(27) Bertolazzi, S.; Brivio, J.; Kis, A. Stretching and Breaking of Ultrathin MoS_2. *ACS Nano* **2011**, *5* (12), 9703–9709. doi: 10.1021/nn203879f.

(28) Duerloo, K. A. N.; Ong, M. T.; Reed, E. J. Intrinsic Piezoelectricity in Two-Dimensional Materials. *J. Phys. Chem. Lett.* **2012**, *3* (19), 2871–2876. doi: 10.1021/jz3012436.

(29) Tiras, E.; Ardali, S.; Tiras, T.; Arslan, E.; Cakmakyapan, S.; Kazar, O.; Hassan, J.; Janzén, E.; Ozbay, E. Effective Mass of Electron in Monolayer Graphene: Electron-Phonon Interaction. *J. Appl. Phys.* **2013**, *113* (4), 43708. doi: 10.1063/1.4789385.

(30) Feng, J.; Qian, X.; Huang, C. W.; Li, J. Strain-Engineered Artificial Atom as a Broad-Spectrum Solar Energy Funnel. *Nat. Photonics* **2012**, *6* (12), 866–872. doi: 10.1038/nphoton.2012.285.

(31) Zhang, L.; Wu, H. Bin; Yan, Y.; Wang, X.; Lou, X. W. Hierarchical MoS_2 Microboxes Constructed by Nanosheets with Enhanced Electrochemical Properties for Lithium Storage and Water Splitting. *Energy Environ. Sci.* **2014**, *7* (10), 3302–3306. doi: 10.1039/c4ee01932f.

(32) Liu, N.; Guo, Y.; Yang, X.; Lin, H.; Yang, L.; Shi, Z.; Zhong, Z.; Wang, S.; Tang, Y.; Gao, Q. Microwave-Assisted Reactant-Protecting Strategy toward Efficient MoS_2 Electrocatalysts in Hydrogen Evolution Reaction. *ACS Appl. Mater. Interfaces* **2015**, *7* (42), 23741–23749. doi: 10.1021/acsami.5b08103.

(33) Li, B. L.; Setyawati, M. I.; Zou, H. L.; Dong, J. X.; Luo, H. Q.; Li, N. B.; Leong, D. T. Emerging 0D Transition-Metal Dichalcogenides for Sensors, Biomedicine, and Clean Energy. *Small* **2017**, *13* (31), 1–20. doi: 10.1002/smll.201700527.

(34) Guo, Y.; Li, J. MoS_2 Quantum Dots: Synthesis, Properties and Biological Applications. *Mater. Sci. Eng. C* **2020**, *109*, 2–13. doi: 10.1016/j.msec.2019.110511.

(35) Zhang, W.; Du, J.; Liu, Z.; Zhang, D.; Wei, Q.; Liu, H.; Ma, W.; Ren, W.; Cheng, H. M. Production of Carbon Dots during the Liquid Phase Exfoliation of MoS_2 Quantum Dots. *Carbon N. Y.* **2019**, *155*, 243–249. doi: 10.1016/j.carbon.2019.08.067.

(36) Gopalakrishnan, D.; Damien, D.; Shaijumon, M. M. MoS_2 Quantum Dot-Interspersed Exfoliated MoS_2 Nanosheets. *ACS Nano* **2014**, No. 5, 5297–5303. Doi: 10.1021/nn501479e

(37) Wang, T.; Liu, L.; Zhu, Z.; Papakonstantinou, P.; Hu, J.; Liu, H.; Li, M. Enhanced Electrocatalytic Activity for Hydrogen Evolution Reaction from Self-Assembled Monodispersed Molybdenum Sulfide Nanoparticles on an Au Electrode. *Energy Environ. Sci.* **2013**, *6* (2), 625–633. doi: 10.1039/c2ee23513g.

(38) Meng, X.; Li, Z.; Zeng, H.; Chen, J.; Zhang, Z. MoS_2 Quantum Dots-Interspersed Bi_2WO_6 Heterostructures for Visible Light-Induced Detoxification and Disinfection. *Appl. Catal. B Environ.* **2017**, *210*, 160–172. doi: 10.1016/j.apcatb.2017.02.083.

(39) Gopalakrishnan, D.; Damien, D.; Li, B.; Gullappalli, H.; Pillai, V. K.; Ajayan, P. M.; Shaijumon,

M. M. Electrochemical Synthesis of Luminescent MoS_2 Quantum Dots. *Chem. Commun.* **2015**, *51* (29), 6293–6296. doi: 10.1039/c4cc09826a.

(40) Cao, X.; Ding, C.; Zhang, C.; Gu, W.; Yan, Y.; Shi, X.; Xian, Y. Transition Metal Dichalcogenide Quantum Dots: Synthesis, Photoluminescence and Biological Applications. *J. Mater. Chem. B* **2018**, *6* (48), 8011–8036. doi: 10.1039/c8tb02519c.

(41) Shrivastava, M.; Kumari, R.; Parra, M. R.; Pandey, P.; Siddiqui, H.; Haque, F. Z. Electrochemical Synthesis of MoS_2 Quantum Dots Embedded Nanostructured Porous Silicon with Enhanced Electroluminescence Property. *Opt. Mater. (Amst).* **2017**, *73*, 763–771. doi: 10.1016/j.optmat.2017.09.029.

(42) Li, B. L.; Chen, L. X.; Zou, H. L.; Lei, J. L.; Luo, H. Q.; Li, N. B. Electrochemically Induced Fenton Reaction of Few-Layer MoS_2 Nanosheets: Preparation of Luminescent Quantum Dots via a Transition of Nanoporous Morphology. *Nanoscale* **2014**, *6* (16), 9831–9838. doi: 10.1039/c4nr02592j.

(42) Qiao, W.; Yan, S.; Song, X.; Zhang, X.; He, X.; Zhong, W.; Du, Y. Luminescent Monolayer MoS_2 Quantum Dots Produced by Multi-Exfoliation Based on Lithium Intercalation. *Appl. Surf. Sci.* **2015**, *359*, 130–136. doi: 10.1016/j.apsusc.2015.10.089.

(43) Grayfer, E. D.; Kozlova, M. N.; Fedorov, V. E. Colloidal 2D Nanosheets of MoS_2 and Other Transition Metal Dichalcogenides through Liquid-Phase Exfoliation. *Adv. Colloid Interface Sci.* **2017**, *245*, 40–61. doi: 10.1016/j.cis.2017.04.014.

(44) An, S. J.; Park, D. Y.; Lee, C.; Bang, S.; Nguyen, D. A.; Kim, S. H.; Kim, H. Y.; Jeong, H. J.; Jeong, M. S. Facile Preparation of Molybdenum Disulfide Quantum Dots Using a Femtosecond Laser. *Appl. Surf. Sci.* **2020**, *511*, 145507. doi: 10.1016/j.apsusc.2020.145507.

(45) Ren, X.; Pang, L.; Zhang, Y.; Ren, X.; Fan, H.; Liu, S. One-Step Hydrothermal Synthesis of Monolayer MoS_2 Quantum Dots for Highly Efficient Electrocatalytic Hydrogen Evolution. *J. Mater. Chem. A* **2015**, *3* (20), 10693–10697. doi: 10.1039/c5ta02198g.

(46) Mohanty, B.; Ghorbani-Asl, M.; Kretschmer, S.; Ghosh, A.; Guha, P.; Panda, S. K.; Jena, B.; Krasheninnikov, A. V.; Jena, B. K. MoS_2 Quantum Dots as Efficient Catalyst Materials for the Oxygen Evolution Reaction. *ACS Catal.* **2018**, *8* (3), 1683–1689. doi: 10.1021/acscatal.7b03180.

(47) Gan, X.; Zhao, H.; Quan, X. Two-Dimensional MoS_2: A Promising Building Block for Biosensors. *Biosens. Bioelectron.* **2017**, *89*, 56–71. doi: 10.1016/j.bios.2016.03.042.

(48) Li, H.; Wu, J.; Yin, Z.; Zhang, H. Preparation and Applications of Mechanically Exfoliated Single-Layer and Multilayer MoS_2 and WSe_2 Nanosheets. *Acc. Chem. Res.* **2014**, *47* (4), 1067–1075. doi: 10.1021/ar4002312.

(49) Yin, Z.; Li, H.; Li, H.; Jiang, L.; Shi, Y.; Sun, Y.; Lu, G.; Zhang, Q.; Chen, X.; Zhang, H. Single-Layer MoS_2 Phototransistors. *ACS Nano* **2012**, *6* (1), 74–80. doi: 10.1021/nn2024557.

(50) Ghatak, S.; Pal, A. N.; Ghosh, A. Nature of Electronic States in Atomically Thin MoS_2 Field-Effect Transistors. *ACS Nano* **2011**, *5* (10), 7707–7712. doi: 10.1021/nn202852j.

(51) Ciesielski, A.; Samorì, P. Graphene via Sonication Assisted Liquid-Phase Exfoliation. *Chem. Soc. Rev.* **2014**, *43* (1), 381–398. doi: 10.1039/c3cs60217f.

(52) Tang, Z.; Wei, Q.; Guo, B. A Generic Solvent Exchange Method to Disperse MoS_2 in Organic Solvents to Ease the Solution Process. *Chem. Commun.* **2014**, *50* (31), 3934–3937. doi: 10.1039/c4cc00425f.

(53) Li, Y.; Yin, X.; Wu, W. Preparation of Few-Layer MoS_2 Nanosheets via an Efficient Shearing Exfoliation Method. *Ind. Eng. Chem. Res.* **2018**, *57* (8), 2838–2846. doi: 10.1021/acs.iecr.7b04087.

(54) Gupta, A.; Arunachalam, V.; Vasudevan, S. Water Dispersible, Positively and Negatively Charged MoS_2 Nanosheets: Surface Chemistry and the Role of Surfactant Binding. *J. Phys. Chem. Lett.* **2015**, *6* (4), 739–744. doi: 10.1021/acs.jpclett.5b00158.

(55) Guardia, L.; Paredes, J. I.; Rozada, R.; Villar-Rodil, S.; Martínez-Alonso, A.; Tascón, J. M. D. Production of Aqueous Dispersions of Inorganic Graphene Analogues by Exfoliation and Stabilization with Non-Ionic Surfactants. *RSC Adv.* **2014**, *4* (27), 14115–14127. doi: 10.1039/c4ra00212a.

(56) Liu, Y. D.; Ren, L.; Qi, X.; Yang, L. W.; Hao, G. L.; Li, J.; Wei, X. L.; Zhong, J. X. Preparation, Characterization and Photoelectrochemical Property of Ultrathin MoS_2 Nanosheets via Hydrothermal Intercalation and Exfoliation Route. *J. Alloys Compd.* **2013**, *571*, 37–42. doi: 10.1016/j.jallcom.2013.03.031.

(57) Joensen, P.; Frindt, R. F.; Morrison, S. R. Single-Layer MoS_2. *Mater. Res. Bull.* **1986**, *21* (4), 457–461. doi: 10.1016/0025-5408(86)90011-5.

(58) Yeon, C.; Yun, S. J.; Yang, J.; Youn, D. H.; Lim, J. W. Na-Cation-Assisted Exfoliation of MX_2 (M = Mo, W; X = S, Se) Nanosheets in an Aqueous Medium with the Aid of a Polymeric Surfactant for Flexible Polymer-Nanocomposite Memory Applications. *Small* **2018**, *14* (2), 1–10. doi: 10.1002/smll.201702747.

(59) Yu, H.; Zhu, H.; Dargusch, M.; Huang, Y. A Reliable and Highly Efficient Exfoliation Method for Water-Dispersible MoS_2 Nanosheet. *J. Colloid Interface Sci.* **2018**, *514*, 642–647. doi: 10.1016/j.jcis.2018.01.006.

(60) Lee, S. K.; Chu, D.; Song, D. Y.; Pak, S. W.; Kim, E. K. Electrical and Photovoltaic Properties of Residue-Free MoS_2 Thin Films by Liquid Exfoliation Method. *Nanotechnology* **2017**, *28* (19), 195703. doi: 10.1088/1361-6528/aa6740.

(61) You, X.; Liu, N.; Lee, C. J.; Pak, J. J. An Electrochemical Route to MoS_2 Nanosheets for Device Applications. *Mater. Lett.* **2014**, *121*, 31–35. doi: 10.1016/j.matlet.2014.01.052.

(62) Zeng, Z.; Yin, Z.; Huang, X.; Li, H.; He, Q.; Lu, G.; Boey, F.; Zhang, H. Single-Layer

Semiconducting Nanosheets: High-Yield Preparation and Device Fabrication. *Angew. Chemie* **2011**, *123* (47), 11289–11293. doi: 10.1002/ange.201106004.

(63) Chen, F.; Jiang, X.; Shao, J.; Fu, L.; Zhao, S.; Su, W. The Synthesis and Identification of Complete Stacking Bilayer MoS_2 Flakes with Unconventional Shapes via Chemical Vapor Deposition. *Superlattices Microstruct.* **2021**, *158*, 107023. doi: 10.1016/j.spmi.2021.107023.

(64) Pondick, J. V.; Woods, J. M.; Xing, J.; Zhou, Y.; Cha, J. J. Stepwise Sulfurization from MoO_3 to MoS_2 via Chemical Vapor Deposition. *ACS Appl. Nano Mater.* **2018**, *1* (10), 5655–5661. doi: 10.1021/acsanm.8b01266.

(65) Perkgoz, N. K.; Bay, M. Investigation of Single-Wall MoS_2 Monolayer Flakes Grown by Chemical Vapor Deposition. *Nano-Micro Lett.* **2016**, *8* (1), 70–79. doi: 10.1007/s40820-015-0064-2.

(66) Chowdhury, S.; Roy, A.; Liu, C.; Alam, M. H.; Ghosh, R.; Chou, H.; Akinwande, D.; Banerjee, S. K. Two-Step Growth of Uniform Monolayer MoS_2 Nanosheets by Metal-Organic Chemical Vapor Deposition. *ACS Omega* **2021**, *6* (15), 10343–10351. doi: 10.1021/acsomega.1c00727.

(67) Liu, L.; Qiu, H.; Wang, J.; Xu, G.; Jiao, L. Atomic MoS_2 Monolayers Synthesized from a Metal-Organic Complex by Chemical Vapor Deposition. *Nanoscale* **2016**, *8* (8), 4486–4490. doi: 10.1039/c5nr09089j.

(68) Fei, L.; Lei, S.; Zhang, W. B.; Lu, W.; Lin, Z.; Lam, C. H.; Chai, Y.; Wang, Y. Direct TEM Observations of Growth Mechanisms of Two-Dimensional MoS_2 Flakes. *Nat. Commun.* **2016**, *7*, 1–7. doi: 10.1038/ncomms12206.

(69) Lee, S. J.; Son, Y. S.; Choi, J. H.; Kim, S. S.; Park, S. Y. Morphology and Catalytic Performance of MoS_2 Hydrothermally Synthesized at Various Ph Values. *Catalysts* **2021**, *11* (10), 1–12. doi: 10.3390/catal11101229.

(70) Song, T. S.; Fu, L.; Wan, N.; Wu, J.; Xie, J. Hydrothermal Synthesis of MoS_2 Nanoflowers for an Efficient Microbial Electrosynthesis of Acetate from CO_2. *J. CO2 Util.* **2020**, *41*, 101231. doi: 10.1016/j.jcou.2020.101231.

(71) Wu, D.; Zhang, C.; Xu, S.; Zhu, Y.; Xiong, D.; Wang, L.; Chu, P. K. Fabrication and Enhanced Supercapacitance of Hollow Nanostructured MoS_2 Prepared by a CATB-Assisted Hydrothermal Process. *Mater. Lett.* **2016**, *184*, 96–99. doi: 10.1016/j.matlet.2016.08.033.

(72) Huang, Z.; Qi, Y.; Yu, D.; Zhan, J. Radar-like MoS_2 Nanoparticles as a Highly Efficient 808 Nm Laser-Induced Photothermal Agent for Cancer Therapy. *RSC Adv.* **2016**, *6* (37), 31031–31036. doi: 10.1039/c6ra03226e.

(73) Chen, J.; Xu, Z.; Hu, Y.; Yi, M. PEG-Assisted Solvothermal Synthesis of MoS_2 Nanosheets with Enhanced Tribological Property. *Lubr. Sci.* **2020**, *32* (6), 273–282. doi: 10.1002/ls.1501.

(74) Wang, Q.; Jia, F.; Huang, A.; Qin, Y.; Song, S.; Li, Y.; Arroyo, M. A. C. MoS_2@sponge with

Double Layer Structure for High-Efficiency Solar Desalination. *Desalination* **2020**, *481*, 114359. doi: 10.1016/j.desal.2020.114359.

(75) Chen, P.; Zeng, S.; Zhao, Y.; Kang, S.; Zhang, T.; Song, S. Synthesis of Unique-Morphological Hollow Microspheres of MoS_2@montmorillonite Nanosheets for the Enhancement of Photocatalytic Activity and Cycle Stability. *J. Mater. Sci. Technol.* **2020**, *41*, 88–97. doi: 10.1016/j.jmst.2019.09.021.

(76) Zhu, L.; Ji, J.; Liu, J.; Mine, S.; Matsuoka, M.; Zhang, J.; Xing, M. Designing 3D-MoS_2 Sponge as Excellent Cocatalysts in Advanced Oxidation Processes for Pollutant Control. *Angew. Chemie* **2020**, *132* (33), 14072–14080. doi: 10.1002/ange.202006059.

(77) Chen, P.; Liang, Y.; Yang, B.; Jia, F.; Song, S. In-Situ Photo-Reduction of Au(I) for Efficient Recovery of Gold Thiosulfate by 3D MoS_2/Chitosan Aerogel. *ACS Sustain. Chem. Eng.* **2020**, *8* (9), 3673–3680. doi: 10.1016/j.hydromet.2020.105514.

(78) Zhang, Y.; Zuo, L.; Huang, Y.; Zhang, L.; Lai, F.; Fan, W.; Liu, T. In-Situ Growth of Few-Layered MoS_2 Nanosheets on Highly Porous Carbon Aerogel as Advanced Electrocatalysts for Hydrogen Evolution Reaction. *ACS Sustain. Chem. Eng.* **2015**, *3* (12), 3140–3148. doi: 10.1021/acssuschemeng.5b00700.

(79) Xie, Y.; Guo, F.; Mao, J.; Huang, J.; Chen, Z.; Jiang, Y.; Lai, Y. Freestanding MoS_2@carbonized Cellulose Aerogel Derived from Waste Cotton for Sustainable and Highly Efficient Particulate Matter Capturing. *Sep. Purif. Technol.* **2021**, *254*, 117571. doi: 10.1016/j.seppur.2020.117571.

(80) Kim, K.; Tiwari, A. P.; Hyun, G.; Novak, T. G.; Jeon, S. Improving Electrochemical Active Area of MoS_2 via Attached on 3D-Ordered Structures for Hydrogen Evolution Reaction. *Int. J. Hydrogen Energy* **2019**, *44* (52), 28143–28150. doi: 10.1016/j.ijhydene.2019.09.071.

(81) Wang, W.; Yang, P.; Jian, Z.; Li, H.; Xing, Y.; Zhang, S. Rational Design of a 3D MoS_2/dual-Channel Graphene Framework Hybrid as a Free-Standing Electrode for Enhanced Lithium Storage. *J. Mater. Chem. A* **2018**, *6* (28), 13797–13805. doi: 10.1039/c8ta03272f.

(82) Xiang, Z. C.; Zhang, Z.; Xu, X. J.; Zhang, Q.; Yuan, C. MoS_2 Nanosheets Array on Carbon Cloth as a 3D Electrode for Highly Efficient Electrochemical Hydrogen Evolution. *Carbon N. Y.* **2016**, *98*, 84–89. doi: 10.1016/j.carbon.2015.10.071.

(83) Geng, H.; Zhang, X.; Xie, W.; Zhao, P.; Wang, G.; Liao, J.; Dong, L. Lightweight and Broadband 2D MoS_2 nanosheets/3D Carbon Nanofibers Hybrid Aerogel for High-Efficiency Microwave Absorption. *J. Colloid Interface Sci.* **2022**, *609*, 33–42. doi: 10.1016/j.jcis.2021.11.192.

(84) Zhou, J.; Qin, J.; Zhang, X.; Shi, C.; Liu, E.; Li, J.; Zhao, N.; He, C. 2D Space-Confined Synthesis of Few-Layer MoS_2 Anchored on Carbon Nanosheet for Lithium-Ion Battery Anode. *ACS Nano* **2015**, *9* (4), 3837–3848. doi: 10.1021/nn506850e.

(85) Li, L.; Chen, C.; Su, J.; Kuang, P.; Zhang, C.; Yao, Y.; Huang, T.; Yu, A. Three-Dimensional

MoS:X(1<x<2) Nanosheets Decorated Graphene Aerogel for Lithium-Oxygen Batteries. *J. Mater. Chem. A* **2016**, *4* (28), 10986–10991. doi: 10.1039/c6ta03804b.

(86) Yang, M. H.; Jeong, J. M.; Huh, Y. S.; Choi, B. G. High-Performance Supercapacitor Based on Three-Dimensional MoS_2/graphene Aerogel Composites. *Compos. Sci. Technol.* **2015**, *121*, 123–128. doi: 10.1016/j.compscitech.2015.11.004.

(87) Gigot, A.; Fontana, M.; Serrapede, M.; Castellino, M.; Bianco, S.; Armandi, M.; Bonelli, B.; Pirri, C. F.; Tresso, E.; Rivolo, P. Mixed 1T-2H Phase MoS_2/Reduced Graphene Oxide as Active Electrode for Enhanced Supercapacitive Performance. *ACS Appl. Mater. Interfaces* **2016**, *8* (48), 32842–32852. doi: 10.1021/acsami.6b11290.

(88) Yuan, J.; Zhu, J.; Wang, R.; Deng, Y.; Zhang, S.; Yao, C.; Li, Y.; Li, X.; Xu, C. 3D Few-Layered MoS_2/graphene Hybrid Aerogels on Carbon Fiber Papers: A Free-Standing Electrode for High-Performance Lithium/Sodium-Ion Batteries. *Chem. Eng. J.* **2020**, *398*, 125592. doi: 10.1016/j.cej.2020.125592.

(89) Liu, H..; Lv, H.; Xu, Q.; Liu, H.; Wang, Y. G. A Few-Layered MoS_2 Nanosheets/nitrogen-Doped Graphene 3D Aerogel as a High Performance and Long-Term Stability Supercapacitor Electrode. *Nanoscale* **2019**, *11* (10), 4318–4327. doi: 10.1039/c8nr05620j.

(90) Lee, W. S. V.; Peng, E.; Loh, T. A. J.; Huang, X.; Xue, J. M. Few-Layer MoS_2-Anchored Graphene Aerogel Paper for Free-Standing Electrode Materials. *Nanoscale* **2016**, *8* (15), 8042–8047. doi: 10.1039/c6nr00340k.

(91) Wang, S.; Wang, R.; Zhao, Q.; Ren, L.; Wen, J.; Chang, J.; Fang, X.; Hu, N.; Xu, C. Freeze-Drying Induced Self-Assembly Approach for Scalable Constructing MoS_2/graphene Hybrid Aerogels for Lithium-Ion Batteries. *J. Colloid Interface Sci.* **2019**, *544*, 37–45. doi: 10.1016/j.jcis.2019.02.078.

(92) Das, S.; Ghosh, R.; Routh, P.; Shit, A.; Mondal, S.; Panja, A.; Nandi, A. K. Conductive MoS_2 Quantum Dot/Polyaniline Aerogel for Enhanced Electrocatalytic Hydrogen Evolution and Photoresponse Properties. *ACS Appl. Nano Mater.* **2018**, *1* (5), 2306–2316. doi: 10.1021/acsanm.8b00373.

(93) Zhang, X.; Nie, Y.; Zhang, Q.; Liang, Z.; Wang, P.; Ma, Q. Polydopamine nanoparticles@MoS_2 Nanosheet Aerogel-Based ECL Sensing System for MiRNA-126 Detection. *Chem. Eng. J.* **2021**, *411*, 128428. doi: 10.1016/j.cej.2021.128428.

(94) Jaiswal, M. K.; Carrow, J. K.; Gentry, J. L.; Gupta, J.; Altangerel, N.; Scully, M.; Gaharwar, A. K. Vacancy-Driven Gelation Using Defect-Rich Nanoassemblies of 2D Transition Metal Dichalcogenides and Polymeric Binder for Biomedical Applications. *Adv. Mater.* **2017**, *29* (36), 1–9. doi: 10.1002/adma.201702037.

(95) Wang, Q.; Guo, Q.; Jia, F.; Li, Y.; Song, S. Facile Preparation of Three-Dimensional MoS_2

Aerogels for Highly Efficient Solar Desalination. *ACS Appl. Mater. Interfaces* **2020**, *12* (29), 32673–32680. doi: 10.1021/acsami.0c07162.

(96) Yang, L.; Mukhopadhyay, A.; Jiao, Y.; Yong, Q.; Chen, L.; Xing, Y.; Hamel, J.; Zhu, H. Ultralight, Highly Thermally Insulating and Fire Resistant Aerogel by Encapsulating Cellulose Nanofibers with Two-Dimensional MoS_2. *Nanoscale* **2017**, *9* (32), 11452–11462. doi: 10.1039/c7nr02243c.

(97) Cheng, J. B.; Zhao, H. B.; Cao, M.; Li, M. E.; Zhang, A. N.; Li, S. L.; Wang, Y. Z. Banana Leaflike C-Doped MoS_2 Aerogels toward Excellent Microwave Absorption Performance. *ACS Appl. Mater. Interfaces* **2020**, *12* (23), 26301–26312. doi: 10.1021/acsami.0c01841.

(98) Jia, F.; Liu, C.; Yang, B.; Zhang, X.; Yi, H.; Ni, J.; Song, S. Thermal Modification of Molybdenum Disulfide Surface for Tremendous Improvement of Hg^{2+} Adsorption from Aqueous Solution. *ACS Sustain. Chem. Eng.* **2018**, *6* (7), 9065–9073. doi: 10.1021/acssuschemeng.8b01412.

(99) Liu, C.; Kong, D.; Hsu, P. C.; Yuan, H.; Lee, H. W.; Liu, Y.; Wang, H.; Wang, S.; Yan, K.; Lin, D.; et al. Rapid Water Disinfection Using Vertically Aligned MoS_2 Nanofilms and Visible Light. *Nat. Nanotechnol.* **2016**, *11* (12), 1098–1104. doi: 10.1038/nnano.2016.138.

(100) Yao, K.; Xu, Z.; Huang, J.; Ma, M.; Fu, L.; Shen, X.; Li, J.; Fu, M. Bundled Defect-Rich MoS_2 for a High-Rate and Long-Life Sodium-Ion Battery: Achieving 3D Diffusion of Sodium Ion by Vacancies to Improve Kinetics. *Small* **2019**, *15* (12), 1–7. doi: 10.1002/smll.201805405.

(101) Yang, Z.; Zhu, L.; Lv, C.; Zhang, R.; Wang, H.; Wang, J.; Zhang, Q. Defect Engineering of Molybdenum Disulfide for Energy Storage. *Mater. Chem. Front.* **2021**, *5* (16), 5880–5896. doi: 10.1039/d1qm00442e.

(102) He, Z.; Zhao, R.; Chen, X.; Chen, H.; Zhu, Y.; Su, H.; Huang, S.; Xue, J.; Dai, J.; Cheng, S.; et al. Defect Engineering in Single-Layer MoS_2 Using Heavy Ion Irradiation. *ACS Appl. Mater. Interfaces* **2018**, *10* (49), 42524–42533. doi: 10.1021/acsami.8b17145.

(103) Thiruraman, J. P.; Fujisawa, K.; Danda, G.; Das, P. M.; Zhang, T.; Bolotsky, A.; Perea-López, N.; Nicolaï, A.; Senet, P.; Terrones, M.; et al. Angstrom-Size Defect Creation and Ionic Transport through Pores in Single-Layer MoS_2. *Nano Lett.* **2018**, *18* (3), 1651–1659. doi: 10.1021/acs.nanolett.7b04526.

(104) Zhao, G. Y.; Deng, H.; Tyree, N.; Guy, M.; Lisfi, A.; Peng, Q.; Yan, J. A.; Wang, C.; Lan, Y. Recent Progress on Irradiation-Induced Defect Engineering of Two-Dimensional 2H-MoS_2 Few Layers. *Appl. Sci.* **2019**, *9* (4), 678–731. doi: 10.3390/app9040678.

(105) Mishra, P.; Tangi, M.; Ng, T. K.; Hedhili, M. N.; Anjum, D. H.; Alias, M. S.; Tseng, C. C.; Li, L. J.; Ooi, B. S. Impact of N-Plasma and Ga-Irradiation on MoS_2 Layer in Molecular Beam Epitaxy. *Appl. Phys. Lett.* **2017**, *110* (1), 0–5. doi: 10.1063/1.4973371.

(106) Ochedowski, O.; Marinov, K.; Wilbs, G.; Keller, G.; Scheuschner, N.; Severin, D.; Bender,

M.; Maultzsch, J.; Tegude, F. J.; Schleberger, M. Radiation Hardness of Graphene and MoS_2 Field Effect Devices against Swift Heavy Ion Irradiation. *J. Appl. Phys.* **2013**, *113* (21), 214306. doi: 10.1063/1.4808460.

(107) Madauß, L.; Ochedowski, O.; Lebius, H.; Ban-D'Etat, B.; Naylor, C. H.; Johnson, A. T. C.; Kotakoski, J.; Schleberger, M. Defect Engineering of Single- and Few-Layer MoS_2 by Swift Heavy Ion Irradiation. *2D Mater.* **2017**, *4* (1), 15034. doi: 10.1088/2053-1583/4/1/015034.

(108) Guo, H.; Sun, Y.; Zhai, P.; Yao, H.; Zeng, J.; Zhang, S.; Duan, J.; Hou, M.; Khan, M.; Liu, J. Swift-Heavy Ion Irradiation-Induced Latent Tracks in Few- and Mono-Layer MoS_2. *Appl. Phys. A Mater. Sci. Process.* **2016**, *122* (4), 1–7. doi: 10.1007/s00339-016-9940-y.

(109) Mignuzzi, S.; Pollard, A. J.; Bonini, N.; Brennan, B.; Gilmore, I. S.; Pimenta, M. A.; Richards, D.; Roy, D. Effect of Disorder on Raman Scattering of Single-Layer MoS_2. *Phys. Rev. B - Condens. Matter Mater. Phys.* **2015**, *91* (19), 1–7. doi: 10.1103/PhysRevB.91.195411.

(110) Chen, P.; Ni, J.; Liang, Y.; Yang, B.; Jia, F.; Song, S. Piezo-Photocatalytic Reduction of Au(I) by Defect-Rich MoS_2 Nanoflowers for Efficient Gold Recovery from a Thiosulfate Solution. *ACS Sustain. Chem. Eng.* **2021**, *9* (1), 589–598. doi: 10.1021/acssuschemeng.0c08465.

(111) Jayabal, S.; Saranya, G.; Wu, J.; Liu, Y.; Geng, D.; Meng, X. Understanding the High-Electrocatalytic Performance of Two-Dimensional MoS_2 Nanosheets and Their Composite Materials. *J. Mater. Chem. A* **2017**, *5* (47), 24540–24563. doi: 10.1039/c7ta08327k.

(112) Jia, F.; Liu, C.; Yang, B.; Song, S. Microscale Control of Edge Defect and Oxidation on Molybdenum Disulfide through Thermal Treatment in Air and Nitrogen Atmospheres. *Appl. Surf. Sci.* **2018**, *462*, 471–479. doi: 10.1016/j.apsusc.2018.08.166.

(113) Liu, C.; Wang, Q.; Jia, F.; Song, S. Adsorption of Heavy Metals on Molybdenum Disulfide in Water: A Critical Review. *J. Mol. Liq.* **2019**, *292*, 111390. doi: 10.1016/j.molliq.2019.111390.

(114) Yamamoto, S.; Kaneo, Y.; Maeda, H. Styrene Maleic Acid Anhydride Copolymer (SMA) for the Encapsulation of Sparingly Water-Soluble Drugs in Nanoparticles. *J. Drug Deliv. Sci. Technol.* **2013**, *23* (3), 231–237. Doi: 10.1016/S1773-2247(13)50035-9

(115) Zhou, H.; Yu, F.; Liu, Y.; Zou, X.; Cong, C.; Qiu, C.; Yu, T.; Yan, Z.; Shen, X.; Sun, L.; et al. Thickness-Dependent Patterning of MoS_2 Sheets with Well-Oriented Triangular Pits by Heating in Air. *Nano Res.* **2013**, *6* (10), 703–711. doi: 10.1007/s12274-013-0346-2.

(116) Jia, F.; Sun, K.; Yang, B.; Zhang, X.; Wang, Q.; Song, S. Defect-Rich Molybdenum Disulfide as Electrode for Enhanced Capacitive Deionization from Water. *Desalination* **2018**, *446*, 21–30. doi: 10.1016/j.desal.2018.08.024.

(117) Jariwala, D.; Sangwan, V. K.; Lauhon, L. J.; Marks, T. J.; Hersam, M. C. Emerging Device Applications for Semiconducting Two-Dimensional Transition Metal Dichalcogenides. *ACS Nano* **2014**, *8* (2), 1102–1120. doi: 10.1021/nn500064s.

(118) Behura, S.; Nguyen, P.; Che, S.; Debbarma, R.; Berry, V. Large-Area, Transfer-Free, Oxide-Assisted Synthesis of Hexagonal Boron Nitride Films and Their Heterostructures with MoS_2 and WS_2. *J. Am. Chem. Soc.* **2015**, *137* (40), 13060–13065. doi: 10.1021/jacs.5b07739.

(119) Jin, H.; Guo, C.; Liu, X.; Liu, J.; Vasileff, A.; Jiao, Y.; Zheng, Y.; Qiao, S. Z. Emerging Two-Dimensional Nanomaterials for Electrocatalysis. *Chem. Rev.* **2018**, *118* (13), 6337–6408. doi: 10.1021/acs.chemrev.7b00689.

(120) Luo, P.; Zhuge, F.; Zhang, Q.; Chen, Y.; Lv, L.; Huang, Y.; Li, H.; Zhai, T. Doping Engineering and Functionalization of Two-Dimensional Metal Chalcogenides. *Nanoscale Horizons* **2019**, *4* (1), 26–51. doi: 10.1039/c8nh00150b.

(121) Suh, J.; Park, T. E.; Lin, D. Y.; Fu, D.; Park, J.; Jung, H. J.; Chen, Y.; Ko, C.; Jang, C.; Sun, Y.; et al. Doping against the Native Propensity of MoS_2: Degenerate Hole Doping by Cation Substitution. *Nano Lett.* **2014**, *14* (12), 6976–6982. doi: 10.1021/nl503251h.

(122) Tosun, M.; Chan, L.; Amani, M.; Roy, T.; Ahn, G. H.; Taheri, P.; Carraro, C.; Ager, J. W.; Maboudian, R.; Javey, A. Air-Stable N-Doping of WSe_2 by Anion Vacancy Formation with Mild Plasma Treatment. *ACS Nano* **2016**, *10* (7), 6853–6860. doi: 10.1021/acsnano.6b02521.

(123) Xu, E. Z.; Liu, H. M.; Park, K.; Li, Z.; Losovyj, Y.; Starr, M.; Werbianskyj, M.; Fertig, H. A.; Zhang, S. X. P-Type Transition-Metal Doping of Large-Area MoS_2 Thin Films Grown by Chemical Vapor Deposition. *Nanoscale* **2017**, *9* (10), 3576–3584. doi: 10.1039/c6nr09495c.

(124) Zhang, K.; Feng, S.; Wang, J.; Azcatl, A.; Lu, N.; Addou, R.; Wang, N.; Zhou, C.; Lerach, J.; Bojan, V.; et al. Manganese Doping of Monolayer MoS_2: The Substrate Is Critical. *Nano Lett.* **2015**, *15* (10), 6586–6591. doi: 10.1021/acs.nanolett.5b02315.

(125) Wang, J.; Fang, H.; Wang, X.; Chen, X.; Lu, W.; Hu, W. Recent Progress on Localized Field Enhanced Two-Dimensional Material Photodetectors from Ultraviolet—Visible to Infrared. *Small* **2017**, *13* (35), 1–17. doi: 10.1002/smll.201700894.

(126) Lee, S.; Lee, Y. T.; Park, S. G.; Lee, K. H.; Kim, S. W.; Hwang, D. K.; Lee, K. Dimensional Crossover Transport Induced by Substitutional Atomic Doping in $SnSe_2$. *Adv. Electron. Mater.* **2018**, *4* (4), 1–6. doi: 10.1002/aelm.201700563.

(127) Yazdani, S.; Yarali, M.; Cha, J. J. Recent Progress on in Situ Characterizations of Electrochemically Intercalated Transition Metal Dichalcogenides. *Nano Res.* **2019**, *12* (9), 2126–2139. doi: 10.1007/s12274-019-2408-6.

(128) Li, Y.; Cain, J. D.; Hanson, E. D.; Murthy, A. A.; Hao, S.; Shi, F.; Li, Q.; Wolverton, C.; Chen, X.; Dravid, V. P. Au@MoS_2 Core-Shell Heterostructures with Strong Light-Matter Interactions. *Nano Lett.* **2016**, *16* (12), 7696–7702. doi: 10.1021/acs.nanolett.6b03764.

(129) Kiriya, D.; Tosun, M.; Zhao, P.; Kang, J. S.; Javey, A. Air-Stable Surface Charge Transfer Doping of MoS_2 by Benzyl Viologen. *J. Am. Chem. Soc.* **2014**, *136* (22), 7853–7856. doi:

10.1021/ja5033327.

(130) Zhan, W.; Yuan, Y.; Yao, X.; Yang, B., Jia, F.; Lin, C.; Arauz-lara, J.; Song, S. Efficient Recovery of Gold(I) from Thiosulfate Solution through Photocatalytic Reduction with Mn(II)-Doped MoS_2. *ACS Sustainable Chem. Eng.* **2021**, 9, 11681-11690.doi: 10.1021/acssuschemeng.1c02160.

(131) Huo, N.; Konstantatos, G. Ultrasensitive All-2D MoS_2 Phototransistors Enabled by an out-of-Plane MoS_2 PN Homojunction. *Nat. Commun.* **2017**, *8* (1), 1–6. doi: 10.1038/s41467-017-00722-1.

(132) Li, Y.; Xu, C.; Hu, P.; Zhen, L. Carrier Control of MoS_2 Nanoflakes by Functional Self-Assembled Monolayers. *ACS Nano* **2013**, *7* (9), 7795–7804. doi: 10.1021/nn402682j.

(133) Fang, H.; Tosun, M.; Seol, G.; Chang, T. C.; Takei, K.; Guo, J.; Javey, A. Degenerate N-Doping of Few-Layer Transition Metal Dichalcogenides by Potassium. *Nano Lett.* **2013**, *13* (5), 1991–1995. doi: 10.1021/nl400044m.

(134) Chang, Y. M.; Yang, S. H.; Lin, C. Y.; Chen, C. H.; Lien, C. H.; Jian, W. Bin; Ueno, K.; Suen, Y. W.; Tsukagoshi, K.; Lin, Y. F. Reversible and Precisely Controllable P/n-Type Doping of $MoTe_2$ Transistors through Electrothermal Doping. *Adv. Mater.* **2018**, *30* (13), 1–7. doi: 10.1002/adma.201706995.

(135) Tongay, S. Preface to a Special Topic: 2D Materials and Applications. *Appl. Phys. Rev.* **2018**, *5* (1), 2017–2019. doi: 10.1063/1.5024369.

(136) Tongay, S.; Zhou, J.; Ataca, C.; Liu, J.; Kang, J. S.; Matthews, T. S.; You, L.; Li, J.; Grossman, J. C.; Wu, J. Broad-Range Modulation of Light Emission in Two-Dimensional Semiconductors by Molecular Physisorption Gating. *Nano Lett.* **2013**, *13* (6), 2831–2836. doi: 10.1021/nl4011172.

(137) Nan, H.; Wang, Z.; Wang, W.; Liang, Z.; Lu, Y.; Chen, Q.; He, D.; Tan, P.; Miao, F.; Wang, X.; et al. Strong Photoluminescence Enhancement of MoS_2 through Defect Engineering and Oxygen Bonding. *ACS Nano* **2014**, *8* (6), 5738–5745. doi: 10.1021/nn500532f.

(138) Lei, S.; Wang, X.; Li, B.; Kang, J.; He, Y.; George, A.; Ge, L.; Gong, Y.; Dong, P.; Jin, Z.; et al. Surface Functionalization of Two-Dimensional Metal Chalcogenides by Lewis Acid-Base Chemistry. *Nat. Nanotechnol.* **2016**, *11* (5), 465–471. doi: 10.1038/nnano.2015.323.

(139) Cai, L.; McClellan, C. J.; Koh, A. L.; Li, H.; Yalon, E.; Pop, E.; Zheng, X. Rapid Flame Synthesis of Atomically Thin MoO_3 down to Monolayer Thickness for Effective Hole Doping of WSe_2. *Nano Lett.* **2017**, *17* (6), 3854–3861. doi: 10.1021/acs.nanolett.7b01322.

(140) McDonnell, S.; Azcatl, A.; Addou, R.; Gong, C.; Battaglia, C.; Chuang, S.; Cho, K.; Javey, A.; Wallace, R. M. Hole Contacts on Transition Metal Dichalcogenides: Interface Chemistry and Band Alignments. *ACS Nano* **2014**, *8* (6), 6265–6272. doi: 10.1021/nn501728w.

(141) Sarkar, D.; Xie, X.; Kang, J.; Zhang, H.; Liu, W.; Navarrete, J.; Moskovits, M.; Banerjee, K. Functionalization of Transition Metal Dichalcogenides with Metallic Nanoparticles: Implications

for Doping and Gas-Sensing. *Nano Lett.* **2015**, *15* (5), 2852–2862. doi: 10.1021/nl504454u.

(142) Javey, A.; Tu, R.; Farmer, D. B.; Guo, J.; Gordon, R. G.; Dai, H. High Performance N-Type Carbon Nanotube Field-Effect Transistors with Chemically Doped Contacts. *Nano Lett.* **2005**, *5* (2), 345–348. doi: 10.1021/nl047931j.

(143) Jean, R. Molecular Bulk Heterojunctions: An Emerging Approach to Organic Solar Cells. *Acc. Chem. Res.* **2009**, *42* (11), 1719–1730. doi: 10.1021/ar900041b.

(144) Lin, J.; Zhong, J.; Zhong, S.; Li, H.; Zhang, H.; Chen, W. Modulating Electronic Transport Properties of MoS_2 Field Effect Transistor by Surface Overlayers. *Appl. Phys. Lett.* **2013**, *103* (6), 63109. doi: 10.1063/1.4818463.

(145) Rai, A.; Valsaraj, A.; Movva, H. C. P.; Roy, A.; Ghosh, R.; Sonde, S.; Kang, S.; Chang, J.; Trivedi, T.; Dey, R.; et al. Air Stable Doping and Intrinsic Mobility Enhancement in Monolayer Molybdenum Disulfide by Amorphous Titanium Suboxide Encapsulation. *Nano Lett.* **2015**, *15* (7), 4329–4336. doi: 10.1021/acs.nanolett.5b00314.

(146) Shi, Y.; Huang, J. K.; Jin, L.; Hsu, Y. Te; Yu, S. F.; Li, L. J.; Yang, H. Y. Selective Decoration of Au Nanoparticles on Monolayer MoS_2 Single Crystals. *Sci. Rep.* **2013**, *3*, 1–7. doi: 10.1038/srep01839.

(147) Du, Y.; Liu, H.; Neal, A. T.; Si, M.; Ye, P. D. Molecular Doping of Multilayer MoS_2 Field-Effect Transistors: Reduction in Sheet and Contact Resistances. *IEEE Electron Device Lett.* **2013**, *34* (10), 1328–1330. doi: 10.1109/LED.2013.2277311.

(148) Dolui, K.; Rungger, I.; Das Pemmaraju, C.; Sanvito, S. Possible Doping Strategies for MoS_2 Monolayers: An Ab Initio Study. *Phys. Rev. B - Condens. Matter Mater. Phys.* **2013**, *88* (7), 1–9. doi: 10.1103/PhysRevB.88.075420.

(149) Zhan, W.; Jia, F.; Yuan, Y.; Liu, C.; Sun, K.; Yang, B.; Song, S. Controllable Incorporation of Oxygen in MoS_2 for Efficient Adsorption of Hg^{2+} in Aqueous Solutions. *J. Hazard. Mater.* **2020**, *384*, 121382. doi: 10.1016/j.jhazmat.2019.121382.

(150) Title, R. S.; Shafer, M. W. Band Structure of the Layered Transition-Metal Dichalcogenides: An Experimental Study by Electron Paramagnetic Resonance on Nb-Doped MoS_2. *Phys. Rev. Lett.* **1972**, *28* (13), 808–810. doi: 10.1103/PhysRevLett.28.808.

(151) Laskar, M. R.; Nath, D. N.; Ma, L.; Lee, E. W.; Lee, C. H.; Kent, T.; Yang, Z.; Mishra, R.; Roldan, M. A.; Idrobo, J. C.; et al. P-Type Doping of MoS_2 Thin Films Using Nb. *Appl. Phys. Lett.* **2014**, *104* (9), 104–108. doi: 10.1063/1.4867197.

(151) Gao, J.; Kim, Y. D.; Liang, L.; Idrobo, J. C.; Chow, P.; Tan, J.; Li, B.; Li, L.; Sumpter, B. G.; Lu, T. M.; et al. Transition-Metal Substitution Doping in Synthetic Atomically Thin Semiconductors. *Adv. Mater.* **2016**, *28* (44), 9735–9743. doi: 10.1002/adma.201601104.

(152) Lin, Y. C.; Dumcenco, D. O.; Komsa, H. P.; Niimi, Y.; Krasheninnikov, A. V.; Huang, Y. S.;

Suenaga, K. Properties of Individual Dopant Atoms in Single-Layer MoS_2: Atomic Structure, Migration, and Enhanced Reactivity. *Adv. Mater.* **2014**, *26* (18), 2857–2861. doi: 10.1002/adma.201304985.

(153) Ramasubramaniam, A.; Naveh, D. Mn-Doped Monolayer MoS_2: An Atomically Thin Dilute Magnetic Semiconductor. *Phys. Rev. B - Condens. Matter Mater. Phys.* **2013**, *87* (19), 1–7. doi: 10.1103/PhysRevB.87.195201.

(154) Li, H.; Duan, X.; Wu, X.; Zhuang, X.; Zhou, H.; Zhang, Q.; Zhu, X.; Pan, A.; Duan, X. Growth of Alloy $MoS_{2X}Se_{2(1-X)}$ Nanosheets with Fully Tunable Chemical Compositions and Optical Properties. *J. Am. Chem. Soc.* **2014**, *2*, 8–11. doi: 10.1021/ja500069b.

(155) Ma, Q.; Isarraraz, M.; Wang, C. S.; Preciado, E.; Klee, V.; Bobek, S.; Yamaguchi, K.; Li, E.; Odenthal, P. M.; Nguyen, A.; et al. Postgrowth Tuning of the Bandgap of Single-Layer Molybdenum Disulfide Films by Sulfur/selenium Exchange. *ACS Nano* **2014**, *8* (5), 4672–4677. doi: 10.1021/nn5004327.

(156) Zhou, W.; Hou, D.; Sang, Y.; Yao, S.; Zhou, J.; Li, G.; Li, L.; Liu, H.; Chen, S. MoO2 Nanobelts@nitrogen Self-Doped MoS_2 Nanosheets as Effective Electrocatalysts for Hydrogen Evolution Reaction. *J. Mater. Chem. A* **2014**, *2* (29), 11358–11364. doi: 10.1039/c4ta01898b.

(157) Qin, S.; Lei, W.; Liu, D.; Chen, Y. In-Situ and Tunable Nitrogen-Doping of MoS_2 Nanosheets. *Sci. Rep.* **2014**, *4*, 1–5. doi: 10.1038/srep07582.

(158) Chen, M.; Nam, H.; Wi, S.; Ji, L.; Ren, X.; Bian, L.; Lu, S.; Liang, X. Stable Few-Layer MoS_2 Rectifying Diodes Formed by Plasma-Assisted Doping. *Appl. Phys. Lett.* **2013**, *103* (14), 9–13. doi: 10.1063/1.4824205.

(159) Nipane, A.; Karmakar, D.; Kaushik, N.; Karande, S.; Lodha, S. Few-Layer MoS_2 P-Type Devices Enabled by Selective Doping Using Low Energy Phosphorus Implantation. *ACS Nano* **2016**, *10* (2), 2128–2137. doi: 10.1021/acsnano.5b06529.

(160) Wan, J.; Lacey, S. D.; Dai, J.; Bao, W.; Fuhrer, M. S.; Hu, L. Tuning Two-Dimensional Nanomaterials by Intercalation: Materials, Properties and Applications. *Chem. Soc. Rev.* **2016**, *45* (24), 6742–6765. doi: 10.1039/c5cs00758e.

(161) Gao, Y.; Hu, M.; Mi, B. Membrane Surface Modification with TiO_2-Graphene Oxide for Enhanced Photocatalytic Performance. *J. Memb. Sci.* **2014**, *455*, 349–356. doi: 10.1016/j.memsci.2014.01.011.

(162) Dumcenco, D.; Ovchinnikov, D.; Marinov, K.; Lazic, P.; Gibertini, M.; Marzari, N.; Sanchez, O. L.; Kung, Y.; Krasnozhon, D.; Chen, M.; Bertolazzi, S.; Gillet, P.; Fontcuberta, A.; Radenovic, A.; Kis, A. Large-Area Epitaxial Monolayer MoS_2. *ACS Nano* **2015**, No. 4, 4611–4620. doi: 10.1021/acsnano.5b01281.

(163) Guo, Y.; Wei, Y.; Li, H.; Zhai, T. Layer Structured Materials for Advanced Energy Storage

and Conversion. *Small* **2017**, *13* (45), 1–22. doi: 10.1002/smll.201701649.

(164) Enyashin, A. N.; Yadgarov, L.; Houben, L.; Popov, I.; Weidenbach, M.; Tenne, R.; Bar-Sadan, M.; Seifert, G. New Route for Stabilization of 1T-WS_2 and MoS_2 Phases. *J. Phys. Chem. C* **2011**, *115* (50), 24586–24591. doi: 10.1021/jp2076325.

(165) Lukowski, M. A.; Daniel, A. S.; Meng, F.; Forticaux, A.; Li, L.; Jin, S. Enhanced Hydrogen Evolution Catalysis from Chemically Exfoliated Metallic MoS_2 Nanosheets. *J. Am. Chem. Soc.* **2013**, *135* (28), 10274–10277. doi: 10.1021/ja404523s.

(166) Acerce, M.; Voiry, D.; Chhowalla, M. Metallic 1T Phase MoS_2 Nanosheets as Supercapacitor Electrode Materials. *Nat. Nanotechnol.* **2015**, *10* (4), 313–318. doi: 10.1038/nnano.2015.40.

(167) Gong, Y.; Yuan, H.; Wu, C. L.; Tang, P.; Yang, S. Z.; Yang, A.; Li, G.; Liu, B.; Van De Groep, J.; Brongersma, M. L.; et al. Spatially Controlled Doping of Two-Dimensional SnS_2 through Intercalation for Electronics. *Nat. Nanotechnol.* **2018**, *13* (4), 294–299. doi: 10.1038/s41565-018-0069-3.

(168) Koski, K. J.; Wessells, C. D.; Reed, B. W.; Cha, J. J.; Kong, D.; Cui, Y. Chemical Intercalation of Zerovalent Metals into 2D Layered Bi_2Se_3 Nanoribbons. *J. Am. Chem. Soc.* **2012**, *134* (33), 13773–13779. doi: 10.1021/ja304925t.

(169) Chen, K. P.; Chung, F. R.; Wang, M.; Koski, K. J. Dual Element Intercalation into 2D Layered Bi_2Se_3 Nanoribbons. *J. Am. Chem. Soc.* **2015**, *137* (16), 5431–5437. doi: 10.1021/jacs.5b00666.

(170) Kumar, P.; Skomski, R.; Pushpa, R. Magnetically Ordered Transition-Metal-Intercalated WSe_2. *ACS Omega* **2017**, *2* (11), 7985–7990. doi: 10.1021/acsomega.7b01164.

(171) Morosan, E.; Zandbergen, H. W.; Dennis, B. S.; Bos, J. W. G.; Onose, Y.; Klimczuk, T.; Ramirez, A. P.; Ong, N. P.; Cava, R. J. Superconductivity in $CuxTiSe_2$. *Nat. Phys.* **2006**, *2* (8), 544–550. doi: 10.1038/nphys360.

(172) Chen, Z.; Leng, K.; Zhao, X.; Malkhandi, S.; Tang, W.; Tian, B.; Dong, L.; Zheng, L.; Lin, M.; Yeo, B. S.; et al. Interface Confined Hydrogen Evolution Reaction in Zero Valent Metal Nanoparticles-Intercalated Molybdenum Disulfide. *Nat. Commun.* **2017**, *8*, 1–9. doi: 10.1038/ncomms14548.

(173) Yuwen, L.; Xu, F.; Xue, B.; Luo, Z.; Zhang, Q.; Bao, B.; Su, S.; Weng, L.; Huang, W.; Wang, L. General Synthesis of Noble Metal (Au, Ag, Pd, Pt) Nanocrystal Modified MoS_2 Nanosheets and the Enhanced Catalytic Activity of Pd-MoS_2 for Methanol Oxidation. *Nanoscale* **2014**, *6* (11), 5762–5769. doi: 10.1039/c3nr06084e.

(174) Sun, K.; Jia, F.; Yang, B.; Lin, C.; Li, X.; Song, S. Synergistic Effect in the Reduction of Cr(VI) with Ag-MoS_2 as Photocatalyst. *Appl. Mater. Today* **2019**, *2*, 100453. doi: 10.1016/j.apmt.2019.100453.

(175) Guo, M.; Xing, Z.; Zhao, T.; Qiu, Y.; Tao, B.; Li, Z.; Zhou, W. Hollow Flower-like Polyhedral

α-Fe_2O_3/Defective MoS_2/Ag Z-Scheme Heterojunctions with Enhanced Photocatalytic-Fenton Performance via Surface Plasmon Resonance and Photothermal Effects. *Appl. Catal. B Environ.* **2020**, *272*, 118978. doi: 10.1016/j.apcatb.2020.118978.

(176) Yin, Z.; Chen, B.; Bosman, M.; Cao, X.; Chen, J.; Zheng, B.; Zhang, H. Au Nanoparticle-Modified MoS_2 Nanosheet-Based Photoelectrochemical Cells for Water Splitting. *Small* **2014**, *10* (17), 3537–3543. doi: 10.1002/smll.201400124.

(177) Luo, Y.; Huang, D.; Li, M.; Xiao, X.; Shi, W.; Wang, M.; Su, J.; Shen, Y. MoS_2 Nanosheet Decorated with Trace Loads of Pt as Highly Active Electrocatalyst for Hydrogen Evolution Reaction. *Electrochim. Acta* **2016**, *219*, 187–193. doi: 10.1016/j.electacta.2016.09.151.

(178) Sun, W. D.; Wang, J.; Wang, K. W.; Pan, J. J.; Wang, R.; Wen, M.; Zhang, K. Turbulence-like Cu/MoS_2 Films: Structure, Mechanical and Tribological Properties. *Surf. Coatings Technol.* **2021**, *422*, 127490. doi: 10.1016/j.surfcoat.2021.127490.

(179) Lan, S.; Jing, B.; Yu, C.; Yan, D.; Li, Z.; Ao, Z.; Zhu, M. Protrudent Iron Single-Atom Accelerated Interfacial Piezoelectric Polarization for Self-Powered Water Motion Triggered Fenton-Like Reaction. *Small* **2022**, *18* (2). doi: 10.1002/smll.202105279.

(180) He, X.; Wu, P.; Wang, S.; Wang, A.; Wang, C.; Ding, P. Inactivation of Harmful Algae Using Photocatalysts: Mechanisms and Performance. *J. Clean. Prod.* **2021**, *289*, 125755. doi: 10.1016/j.jclepro.2020.125755.

(181) Yang, X.; Chen, Z.; Zhao, W.; Liu, C.; Qian, X.; Zhang, M.; Wei, G.; Khan, E.; Hau Ng, Y.; Sik Ok, Y. Recent Advances in Photodegradation of Antibiotic Residues in Water. *Chem. Eng. J.* **2021**, *405*, 126806. doi: 10.1016/j.cej.2020.126806.

(182) Zhan, W.; Yuan, Y.; Yang, B.; Jia, F.; Song, S. Construction of MoS_2 Nano-Heterojunction via ZnS Doping for Enhancing in-Situ Photocatalytic Reduction of Gold Thiosulfate Complex. *Chem. Eng. J.* **2020**, *394*, 124866. doi: 10.1016/j.cej.2020.124866.

(183) Marschall, R. Semiconductor Composites: Strategies for Enhancing Charge Carrier Separation to Improve Photocatalytic Activity. *Adv. Funct. Mater.* **2014**, *24* (17), 2421–2440. doi: 10.1002/adfm.201303214.

(184) Zhou, H.; Qu, Y.; Zeid, T.; Duan, X. Towards Highly Efficient Photocatalysts Using Semiconductor Nanoarchitectures. *Energy Environ. Sci.* **2012**, *5* (5), 6732–6743. doi: 10.1039/c2ee03447f.

(185) Lu, L.; Wu, B.; Shi, W.; Cheng, P. Metal–organic Framework-Derived Heterojunctions as Nanocatalysts for Photocatalytic Hydrogen Production. *Inorg. Chem. Front.* **2019**, *6* (12), 3456–3467. doi: 10.1039/c9qi00964g.

(186) Ma, S.; Xie, J.; Wen, J.; He, K.; Li, X.; Liu, W.; Zhang, X. Constructing 2D Layered Hybrid CdS nanosheets/MoS_2 Heterojunctions for Enhanced Visible-Light Photocatalytic H_2 Generation.

Appl. Surf. Sci. **2017**, *391*, 580–591. doi: 10.1016/j.apsusc.2016.07.067.

(187) Lu, X.; Jin, Y.; Zhang, X.; Xu, G.; Wang, D.; Lv, J.; Zheng, Z.; Wu, Y. Controllable Synthesis of Graphitic C_3N_4/ultrathin MoS_2 Nanosheet Hybrid Nanostructures with Enhanced Photocatalytic Performance. *Dalt. Trans.* **2016**, *45* (39), 15406–15414. doi: 10.1039/c6dt02247b.

(188) He, M.; Sun, K.; Suryawanshi, M. P.; Li, J.; Hao, X. Interface Engineering of P-N Heterojunction for Kesterite Photovoltaics: A Progress Review. *J. Energy Chem.* **2021**, *60*, 1–8. doi: 10.1016/j.jechem.2020.12.019.

(189) Low, J.; Yu, J.; Jaroniec, M.; Wageh, S.; Al-Ghamdi, A. A. Heterojunction Photocatalysts. *Adv. Mater.* **2017**, *29* (20), 1601694. doi: 10.1002/adma.201601694.

(190) Yu, W.; Zhang, S.; Chen, J.; Xia, P.; Richter, M. H.; Chen, L.; Xu, W.; Jin, J.; Chen, S.; Peng, T. Biomimetic Z-Scheme Photocatalyst with a Tandem Solid-State Electron Flow Catalyzing H_2 Evolution. *J. Mater. Chem. A* **2018**, *6* (32), 15668–15674. doi: 10.1039/c8ta02922a.

(191) Low, J.; Dai, B.; Tong, T.; Jiang, C.; Yu, J. In Situ Irradiated X-Ray Photoelectron Spectroscopy Investigation on a Direct Z-Scheme TiO_2/CdS Composite Film Photocatalyst. *Adv. Mater.* **2019**, *31* (6), 1–5. doi: 10.1002/adma.201802981.

(192) Qi, K.; Cheng, B.; Yu, J.; Ho, W. A Review on TiO_2-Based Z-Scheme Photocatalysts. *Cuihua Xuebao/Chinese J. Catal.* **2017**, *38* (12), 1936–1955. doi: 10.1016/S1872-2067(17)62962-0.

(193) Ani, I. J.; Akpan, U. G.; Olutoye, M. A.; Hameed, B. H. Photocatalytic Degradation of Pollutants in Petroleum Refinery Wastewater by TiO_2- and ZnO-Based Photocatalysts: Recent Development. *J. Clean. Prod.* **2018**, *205*, 930–954. doi: 10.1016/j.jclepro.2018.08.189.

(194) Xiong, T.; Wen, M.; Dong, F.; Yu, J.; Han, L.; Lei, B.; Zhang, Y.; Tang, X.; Zang, Z. Three Dimensional Z-Scheme $(BiO)_2CO_3$/MoS_2 with Enhanced Visible Light Photocatalytic NO Removal. *Appl. Catal. B Environ.* **2016**, *199*, 87–95. doi: 10.1016/j.apcatb.2016.06.032.

(195) Zhang, W.; Xiao, X.; Li, Y.; Zeng, X.; Zheng, L.; Wan, C. Liquid-Exfoliation of Layered MoS_2 for Enhancing Photocatalytic Activity of TiO_2/g-C_3N_4 Photocatalyst and DFT Study. *Appl. Surf. Sci.* **2016**, *389*, 496–506. doi: 10.1016/j.apsusc.2016.07.154.

(196) Fu, J.; Xu, Q.; Low, J.; Jiang, C.; Yu, J. Ultrathin 2D/2D WO_3/g-C_3N_4 Step-Scheme H_2-Production Photocatalyst. *Appl. Catal. B Environ.* **2019**, *243*, 556–565. doi: 10.1016/j.apcatb.2018.11.011.

(197) He, F.; Meng, A.; Cheng, B.; Ho, W.; Yu, J. Enhanced Photocatalytic H_2-Production Activity of WO_3/TiO_2 Step-Scheme Heterojunction by Graphene Modification. *Chinese J. Catal.* **2020**, *41* (1), 9–20. doi: 10.1016/S1872-2067(19)63382-6.

(198) Xu, Q.; Zhang, L.; Cheng, B.; Fan, J.; Yu, J. S-Scheme Heterojunction Photocatalyst. *Chem* **2020**, *6* (7), 1543–1559. doi: 10.1016/j.chempr.2020.06.010.

(199) He, X.; Wang, A.; Wu, P.; Tang, S.; Zhang, Y.; Li, L.; Ding, P. Photocatalytic Degradation of

Microcystin-LR by Modified TiO_2 Photocatalysis: A Review. *Sci. Total Environ.* **2020**, *743*, 140694. doi: 10.1016/j.scitotenv.2020.140694.

(200) Alshamsi, H. A.; Beshkar, F.; Amiri, O.; Salavati-Niasari, M. Porous Hollow $Ag/Ag_2S/Ag_3PO_4$ Nanocomposites as Highly Efficient Heterojunction Photocatalysts for the Removal of Antibiotics under Simulated Sunlight Irradiation. *Chemosphere* **2021**, *274*, 129765. doi: 10.1016/j.chemosphere.2021.129765.

(201) Fan, H.; Zhou, H.; Li, W.; Gu, S.; Zhou, G. Facile Fabrication of 2D/2D Step-Scheme $In_2S_3/Bi_2O_2CO_3$ Heterojunction towards Enhanced Photocatalytic Activity. *Appl. Surf. Sci.* **2020**, *504*, 144351. doi: 10.1016/j.apsusc.2019.144351.

(202) Di Bartolomeo, A. Graphene Schottky Diodes: An Experimental Review of the Rectifying Graphene/semiconductor Heterojunction. *Phys. Rep.* **2016**, *606*, 1–58. doi: 10.1016/j.physrep.2015.10.003.

(203) Sajan, C. P.; Wageh, S.; Al-Ghamdi, A. A.; Yu, J.; Cao, S. TiO_2 Nanosheets with Exposed {001} Facets for Photocatalytic Applications. *Nano Res.* **2016**, *9* (1), 3–27. doi: 10.1007/s12274-015-0919-3.

(204) Yu, J.; Low, J.; Xiao, W.; Zhou, P.; Jaroniec, M. Enhanced Photocatalytic CO_2-Reduction Activity of Anatase TiO_2 by Coexposed {001} and {101} Facets. *J. Am. Chem. Soc.* **2014**, *136* (25), 8839–8842. doi: 10.1021/ja5044787.

(205) Zhou, K.; Li, Y. Catalysis Based on Nanocrystals with Well-Defined Facets. *Angew. Chemie - Int. Ed.* **2012**, *51* (3), 602–613. doi: 10.1002/anie.201102619.

(206) Zhang, X.; Jia, F.; Yang, B.; Song, S. Oxidation of Molybdenum Disulfide Sheet in Water under in Situ Atomic Force Microscopy Observation. *J. Phys. Chem. C* **2017**, *121* (18), 9938–9943. doi: 10.1021/acs.jpcc.7b01863.

(207) Zafar, F.; Wang, H. P.; Lv, C. J.; Ullah, M. H.; Liu, C. Y.; Hua, Y. J.; Mei, L. H.; Huang, J. Enhancement of GAD Storage Stability with Immobilization on PDA-Coated Superparamagnetic Magnetite Nanoparticles. *Catalysts* **2019**, *9* (11). doi: 10.3390/catal9110969.

(208) Wang, Y.; Zeng, S.; Sun, K.; Yang, B.; Jia, F.; Song, S. Highly Stable MoS_2@PDA Composite for Enhanced Reduction of $AuCl_4^-$. *Chem. Phys. Lett.* **2020**, *747*, 137350. doi: 10.1016/j.cplett.2020.137350.

(209) Sun, K.; Mao, S.; Zhan, W.; Liu, C.; Jia, F.; Song, S. In-Situ Reduction of $Au(S_2O_3)_2^{3-}$ for Efficient Recovery of Gold with Magnetically Separable Shell-Core Structured MoS_2@Fe_3O_4 Composite. *Hydrometallurgy* **2020**, *198*, 105514. doi: 10.1016/j.hydromet.2020.105514.

(210) Wang, Q.; Peng, L.; Gong, Y.; Jia, F.; Song, S.; Li, Y. Mussel-Inspired Fe_3O_4 @Polydopamine(PDA)-MoS_2 Core–shell Nanosphere as a Promising Adsorbent for Removal of Pb^{2+} from Water. *J. Mol. Liq.* **2019**, *282*, 598–605. doi: 10.1016/j.molliq.2019.03.

Chapter III. Regulating chemisorption and electrosorption activity for efficient uptake of rare earth elements in low concentration on oxygen-doped molybdenum disulfide

3.1. Introduction

Increasing demands in batteries[1,2], electronics[3], nuclear industry[4] and other vital fields[5], REEs have been widely applied because of their distinctive physical and chemical properties[6]. Primary and secondary resource, likes ores[7], manufacturing generated waste[8,9] and materials based on REEs[10,11], are important roles as resource for REEs. However, generated wastes and effluents during extracting process from most resources with low level of REEs will seriously contaminate ecological environment and cause damages to human health owing to their carcinogenicity and genotoxicity[12,13]. Therefore, it is of urgent need to recover REEs in low concentration range from aqueous solutions.

Till now, the main methods for separating and/or recovering REEs from aqueous solutions are chemical precipitation[14,15], ion exchange[16,17], solvent extraction[18–20], crystallization[21–23] and sorption[24–26]. Although various methods have been used for recovering REEs, these conventional methods present several disadvantages like extreme temperature requirement or high consumption of chemicals. Among these strategies, sorption is widely researched thanks to its economic, environmentally friendly, as well as effective properties. Plenty of materials including activated carbon[27,28], natural materials functionalized with reactive groups[29,30], algal reousrces[31], minerals[32,33], Cryogel[34,35], modified resin micro-particles[26] have been adopted to recover REEs including lanthanum (La), yttrium (Y), gadolinium (Gd), neodymium (Nd), terbium (Tb), etc. Nevertheless, the recovery of REEs is far from the full potential in low concentration because of the lack of incentives and technological constraints. Thus, it is of great necessity to explore an efficient method to recover REEs for sustainable development of the environment.

Electrosorption combining adsorbate with electrochemistry in a system occurs with the application of electricity during adsorption process[36–38]. In the electrolytic cell, potentiostat works as a current and voltage resource, and two or more electrodes connected to an external circuit[39]. The target ions will be firstly induced for immigration and then overcome the electrostatic repulsion between electrodes and mobile ions in

the external electric field[40]. The surface of material coated on the working electrode reacts only one type of the components in the electrolyte. Therefore, the interaction between electrolyte and electrode belongs to chemisorption and electrosorption coupling (CEC) process, which is beneficial for the removal or recovery of targeted ions from solutions.

CEC process strongly relies on the materials with its surficial properties for efficient adsorption, and it could realize highly recovery and selectivity with specific ion. It was proved to have great potential application advantage in heavy metal ions[41–43] like Cr^{3+}, Cd^{2+}, Pb^{2+}, Ni^{2+}, Co^{2+}, Cu^{2+} and Fe^{3+}. Benefited from its rich sulfur atoms in the structure, molybdenum disulfide (MoS_2)[44–48] has long been recognized as an outperformer in the sorption of acid metal ions based on the theory of hard and soft acids and bases such as Hg^{2+}, Pb^{2+}, Cu^{2+}, Zn^{2+}, *et, al*. Motivated by the electric performance of MoS_2 as electrode as well as its earth abundance and nontoxic, it is timely to investigate whether it could be used as electrode in the recovery of REEs from aqueous solutions.

Due to the relevance of electrochemistry performance of electrode and its intrinsic conductivity, the heteroatom doping emerged as a powerful tool to tune its electronic properties[49,50]. The heteroatoms doping strategies have been widely applied in various fields[51–54] including hydrogen evolution reaction, capacitive deionization, batteries, etc. It's reported that charge transfer from incorporated atoms could modify electric order, like charge density and conductivity. The instead of S atoms with O atoms would enhance the interface characteristics in the application[55–57]. Consequently, great efforts should be devoted into the understanding of electrochemistry performance of electrodes under the recovery of REEs in low concentration from aqueous solutions.

Herein, we explored the recovery of REEs, especially La(III), Gd(III) and Y(III), as represented REEs, in low concentration range from aqueous solutions. Besides, more insights were provided the above-mentioned issues on MoS_2 as electrodes for adsorption of targeted ions. The fact that MoS_2 with S-Mo-S lamellar structure belonging to typical transition metal sulfide not only enables interaction with REEs by rich S atoms but also permits the modulating of chemical and electrical properties through facile heteroatom doping. Considering strong hydration of REEs, O atoms were introduced into the structure of MoS_2 for improving hydrophilicity, interaction ability, and electrical properties. We further applied voltage on MoS_2 electrode for inducing immigration of REEs and overcoming electrostatic repulsion between surface and target ions in external electric filed. The experimental studies about CEC process via

O-doped MoS_2 electrode showed efficient REEs recovery performance, in consistent with our theorical prediction. REEs recovery through CEC process via O-doped MoS_2 electrode revealed in this study deepens our understanding on the interaction, immigration, and recovery mechanism of REEs on transition metal sulfides, and helps to guide a thought for recovering REEs in low concentration range over green and recyclable uses.

3.2. Materials and methods

3.2.1. Materials

Conductive carbon black was obtained from the Cabot Corporation. Lanthanum nitrate hexahydrate ($LaN_3O_9 \cdot 6H_2O$, 99.9%), cerium nitrate hexahydrate ($CeN_3O_9 \cdot 6H_2O$, 99.9%), praseodymium nitrate hexahydrate ($PrN_3O_9 \cdot 6H_2O$, 99.9%), neodymium nitrate hexahydrate ($NdN_3O_9 \cdot 6H_2O$, 99.9%), dysprosium nitrate hexahydrate ($DyN_3O_9 \cdot 6H_2O$, 99.9%), erbium nitrate hexahydrate ($ErN_3O_9 \cdot 6H_2O$, 99.9%), ytterbium nitrate hexahydrate ($YbN_3O_9 \cdot 5H_2O$, 99.9%), gadolinium nitrate hexahydrate ($GdN_3O_9 \cdot 6H_2O$, 99.9%), yttrium nitrate hexahydrate ($YN_3O_9 \cdot 6H_2O$, 99.9%) and molybdenum oxide (MoO_2) are originated from Aladdin Co., China. Ammonium molybdate tetrahydrate ($(NH_4)_6Mo_7O_{24} \cdot 4H_2O$), thiourea ($CN_2H_4S$), nitric acid ($HNO_3$), sodium hydroxide (NaOH), Polytetrafluoroethylene ($(C_2F_4)_n$), ammonium chloride (NH_4Cl), sodium sulfate (Na_2SO_4), sodium chloride (NaCl), potassium chloride (KCl), calcium chloride ($CaCl_2$), magnesium chloride ($MgCl_2$), aluminum chloride hexahydrate ($AlCl_3 \cdot 6H_2O$), and iron chloride ($FeCl_3$) were supplied by Sinopharm Chemical Reagent Co., Ltd., China. Deionized water (18.2 MΩ cm) was throughout the whole experiment.

3.2.2. Samples and electrode preparation

Hydrothermal treatment was carried out using a 100 mL Teflon-lined stainless-steel autoclave for synthesizing MoS_2 at 220°C. Different O doping concentration was controlled by adjusting the synthesized temperature (200°C, 180°C and 160°C). 2 mmol $NH_4)_6Mo_7O_{24} \cdot 4H_2O$ and 60 mmol CN_2H_4S were dissolved in 72 mL distilled water by stirring. After this, the solution was transferred a 100 mL Teflon-lined stainless-steel autoclave at various temperature for 24 hours. Followed, after cooling down to normal temperature, products were collected by filtration and being washed using water and ethanol. Finally, they were dried by freeze drying at -60°C in vacuum. The

incorporation of O atoms into the structure of MoS_2 could be easily achieved by adjusting temperature (200°C, 180°C and 160°C) during hydrothermal process. The prepared samples were note as S220, S200, S180 and S160 according to the variable temperature. Electrode was prepared through coating samples on the surface of titanium plate. Considering the stability of titanium and wide application of titanium plate in ions adsorption[58–60], titanium plate as substrate was adopted to coat MoS_2 and O-doped MoS_2 materials. Firstly, 80 mg samples, 10 mg conductive carbon black and 0.8 mL 0.125 mg/L polyvinylidene fluoride (dissolved in DMA) were added in sapphire mortar and grinded. Then, the mixture was coated on titanium plate. Sequentially, prepared electrodes were heated at 60°C for 3 h. Finally, the electrodes were immerged in the deionized water for 12 h, and then dried for 6 h. Before test, the mass of samples on the plate were weighed and calculated according to mass ratio, about 38±4 mg.

3.2.3. Experimental design

REEs recovery experiments were performed in a self-made cell with an external power supply, and the 200 mL solution with a certain REEs concentration and pH was pumped at a rate of 45 rpm through a peristaltic pump (YZ1515x, China). No adjustment for solution pH during the whole operation. REEs concentrations were measured using an Origin Aquamate 8000 UV-vis Spectrophotometer (Lambda 750S). Tested solution was collected at predetermined time intervals from the cell, and the corresponding recovery performances were evaluated via adsorption capacity (Q) and recovery (R) as following equations:

$$Q = \frac{C_0 V_0 - C_t V_t}{A \times m} \quad (1)$$

$$R = \frac{C_0 - C_t}{C_0} \times 100\% \quad (2)$$

Where C_0 and C_t represented the REEs concentration at the initial and t moment during the recovery operations, respectively, mg/L; V_0 and V_t were the volume of REEs solution at the initial and t moment, respectively, L; A exhibited the effective surface area with samples on the surface of electrode, dm^2; m was the mass of samples used in the mixture of electrodes, mg.

3.2.4. Simulations

Interaction between REEs and oxygen doping MoS_2 was calculated based on the density functional theory calculation (DMol3 program). The exchange and correlation

between electrons were described by Generalized Gradient Approximation (GGA) formulated by Perdew-Bruker-Ernzerh (PBE). Cutoff energy for auxiliary plane waves was set to 340 eV. Brillouin zone was sampled by 5x5x1 k-points for the optimization of model. A vacuum length of 20 Å was used to avoid the interaction between the neighboring images. With the aim of investigating REEs recovery performance on O-doped MoS_2 in high concentration, various number of REEs (1, 2, 3, 4) was applied. Stability of O-doped MoS_2 was characterized according to the formation energies as follows:

$$E_{form} = E_{doped} - E_{pure} + \mu_S - \mu_O \quad (3)$$

Where E_{form} was the formation energy; E_{doped} and E_{pure} represented the total energy of O-doped MoS_2 and MoS_2, respectively; μ_S and μ_O displayed the chemical potentials of S and O atoms, respectively.

Adsorption energy of La(III) on MoS_2 (or O-doped MoS_2) was calculated as follows:

$$E_{ads} = E_{adsorbent+La(III)} - E_{adsorbent} - E_{La(III)} \quad (4)$$

In which E_{ads} meant the adsorption energy between La(III) and MoS_2 (or O-doped MoS_2); $E_{adsorbent+La(III)}$ was the total energy after adsorption of La(III) on MoS_2 (or O-doped MoS_2); $E_{adsorbent}$ displayed the energy of MoS_2 (or O-doped MoS_2); $E_{La(III)}$ was the energy of La(III).

3.2.5. Reusability

Desorption of La(III) from O-doped MoS_2 electrode was performed in 1 M HCl (or 1 M NH_4Cl). The desorption efficiency was calculated as following formula:

$$D = \frac{C_d}{C_0} \times 100\% \quad (5)$$

In which C_d presented the concentration of La(III) in HCl (or NH_4Cl) solution during the desorption process, mg/L.

3.2.6. Characterization

Crystal structure was characterized using powder X-ray diffraction (XRD) by Cu-Kα radiation (D8 Advance, Bruker AXS, Germany). Morphology and size analyses were gained through scanning electron microscopy (SEM) and transmission electron microscopy (TEM) by a Phenom ProX G6 microscope (Netherlands) and JEM-F200 microscope (Japan), respectively. Elemental composition was analyzed on the results of X-ray photoelectron spectroscopy (XPS) (Thermo Scientific K-Alpha, America). Atomic bond information was determined according to the results of Raman spectra

(INVIA, Renishaw, England). Electrochemical characteristics of samples were detected by electrochemical workstation (VersaSTAT-450, PAR, U.S.A. Electrochemical characteristics of samples were determined using cyclic voltammetry (CV) and electrochemical impedance spectroscopy (EIS) (VersaSTAT-450, PAR, U.S.A) with a conventional three-electrode cell in the 1 M Na_2SO_4 solutions. Three electrodes consisted of a platinum as the counter electrode, a standard calomel electrode as the reference electrode, and the samples electrode as the working electrode. Working electrode was prepared by thoroughly mixing samples, conductive carbon black and polytetrafluoroethylene as the same in the CEC electrode on titanium plate.

3.3. Results and discussion

3.3.1. Structural and compositional analysis

Crystalline structure of obtained samples at various synthesis temperature (220℃, 210℃, 200℃, 190℃, 180℃, 170℃ and 160℃) was characterized via XRD (Figure 3-1a), in order to investigate the influence of synthesis temperature on structure of MoS_2 and possibility of oxygen doping. Typical peaks located at around 14°, 33°, 39° and 59° were ascribed to diffractions of (002), (100), (103) and (110) planes[61] of 2H-MoS_2 (JCPDS 37-1492), respectively. Compared with XRD result of MoO_2 (Figure 3-1b), no peaks for MoO_2 appeared, indicating the absence of MoO_2 substance. As seen from the XRD result of MoO_2, main peaks at 26.03°, 37.01°, 53.50°, 60.24°, and 66.65° were corresponding to (-111), (111), (-312), (031) and (402) lattice plane[62–64] of MoO_2 (JCPDS 00-032-0671), respectively, indicating high purity of samples. The lower synthesized temperature broadened and shifted all the peaks to lower angle compared with synthesized temperature at 220℃, indicating the decrease of crystallinity[65]. And inferior crystallinity of MoS_2 might lead oxygen atoms dope into the structure. Bond structure of synthesized samples was determined by Raman spectra (Figure 3-1c), where two dominant peaks at around 375 and 403 cm^{-1} were corresponding to the in-plane E^1_{2g} and out-of-plane A_{1g} vibrational modes of Mo-S bond in hexagonal MoS_2. In contrast with S220, the intensity of E^1_{2g} and A_{1g} peaks weakened, which was significantly correlated with decreased crystal degree. In addition, decreased crystal degree would shift and broaden E^1_{2g} and A_{1g} peaks. Beside E^1_{2g} and A_{1g} modes, generated peaks at about 284 and 334 cm^{-1} could be ascribed to the vibration modes of Mo-O bonds, demonstrating the oxygen doping under the decrease of synthesizing temperature[66]. Peaks of Mo-O bond in obtained samples were different from that in

MoO_2 because of different structure of the two kinds materials. The appeared peaks become more obvious with comparison of E^1_{2g} and A_{1g} modes as declined synthesized temperature, suggesting an increasement of oxygen dopant concentration. Related oxygen atomic concentration from EDS results and ratio of Mo-O bond from XPS results in Figure 3-1d verified that the doping oxygen content increased as synthesized temperature dropped.

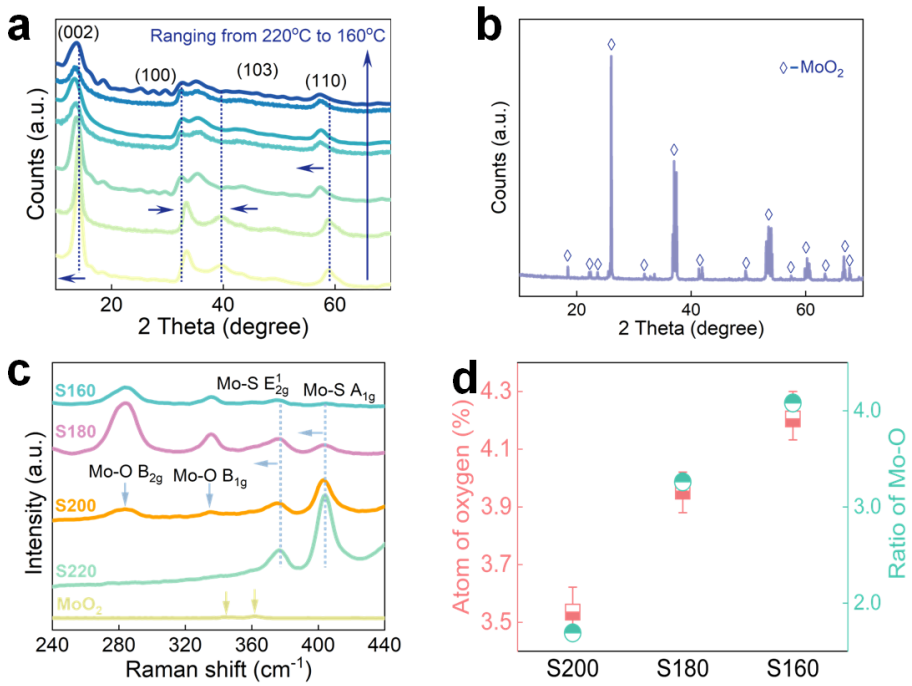

Figure 3-1. XRD spectra of (a) samples obtained at various synthesis temperature and (b) MoO_2. (c) Raman patterns, (d) oxygen content and ratio of Mo-O bond of MoS_2 and O-doped MoS_2.

Atomic valence states and bonding configuration of obtained samples were determined by XPS. Characteristic peaks of Mo 3*d*, S 2*p* and O 1*s* appeared in the survey (Figure 3-2a). Mo 3*d* spectrum (Figure 3-2b) was fitted to the doublet peaks at ~228.3 and 231.4 eV, corresponding to Mo^{4+} in Mo-S bonds, while the doublet peaks at ~229.6 and 233.0 eV were originated from the Mo^{6+} peaks for oxygen doped $MoS_{2-x}O_x$[67]. Peaks affected by generation of Mo-O bond and declined crystallinity shifted. S 2*p* spectrum (Figure 3-2c) was divided into four sets of peaks, ~162,5, 163.6 and 164.6 peaks, belonged to S $2p_{3/2}$, $2p_{1/2}$, and S_2^{2-}[68]. The formation of S_2^{2-} peaks could be attributed to the O doping MoS_2[69]. In addition, shift of peaks was due to varying crystallinity. In the O 1*s* spectrum (Figure 3-2d), the peak at ~532.3 eV for S220 presented adsorbed water[70]. With decreasing synthesis temperature, the peak moved, and situating at ~530.2 eV was assigned to Mo-O bond[71], confirming that oxygen atoms were successfully incorporated into the structure of MoS_2.

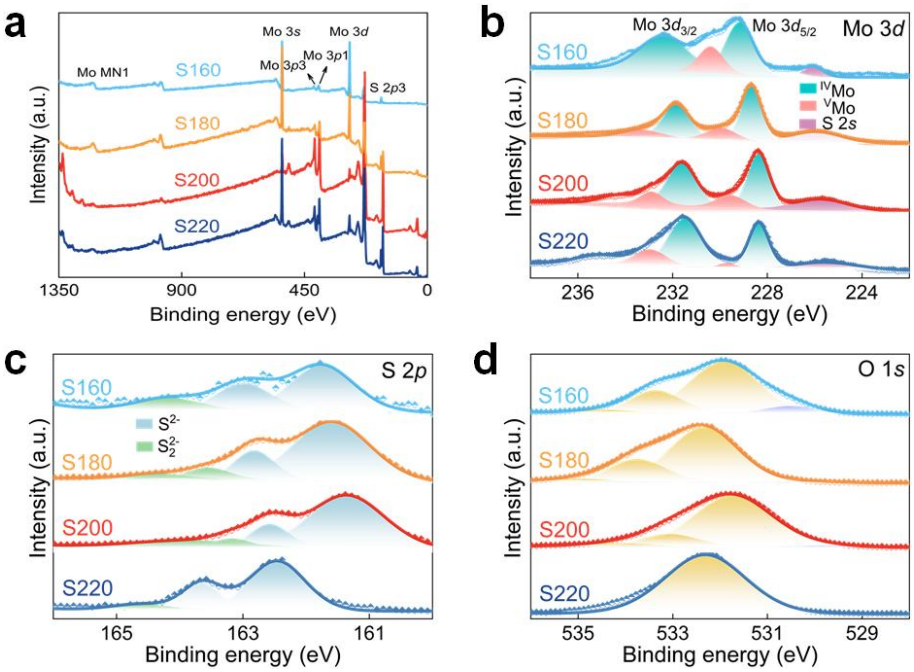

Figure 3-2. XPS (a) survey, deconvoluted high-resolution XPS spectra of (b) Mo 3*d*, (c) S 2*p* and (d) O1*s* of obtained samples at various synthesis temperature.

With the aim of investigating the morphology of O-doped MoS_2, SEM-EDS (Figure 3-3) and TEM (Figure 3-5a) test were carried out. All the samples possessed the nanoflower morphology with ultrathin nanosheets. Notably, the edges became obscurer as synthesized temperature decreased, which suggested the lower crystallinity (in agree with the results of XRD and Raman). Elemental Mo, S and O were exhibited as inert picture (Figure 3-3), indicating the existence of O atoms. Through SEM and corresponding EDS diagram of O-doped MoS_2 (Figure 3-4), as well as the proportions of Mo, S and O, it showed that the evenly distribution of all the elements and increased oxygen content as decreased synthesis temperature. Furthermore, structural characteristics of O-doped MoS_2 were researched according to HRTEM (Figure 3-5b). The distorted areas as marked in green circles demonstrated the generation of crystal defects, which would introduce the enhancement of conductivity[72]. A lattice fringe with spacing of 0.625 nm belonged to the (002) plane of MoS_2. More crystal facets originating from MoS_2 were observed through selected area electron diffraction (SAED) test (Figure 3-5c). Further, TEM image and corresponding elemental mapping images (Figure 3-5d) of O doping MoS_2 confirmed the presence of Mo, S and O elements and the homogenous distribution.

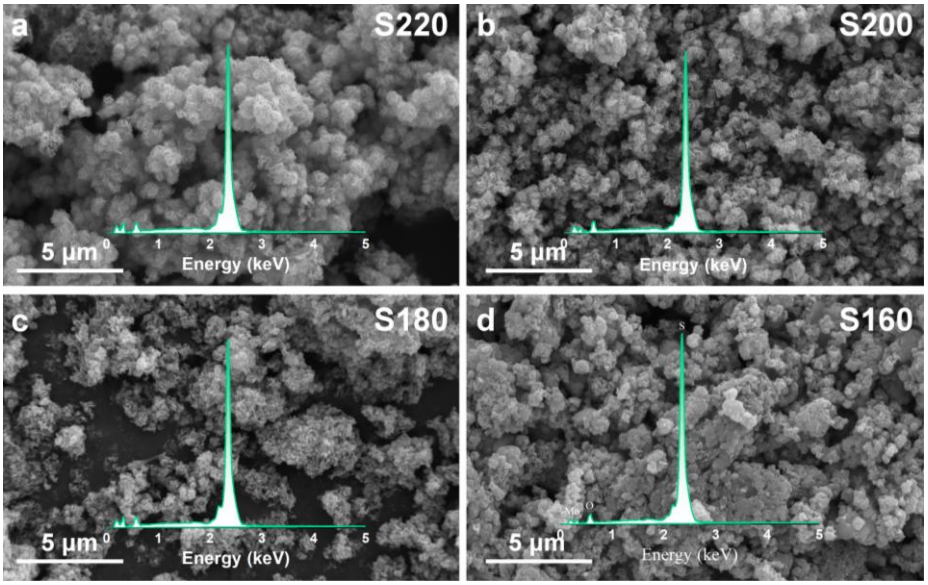

Figure 3-3. SEM-EDS of samples synthesized at different temperature: (a) 220°C; (b) 200°C; (c) 180°C; (d) 160°C.

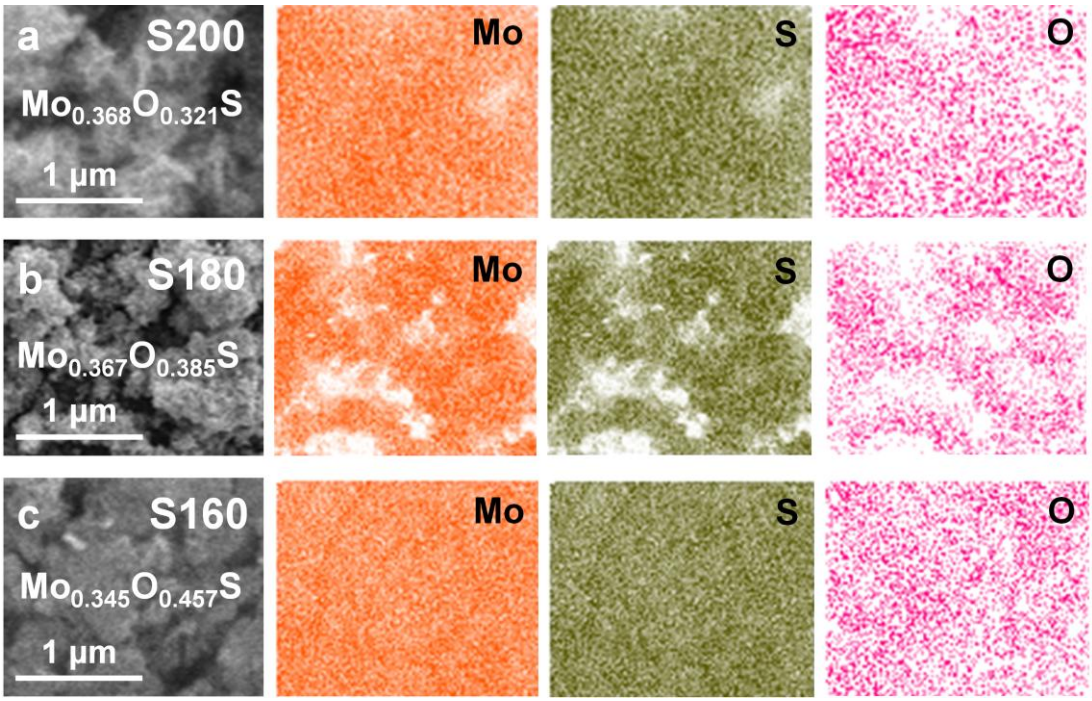

Figure 3-4. SEM and corresponding EDS diagrams of O-doped MoS_2 electrode: (a) 200°C; (b) 180°C; (c) 160°C (Insert proportions of Mo, S and O as chemical formula was normalized calculated through S content as the basis). SEM and corresponding EDS diagrams of O-doped MoS_2 electrode: (a) 200°C; (b) 180°C; (c) 160°C (Insert proportions of Mo, S and O as chemical formula was normalized calculated through S content as the basis).

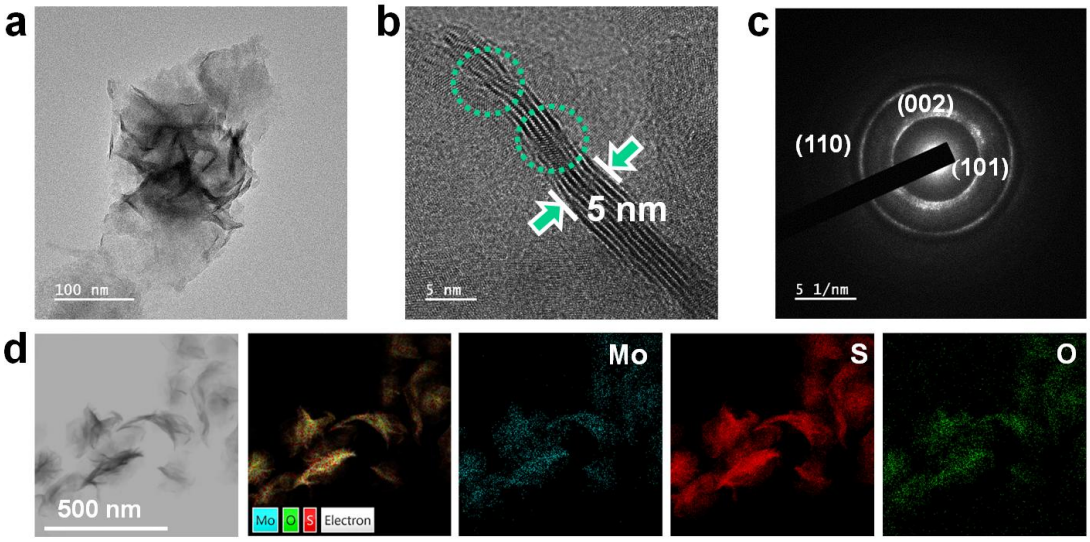

Figure 3-5. (a) TEM image, (b) HRTEM image, (c) SAED pattern, (d) TEM image and corresponding elemental mapping of O-doped MoS_2.

3.3.2. La(III) recovery by CEC

The ability of O-doped MoS_2 electrode through CEC to recover REEs was investigated. During recovery process, O-doped MoS_2 was coated on titanium plate as both cathode and anode. As seen in the digital images (Figure 3-6a, 3-6b, and 3-6c), the electrode after recovery kept almost same with that before use, revealing the stable coating of samples on titanium plate. For comparison, recovery abilities of electrodes with O-doped MoS_2 only as cathode, or anode or without O-doped MoS_2 electrodes were explored. The results displayed that O-doped MoS_2 as both cathode and anode performed the largest REEs recovery, which was up to adsorption capacity (Figure 3-6d) of 365.71 mg/(g·dm^2) and corresponding recovery (Figure 3-6e) of 91.43%. Adsorption capacity (or recovery) using O-doped MoS_2 as both electrodes was more than 5 and 11 folds than that using O-doped MoS_2 as cathode and anode, respectively, demonstrating that both electrodes with O-doped MoS_2 electrode would enhance transfer of ions in the solutions. The benefits of this dual-plate electrodes are rapid diffusion of targeted ions into the trench and improved specificity from two applied electrode potentials[73]. O-doped MoS_2 was served as one electrode (cathode or anode) to study the recovery performance. Recovery by O-doped MoS_2 cathode was higher than O-doped MoS_2 anode, since cathode was negatively charged, which was benefit of the adsorption of positively charged La(III) through electrostatic interaction. As for titanium plate without O-doped MoS_2, adsorption capacity and recovery were almost zero, indicating that there was no interaction between targeted ions and the substrate.

Besides, the pseudo-first-order model and the pseudo-second-order models were applied to study the adsorption process, and corresponding fitting data were exhibited in Table 3-1. The results showed that the adsorption process was well fitted by two models, including physical and chemical adsorption.

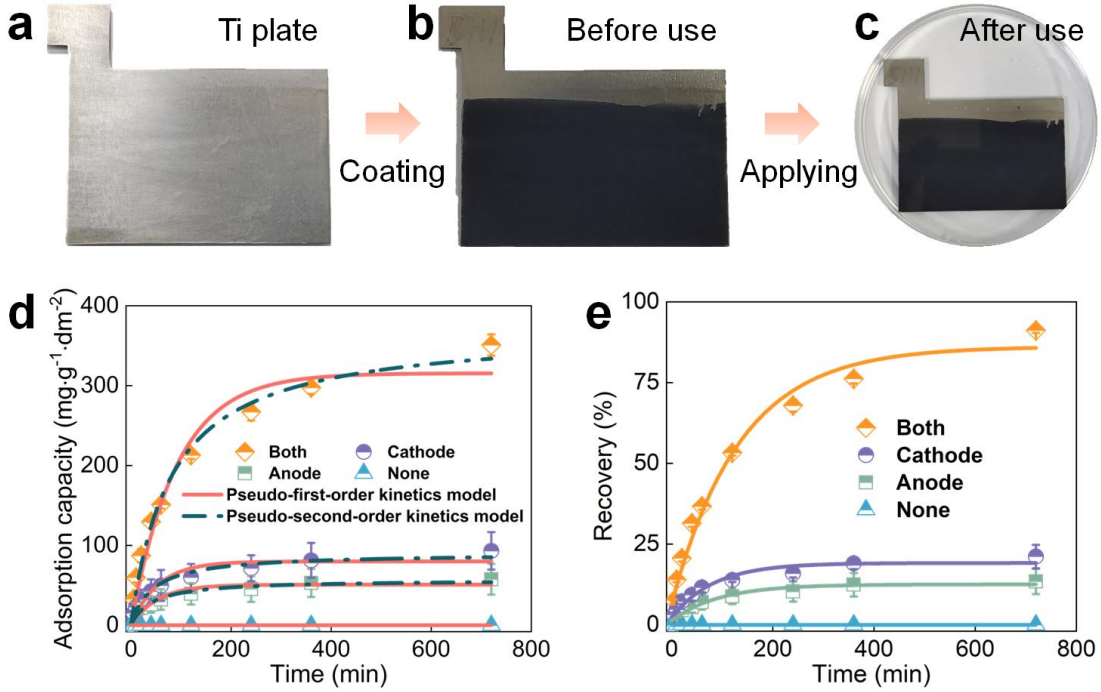

Figure 3-6. Digital images of (a) Ti plate, electrode (b) before and (c) after use in aqueous solutions. (d) Adsorption capacity and (e) recovery of La(III) on O-doped MoS_2 at an initial concentration of 10 mg/L.

Table 3-1. Kinetic parameters for La(III) recovery.

	Pseudo-first-order kinetic model			Pseudo-second-order kinetic model		
	q_e (mg/(g·dm^2)	k_1 (min^{-1})	R^2	q_e (mg/(g·dm^2)	K_2 (min^{-1})	R^2
Both	315.4409	0.0110	0.966	370.6622	0.00003382	0.989
Cathode	79.8523	0.0186	0.926	90.2004	0.00002590	0.972
Anode	50.7445	0.0190	0.934	57.0419	0.00004261	0.978

La(III) recovery performance of at various initial concentrations was measured, in order to study the applicability (Figure 3-7a). As the increase of initial concentration, adsorption increased and then reached balance, while the recovery dropped with concentration higher than 5 mg/L, demonstrating that saturation of recovery sites. When the initial concentration was lower than 5 mg/L, O-doped MoS_2 electrode could obtain recovery of 100%. The recovery was higher than 90% within a low concentration range.

In comparison with previous works, recovery efficiency based on adsorption capacity and recovery time was normalized, as displayed in Table 3-2, and this work exhibited superior recovery ability. Recovery mechanism of O-doped MoS_2 by CEC was studied by XPS. After recovery, the peaks for La(III) could be found in the survey spectrum (Figure 3-7b). Species of O-doped MoS_2 existed in the electrode after La(III) recovery by CEC process. The slight shift of peaks in Mo 3*d* of anode might be attributed to oxidation (Figure 3-7c), while the changes appeared in S 2*p* (Figure 3-7d) and O 1*s* (Figure 3-7e) could be ascribed to the interaction between S and O atoms with La(III). Moreover, the peaks centered at ~832.92, ~851.8, and ~856.9 eV for La $3d_{5/2}$ and La $3d_{3/2}$ (Figure 3-7f) could be explained as the transfer of electrons from S or O atoms to La(III), thus to form La-S or La-O coordination bond. All these results manifested that the O atoms and S atoms were the dominant sites for chemisorption of La(III).

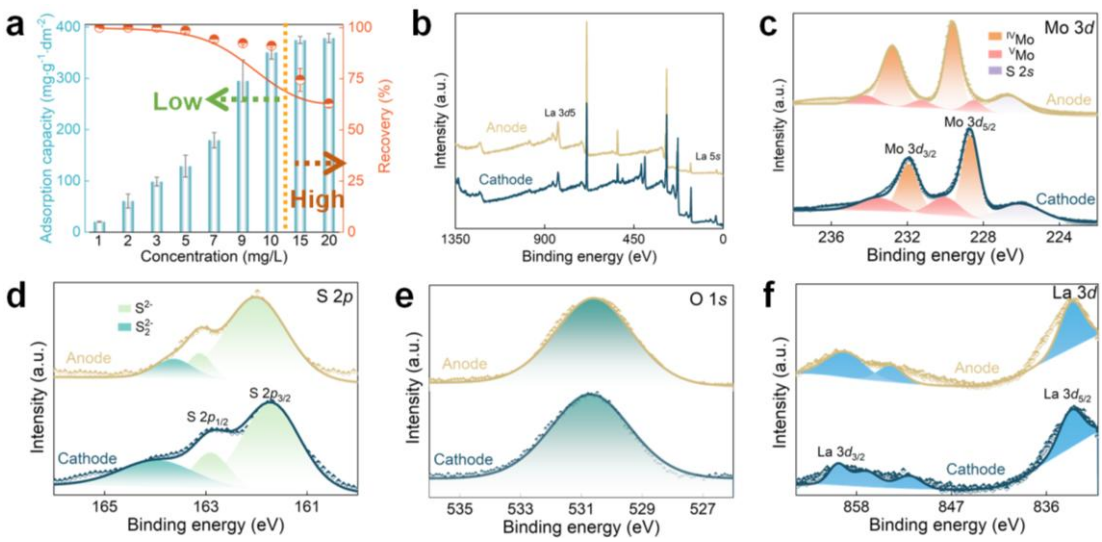

Figure 3-7. (a) Recovery of La(III) at various initial concentration. (b) Survey spectrum and high-resolution XPS spectra of (c) Mo 3d, (d) S 2p, (e) O 1s and (f) La 3d after the recovery of La(III).

Apart from the above results about the adsorption of La(III), TEM and related elemental mapping of O-doped MoS_2 sample after La(III) recovery confirmed the evenly distribution of Mo, S, O, and La (Figure 3-8d). According to the results of HRTEM (Figure 3-8a, 3-8b, and 3-8c), the structure of O-doped MoS_2 after recovery was almost identical to its pre-recovery state. TEM result showed that existence of O-doped MoS_2 was still with nanoflower morphology. Distorted areas as marked in green circles were crystal defects[74] in HRTEM results. Therefore, La(III) could be successfully recovered by O-doped MoS_2 electrode through the CEC process.

Table 3-2. Comparison of La(III) recovery in the work with previous literatures.

Materials	Initial concentration (mg/L)	Adsorption capacity (mg/g)	Efficiency (mg/(g·min))	Ref.
Amberlite XAD-7 resin	200	7.342	0.041	[75]
Purolite S950	200	22.45	0.062	[76]
Carbon nanotube	100	23.23	0.032	[77]
Titanium oxide	100	12.31	0.035	[78]
Activated carbon functionalized	50	10.14	0.051	[79]
$[Zn(bim)_2(bdc)]_n$ MOF	25	8.85	0.051	[80]
Ca−Alginate Beads	25	6.373	0.004	[81]
GO composite	25	3.292	0.022	[82]
Fe_3O_4/GNPs	10	3.84	0.032	[83]
CEC with O-doped MoS_2	9.92	65.82	0.091	This work

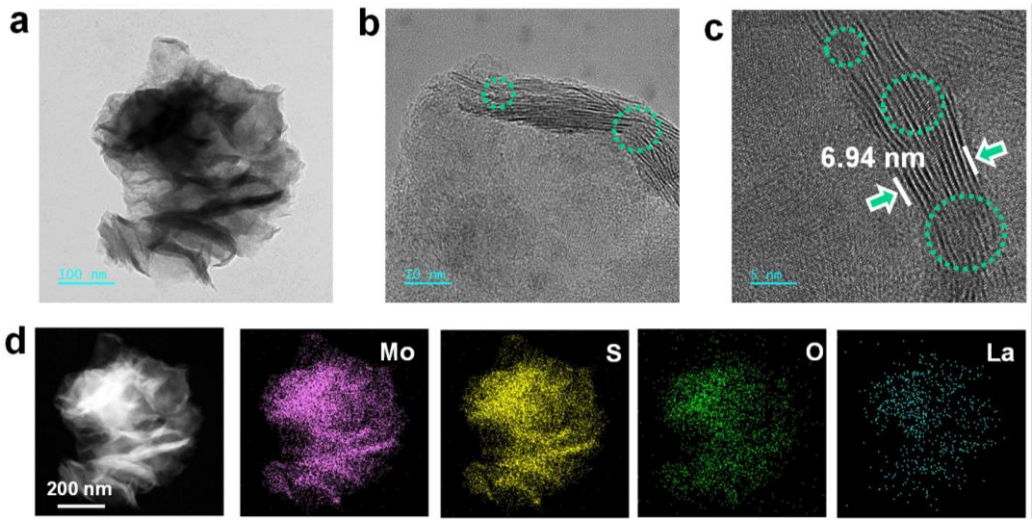

Figure 3-8. (a) TEM, (b, c) HRTEM images, and (d) TEM image and related elemental mapping: Mo, S, O and La of O-doped MoS_2 after the recovery of La(III).

3.3.3. Effects of environmental conditions and ion storage

MoS_2 and O-doped MoS_2 with various O doping concentrations as electrodes for La(III) recovery were investigated (Figure 3-9a). Note that incorporation of O atoms into MoS_2 strengthened recovery of La(III), and the highest adsorption capacity and recovery were almost 1.45 and 2.25 times higher than that of MoS_2, respectively. The enhanced recovery might occur from improved affinity between electrode with targeted ions and specific capacitance in the electrical double layer. Compared with MoO_2 electrode, adsorption capacity and recovery using O-doped MoS_2 electrode was better. Because of different crystal structure of MoS_2 and MoO_2, MoS_2 possessed better conductivity and surface area with sulfur atoms. REEs could be efficiently recovered through oxygen doping engineering on MoS_2 for improving electrochemical and chemical properties. La(III) recovery was reduced since doping an excessive amount of oxygen atoms would weaken the specific capacitance for ion adsorption, as proved in previous work[84]. After that, charging voltage on CEC process of recovery was researched. Figure 3-9b presented the adsorption capacity and recovery of La(III) at various applied voltage. Here, it could be seen that La(III) recovery enhanced quickly upon applying the charging voltage, and then tended to a stable stage, indicating the occurrence of strong electrostatic interaction at beginning and then reached saturation of adsorption sites on O-doped MoS_2 electrode. Effect of distance between two electrodes on La(III) recovery was employed (Figure 3-9c). Adsorption capacity and recovery declined with the increase of distance. At greater distance, resistance between two electrodes was enhanced, and the electrical double layer was induced. As a result, the adsorption capacity and recovery ability were reduced. The influence of pH on La(III) recovery was studied (Figure 3-9d). The higher pH, the higher La(III) recovery by CEC process was achieved, which was owing to the less active sites occupied by H^+. Apart from the above variants, as increase of pH, O-doped MoS_2 possessed more negative charges, being in favor of the adsorption of La(III) according to electrostatic interaction (Figure 3-9e). The balance of recovery was owing to saturation of active sites. To evaluate the application of CEC method in actually by O-doped MoS_2 electrode, recovery of La(III) was tested in a binary mixed solution (Figure 3-9f). As could be found, the adsorption capacity and recovery were minimally affected, and ions with higher valence exhibited stronger competition with La(III). Anyway, the adsorption capacity and recovery kept at a high level.

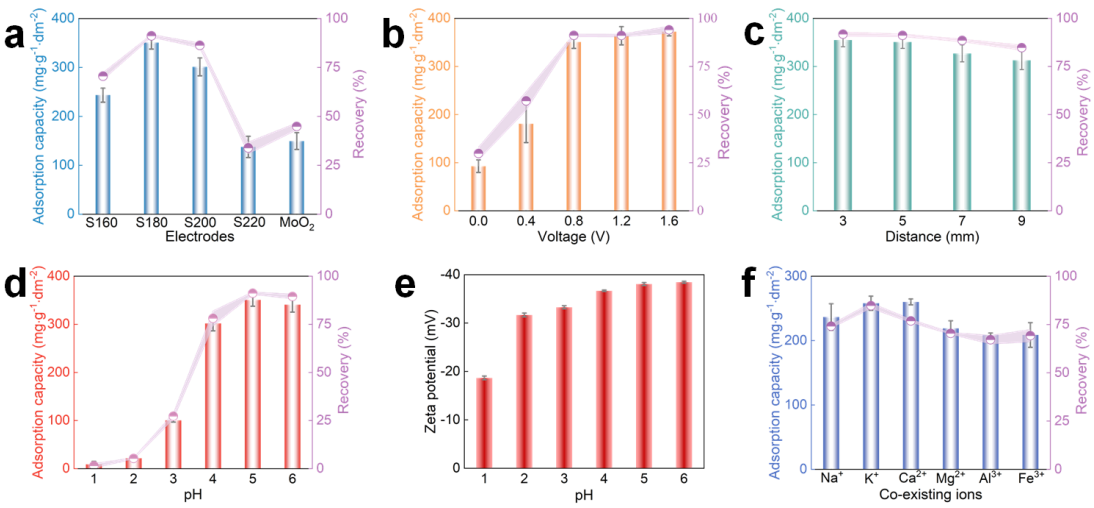

Figure 3-9. (a) Adsorption capacity and recovery of La(III) on MoS_2 and O-doped MoS_2 with different O doping concentration. Effect of (b) charging voltage, (c) distance between two electrodes, and (d) pH on the CEC process of La(III) recovery. (e) Zeta potential of O-doped MoS_2 at various pH. (f) Effect of co-existence ions on recovery performance of La(III).

In CEC process for ions recovery, it is related with electrical double layer for storage of ions and interaction between electrode and ions. Here, the electrochemical performances of MoO_2, MoS_2 and O-doped MoS_2 electrodes were tested by CV in a 1 M Na_2SO_4 solution (Figure 3-10a and 3-10b). The results showed that MoS_2 and O-doped MoS_2 obtained good capacitance property, and capacitance firstly increased and then declined with the enhanced O doping concentration. Among these materials, S180 exhibited the best adsorption capacity. Better ion storage ability appeared on O-doped MoS_2 electrode than that on MoO_2 electrode. Further, the resistance of ions transfer was examined through EIS test (Figure 3-10c). The calculated charge-transfer resistance (R_{ct}) based on circuit were 5.65, 3.10, 2.37, 2.63 Ω for S160, S180, S200, and S220, respectively. Compared with R_{ct} of MoO_2 at 76.56 Ω (Figure 3-10d), all the MoS_2 and O-doped MoS_2 had lower ion transfer ability. Moreover, it was revealed that the incorporation of O atoms would reduce the ions transfer resistance where S180 had the smallest charge transfer resistance among MoS_2 and O-doped MoS_2 electrodes due to its good electric conductivity. Improved contact resistance was attributed to formation of Mo-O bond with a lower Schottky barrier compared with Mo-S bond[85]. After oxygen doping, disordered structure generated more active unsaturated sulfur atoms, thus to tune electronic structure[86]. A decline of R_{ct} from S160 to S180 was originated from the decreased disorder degree. The above results demonstrated that O-doped MoS_2 had better electrical double layer for the ions storage and lower resistance for the ions transfer.

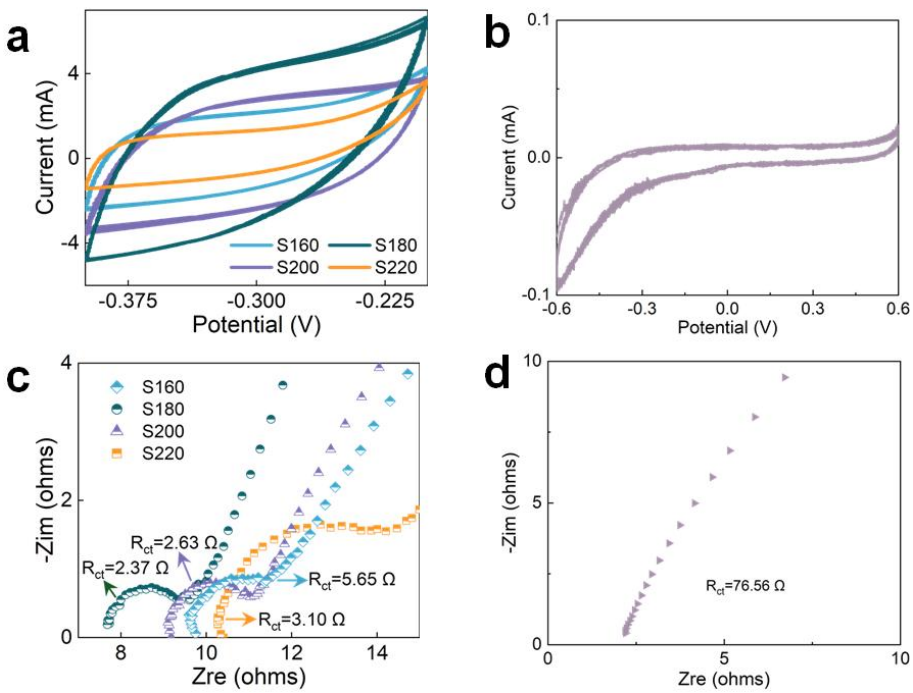

Figure 3-10. CV curves of (a) MoS_2, O-doped MoS_2, and (b) MoO_2 in 1 M Na_2SO_4 solution. (c) EIS results of MoS_2, O-doped MoS_2, and (d) MoO_2 in 1 M Na_2SO_4 solution.

3.3.4. Interaction in CEC process

To account for interaction performance between La(III) and O-doped MoS_2, DFT was adopted to consider adsorption of La(III) on different O doping concentrations of MoS_2. Firstly, MoS_2 and possible structure of O-doped MoS_2 were optimized (Figure 3-11a, 3-11b, 3-11c, 3-11d, and 3-11e). According to related electron density maps of O-doped MoS_2 (Figure 3-11f and 3-11g) with different doping concentrations, it was demonstrated that O atoms could strongly bind with Mo atoms. The shift of doped atoms related to the atomic volume, and O shifted inward because of the smaller volume compared with S atom[87]. Besides, bond length of Mo-O was shorter than that of Mo-S, which was ascribed to the stronger electronegativity of O atoms. With more O atoms doping, structure of O-doped MoS_2 became more distorted in consistent with experimental results. Formation energy was calculated for further investigating the stability of O-doped MoS_2 (Figure 3-11h). Negative formation energy exhibited the possibility of a spontaneous reaction for O doping. The highest absolute value of formation energy was MoS_2-$2O_{(3)}$ in MoS_2 with two substituted S atoms by O atoms, indicating that its status as the most stable structure at this doping concentration. In the subsequent adsorption study, MoS_2-$2O_{(3)}$ was utilized as the model for the incorporation of two O atoms doping.

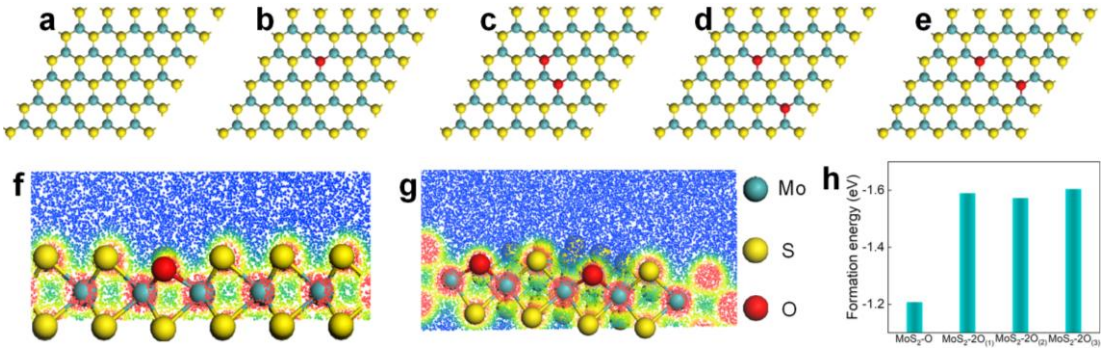

Figure 3-11. Top views of the supercell models of (a) MoS_2, (b) MoS_2-O, (c) MoS_2-$2O_{(1)}$, (d) MoS_2-$2O_{(2)}$ and (e) MoS_2-$2O_{(3)}$. Electron density maps of (f) MoS_2-O and (g) MoS_2-2O. (h) Formation energy of MoS_2 and O-doped MoS_2.

Calculated interaction energy of La(III) and MoS_2 with and without O incorporation was displayed in Figure 3-12a. Adsorption energy between La(III) and O-doped MoS_2 was superior to that of MoS_2. Adsorption energy was enhanced with more oxygen atoms doped, showing that the incorporated O atoms had strong interaction ability with La(III). To figure out reason of decreased recovery in high concentration, adsorption energy between various concentration of La(III) and O-doped MoS_2 was calculated (Figure 3-12b). Interaction between La(III) and O-doped MoS_2 was strengthened at first and then to plateaued. As a consequence, in high concentration situation, La(III) recovery will decline, but adsorption capacity was apt to balance. Except this, there was repulsion among La(III) because of electrostatic force with same positive charges. With adsorbing more La(III), stronger interaction between targeted ions and electrodes should be considered. Moreover, interacted orbitals of La(III) and S (or O atoms) were used for further clarifying adsorption process (Figure 3-12d). *S*, *p* and *d* orbitals in La(III) bound strongly with S *p* and O *s*, *p* orbitals, demonstrating the interaction between La and S, O atoms. Compared with the results in MoS_2 without (Figure 3-12e) and with more O doping centration (Figure 3-12f) system, interaction between MoS_2 and La(III) was enhanced as more O atoms introduced. Based on Mulliken atomic charge changes (ΔQ) (Figure 3-12c), the charge changes between La(III) and MoS_2 (or O-doped MoS_2) before and after adsorption were calculated. Lost charges of La(III) transferred to nearby S or O atoms, exhibiting the tough interaction between La(III) and S or O atoms.

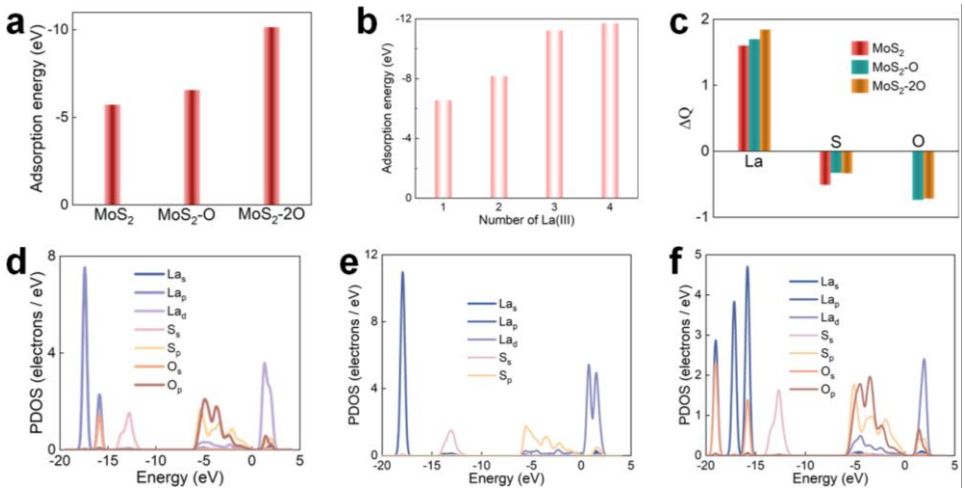

Figure 3-12. (a) Adsorption energy between La(III) and MoS_2 (or O-doped MoS_2). (b) Adsorption energy between various concentration La(III) and O-doped MoS_2. (c) Mulliken atomic charge changes of La(III), S and O in the system of La(III) adsorption on O-doped MoS_2. PDOS of La(III), S and O in the system of La(III) adsorption on (d) O-doped MoS_2, (e) MoS_2, and (f) MoS_2-2O.

To obtain an insight into the adsorption sites of O and S atoms, the view after adsorption was provide in Figure 3-13. The distance between La(III) and O atom was closer than that with S atom, illustrating stronger interaction of La(III) and O atom, owing to more electronegativity[88,89]. The phenomenon was also demonstrated by the higher atomic charge transfer of O atom. Compared with MoS_2 system, higher positive charge of La(III) was originated from the stronger interaction that in the O-doped MoS_2 system. And the promoted interaction in O-doped MoS_2 was due to the interaction between La(III) and O atoms. The above results proved that the incorporation of oxygen atoms would strengthen chemical interaction of La(III) and MoS_2.

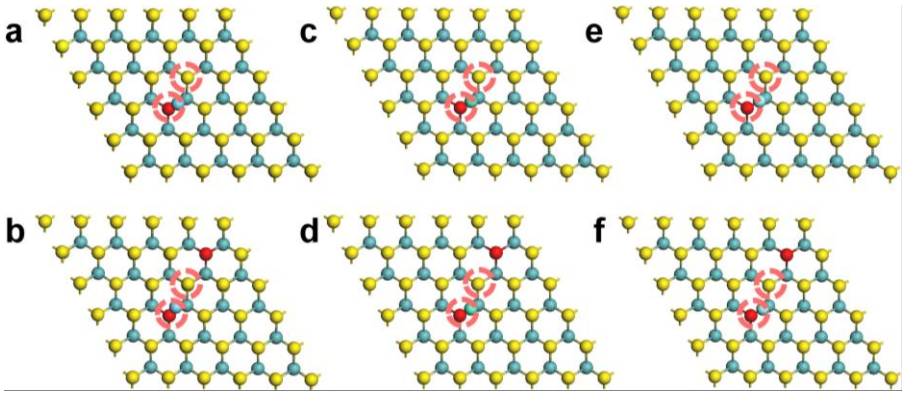

Figure 3-13. Top views of (a ,b) La(III), (c, d) Gd(III) and (e, f) Y(III) adsorption on MoS_2-O and MoS_2-$2O_{(3)}$ (Circled atoms are used for Mulliken atomic charge changes analysis).

3.3.5. Adsorption and desorption cycles

Reusability of materials was crucial to the application of CEC process. Here, desorption of La(III) from O-doped MoS_2 was investigated using HCl and NH_4Cl. It turned out that HCl (Figure 3-14a) and NH_4Cl (Figure 3-14b) could efficiently desorb La(III) from O-doped MoS_2 electrode. At approximately 60 min, the total desorption efficiency exceeded 90%. The total desorption and corresponding desorption efficiency reached almost 10 mg/L and 100% within 120 min, respectively. Judging from the color of the desorption solutions (Figure 3-15a), it changed from dark to light color for desorption of cathode, which meant that the adsorption of La(III) was mainly completed on cathode, and the results were also confirmed by the desorption efficiency. Subsequently, the consecutive cycles of O-doped MoS_2 electrode using HCl (Figure 3-14c) and NH_4Cl (Figure 3-14d) for desorption were studied. During the repeated experiment, a small amount of the samples would drop in all solution, resulting a part of dropped recovery performance. As the increased adsorption and desorption circles, adsorption capacity and recovery dropped, demonstrating that the desorption would destroy active sites of O-doped MoS_2. Besides, the results proved that interaction between La(III) and O-doped MoS_2 was attributed to the physical and chemical sorption. While, the adsorption and desorption circles performance using NH_4Cl was better than that by HCl, originating from instability of MoS_2 in acid solution.

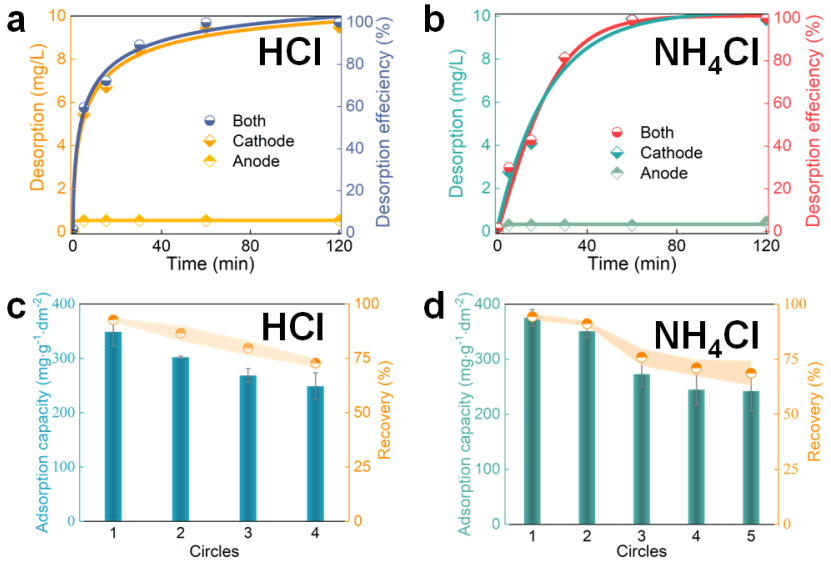

Figure 3-14. (a) Desorption of La(III) from O-doped MoS_2 electrode by HCl and (c) related recovery circles. (b) Desorption of La(III) from O-doped MoS_2 electrode by NH_4Cl and (d) related recovery circles.

After adsorption and desorption circles, the crystal structure (Figure 3-15b) and

bonding component (Figure 3-15c) of O-doped MoS_2 was still in consistent as before, indicating that the method to desorb La(III) from O-doped MoS_2 would not damage the whole structure. Moreover, morphology and elemental distribution (Figure 3-15d) of O-doped MoS_2 was not destroyed, which exhibited the good recyclability of O-doped MoS_2 electrode. The method favorably contributed to a better understanding of the desorption process and provided valuable guidance to the recovery of REEs and reusability to achieve the actual application.

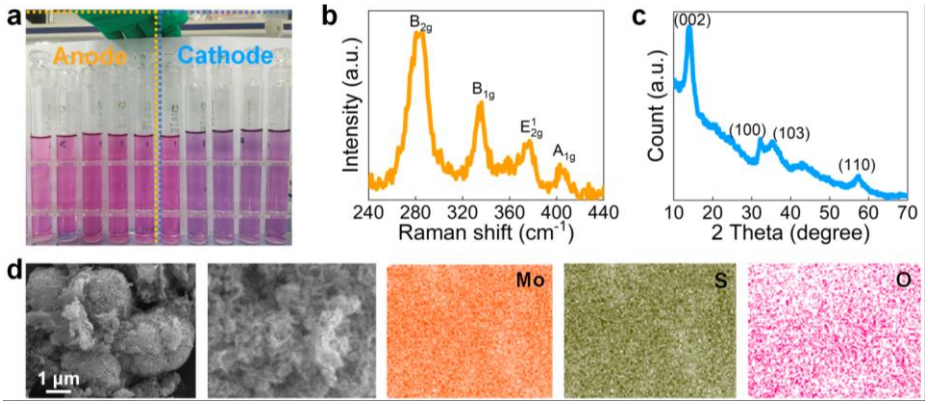

Figure 3-15. (a) The color comparison of anode and cathode after desorption. (b) XRD pattern and (c) Raman spectrum of O-doped MoS_2 after desorption. (d) SEM images and corresponding elemental mapping: Mo, S, and O of O-doped MoS_2 after the desorption of La(III).

3.3.6. Recovery of other REEs

Furthermore, the performances by O-doped MoS_2 electrode in CEC process for recovery of other REEs were explored (Figure 3-16). It revealed that all REEs could be recovered through O-doped MoS_2 electrode in CEC process, and with good recovery. Different REEs recovery behaviors were related with their out nuclear electro shell and formation of ions in aqueous solutions.

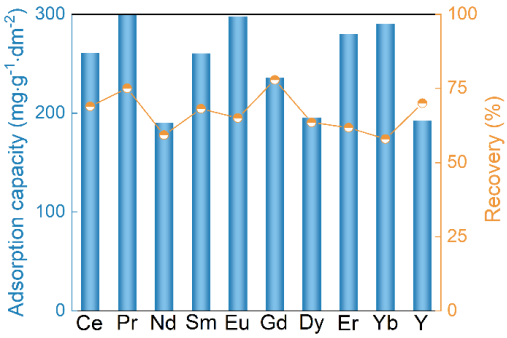

Figure 3-16. Recovery of other REEs by O-doped MoS_2 in CEC process at an initial concentration of 10 mg/L.

Here, Gd(III) and Y(III) were chosen as medium and heavy REEs to study more

recovery behaviors using O-doped MoS_2 electrode. Adsorption capacity of Gd(III) and Y(III) in Figure 3-17a and 3-17d showed the similar increasing trend as time comparing with that of La(III). The pseudo-first-order model and the pseudo-second-order models for fitting by O-doped MoS_2 and MoO_2 electrode were exhibited in Table 3-3 and 3-4, respectively. It revealed that the adsorption process for Gd(III) and Y(III) were physical and chemical adsorption. As well, adsorption capacity and recovery using O-doped MoS_2 were better than that by MoO_2. Factors affecting Gd(III) and Y(III) recovery including pH and voltage were studied. As displayed in Figure 3-17b and 3-17e, the similar tendency of recovery was resulted from enhanced electrostatic interaction of La(III) and O-doped MoS_2. For recovery under various voltage values (Figure 3-17c and 3-17f), higher electrostatic interaction would be strengthened between electrode and REEs.

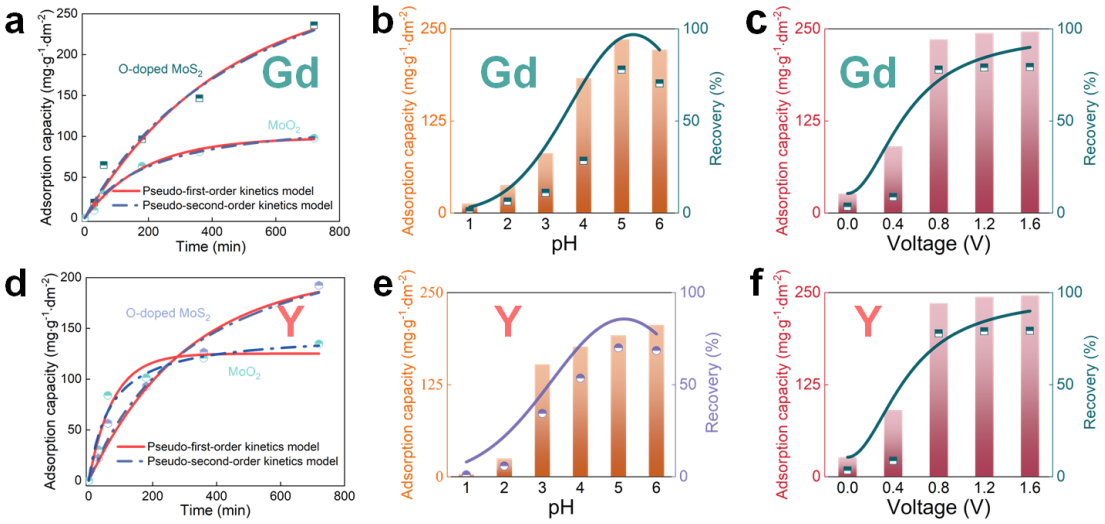

Figure 3-17. Adsorption capacity of (a) Gd(III) and (d) Y(III) on O-doped MoS_2 at an initial concentration of 10 mg/L. Effect of pH, and voltage on (c, d) Gd(III) and (e, f) Y(III) recovery by an O-doped MoS_2 electrode.

Table 3-3. Kinetic parameters for Gd(III) and Y(III) recovery via O-doped MoS_2 electrode.

	Pseudo-first-order kinetic model			Pseudo-second-order kinetic model		
	q_e (mg/(g·dm^2)	k_1 (min^{-1})	R^2	q_e (mg/(g·dm^2)	K_2 (min^{-1})	R^2
Gd(III)	285.52359	0.00229	0.97351	408.52124	0.0000043714	0.97734
Y(III)	205.43766	0.00326	0.96573	273.43303	0.0000106466	0.97604

Table 3-4. Kinetic parameters for Gd(III) and Y(III) recovery via MoO_2 electrode.

	Pseudo-first-order kinetic model			Pseudo-second-order kinetic model		
	q_e (mg/(g·dm^2)	k_1 (min^{-1})	R^2	q_e (mg/(g·dm^2)	K_2 (min^{-1})	R^2
Gd(III)	98.63859	0.00536	0.99394	126.54959	0.0000033939	0.99230
Y(III)	125.19222	0.0132	0.95744	145.49836	0.0000110119	0.96676

In Figure 3-18a and 3-18c, the results showed that adsorption capacities of Gd(III) and Y(III) were 176 and 170 mg/(g·dm^2) at the initial concentration of 5 mg/L, and related recovery of 95.6% and 93.1%, respectively. As increasing of initial concentration, adsorption capacity and recovery declined resulting from the limited ion storage in electric double layer. When the initial concentration was lower than 5 mg/L, recovery achieved 100%, which exhibited excellent recovery of rare earth elements in the low concentration range. According to the results of SEM and related elemental mapping (Figure 3-18b and 3-18d), Gd(III) and Y(III) recovery on the surface of O-doped MoS_2 electrode were demonstrated. Comparing with previous works, as shown in Table 3-5 and 3-6, Gd(III) and Y(III) recovery ability using O-doped MoS_2 electrode was better.

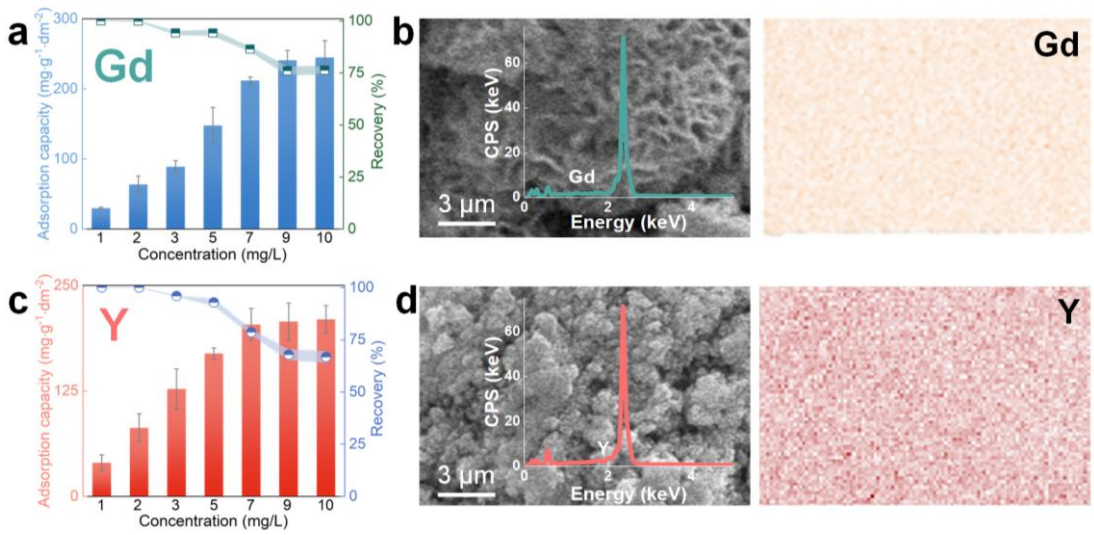

Figure 3-18. Adsorption capacity and recovery of (a) Gd(III) and (c) Y(III) at various initial concentrations. SEM and related elemental mapping of O-doped MoS_2 electrode after (b) Gd(III) and (d) Y(III) recovery.

Table 3-5. Comparison of Gd(III) recovery in the work with previous literatures.

Materials	Initial concentration (mg/L)	Adsorption capacity (mg/g)	Efficiency (mg/(g·min))	Ref.
INFCF	36.87	32.72	0.023	[90]
IMCFs	50	14.30	0.020	[91]
ZrSiSb	100	7.0	0.058	[92]
CMC sponge	50	38.64	0.053	[93]
CEC with O-doped MoS_2	9.86	38.72	0.053	This work

Table 3-6. Comparison of Y(III) recovery in the work with previous literatures.

Materials	Initial concentration (mg/L)	Adsorption capacity (mg/g)	Efficiency (mg/(g·min))	Ref.
Exchange resin	100	3.50	0.039	[94]
Regenerated ion-exchange	88.9	34.70	0.024	[95]
GO composite	30	3.89	0.026	[82]
FeNPs	25	4.74	0.020	[96]
CEC with O-doped MoS_2	9.83	31.68	0.044	This work

To further verify the interaction between Gd(III), Y(III) and doped MoS_2, DFT was applied. Adsorption energy of Y(III) and O-doped MoS_2 was lower than Y(III) of O-doped MoS_2 (Figure 3-19a), and the binding energy with La(III) (Figure 3-12a) was the lowest. Higher interaction strengthened the recovery of REEs by CEC process. Besides, interaction of Gd(III) and Y(III) in high concentration with O-doped MoS_2 was given in Figure 3-19b and 3-19c, respectively. Similar phenomenon with enhancing and balancing interaction was observed, originating from limited adsorption sites. With the purpose of investigating the binding orbitals between Gd(III) or Y(III) and O-doped MoS_2, PDOS of Gd(III), Y(III) and nearby S, O atoms were exhibited in Figure 3-19d and 3-19e. Whatever La(III), Gd(III) or Y(III), REEs could bind tightly with S and O

atoms on the surface of O-doped MoS_2. Compared with Y(III) and La(III) (Figure 3-12d), *f* orbitals in Gd(III) participated in the interaction with S and O atoms, which enhanced the chemisorption of Gd(III) to some extent. The more negative charged O atom that S atom demonstrated that interaction between Y(III) or Gd(III) with O atoms were stronger than them with S atoms, which could be seen in the closer distance of REEs and O atom in Figure 3-13 as well. Moreover, Mulliken atomic charge changes showed that REEs connect with S and O atoms (Figure 3-19f), and Gd(III) bound to O-doped MoS_2 more strongly than Y(III). The greater force between the S atoms may be attributed to the higher atomic charge changes in Gd(III).

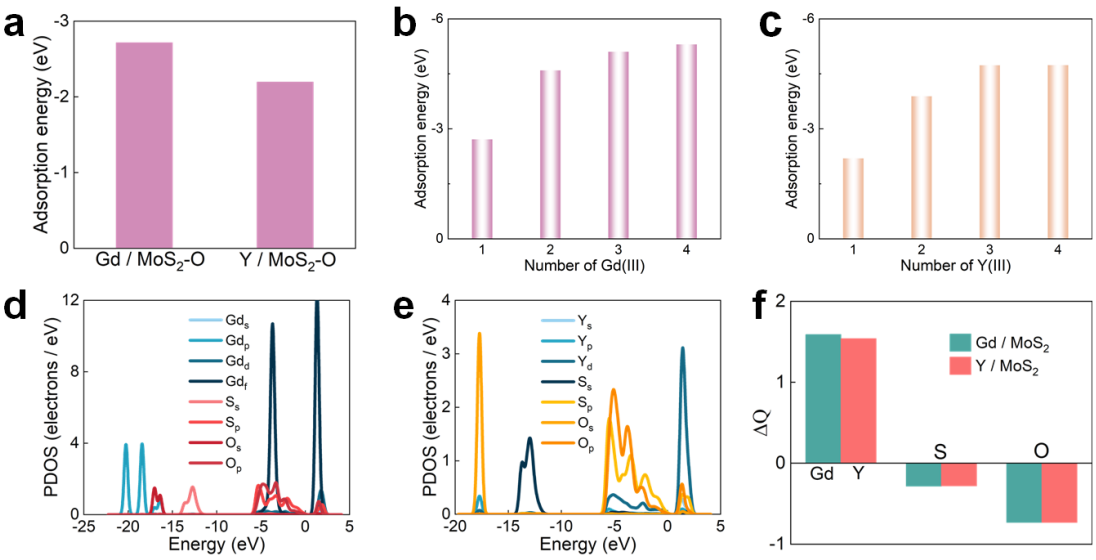

Figure 3-19. (a) Adsorption energy between Gd(III) (or Y(III)) and O-doped MoS_2. Adsorption energy between various concentration of (b) Gd(III) or (c) Y(III) and O-doped MoS_2. (d) PDOS of Gd(III), S and O in the system of Gd(III) adsorption on O-doped MoS_2. (e) PDOS of Y(III), S and O in the system of Y(III) adsorption on O-doped MoS_2. (f) Mulliken atomic charge changes of Gd(III) (or Y(III)), S and O in the system of Gd(III) (or Y(III)) adsorption on O-doped MoS_2.

3.4. Conclusions

The recovery of REEs from aqueous solutions in low concentrations based on the design of O-doped MoS_2 electrode was proposed. The CEC process with O-doped MoS_2 electrode reached REEs recovery of ~100% when the initial concentration was at a certain value. Max adsorption capacity of REEs of 365.71 mg/(g·dm^2) was obtained. In a multicomponent solution, the adsorption capacity and recovery were slighted affected. The parameters of CEC process, including pH, applied voltage, distance

between electrodes, and initial concentrations, were detailly investigated. The efficient recovery of REEs could be attributed to the enhanced transfer rate and electric double layer thinness for REEs storage. Further, the strong interaction between doping O atoms and REEs helped strengthen the chemical interaction. The REEs recovery was impacted by different binding forces between REEs and O-doped MoS_2. Apart from the above results, the desorption efficiency from O-doped MoS_2 electrode reached ~100% within 120 min, and the electrode exhibited good stability. Therefore, this study proposed a novel process to recover REEs from aqueous solutions, and could be used some light on the reusing of resource recycling and environmental application.

3.5. References

(1) Ji, H.; Wu, J.; Cai, Z.; Liu, J.; Kwon, D. H.; Kim, H.; Urban, A.; Papp, J. K.; Foley, E.; Tian, Y.; Balasubramanian, M.; Kim, H.; Clément, R. J.; McCloskey, B. D.; Yang, W.; Ceder, G. Ultrahigh Power and Energy Density in Partially Ordered Lithium-Ion Cathode Materials. *Nature Energy* **2020**, *5* (3), 213–221. https://doi.org/10.1038/s41560-020-0573-1.

(2) Bombelli, P.; Savanth, A.; Scarampi, A.; Rowden, S. J. L.; Green, D. H.; Erbe, A.; Årstøl, E.; Jevremovic, I.; Hohmann-Marriott, M. F.; Trasatti, S. P.; Ozer, E.; Howe, C. J. Powering a Microprocessor by Photosynthesis. *Energy Environ Sci* **2022**, *15* (6), 2529–2536. https://doi.org/10.1039/D2EE00233G.

(3) Zeng, Z.; Xu, Y.; Zhang, Z.; Gao, Z.; Luo, M.; Yin, Z.; Zhang, C.; Xu, J.; Huang, B.; Luo, F.; Du, Y.; Yan, C. Rare-Earth-Containing Perovskite Nanomaterials: Design, Synthesis, Properties and Applications. *Chem Soc Rev* **2020**, *49* (4), 1109–1143. https://doi.org/10.1039/C9CS00330D.

(4) Kostelnik, T. I.; Orvig, C. Radioactive Main Group and Rare Earth Metals for Imaging and Therapy. *Chem Rev* **2019**, *119* (2), 902–956. https://doi.org/10.1021/ACS.CHEMREV.8B00294.

(5) Waldherr, G.; Wang, Y.; Zaiser, S.; Jamali, M.; Schulte-Herbrüggen, T.; Abe, H.; Ohshima, T.; Isoya, J.; Du, J. F.; Neumann, P.; Wrachtrup, J. Quantum Error Correction in a Solid-State Hybrid Spin Register. *Nature* **2014**, *506* (7487), 204–207. https://doi.org/10.1038/nature12919.

(6) Förster, S. C.; Heinze, K.; Pandey, R. K.; Ng, D. K. P.; Torres, T.; Dumoulin, F.; Fö, C. Photophysics and Photochemistry with Earth-Abundant Metals – Fundamentals and Concepts. *Chem Soc Rev* **2020**, *49* (4), 1057–1070. https://doi.org/10.1039/C9CS00573K.

(7) Borst, A. M.; Smith, M. P.; Finch, A. A.; Estrade, G.; Villanova-de-Benavent, C.; Nason, P.; Marquis, E.; Horsburgh, N. J.; Goodenough, K. M.; Xu, C.; Kynický, J.; Geraki, K. Adsorption of Rare Earth Elements in Regolith-Hosted Clay Deposits. *Nature Communications* **2020**, *11* (1), 1–15. https://doi.org/10.1038/s41467-020-17801-5.

(8) Alonso, E.; Sherman, A. M.; Wallington, T. J.; Everson, M. P.; Field, F. R.; Roth, R.; Kirchain,

R. E. Evaluating Rare Earth Element Availability: A Case with Revolutionary Demand from Clean Technologies. *Environ Sci Technol* **2012**, *46* (6), 3406–3414. https://doi.org/10.1021/ES203518D.

(9) Fan, M. C.; Wozny, J.; Gong, J.; Kang, Y. Q.; Wang, X. S.; Zhang, Z. X.; Zhou, G. M.; Zhao, Y.; Li, B. H.; Kang, F. Y. Lithium Metal Recycling from Spent Lithium-Ion Batteries by Cathode Overcharging Process. *Rare Metals* **2022**, *41* (6), 1843–1850. https://doi.org/10.1007/S12598-021-01918-7/FIGURES/5.

(10) Zheng, B.; Fan, J.; Chen, B.; Qin, X.; Wang, J.; Wang, F.; Deng, R.; Liu, X. Rare-Earth Doping in Nanostructured Inorganic Materials. *Chem Rev* **2022**, *122* (6), 5519–5603. https://doi.org/10.1021/ACS.CHEMREV.1C00644.

(11) Bian, Y. Y.; Guo, S. Q.; Xu, Y. L.; Tang, K.; Lu, X. G.; Ding, W. Z. Recovery of Rare Earth Elements from Permanent Magnet Scraps by Pyrometallurgical Process. *Rare Metals* **2022**, *41* (5), 1697–1702. https://doi.org/10.1007/S12598-015-0554-X/TABLES/3.

(12) Kegl, T.; Košak, A.; Lobnik, A.; Novak, Z.; Kralj, A. K.; Ban, I. Adsorption of Rare Earth Metals from Wastewater by Nanomaterials: A Review. *J Hazard Mater* **2020**, *386*, 121632. https://doi.org/10.1016/J.JHAZMAT.2019.121632.

(13) Naidu, G.; Ryu, S.; Thiruvenkatachari, R.; Choi, Y.; Jeong, S.; Vigneswaran, S. A Critical Review on Remediation, Reuse, and Resource Recovery from Acid Mine Drainage. *Environmental Pollution* **2019**, *247*, 1110–1124. https://doi.org/10.1016/J.ENVPOL.2019.01.085.

(14) Zou, D.; Li, H.; Deng, Y.; Chen, J.; Bai, Y. Recovery of Lanthanum and Cerium from Rare Earth Polishing Powder Wastes Utilizing Acid Baking-Water Leaching-Precipitation Process. *Sep Purif Technol* **2021**, *261*, 118244. https://doi.org/10.1016/J.SEPPUR.2020.118244.

(15) Binnemans, K.; Jones, P. T.; Blanpain, B.; Van Gerven, T.; Yang, Y.; Walton, A.; Buchert, M. Recycling of Rare Earths: A Critical Review. *J Clean Prod* **2013**, *51*, 1–22. https://doi.org/10.1016/J.JCLEPRO.2012.12.037.

(16) Wang, K.; Adidharma, H.; Radosz, M.; Wan, P.; Xu, X.; Russell, C. K.; Tian, H.; Fan, M.; Yu, J. Recovery of Rare Earth Elements with Ionic Liquids. *Green Chemistry* **2017**, *19* (19), 4469–4493. https://doi.org/10.1039/C7GC02141K.

(17) Hermassi, M.; Granados, M.; Valderrama, C.; Ayora, C.; Cortina, J. L. Recovery of Rare Earth Elements from Acidic Mine Waters: An Unknown Secondary Resource. *Science of The Total Environment* **2022**, *810*, 152258. https://doi.org/10.1016/J.SCITOTENV.2021.152258.

(18) Li, Z.; Li, X.; Raiguel, S.; Binnemans, K. Separation of Transition Metals from Rare Earths by Non-Aqueous Solvent Extraction from Ethylene Glycol Solutions Using Aliquat 336. *Sep Purif Technol* **2018**, *201*, 318–326. https://doi.org/10.1016/J.SEPPUR.2018.03.022.

(19) Ramasamy, D. L.; Porada, S.; Sillanpää, M. Marine Algae: A Promising Resource for the Selective Recovery of Scandium and Rare Earth Elements from Aqueous Systems. *Chemical*

Engineering Journal **2019**, *371*, 759–768. https://doi.org/10.1016/J.CEJ.2019.04.106.

(20) Omodara, L.; Pitkäaho, S.; Turpeinen, E. M.; Saavalainen, P.; Oravisjärvi, K.; Keiski, R. L. Recycling and Substitution of Light Rare Earth Elements, Cerium, Lanthanum, Neodymium, and Praseodymium from End-of-Life Applications - A Review. *J Clean Prod* **2019**, *236*, 117573. https://doi.org/10.1016/J.JCLEPRO.2019.07.048.

(21) Bao, X. jun; Zhang, Z. jie; Luo, T. zhong; Wu, X. tao; Xie, Z. shan; Lan, S. kun; Xie, S. zhong; Zhou, D. bi. Conversion of Cerium and Lanthanum from Rare Earth Polishing Powder Wastes to CeO_2 and $La_{0.6}Ca_{0.4}CoO_3$. *Hydrometallurgy* **2020**, *193*, 105317. https://doi.org/10.1016/J.HYDROMET.2020.105317.

(22) Yu, B. S.; Jiang, J. L.; Yang, C. C. Conversion of Lanthanum and Cerium Recovered from Hazardous Waste Polishing Powders to Hazardous Ammonia Decomposition Catalysts. *J Hazard Mater* **2019**, *379*, 120773. https://doi.org/10.1016/J.JHAZMAT.2019.120773.

(23) López, J.; Reig, M.; Gibert, O.; Cortina, J. L. Integration of Nanofiltration Membranes in Recovery Options of Rare Earth Elements from Acidic Mine Waters. *J Clean Prod* **2019**, *210*, 1249–1260. https://doi.org/10.1016/J.JCLEPRO.2018.11.096.

(24) Kegl, T.; Košak, A.; Lobnik, A.; Novak, Z.; Kralj, A. K.; Ban, I. Adsorption of Rare Earth Metals from Wastewater by Nanomaterials: A Review. *J Hazard Mater* **2020**, *386*, 121632. https://doi.org/10.1016/J.JHAZMAT.2019.121632.

(25) Yang, X.; Debeli, D. K.; Shan, G.; Pan, P. Selective Adsorption and High Recovery of La3+ Using Graphene Oxide/Poly (N-Isopropyl Acrylamide-Maleic Acid) Cryogel. *Chemical Engineering Journal* **2020**, *379*, 122335. https://doi.org/10.1016/J.CEJ.2019.122335.

(26) Galhoum, A. A.; Elshehy, E. A.; Tolan, D. A.; El-Nahas, A. M.; Taketsugu, T.; Nishikiori, K.; Akashi, T.; Morshedy, A. S.; Guibal, E. Synthesis of Polyaminophosphonic Acid-Functionalized Poly(Glycidyl Methacrylate) for the Efficient Sorption of La(III) and Y(III). *Chemical Engineering Journal* **2019**, *375*, 121932. https://doi.org/10.1016/J.CEJ.2019.121932.

(27) Gao, Y.; Xu, L.; Zhang, M.; Zhang, Q.; Yang, Z.; Yang, J.; Xu, Z.; Lv, Y.; Wang, Y. Ultra-Selective Ion Sieve for Thorium Recovery from Rare Earth Elements Using Oxygen-Rich Microporous Carbon Adsorption. *J Hazard Mater* **2021**, *417*, 126115. https://doi.org/10.1016/J.JHAZMAT.2021.126115.

(28) Awual, M. R.; Hasan, M. M.; Znad, H. Organic–Inorganic Based Nano-Conjugate Adsorbent for Selective Palladium(II) Detection, Separation and Recovery. *Chemical Engineering Journal* **2015**, *259*, 611–619. https://doi.org/10.1016/J.CEJ.2014.08.028.

(29) Javadian, H.; Ruiz, M.; Saleh, T. A.; Sastre, A. M. Ca-Alginate/Carboxymethyl Chitosan/$Ni_{0.2}Zn_{0.2}Fe_{2.6}O_4$ Magnetic Bionanocomposite: Synthesis, Characterization and Application for Single Adsorption of Nd^{+3}, Tb^{+3}, and Dy^{+3} Rare Earth Elements from Aqueous

Media. *J Mol Liq* **2020**, *306*, 112760. https://doi.org/10.1016/J.MOLLIQ.2020.112760.

(30) Liu, J.; Zeng, L.; Liao, S.; Liao, X.; Liu, J.; Mao, J.; Chen, Y.; Qiu, T.; Ren, S. Highly Efficient Enrichment and Adsorption of Rare Earth Ions (Yttrium(III)) by Recyclable Magnetic Nitrogen Functionalized Mesoporous Expanded Perlite. *Chinese Chemical Letters* **2020**, *31* (10), 2849–2853. https://doi.org/10.1016/J.CCLET.2020.08.017.

(31) Jacinto, J.; Henriques, B.; Duarte, A. C.; Vale, C.; Pereira, E. Removal and Recovery of Critical Rare Elements from Contaminated Waters by Living Gracilaria Gracilis. *J Hazard Mater* **2018**, *344*, 531–538. https://doi.org/10.1016/J.JHAZMAT.2017.10.054.

(32) Roosen, J.; Spooren, J.; Binnemans, K. Adsorption Performance of Functionalized Chitosan–Silica Hybrid Materials toward Rare Earths. *J Mater Chem A Mater* **2014**, *2* (45), 19415–19426. https://doi.org/10.1039/C4TA04518A.

(33) Borst, A. M.; Smith, M. P.; Finch, A. A.; Estrade, G.; Villanova-de-Benavent, C.; Nason, P.; Marquis, E.; Horsburgh, N. J.; Goodenough, K. M.; Xu, C.; Kynický, J.; Geraki, K. Adsorption of Rare Earth Elements in Regolith-Hosted Clay Deposits. *Nature Communications* **2020**, *11* (1), 1–15. https://doi.org/10.1038/s41467-020-17801-5.

(34) Zhang, Y.; Bian, T.; Jiang, R.; Zhang, Y.; Zheng, X.; Li, Z. Bionic Chitosan-Carbon Imprinted Aerogel for High Selective Recovery of Gd(III) from End-of-Life Rare Earth Productions. *J Hazard Mater* **2021**, *407*, 124347. https://doi.org/10.1016/J.JHAZMAT.2020.124347.

(35) Yang, X.; Debeli, D. K.; Shan, G.; Pan, P. Selective Adsorption and High Recovery of La^{3+} Using Graphene Oxide/Poly (N-Isopropyl Acrylamide-Maleic Acid) Cryogel. *Chemical Engineering Journal* **2020**, *379*, 122335. https://doi.org/10.1016/J.CEJ.2019.122335.

(36) Srimuk, P.; Su, X.; Yoon, J.; Aurbach, D.; Presser, V. Charge-Transfer Materials for Electrochemical Water Desalination, Ion Separation and the Recovery of Elements. *Nature Reviews Materials* **2020**, *5* (7), 517–538. https://doi.org/10.1038/s41578-020-0193-1.

(37) Yin, H.; Zhao, S.; Wan, J.; Tang, H.; Chang, L.; He, L.; Zhao, H.; Gao, Y.; Tang, Z.; Yin, H.; Zhao, S.; Wan, J.; Tang, H.; Chang, L.; He, L.; Gao, Y.; Tang, Z.; Zhao, H. Three-Dimensional Graphene/Metal Oxide Nanoparticle Hybrids for High-Performance Capacitive Deionization of Saline Water. *Advanced Materials* **2013**, *25* (43), 6270–6276. https://doi.org/10.1002/ADMA.201302223.

(38) Zhang, J.; Fang, J.; Han, J.; Yan, T.; Shi, L.; Zhang, D. N, P, S Co-Doped Hollow Carbon Polyhedra Derived from MOF-Based Core–Shell Nanocomposites for Capacitive Deionization. *J Mater Chem A Mater* **2018**, *6* (31), 15245–15252. https://doi.org/10.1039/C8TA04813D.

(39) Mao, M.; Yan, T.; Shen, J.; Zhang, J.; Zhang, D. Selective Capacitive Removal of Heavy Metal Ions from Wastewater over Lewis Base Sites of S-Doped Fe-N-C Cathodes via an Electro-Adsorption Process. *Environ Sci Technol* **2021**, *55* (11), 7665–7673.

https://doi.org/10.1021/ACS.EST.1C01483.

(40) Tang, W.; Wang, X.; Zeng, G.; Liang, J.; Li, X.; Xing, W.; He, D.; Tang, L.; Liu, Z. Electro-Assisted Adsorption of Zn(II) on Activated Carbon Cloth in Batch-Flow Mode: Experimental and Theoretical Investigations. *Environ Sci Technol* **2019**, *53* (5), 2670–2678. https://doi.org/10.1021/ACS.EST.8B05909.

(41) Mao, M.; Yan, T.; Shen, J.; Zhang, J.; Zhang, D. Capacitive Removal of Heavy Metal Ions from Wastewater via an Electro-Adsorption and Electro-Reaction Coupling Process. *Environ Sci Technol* **2021**, *55* (5), 3333–3340. https://doi.org/10.1021/ACS.EST.0C07849.

(42) Zhan, W.; Yuan, Y.; Zhang, X.; Liang, Y.; Song, S.; de Jesús Martínez-López, M.; Arauz-Lara, J. L.; Jia, F. Efficient and Selective Lead(II) Removal within a Wide Concentration Range through Chemisorption and Electrosorption Coupling Process via Defective MoS_2 Electrode. *Sep Purif Technol* **2024**, *329*, 125183. https://doi.org/10.1016/J.SEPPUR.2023.125183.

(43) Mao, M.; Yan, T.; Shen, J.; Zhang, J.; Zhang, D. Selective Capacitive Removal of Heavy Metal Ions from Wastewater over Lewis Base Sites of S-Doped Fe-N-C Cathodes via an Electro-Adsorption Process. *Environ Sci Technol* **2021**, *55* (11), 7665–7673. https://doi.org/10.1021/ACS.EST.1C01483.

(44) Zhan, W.; Yuan, Y.; Yang, B.; Jia, F.; Song, S. Construction of MoS_2 Nano-Heterojunction via ZnS Doping for Enhancing in-Situ Photocatalytic Reduction of Gold Thiosulfate Complex. *Chemical Engineering Journal* **2020**, *394*, 124866. https://doi.org/10.1016/j.cej.2020.124866.

(45) Zhan, W.; Jia, F.; Yuan, Y.; Liu, C.; Sun, K.; Yang, B.; Song, S. Controllable Incorporation of Oxygen in MoS_2 for Efficient Adsorption of Hg^{2+} in Aqueous Solutions. *J Hazard Mater* **2020**, *384*, 121382. https://doi.org/10.1016/j.jhazmat.2019.121382.

(46) Radisavljevic, B.; Radenovic, A.; Brivio, J.; Giacometti, V.; Kis, A. Single-Layer MoS_2 transistors. *Nat Nanotechnol* **2011**, *6* (3), 147–150. https://doi.org/10.1038/nnano.2010.279.

(47) Liu, T.; Shi, S.; Liang, C.; Shen, S.; Cheng, L.; Wang, C.; Song, X.; Goel, S.; Barnhart, T. E.; Cai, W.; Liu, Z. Iron Oxide Decorated MoS_2 Nanosheets with Double PEGylation for Chelator-Free Radiolabeling and Multimodal Imaging Guided Photothermal Therapy. *ACS Nano* **2015**, *9* (1), 950–960. https://doi.org/10.1021/nn506757x.

(48) Ai, K.; Ruan, C.; Shen, M.; Lu, L. MoS_2 Nanosheets with Widened Interlayer Spacing for High-Efficiency Removal of Mercury in Aquatic Systems. *Adv Funct Mater* **2016**, *26* (30), 5542–5549. https://doi.org/10.1002/adfm.201601338.

(49) Pham, V. P.; Yeom, G. Y. Recent Advances in Doping of Molybdenum Disulfide: Industrial Applications and Future Prospects. *Advanced Materials* **2016**, *28* (41), 9024–9059. https://doi.org/10.1002/adma.201506402.

(50) Zou, J.; Cai, Z.; Lai, Y.; Tan, J.; Zhang, R.; Feng, S.; Wang, G.; Lin, J.; Liu, B.; Cheng, H.-M.

Doping Concentration Modulation in Vanadium-Doped Monolayer Molybdenum Disulfide for Synaptic Transistors. *ACS Nano* **2021**, *15* (4), 7340–7347. https://doi.org/10.1021/acsnano.1c00596.

(51) Yu, X.-Y.; Hu, H.; Wang, Y.; Chen, H.; Lou, X. W. D. Ultrathin MoS_2 Nanosheets Supported on N-Doped Carbon Nanoboxes with Enhanced Lithium Storage and Electrocatalytic Properties. *Angewandte Chemie International Edition* **2015**, *54* (25), 7395–7398. https://doi.org/10.1002/anie.201502117.

(52) Pierucci, D.; Henck, H.; Ben Aziza, Z.; Naylor, C. H.; Balan, A.; Rault, J. E.; Silly, M. G.; Dappe, Y. J.; Bertran, F.; Le Fèvre, P.; Sirotti, F.; Johnson, A. T. C.; Ouerghi, A. Tunable Doping in Hydrogenated Single Layered Molybdenum Disulfide. *ACS Nano* **2017**, *11* (2), 1755–1761. https://doi.org/10.1021/acsnano.6b07661.

(53) Wang, H.; Xiao, X.; Liu, S.; Chiang, C.-L.; Kuai, X.; Peng, C.-K.; Lin, Y.-C.; Meng, X.; Zhao, J.; Choi, J.; Lin, Y.-G.; Lee, J.-M.; Gao, L. Structural and Electronic Optimization of MoS_2 Edges for Hydrogen Evolution. *J Am Chem Soc* **2019**, *141* (46), 18578–18584. https://doi.org/10.1021/jacs.9b09932.

(54) Deng, S.; Luo, M.; Ai, C.; Zhang, Y.; Liu, B.; Huang, L.; Jiang, Z.; Zhang, Q.; Gu, L.; Lin, S.; Wang, X.; Yu, L.; Wen, J.; Wang, J.; Pan, G.; Xia, X.; Tu, J. Synergistic Doping and Intercalation: Realizing Deep Phase Modulation on MoS_2 Arrays for High-Efficiency Hydrogen Evolution Reaction. *Angewandte Chemie International Edition* **2019**, *58* (45), 16289–16296. https://doi.org/10.1002/anie.201909698.

(55) Li, S.; Liu, Y.; Zhao, X.; Cui, K.; Shen, Q.; Li, P.; Qu, X.; Jiao, L. Molecular Engineering on MoS_2 Enables Large Interlayers and Unlocked Basal Planes for High-Performance Aqueous Zn-Ion Storage. *Angewandte Chemie International Edition* **2021**, *60* (37), 20286–20293. https://doi.org/10.1002/anie.202108317.

(56) Sun, B.; Liang, Z.; Qian, Y.; Xu, X.; Han, Y.; Tian, J. Sulfur Vacancy-Rich O-Doped 1T-MoS2 Nanosheets for Exceptional Photocatalytic Nitrogen Fixation over CdS. *ACS Appl Mater Interfaces* **2020**, *12* (6), 7257–7269. https://doi.org/10.1021/acsami.9b20767.

(57) Nan, H.; Wang, Z.; Wang, W.; Liang, Z.; Lu, Y.; Chen, Q.; He, D.; Tan, P.; Miao, F.; Wang, X.; Wang, J.; Ni, Z. Strong Photoluminescence Enhancement of MoS_2 through Defect Engineering and Oxygen Bonding. *ACS Nano* **2014**, *8* (6), 5738–5745. https://doi.org/10.1021/nn500532f.

(58) Ma, X.; Sun, Z.; Hu, X. Synthesis of Tin and Molybdenum Co-Doped TiO_2 Nanotube Arrays for the Photoelectrocatalytic Oxidation of Phenol in Aqueous Solution. *Mater Sci Semicond Process* **2018**, *85*, 150–159. https://doi.org/10.1016/j.mssp.2018.05.026.

(59) Faraji, M.; Abedini, A. Surface Photochemical Modification of TiO_2 Nanotube/Ti Plates for Photocatalytic Elimination of Methylene Orange Dye. *International Journal of Environmental Science and Technology* **2019**, *16* (2), 909–920. https://doi.org/10.1007/s13762-018-1660-8.

(60) Kawabata, S.; Asano, K.; Miyazawa, A.; Satoh, T.; Tabata, Y. Electrodeposition of Pronectin for Titanium to Augment Gingival Epithelium Adhesion. *J Tissue Eng Regen Med* **2013**, *7* (5), 348–352. https://doi.org/10.1002/term.527.

(61) Zhan, W.; Yuan, Y.; Yao, X.; Yang, B.; Jia, F.; Lin, C.; Arauz-Lara, J. L.; Song, S. Efficient Recovery of Gold(I) from Thiosulfate Solutions through Photocatalytic Reduction with Mn(II)-Doped MoS_2. *ACS Sustain Chem Eng* **2021**, *9* (35), 11681–11690. https://doi.org/10.1021/acssuschemeng.1c02160.

(62) Liu, Y.; Li, J.; Das, A.; Kim, H.; Jones, L. O.; Ma, Q.; Bedzyk, M. J.; Schatz, G. C.; Kratish, Y.; Marks, T. J. Synthesis and Structure-Activity Characterization of a Single-Site MoO_2 Catalytic Center Anchored on Reduced Graphene Oxide. *J Am Chem Soc* **2021**, *143* (51), 21532–21540. https://doi.org/10.1021/JACS.1C07236.

(63) Zhang, H. J.; Wu, T. H.; Wang, K. X.; Wu, X. Y.; Chen, X. T.; Jiang, Y. M.; Wei, X.; Chen, J. S. Uniform Hierarchical MoO_2/Carbon Spheres with High Cycling Performance for Lithium Ion Batteries. *J Mater Chem A Mater* **2013**, *1* (39), 12038–12043. https://doi.org/10.1039/C3TA12566A.

(64) Aftab, J.; Ali, A.; Mehmood, S.; Aftab, A.; Ahmad, I.; Bhopal, M. F.; Hussain, M.; Shah, Z. U.; Shah, A. U.; Padhiar, M. A.; Wang, M.; Bhatti, A. S. Facile Synthesis of Synergetic MoO_2/MoS_2@GO Nanohybrid as Energy-Efficient Electrode Material for High-Performance Asymmetric Supercapacitor Applications. *J Energy Storage* **2023**, *74*, 109324. https://doi.org/10.1016/J.EST.2023.109324.

(65) Ge, J.; Zhang, D.; Jin, J.; Han, X.; Wang, Y.; Zhang, F.; Lei, X. Oxygen Atoms Substituting Sulfur Atoms of MoS_2 to Activate the Basal Plane and Induce the Phase Transition for Boosting Hydrogen Evolution. *Mater Today Energy* **2021**, *22*, 100854. https://doi.org/10.1016/j.mtener.2021.100854.

(66) Tang, J.; Wei, Z.; Wang, Q.; Wang, Y.; Han, B.; Li, X.; Huang, B.; Liao, M.; Liu, J.; Li, N.; Zhao, Y.; Shen, C.; Guo, Y.; Bai, X.; Gao, P.; Yang, W.; Chen, L.; Wu, K.; Yang, R.; Shi, D.; Zhang, G. In Situ Oxygen Doping of Monolayer MoS_2 for Novel Electronics. *Small* **2020**, *16* (42), 2004276. https://doi.org/10.1002/smll.202004276.

(67) Zhao, Y.; Song, J. G.; Ryu, G. H.; Ko, K. Y.; Woo, W. J.; Kim, Y.; Kim, D.; Lim, J. H.; Lee, S.; Lee, Z.; Park, J.; Kim, H. Low-Temperature Synthesis of 2D MoS_2 on a Plastic Substrate for a Flexible Gas Sensor. *Nanoscale* **2018**, *10* (19), 9338–9345. https://doi.org/10.1039/C8NR00108A.

(68) Yuan, Y.; Yang, B.; Jia, F.; Song, S. Reduction Mechanism of Au Metal Ions into Au Nanoparticles on Molybdenum Disulfide. *Nanoscale* **2019**, *11* (19), 9488–9497. https://doi.org/10.1039/c8nr09420a.

(69) Tang, D.; Li, J.; Yang, Z.; Jiang, X.; Huang, L.; Guo, X.; Li, Y.; Zhu, J.; Sun, X. Fabrication and Mechanism Exploration of Oxygen-Incorporated 1T-MoS_2 with High Adsorption Performance

on Methylene Blue. *Chemical Engineering Journal* **2022**, *428*, 130954. https://doi.org/10.1016/J.CEJ.2021.130954.

(70) Zhan, W.; Yuan, Y.; Liu, C.; Chen, P.; Liang, Y.; Wang, Y.; Arauz-Lara, J. L.; Jia, F. Preparation and Application of 0D, 2D and 3D Molybdenite: A Review. *Minerals and Mineral Materials* **2022**, *1* (1), 5. https://doi.org/10.20517/mmm.2022.04.

(71) Liu, J.; Wang, Z.; Li, J.; Cao, L.; Lu, Z.; Zhu, D. Structure Engineering of MoS_2 via Simultaneous Oxygen and Phosphorus Incorporation for Improved Hydrogen Evolution. *Small* **2020**, *16* (4), 1–11. https://doi.org/10.1002/smll.201905738.

(72) Xie, J.; Yang, X.; Xie, Y. Defect Engineering in Two-Dimensional Electrocatalysts for Hydrogen Evolution. *Nanoscale* **2020**, *12* (7), 4283–4294. https://doi.org/10.1039/C9NR09753H.

(73) Hammond, J. L.; Gross, A. J.; Estrela, P.; Iniesta, J.; Green, S. J.; Winlove, C. P.; Winyard, P. G.; Benjamin, N.; Marken, F. Cysteine-Cystine Redox Cycling in a Gold–Gold Dual-Plate Generator-Collector Microtrench Sensor. *Anal Chem* **2014**, *86* (14), 6748–6752. https://doi.org/10.1021/ac501321e.

(74) Luo, N.; Chen, C.; Yang, D.; Hu, W.; Dong, F. S Defect-Rich Ultrathin 2D MoS_2: The Role of S Point-Defects and S Stripping-Defects in the Removal of Cr(VI) via Synergistic Adsorption and Photocatalysis. *Appl Catal B* **2021**, *299*, 120664. https://doi.org/10.1016/J.APCATB.2021.120664.

(75) Yarahmadi, A.; Khani, M. H.; Nasiri Zarandi, M.; amini, Y. Ce(III) and La(III) Ions Adsorption through Amberlite XAD-7 Resin Impregnated via CYANEX-272 Extractant. *Scientific Reports* **2023**, *13* (1), 1–17. https://doi.org/10.1038/s41598-023-34140-9.

(76) Kołodyńska, D.; Fila, D.; Hubicki, Z. Static and Dynamic Studies of Lanthanum(III) Ion Adsorption/Desorption from Acidic Solutions Using Chelating Ion Exchangers with Different Functionalities. *Environ Res* **2020**, *191*, 110171. https://doi.org/10.1016/J.ENVRES.2020.110171.

(77) Huang, L.; Liu, L.; Huang, W.; Zhao, B.; Shen, Z.; Bao, Y.; Znad, H. Recovery of Lanthanum Cations by Functionalized Magnetic Multi-Walled Carbon Nanotube Bundles. *RSC Adv* **2021**, *11* (8), 4751–4759. https://doi.org/10.1039/D0RA09902C.

(78) Kołodyńska, D.; Araucz, K. New Titanium Oxide Sorbent for As(V) and Cr(VI) Removal as Well as La(III) and Nd(III) Recovery. *J Mol Liq* **2020**, *315*, 113720. https://doi.org/10.1016/J.MOLLIQ.2020.113720.

(79) Awwad, N. S.; Gad, H. M. H.; Ahmad, M. I.; Aly, H. F. Sorption of Lanthanum and Erbium from Aqueous Solution by Activated Carbon Prepared from Rice Husk. *Colloids Surf B Biointerfaces* **2010**, *81* (2), 593–599. https://doi.org/10.1016/J.COLSURFB.2010.08.002.

(80) Ammari Allahyari, S.; Saberi, R.; Sepanloo, K.; Lashkari, A. Adsorptive Separation of La(III) from Aqueous Solution via the Synthesized $[Zn(Bim)_2(Bdc)]n$ Metal-Organic Framework. *Journal of Rare Earths* **2021**, *39* (6), 742–748. https://doi.org/10.1016/J.JRE.2020.07.027.

(81) Song, D.; Park, S. J.; Kang, H. W.; Park, S. Bin; Han, J. I. Recovery of Lithium(I), Strontium(II), and Lanthanum(III) Using Ca-Alginate Beads. *J Chem Eng Data* **2013**, *58* (9), 2455–2464. https://doi.org/10.1021/JE400317V.

(82) Xu, X.; Zou, J.; Zhao, X. R.; Jiang, X. Y.; Jiao, F. P.; Yu, J. G.; Liu, Q.; Teng, J. Facile Assembly of Three-Dimensional Cylindrical Egg White Embedded Graphene Oxide Composite with Good Reusability for Aqueous Adsorption of Rare Earth Elements. *Colloids Surf A Physicochem Eng Asp* **2019**, *570*, 127–140. https://doi.org/10.1016/J.COLSURFA.2019.03.022.

(83) Afonso, E. L.; Carvalho, L.; Fateixa, S.; Amorim, C. O.; Amaral, V. S.; Vale, C.; Pereira, E.; Silva, C. M.; Trindade, T.; Lopes, C. B. Can Contaminated Waters or Wastewater Be Alternative Sources for Technology-Critical Elements? The Case of Removal and Recovery of Lanthanides. *J Hazard Mater* **2019**, *380*, 120845. https://doi.org/10.1016/J.JHAZMAT.2019.120845.

(84) Sun, K.; Yao, X.; Yang, B.; Jia, F.; Song, S. Oxygen-Incorporated Molybdenum Disulfide Nanosheets as Electrode for Enhanced Capacitive Deionization. *Desalination* **2020**, *496*, 114758. https://doi.org/10.1016/J.DESAL.2020.114758.

(85) Shen, P. C.; Lin, Y.; Su, C.; McGahan, C.; Lu, A. Y.; Ji, X.; Wang, X.; Wang, H.; Mao, N.; Guo, Y.; Park, J. H.; Wang, Y.; Tisdale, W.; Li, J.; Ling, X.; Aidala, K. E.; Palacios, T.; Kong, J. Healing of Donor Defect States in Monolayer Molybdenum Disulfide Using Oxygen-Incorporated Chemical Vapour Deposition. *Nature Electronics* **2021**, *5* (1), 28–36. https://doi.org/10.1038/s41928-021-00685-8.

(86) Xie, J.; Zhang, J.; Li, S.; Grote, F.; Zhang, X.; Zhang, H.; Wang, R.; Lei, Y.; Pan, B.; Xie, Y. Controllable Disorder Engineering in Oxygen-Incorporated MoS_2 Ultrathin Nanosheets for Efficient Hydrogen Evolution. *J Am Chem Soc* **2013**, *135* (47), 17881–17888. https://doi.org/10.1021/JA408329Q.

(87) Jing, Y.; Tan, X.; Zhou, Z.; Shen, P. Tuning Electronic and Optical Properties of MoS_2 Monolayer via Molecular Charge Transfer. *J. Mater. Chem. A* **2014**, *2* (40), 16892–16897. https://doi.org/10.1039/C4TA03660C.

(88) Wu, Y.; Xu, Q.; Huang, L.; Huang, B.; Hu, P.; Xiao, F.; Li, N. Encapsulation of Sulfur in MoS_2-Modified Metal-Organic Framework-Derived N, O-Codoped Carbon Host for Sodium–Sulfur Batteries. *J Colloid Interface Sci* **2024**, *654*, 649–659. https://doi.org/10.1016/j.jcis.2023.09.134.

(89) Yang, S.; Jiang, Q.; Zhang, K. Few-Layers 2D O–MoS2 TFN Nanofiltration Membranes for Future Desalination. *J Memb Sci* **2020**, *604*, 118052. https://doi.org/10.1016/j.memsci.2020.118052.

(90) Zheng, X.; Bian, T.; Zhang, Y.; Zhang, Y.; Li, Z. Construction of Ion-Imprinted Nanofiber Chitosan Films Using Low-Temperature Thermal Phase Separation for Selective and Efficiency Adsorption of Gd(III). *Cellulose* **2020**, *27* (1), 455–467. https://doi.org/10.1007/S10570-019-02804-3.

(91) Zheng, X.; Zhang, Y.; Bian, T.; Zhang, Y.; Zhang, F.; Yan, Y. Selective Extraction of Gadolinium Using Free-Standing Imprinted Mesoporous Carboxymethyl Chitosan Films with High Capacity. *Cellulose* **2019**, *26* (2), 1209–1219. https://doi.org/10.1007/S10570-018-2124-5.

(92) Abass, M. R.; El-Kenany, W. M.; Eid, M. A. Sorption of Cesium and Gadolinium Ions onto Zirconium Silico Antimonate Sorbent from Aqueous Solutions. *Applied Radiation and Isotopes* **2023**, *192*, 110542. https://doi.org/10.1016/J.APRADISO.2022.110542.

(93) Liu, E.; Shi, J.; Lin, X.; Xu, W.; Feng, L.; Hong, Y. Rational Fabrication of a New Ionic Imprinted Carboxymethyl Chitosan-Based Sponge for Efficient Selective Adsorption of Gd(III). *RSC Adv* **2022**, *12* (5), 3097–3107. https://doi.org/10.1039/D1RA08115B.

(94) Masry, B. A.; Abu Elgoud, E. M.; Rizk, S. E. Modeling and Equilibrium Studies on the Recovery of Praseodymium (III), Dysprosium (III) and Yttrium (III) Using Acidic Cation Exchange Resin. *BMC Chem* **2022**, *16* (1), 1–12. https://doi.org/10.1186/S13065-022-00830-0/TABLES/4.

(95) Vapnik, H.; Elbert, J.; Su, X. Redox-Copolymers for the Recovery of Rare Earth Elements by Electrochemically Regenerated Ion-Exchange. *J Mater Chem A Mater* **2021**, *9* (35), 20068–20077. https://doi.org/10.1039/D1TA03334D.

(96) Yang, Y.; Yan, Q.; Weng, X.; Owens, G.; Chen, Z. Improved Recovery Selectivity of Rare Earth Elements from Mining Wastewater Utilizing Phytosynthesized Iron Nanoparticles. *Water Res* **2023**, *244*, 120486. https://doi.org/10.1016/J.WATRES.2023.120486.

Chapter IV. Trace gadolinium(III) separation and recovery *via* modulating chemisorption activity on defects-rich molybdenum disulfide electrodes

4.1. Introduction

Gadolinium (Gd)[1–3] is one of rare earth elements (REEs) within the lanthanide series, naturally occurring in trivalent state. It presents unique properties of magnetic moment[4], attraction to thermal neutrons, thus being widely applied in neutron absorbers[5–7], magnetic resonance imaging[8–10], magnetic storage[11,12], and other vital fields[13]. Because of the trace amount in application, Gd bypasses waste water treatment plants and be released into aquatic environments[14–16], while the toxicity characteristic brings threat to human[17]. The appearance of Gd blocks transfer of calcium(II) inside the body since similar ionic radius[18]. Herein, conducting trace Gd recovery from aquatic solutions becomes increasingly necessary.

Conventional techniques used for separation or recovery of REEs are ion extraction[19–21], ion-exchange[22–24], chemical precipitation[25–27], and sorption[28–30]. Most of these methods suffer high cost, chemical and energy consumption[31–33]. Even though sorption possesses the advantages of economics and environmental friendliness, there is still a long way to realize highly separation and recovery of Gd. Therefore, it is timely to explore an approach to separate and recover Gd for green development of the environment.

Electrosorption[34–36] is a sorption process including ions immigration in electrolyte, interaction with adsorbate and storage in electric double layer (EDL) under external electricity. Generated electric field is prone to facilitate the ions in aqueous solutions to immigrate to oppositely charged electrode, and being beneficial for targeted ions to overcome the electrostatic repulsion to interact with electrodes[37–39]. It is demonstrated to possess the advantage of metal ions adsorption, for instance, lead(II)[40–42], copper(II)[43–45], nickel(II)[46–48], chromium[49–51], and so on[52].

Considering that the force between guest materials and target ions is the dominated factor for sorption, choosing a proper materials as electrodes to strongly interact with Gd is promising to achieve its efficient separation and recovery. Molybdenum disulfide (MoS_2) with a sandwich structure of S-Mo-S is recognized as a potential electrode for REEs recovery through chemisorption and electrosorption coupling (CEC) process.

However, selective adsorption is hard to realize because of similar extra-nuclear electrons of REEs.

In view of the largest number of unpaired electrons in Gd among REEs, the configuration extra-nuclear electrons of Gd are variant from others. According to valence bond theory, unsaturated S atoms have more lone pairs of electrons, which is prone to strongly interact with Gd. It is reported that MoS_2 with unsaturated S atoms show the great potential application merits in heavy metals. Thus, great efforts need to be devoted to understanding the separation and recovery of trace Gd from aqueous solutions *via* defects-rich MoS_2 electrodes.

Here, we proposed defects-rich MoS_2 (DR-MoS_2) electrodes through controlling the ratio of S and Mo sources for Gd separation and recovery. DR-MoS_2 was coated on the surface of titanium plate to induce Gd immigration and overcome electrostatic repulsion between material interface and target ions. La(III), Gd(III), and Y(III) as respectively represented light, medium, and heavy REEs were chosen for studying the sorption behaviors of REEs on DR-MoS_2 electrodes. The experimental results about Gd separation and recovery revealed efficient recovery performances via DR-MoS_2 electrodes, which was consistent with our prediction. Gd recovery though adjusting the interaction between materials and target on a CEC process in the work helps to guide a thought for targeted trace REEs recovery.

4.2. Materials and methods

4.2.1. Materials

Lanthanum nitrate hexahydrate ($LaN_3O_9 \cdot 6H_2O$, 99.9%), gadolinium nitrate hexahydrate ($GdN_3O_9 \cdot 6H_2O$, 99.9%), and yttrium nitrate hexahydrate ($YN_3O_9 \cdot 6H_2O$, 99.9%) were bought from Aladdin Co., China. Conductive carbon black was originated from the Cabot Corporation. Ammonium molybdate tetrahydrate ($(NH_4)_6Mo_7O_{24} \cdot 4H_2O$), thiourea ($CN_2H_4S$), nitric acid ($HNO_3$), sodium hydroxide (NaOH), Polytetrafluoroethylene ($(C_2F_4)_n$), and ammonium chloride (NH_4Cl), sodium sulfate (Na_2SO_4) were purchased from Sinopharm Chemical Reagent Co., Ltd., China. Deionized water (18.2 MΩ cm) produced by Millipore Super Q system was throughout the whole experiment.

4.2.2. Samples and electrode preparation

Synthesis of DR-MoS_2 was done via adjusting the ratio of Mo and S sources (1:2,

1:3, 1:4, and 1:5) in the hydrothermal route. Mo ($(NH_4)_6Mo_7O_{24}\cdot 4H_2O$) and S ($CN_2H_4S$) sources were dissolved in 72 mL distilled water by stirring. Later, the solution was transferred into a 100 mL Teflon-lined stainless-steel autoclave at 220°C for 18 h. After cooling down to room temperature, the obtained products were washed with pure water and ethanol. Lastly, the black products were dried at -60°C in vacuum environment for 12 h. The obtained samples were named as MoS_2, DR1-MoS_2, DR2-MoS_2, and DR3-MoS_2 according to various ratio of Mo and S sources.

DR-MoS_2 was coated on the surface of titanium plate to fabricate electrode. The mixture including 80 mg DR-MoS_2, 10 mg conductive carbon black, and 0.8 mL polyvinylidene fluoride was grinded in sapphire mortar. After, the samples were coated on surface of titanium plate and heated at 60°C for 3 h to remove excess organic reagents. In the end, the prepared electrodes were immerged in pure water for 12 h, then being dried for 6 h at 60°C.

4.2.3. REEs recovery

La(III), Gd(III), and Y(III) were respectively chosen as light, medium, and heavy REEs to study the REEs recovery behaviors on DR-MoS_2 electrodes. The recovery experiments were carried out in a self-made cell with an external applied voltage of 0.8 V. 200 mL REEs solution with pH of 5 was recycled with rate of 45 rpm by a peristaltic pump. Reacting after a certain time, the solution extracted from the cell was detected using UV-vis spectrophotometer (Aquamate 8000, Lambda 750S). Related recovery performances were assessed by adsorption capacity (Q) and recovery (R) as following equations:

$$Q = \frac{C_0V_0 - C_tV_t}{Am} \quad (1)$$

$$R = \frac{C_0 - C_t}{C_0} \quad (2)$$

where C_0 and C_t respectively mean REEs concentration at the beginning and t moments in the recovery process, mg/L, V_0 and V_t respectively represent the volumes of reaction solution at the beginning and t moments, L, A is surface area for coated samples on titanium plate, dm^2, and m stands for the mass of samples in the coating mixture, mg.

4.2.4. Gd(III) separation

According to the various sorption behaviors of REEs on DR-MoS_2 electrodes,

trace Gd(III) separation from the other two kind of REEs (La(III), and Y(III)) was performed. Specifically, the mixture including La(III), Gd(III), and Y(III) at 1 mg/L each at pH of 5 was applied on studying Gd(III) separation recovery by DR-MoS_2 electrodes with external applied voltage of 0.8 V. To reveal the adsorbed amount on DR-MoS_2 electrodes, REEs desorption was performed in 1 M NH_4Cl solution with 200 mL volume for 2 h. The concentration of all REEs was analyzed by inductively coupled plasma-optical emission spectrometry (ICP-OES, Prodigy 7, America). Separation coefficient of Gd(III) ($S_{Gd(III)/REE}$) was calculated as below equations:

$$D_{REE} = (\frac{C_0 - C_t}{C_t}) \times (\frac{V_t}{V_{srp}}) \quad (3)$$

$$S_{Gd(III)/REE} = \frac{D_{Gd(III)}}{D_{REE}} \quad (4)$$

where D is the distribution ration, V_{srp} represents the volume in desorption aqueous solutions, mL.

4.2.5. Simulations

With the aim of understanding selective Gd(III) sorption from mix REEs solutions, simulations for interaction of La(III), Gd(III), and Y(III) on the interface of DR-MoS_2 through density functional theory was calculated (DMol3 program). The Generalized Gradient Approximation (GGA) together with Perdew-Bruke-Ernzerhof (PBE) was used for describing exchange and correlation between electrons. The electron relaxation with 10^{-5} eV and energy cutoff with 320 eV were set for auxiliary plane waves. Applying vacuum with 20 Å length was to avoid the interaction with neighboring images. Adsorption energy of REEs (E_{ads}) on DR-MoS_2 was calculated as:

$$E_{ads} = E_{REE+DR-MoS2} - E_{DR-MoS2} - E_{REE} \quad (5)$$

Where $E_{REE+DR-MoS2}$ represents the total energy after interaction, $E_{DR-MoS2}$ is the energy of DR-MoS_2, and E_{REE} is the energy of REE.

4.2.6. AFM measurement

The adsorption process of Gd(III) on surface of MoS_2 with edge defects was observed by the atomic force microscope (AFM, Bruker Multimode 8 system, Billerica). MoS_2 sample was directly cut into a bulk with fresh surface and used owing to its natural property of sandwich-like structure. Gd(III) solution with 10 mg/L was dropped on the freshly exposed surface of MoS_2 with edge defects. After being reacted at a certain time, the residual solution was removed by filter paper. AFM was performed on

observing the morphology after drying.

4.2.7. Electrochemical test

Electrochemical characteristics containing cyclic voltammetry (CV) and electrochemical impedance spectroscopy (EIS) were detected with a conventional three-electrode cell in the REEs solution through electrochemical workstation (VersaSTAT-450, RAR, America). Three electrodes contained working electrode with samples, counter electrode with platinum, and reference electrode with a standard calomel. Preparation of working electrode (samples, conductive carbon black, and polytetrafluoroethylene) was via the same procedure applied in recovery experiment.

4.2.8. Characterization

Crystal structure was obtained through X-ray diffraction (XRD) with Cu-Kα radiation (D8 Advance, Bruker AXS, Germany). Morphology was characterized through scanning electron microscopy (SEM, Phenom ProX G6, Netherlands) and transmission electron microscopy (TEM, JEM-F200, Japan). Elemental state information was gained through X-ray photoelectron spectroscopy (XPS, Thermo Scientific K-Alpha, America). Raman (INVIA, Renishaw, England) was conducted on testing atomic bond structure.

4.3. Results and discussion

4.3.1. Phase and morphology

DR-MoS_2 was produced by one-pot thermal synthesis using our previously reported method[53]. Samples were prepared by adjusting the ratio of Mo and S sources, and there were more unsaturated S atoms in the structure of MoS_2 when higher of S resource concentration than Mo resource concentration in the reaction atmosphere. Figure 4-1 showed the structure of samples provided by XRD patterns. Peaks of characteristic diffraction at 14°, 33°, 39°, and 58° were respectively indexed to (002), (100), (103), and (110) plane of 2H-MoS_2 (JCPDS 37-1492). Shape of the peaks kept unchanged, while weakened little in atom interferometer direction, expressing that the microstructure was well preserved.

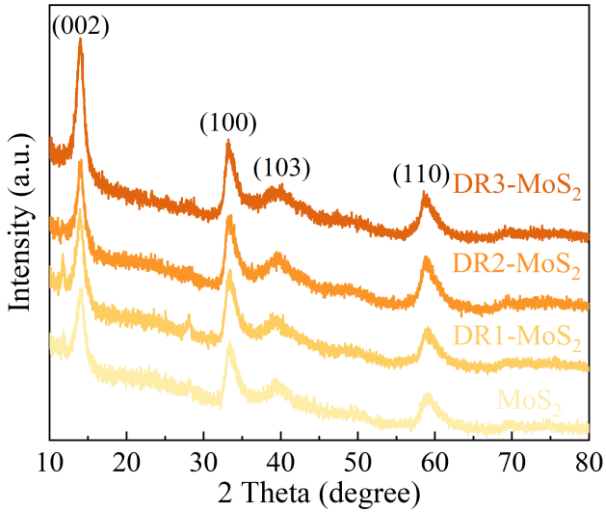

Figure 4-1. XRD patterns of samples with various concentrations of S and Mo sources.

To provide more insight information about the defects in the structure of MoS_2, we performed Raman spectra measurement (Figure 4-2a) on the samples. As could be seen, the two peaks were attributed to binding layer between Mo and S atoms (E^1_{2g} mode) and out-of-plane vibration of S atoms (A_{1g} mode). Shift of peaks to lower wavenumbers suggested the occurrence of defects when more S sources in synthesis process were added. Further, peak intensity ratio of E^1_{2g} and A_{1g} declined as higher dosage of sources (Figure 4-2b), demonstrating the existence of more exposure defects with unsaturated S atoms[54].

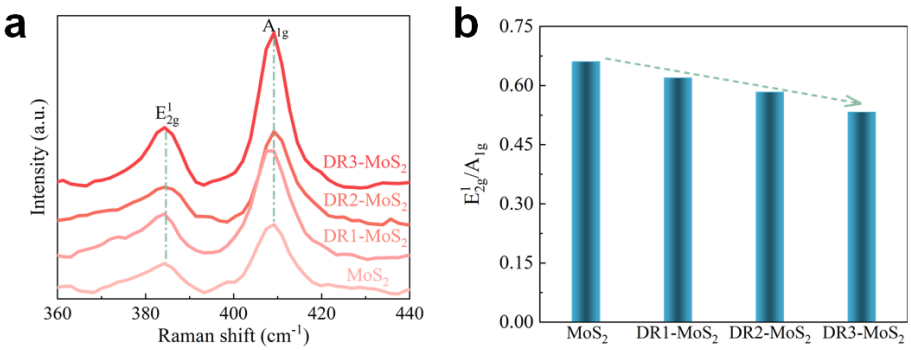

Figure 4-2. (a) Raman spectra, and (b) ratio of E12g and A1g intensity of samples with various concentrations of S and Mo sources.

In order to identify the morphology, TEM and HRTEM images of DR-MoS_2 were shown in Figure 4-3a and 4-3b. Nanosheets with ultrathin edges were uniformly distributed, and (002) and (101) crystal facets of MoS_2 were found through selected area electron diffraction (SAED) result. Slightly alterative interlayer distance in comparison with normal value in Figure 4-3c exhibited the effect of lattice distortion. Moreover, as marked in origine circles and the height profile of fringe, it revealed the broken lamellar structures because of defects. Through EDS mapping results (Figure 4-

3d), it displayed the homogeneous distribution of Mo and S element in all the region of samples, while weak existence of O element was from distortion of MoS_2. Thus, based on the above discussions, various DR-MoS_2 was successfully synthesized by regulating the ratio of Mo and S sources.

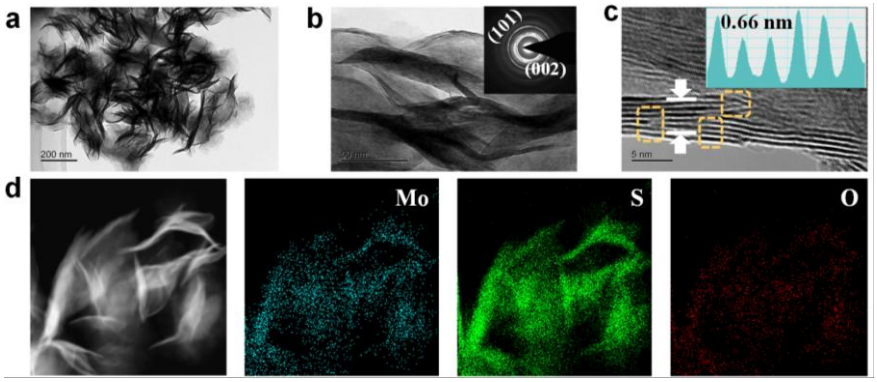

Figure 4-3. Morphology characterization of samples with various concentrations of S and Mo sources. (a) TEM, and (b, c) HRTEM images of DR-MoS_2, insert picture in e and f were SAED image and height profile of fringe, respectively. (d) TEM and corresponding EDS mapping of DR-MoS_2.

4.3.2. REEs sorption behaviors

Given the interaction between REEs and DR-MoS_2, REEs sorption on MoS_2 and DR-MoS_2 electrodes by CEC process were investigated. Figure 4-4a and 4-4b clearly indicated that the adsorption capacity and recovery of Gd(III) on MoS_2 and DR-MoS_2 were highest, and Y(III) took second place, which was related with the binding ability between REEs and electrodes. As introducing more defects into the structure of MoS_2, adsorption capacity and recovery of REEs were all enhanced, verifying that defective structure was beneficial for interaction with REEs. Interestingly, the recovery ability of Gd(III) was mostly obvious because the largest number of unpaired electrons in Gd would interact strongly with unsaturated S atoms in MoS_2.

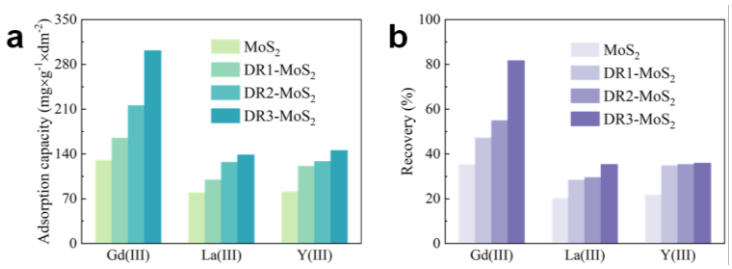

Figure 4-4. (a) Adsorption capacity, and corresponding (b) recovery of La(III), Gd(III), and Y(III) on MoS_2 and DR-MoS_2 electrodes.

DR-MoS_2 electrodes were applied to determine the adsorption kinetics of La(III),

Gd(III), and Y(III) (Figure 4-5). Upon applying a fixed external voltage, REEs adsorption capacity quickly increased and then tended to be stable by a gradual increase time, suggesting the gradual saturation of ions sorption on DR-MoS_2 electrodes. Additionally, it was apparent that the adsorption capacity of REEs in the order of Gd(III), Y(III), and La(III), which might be relevant with interaction ability in outer atomic orbital between REEs and DR-MoS_2.

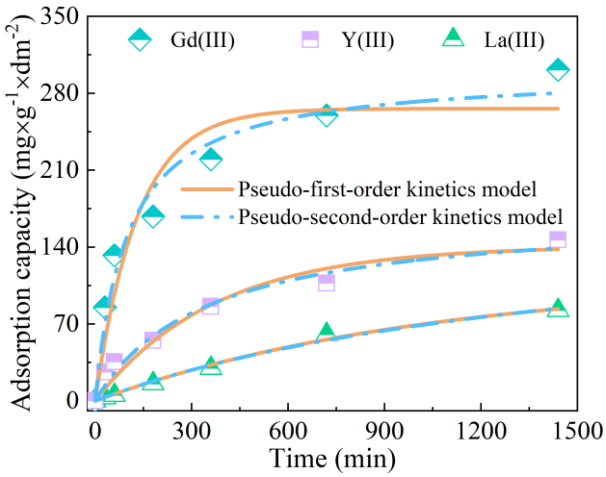

Figure 4-5. Adsorption kinetics of La(III), Gd(III), and Y(III) on DR-MoS_2 electrodes.

The data was analyzed using the pseudo first and second order models as denoted respectively by following equations.

$$q_t = q_e \times [1 - \exp(-k_1 t)] \qquad (6)$$

$$q_t = \frac{t}{\left(\frac{t}{q_e}\right) + \left(\frac{1}{k_2 q_e^2}\right)} \qquad (7)$$

where q_e and q_t were adsorption capacity at equilibrium and t moment, respectively, min, k_1 and k_2 represented the rate constants for first and second order models, respectively, min^{-1}.

The data fitted with the model and the following values of fitting parameters were obtained in Table 4-1. It was observed that the proposed models well agreed with the experimental data and provided a good description of REEs adsorption, though some slight deviations existed in simulation of two models for all REEs adsorption. Two models fitted well for La(III) adsorption process, while pseudo second order model dominated in Gd(III) and Y(III) adsorption. It revealed that physical and chemical interaction occupied a similar position in La(III) adsorption on DR-MoS_2, but chemical interaction was stronger than physical interaction in Gd(III) and Y(III) adsorption on DR-MoS_2, especially Gd(III). The result illustrated that strong chemical interaction happened in Gd(III) recovery from another side view.

Table 4-1. Kinetic parameters for La(III), Gd(III), and Y(III) recovery on DR-MoS_2 electrodes.

	Pseudo-first-order kinetic model			Pseudo-second-order kinetic model		
	q_e (mg/(g·dm^2)	k_1 (min^{-1})	R^2	q_e (mg/(g·dm^2)	K_2 (min^{-1})	R^2
La(III)	111.38	0.0009	0.993	177.42	0.000004	0.992
Gd(III)	265.98	0.0076	0.920	299.32	0.000003	0.970
Y(III)	140.89	0.0006	0.954	178.40	0.000002	0.973

To further investigate the application of DR-MoS_2 electrode in various REEs adsorption behaviors, adsorption capacity and recovery of La(III), Gd(III), and Y(III) under different initial concentrations were investigated in Figure 4-6a, 4-6b, and 4-6c. According to the results, adsorption capacity of all REEs increased with raising initial concentration, while recovery slightly dropped in La(III) and Y(III) adsorption. The reason for such trend was the saturated active sites for La(III) and Y(III). It was noticed that Gd(III) recovery within low concentration remained almost 100%. Figure 4-6d, 4-6e, and 4-6f presented SEM-and corresponding EDS patterns after REEs recovery, and they showed that the adsorption of REEs on DR-MoS_2 and invariant flower-like morphology after REEs recovery. The difference in REEs recovery suggested the possibility in separation of Gd(III) from the both La(III) and Y(III) with similar property.

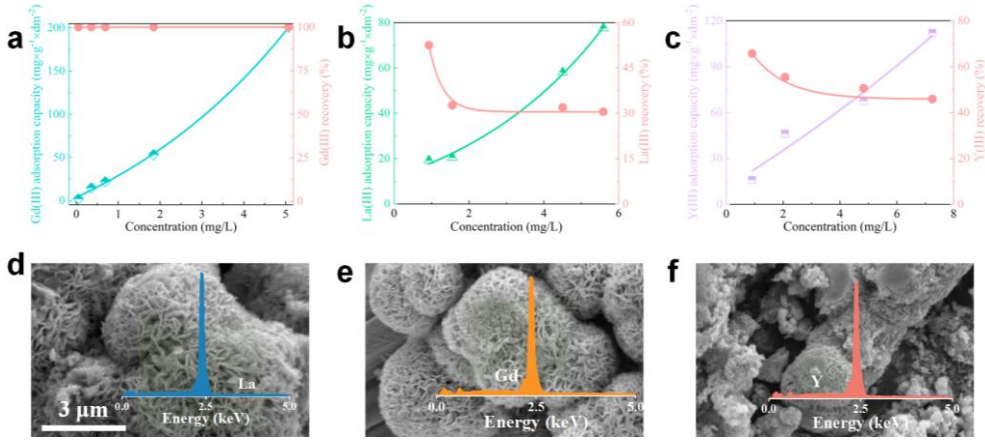

Figure 4-6. (a) Gd(III), (b) La(III), and (c) Y(III) adsorption capacity and corresponding recovery at various initial concentrations on DR-MoS_2 electrodes. SEM and corresponding EDS pattern of DR-MoS_2 electrodes after (d) La(III), (e) Gd(III), and (f) Y(III) recovery.

4.3.3. Optimization experiments and Gd(III) separation

Generally, operation parameters including electrodes-distance, solution pH, and applied voltage were researched on Gd(III) recovery performances. Appropriate electrodes-distance (Figure 4-7a) operated in favor of recovery. Short electrodes-

distance decelerated the flow of reaction solutions, while long electrodes-distance weakened the immigration of target ions in solutions. Adsorption capacity and recovery of Gd(III) as a function of pH medium was given in Figure 4-7b. According to the figure, the adsorption was enhanced up to pH of 5, and then being declined as higher than 5. pH influenced metal ions adsorption either by causing the variation of adsorption sites or by altering the charged species of ions. Upon the increasement of pH, deprotonation of DR-MoS_2 increased, thus to push up number of interacted sites. As for decreased adsorption under high pH value, the changeable species of Gd(III) with more hydration molecules would lessen the interaction with DR-MoS_2. Effects of applied voltage on the CEC process of Gd(III) recovery was investigated (Figure 4-7c). It was noted that adsorption capacity and recovery were significantly improved at a certain mini charging voltage. External electric field caused by voltage facilitated the immigration of ions toward electrodes, thus enhancing the recovery performances. Besides, the charged electrodes was beneficial for the interaction of Gd(III). Evaluating Gd(III) separation performances from La(III) and Y(III) was necessary for the application of CEC method with DR-MoS_2 electrodes in REEs separation. The experiment was performed in a mixture solutions including La(III), Gd(III), and Y(III). Related separation coefficients of Gd(III) with two REEs were calculated and exhibited in Figure 4-7d. It revealed that the CEC method could achieve separation of target ions through adjusting chemisorption. Gd(III) separation coefficient from Y(III) was higher than that from La(III), demonstrating the competition of Gd(III) and Y(III) on reactive sites for chemisorption.

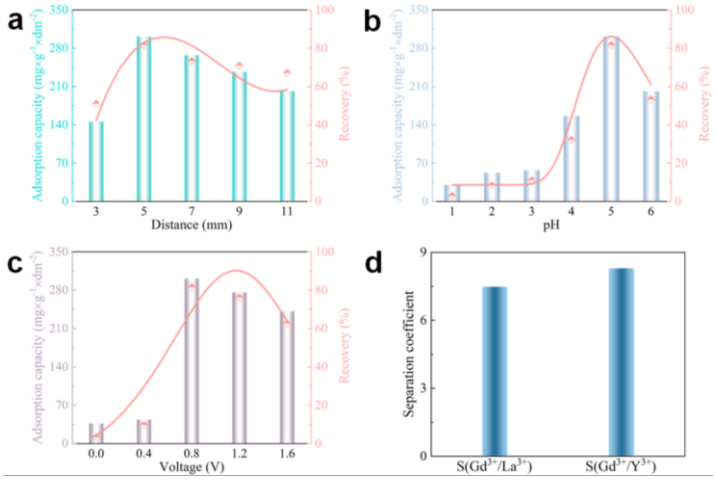

Figure 4-7. Effect of operational parameters on Gd(III) recovery via DR-MoS_2 electrodes: (a) electrodes-distance, (b) solution pH, and (c) applied voltage. (d) Separation coefficient of Gd(III) in the mixture solution with La(III), Gd(III), and Y(III).

XPS analysis was conducted to obtain further information on the surficial

interaction of REES and DR-MoS_2. The survey scan (Figure 4-8a) revealed that DR-MoS_2 was composed of three elements, i.e., Mo, S, and O. After REEs recovery, there appeared three new peaks of La, Gd, and Y elements, demonstrating the adsorption of La(III), Gd(III), and Y(III) on DR-MoS_2 electrodes. From Figure 4-8b, it was observed that the Mo 3*d* spectra were deconvoluted into four species peaks. Peaks at ~231.9 and 228.8 eV were attributed to ^{IV}Mo, which was assigned to Mo-S bonds in MoS_2. The doublet peaks at ~234.9 and 229.9 eV corresponded to the ^{VI}Mo for the distortion of MoS_2. The other peaks at ~232.9 and 230.8 eV indicated the existence of 1T phase MoS_2, which would be induced by the generation of edges. Referring to the S 2*p* spectra (Figure 4-8c), the characteristic peaks at ~162.8 and 161.6 eV were belonging to S^{2-} in MoS_2, while peak at ~163.4 eV originated from S_2^{2-} owing to introduction of defects in the structure. In the spectra of O 1*s* (Figure 4-8d), the divided peaks at ~531.6 and 533.2 eV were ascribed to adsorbed water and $MoS_{2-x}O_x$, respectively. Compared with the peaks of Mo, S, and O elements in DR-MoS_2 before recovery, the peaks apparently shifted to higher binding energy, which confirmed the strong interaction of REEs with DR-MoS_2.

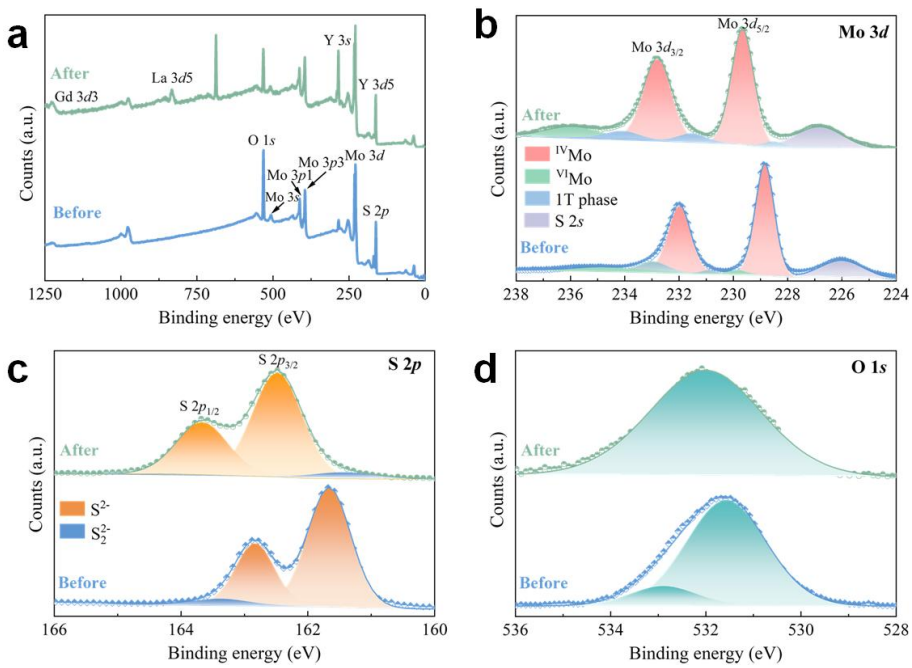

Figure 4-8. XPS spectra: (a) survey spectra, (b) Mo 3*d*, (c) S 2*p*, and (d) O 1*s* of DR-MoS_2 electrodes before and after recovery in REEs mixture solutions.

4.3.4. Competitive Gd(III) capture

The electrochemical performances of MoS_2 and DR-MoS_2 electrodes were tested by cyclic voltammetry (CV) and EIS in Gd(III) solution. Obviously, there were no

redox peaks in CV plots (Figure 4-9a), and all the curves displayed analogous rectangular patterns, which revealed happen of typical electric double layer capacitor form. The enclosed area was positively correlated with electric double layer capacity (EDLC). By introducing more defects into the structure of MoS_2, corresponding EDLC gradually increased, demonstrating that rich defects was in favor of Gd(III) adsorption. Compared with DR-MoS_2 electrode in La(III) and Y(III) solutions (Figure 4-9b), highest EDLC performance in Gd(III) solution suggested a strong ability in Gd(III) separation and recovery from other REEs using DR-MoS_2 electrode, which was consistent with the separation results. Moreover, EIS tests of MoS_2 and DR-MoS_2 electrodes were conducted to examine the resistance of ion immigration, as shown in Figure 4-9c. Higher radius of semicircle represented greater ion immigration resistance. It was clear that DR-MoS_2 electrode possessed a lower ion immigration resistance in comparison with MoS_2, and more defects facilitated the immigration. What's more, strongest ion immigration ability of DR-MoS_2 electrode in Gd(III) solution, compared with EIS results of DR-MoS_2 electrode in La(III) and Y(III) solution (Figure 4-9d), strengthening Gd(III) recovery in REEs solutions.

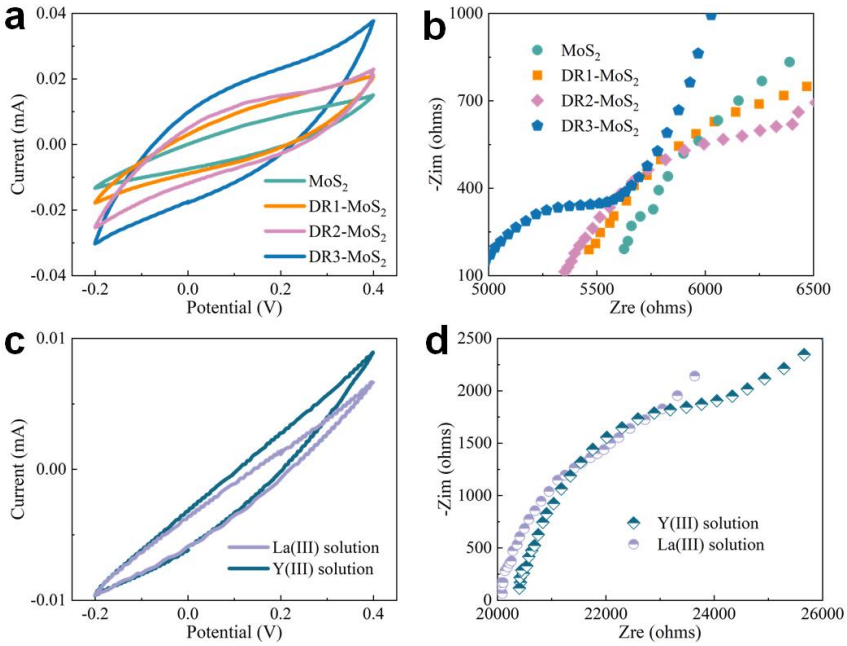

Figure 4-9. (a) CV plots and (b) EIS results of MoS_2 and DR-MoS_2 in Gd(III) solutions. (c) CV curves and (d) EIS results of DR-MoS_2 electrode in the solution of La(III) and Y(III) solutions.

To verify Gd(III) adsorption on defects of MoS_2, AFM was applied to investigate MoS_2 with edge defects after being exposed to Gd(III) solution (Figure 4-10a). Through measuring the thickness difference of grey lines in Figure 4c between two ends, as shown in Figure 4-10b, there existed difference around 100 pm, demonstrating the

appearance of "edge". It was worth noticing that Gd(III) tended to interact the edge of DR-MoS_2. The adsorption layer thickness was around 143 pm, might be ascribed to the multilayer adsorption.

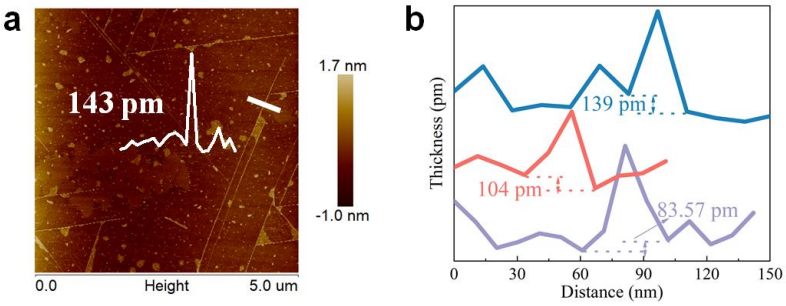

Figure 4-10. (a) AFM image of MoS_2 with edge defects after being exposed to Gd(III) solution for 2 h. (b) Thickness difference of edges between two ends.

For the purpose of studying competitive Gd(III) adsorption on DR-MoS_2, DFT was performed to research the interaction of La(III), Gd(III), and Y(III) with MoS_2 and DR-MoS_2. Initially, possible structure of MoS_2 (Figure 4-11a) and DR-MoS_2 with one S (Figure 4-11b) (or Mo, Figure 4-11c) atom loss as cycled in dotted line were optimized.

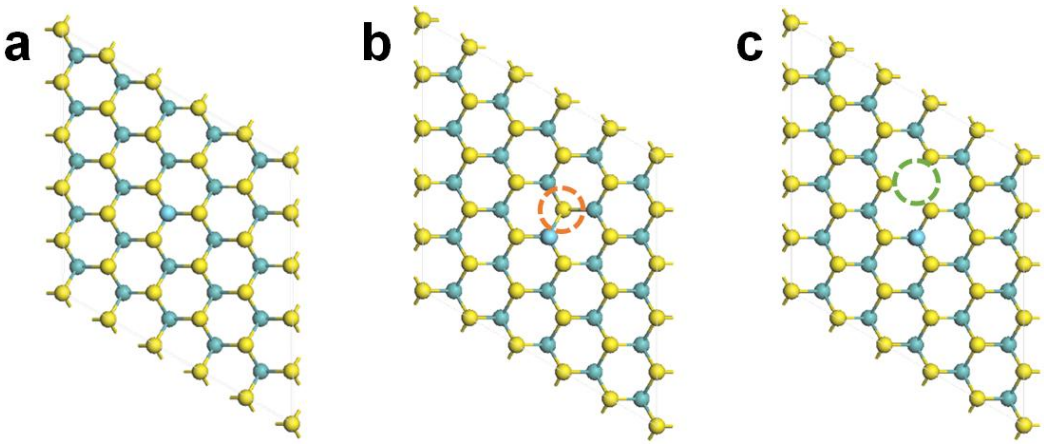

Figure 4-11. Top views of supercell models of (a) MoS_2, (b) MoS_2-S, and MoS_2-Mo.

Then, La(III), Gd(III), and Y(III) adsorption on the surface of three possible structure were calculated. After calculation, the balanced structures for adsorption from top and side views were provided in Figure 4-12. Closest distance of Y(III) rather than La(III) and Gd(III) to the surface of MoS_2, indicating strongest interaction of Y(III) with MoS_2. As for the surface of MoS_2-S, La(III) bound most tightly among the three REEs due to the attraction of unsaturated Mo atom. Interestingly, the interaction behaviors of REEs on the surface of MoS_2-Mo were different from the other two

surfaces, and Gd(III) was most strongly adsorbed.

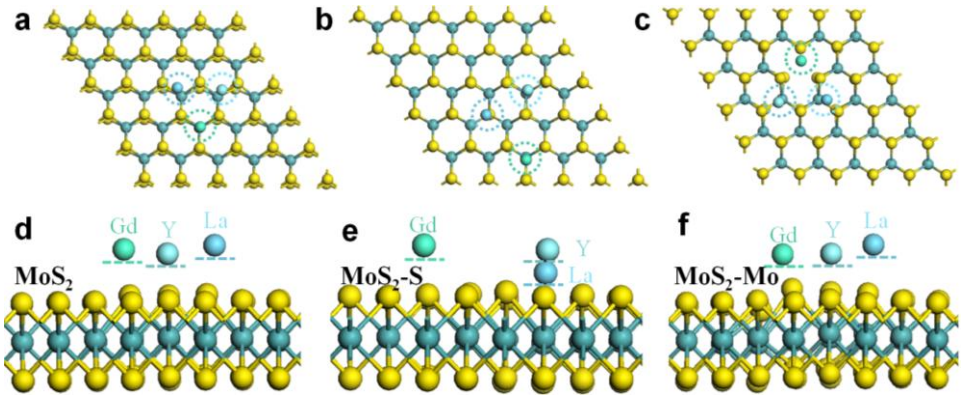

Figure 4-12. Top configuration and side views of La(III), Gd(III), and Y(III) competition adsorption on the surface of (a, d) MoS_2, (b, e) MoS_2-S, and (c, f) MoS_2-Mo.

Various REEs adsorption behaviors on MoS_2 and DR-MoS_2 were demonstrated via adsorption energy (Figure 4-13). There were little differences in the adsorption of three REEs on MoS_2. Gd(III) and Y(III) interaction on the surface of MoS_2-Mo worked the best, while strong interaction of La(III) happened on the surface of MoS_2-S. It could be inferred that the possibility of REEs separation by DR-MoS_2.

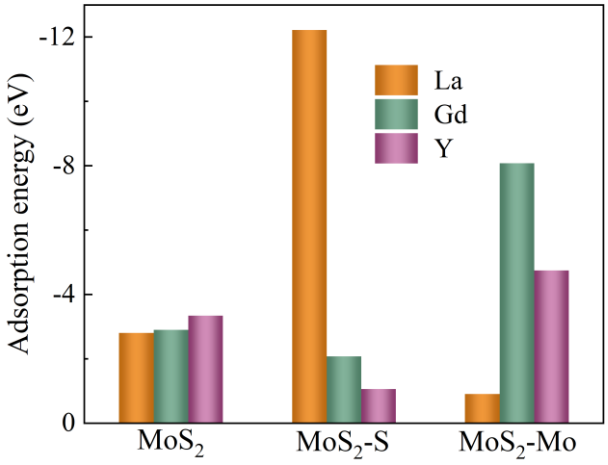

Figure 4-13. Adsorption energies of La(III), Gd(III), Y(III) on MoS_2, MoS_2-S, and MoS_2-Mo.

To reveal which binding atoms dominated the interaction, Mulliken atomic charge changes were performed to investigate La, Gd, Y, S and Mo atoms (Figure 4-14a). As seen, great force between REEs and MoS_2 (or DR-MoS_2) resulted from atomic charge changes in Mo and S atoms. The total lost charges in Mo and S atoms for three REEs were similar, but various REEs gained different distributed charges owing to the diverse interaction. In the sorption of MoS_2-Mo, Gd(III) behaved most superior charge transfer for interaction. Further, the binding orbitals between REEs and electrodes were

investigated by partial density of states (PDOS). Each REE tightly bound with S atoms, especially *p* orbitals, on electrode surface (Figure 4-14b, 4-14c, and 4-14d). Compared with La(III) and Y(III), *f* orbitals in Gd(III) greatly participated in the interaction with S atoms on MoS_2-Mo. As well, the interaction of *d* orbitals in La(III) and *d* orbitals in Mo atoms facilitated La(III) adsorption on MoS_2-S. Therefore, disparate extranuclear atomic orbital interaction led to significantly different chemical interaction.

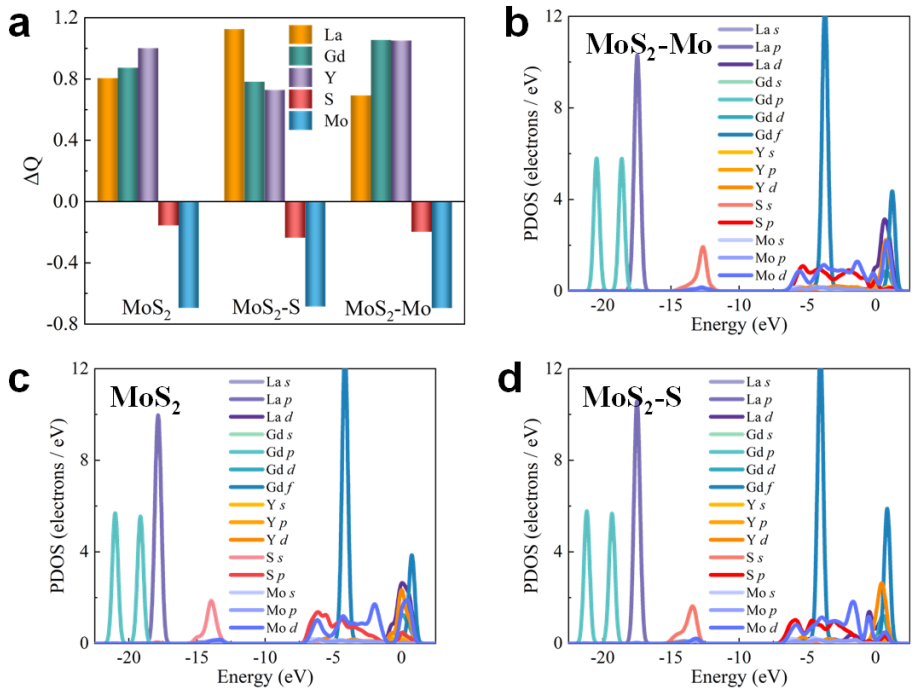

Figure 4-14. (a) Mulliken atomic charge changes of La(III), Gd(III), Y(III), S and Mo in the system of REEs competition adsorption on MoS_2, MoS_2-S, and MoS_2-Mo. PDOS of La(III), Gd(III), Y(III), S and Mo in the system of REEs competition adsorption on (b) MoS_2-Mo, (c) MoS_2, and (d) MoS_2-S.

4.4. Conclusions

Separation and recovery of trace Gd(III) from other similar REEs in aqueous solutions via regulating the chemisorption activity of electrodes was presented. Gd(III) recovery and adsorption capacity achieved almost 100% and 299.32 mg/(g·dm^2) on DR-MoS_2 electrode. In the competitive adsorption experiments, Gd(III) could be highly separated from La(III) and Y(III) because of special interaction *f* orbitals in Gd(III) with *p* orbitals in unsaturated S atoms of DR-MoS_2. In the meantime, super sorption ability enhanced EDLC and weakened charge transfer resistance of electrode in the solution to

strengthen the electrochemical properties of electrodes. Remarkable, strong binding forces of La(III) and unsaturated Mo atoms had the possibility to realize La(III) separation and recovery via MoS_2 with unsaturated Mo atoms defects. Thus, this work might benefit separation and recovery of target trace REEs from aqueous solutions by modulating chemisorption.

4.5. References

(1) Wang, G.; Xu, J.; Ran, L.; Zhu, R.; Ling, B.; Liang, X.; Kang, S.; Wang, Y.; Wei, J.; Ma, L.; Zhuang, Y.; Zhu, J.; He, H. A Green and Efficient Technology to Recover Rare Earth Elements from Weathering Crusts. *Nature Sustainability* **2022**, *6* (1), 81–92. https://doi.org/10.1038/s41893-022-00989-3.

(2) Moriggi, L.; Cannizzo, C.; Dumas, E.; Mayer, C. R.; Ulianov, A.; Helm, L. Gold Nanoparticles Functionalized with Gadolinium Chelates as High-Relaxivity MRI Contrast Agents. *J Am Chem Soc* **2009**, *131* (31), 10828–10829. https://doi.org/10.1021/JA904094T.

(3) Miéville, P.; Jannin, S.; Helm, L.; Bodenhausen, G. Kinetics of Yttrium-Ligand Complexation Monitored Using Hyperpolarized 89Y as a Model for Gadolinium in Contrast Agents. *J Am Chem Soc* **2010**, *132* (14), 5006–5007. https://doi.org/10.1021/JA1013954.

(4) Stasiuk, G. J.; Tamang, S.; Imbert, D.; Poillot, C.; Giardiello, M.; Tisseyre, C.; Barbier, E. L.; Fries, P. H.; De Waard, M.; Reiss, P.; Mazzanti, M. Cell-Permeable Ln(III) Chelate-Functionalized InP Quantum Dots as Multimodal Imaging Agents. *ACS Nano* **2011**, *5* (10), 8193–8201. https://doi.org/10.1021/NN202839W.

(5) Kinyanjui, F. G.; Norberg, S. T.; Knee, C. S.; Ahmed, I.; Hull, S.; Buannic, L.; Hung, I.; Gan, Z.; Blanc, F.; Grey, C. P.; Eriksson, S. G. Crystal Structure and Proton Conductivity of $BaSn_{0.6}Sc_{0.4}O_{3-\delta}$: Insights from Neutron Powder Diffraction and Solid-State NMR Spectroscopy. *J Mater Chem A Mater* **2016**, *4* (14), 5088–5101. https://doi.org/10.1039/C5TA09744D.

(6) Lai, Y. H.; Su, C. Y.; Cheng, H. W.; Chu, C. Y.; Jeng, L. Bin; Chiang, C. S.; Shyu, W. C.; Chen, S. Y. Stem Cell–Nanomedicine System as a Theranostic Bio-Gadolinium Agent for Targeted Neutron Capture Cancer Therapy. *Nature Communications* **2023**, *14* (1), 1–17. https://doi.org/10.1038/s41467-023-35935-0.

(7) Magrasó, A.; Hervoches, C. H.; Ahmed, I.; Hull, S.; Nordström, J.; Skilbred, A. W. B.; Haugsrud, R. In Situ High Temperature Powder Neutron Diffraction Study of Undoped and Ca-Doped $La_{28-x}W_{4+x}O_{54+3x/2}$ (x=0.85). *J Mater Chem A Mater* **2013**, *1* (11), 3774–3782. https://doi.org/10.1039/C3TA00497J.

(8) Kümmerer, K.; Helmers, E. Hospital Effluents as a Source of Gadolinium in the Aquatic Environment. *Environ Sci Technol* **2000**, *34* (4), 573–577. https://doi.org/10.1021/ES990633H.

(9) Fan, Z.; Shi, J. W.; Gao, C.; Gao, G.; Wang, B.; Wang, Y.; He, C.; Niu, C. Gd-Modified MnOx for the Selective Catalytic Reduction of NO by NH_3: The Promoting Effect of Gd on the Catalytic Performance and Sulfur Resistance. *Chemical Engineering Journal* **2018**, *348*, 820–830. https://doi.org/10.1016/J.CEJ.2018.05.038.

(10) Henderson, L.; Neumann, O.; Kaffes, C.; Zhang, R.; Marangoni, V.; Ravoori, M. K.; Kundra, V.; Bankson, J.; Nordlander, P.; Halas, N. J. Routes to Potentially Safer T1 Magnetic Resonance

Imaging Contrast in a Compact Plasmonic Nanoparticle with Enhanced Fluorescence. *ACS Nano* **2018**, *12* (8), 8214–8223. https://doi.org/10.1021/ACSNANO.8B03368.

(11) Chen, F.; Yang, C.; Liu, X.; Zhang, N.; Rong, P.; Liang, S.; Ma, R. Controllable Fabrication of Rare-Earth-Doped $Gd_2O_2SO_4$@SiO_2 Double-Shell Hollow Spheres for Efficient Upconversion Luminescence and Magnetic Resonance Imaging. *ACS Sustain Chem Eng* **2018**, *6* (8), 10463–10471. https://doi.org/10.1021/ACSSUSCHEMENG.8B01828.

(12) An, Q.; Liu, J.; Yu, M.; Wan, J.; Li, D.; Wang, C.; Chen, C.; Guo, J. Multifunctional Magnetic Gd^{3+}-Based Coordination Polymer Nanoparticles: Combination of Magnetic Resonance and Multispectral Optoacoustic Detections for Tumor-Targeted Imaging in Vivo. *Small* **2015**, *11* (42), 5675–5686. https://doi.org/10.1002/SMLL.201501491.

(13) Pierre, V. C.; Botta, M.; Aime, S.; Raymond, K. N. Fe(III)-Templated Gd(III) Self-Assemblies - A New Route toward Macromolecular MRI Contrast Agents. *J Am Chem Soc* **2006**, *128* (29), 9272–9273. https://doi.org/10.1021/JA061323J.

(14) Henriques, B.; Rocha, L. S.; Lopes, C. B.; Figueira, P.; Monteiro, R. J. R.; Duarte, A. C.; Pardal, M. A.; Pereira, E. Study on Bioaccumulation and Biosorption of Mercury by Living Marine Macroalgae: Prospecting for a New Remediation Biotechnology Applied to Saline Waters. *Chemical Engineering Journal* **2015**, *281*, 759–770. https://doi.org/10.1016/J.CEJ.2015.07.013.

(15) Zhao, Y.; Niu, T.; Dong, X.; Yang, Y.; Zhai, W. Robust Graphene-Drum Bridged Carbon Aerogels for Broadband Acoustic and Electromagnetic Attenuation. *J Mater Chem A Mater* **2023**, *11* (43), 23452–23462. https://doi.org/10.1039/D3TA04895K.

(16) Chen, W.; Wang, L.; Zhuo, M.; Liu, Y.; Wang, Y.; Li, Y. Facile and Highly Efficient Removal of Trace Gd(III) by Adsorption of Colloidal Graphene Oxide Suspensions Sealed in Dialysis Bag. *J Hazard Mater* **2014**, *279*, 546–553. https://doi.org/10.1016/J.JHAZMAT.2014.06.075.

(17) Li, Y.; Biswas, R.; Kopcha, W. P.; Dubroca, T.; Abella, L.; Sun, Y.; Crichton, R. A.; Rathnam, C.; Yang, L.; Yeh, Y. W.; Kundu, K.; Rodríguez-Fortea, A.; Poblet, J. M.; Lee, K. B.; Hill, S.; Zhang, J. Structurally Defined Water-Soluble Metallofullerene Derivatives towards Biomedical Applications. *Angewandte Chemie International Edition* **2023**, *62* (3), e202211704. https://doi.org/10.1002/ANIE.202211704.

(18) Martino, C.; Bonaventura, R.; Byrne, M.; Roccheri, M.; Matranga, V. Effects of Exposure to Gadolinium on the Development of Geographically and Phylogenetically Distant Sea Urchins Species. *Mar Environ Res* **2017**, *128*, 98–106. https://doi.org/10.1016/J.MARENVRES.2016.06.001.

(19) Belova, V. V. Development of Solvent Extraction Methods for Recovering Rare Earth Metals. *Theoretical Foundations of Chemical Engineering* **2017**, *51* (4), 599–609. https://doi.org/10.1134/S004057951605002X/METRICS.

(20) Li, K.; Gao, Q.; Yadavalli, G.; Shen, X.; Lei, H.; Han, B.; Xia, K.; Zhou, C. Selective Adsorption of Gd3+ on a Magnetically Retrievable Imprinted Chitosan/Carbon Nanotube Composite with High Capacity. *ACS Appl Mater Interfaces* **2015**, *7* (38), 21047–21055. https://doi.org/10.1021/ACSAMI.5B07560.

(21) yang, M.; Zhou, Y.; Zhang, D.; Zhou, F.; Ning, H.; He, M.; Chi, R. an; Yin, W. Highly Effective and Selective Recovery of Gd(III) from Wastewater by Defective MOFs-Based Ion-Imprinted

Polymer: Performance and Mechanism. *Chemical Engineering Journal* **2023**, *474*, 145782. https://doi.org/10.1016/J.CEJ.2023.145782.

(22) Qi, X. H.; Du, K. Z.; Feng, M. L.; Gao, Y. J.; Huang, X. Y.; Kanatzidis, M. G. Layered $A_2Sn_3S_{7\cdot1.25}H_2O$ (A = Organic Cation) as Efficient Ion-Exchanger for Rare Earth Element Recovery. *J Am Chem Soc* **2017**, *139* (12), 4314–4317. https://doi.org/10.1021/JACS.7B00565.

(23) Vapnik, H.; Elbert, J.; Su, X. Redox-Copolymers for the Recovery of Rare Earth Elements by Electrochemically Regenerated Ion-Exchange. *J Mater Chem A Mater* **2021**, *9* (35), 20068–20077. https://doi.org/10.1039/D1TA03334D.

(24) Nahar, M. S.; Zhang, J. Recovery of Trace Metal Isotopes in Seawater Samples Using Multifunctional Neem (Azadirachta Indica) Biosorbent: A Comparison with Monofunctional NOBIASChelatePA1 Resin. *ACS Sustain Chem Eng* **2013**, *1* (5), 488–495. https://doi.org/10.1021/SC3001433.

(25) Ganesh, R.; Robinson, K. G.; Chu, L.; Kucsmas, D.; Reed, G. D. Reductive Precipitation of Uranium by Desulfovibrio Desulfuricans: Evaluation of Cocontaminant Effects and Selective Removal. *Water Res* **1999**, *33* (16), 3447–3458. https://doi.org/10.1016/S0043-1354(99)00024-X.

(26) Romero-Freire, A.; González, V.; Groenenberg, J. E.; Qiu, H.; Auffan, M.; Cotelle, S.; Giamberini, L. Cytotoxicity and Genotoxicity of Lanthanides for Vicia Faba L. Are Mediated by Their Chemical Speciation in Different Exposure Media. *Science of The Total Environment* **2021**, *790*, 148223. https://doi.org/10.1016/J.SCITOTENV.2021.148223.

(27) Lachaux, N.; Catrouillet, C.; Marsac, R.; Poirier, L.; Pain-Devin, S.; Gross, E. M.; Giamberini, L. Implications of Speciation on Rare Earth Element Toxicity: A Focus on Organic Matter Influence in Daphnia Magna Standard Test. *Environmental Pollution* **2022**, *307*, 119554. https://doi.org/10.1016/J.ENVPOL.2022.119554.

(28) Hu, Y.; Drouin, E.; Larivière, D.; Kleitz, F.; Fontaine, F. G. Highly Efficient and Selective Recovery of Rare Earth Elements Using Mesoporous Silica Functionalized by Preorganized Chelating Ligands. *ACS Appl Mater Interfaces* **2017**, *9* (44), 38584–38593. https://doi.org/10.1021/ACSAMI.7B12589.

(29) Park, J. Y.; Baek, M. J.; Choi, E. S.; Woo, S.; Kim, J. H.; Kim, T. J.; Jung, J. C.; Chae, K. S.; Chang, Y.; Lee, G. H. Paramagnetic Ultrasmall Gadolinium Oxide Nanoparticles as Advanced T 1 MRI Contrast Agent: Account for Large Longitudinal Relaxivity, Optimal Particle Diameter, and in Vivo T1 MR Images. *ACS Nano* **2009**, *3* (11), 3663–3669. https://doi.org/10.1021/NN900761S.

(30) Ali, O. I. M.; Osman, H. H.; Sayed, S. A.; Shalabi, M. E. H. The Removal of Some Rare Earth Elements from Their Aqueous Solutions on By-Pass Cement Dust (BCD). *J Hazard Mater* **2011**, *195*, 62–67. https://doi.org/10.1016/J.JHAZMAT.2011.08.014.

(31) Rademaker, J. H.; Kleijn, R.; Yang, Y. Recycling as a Strategy against Rare Earth Element Criticality: A Systemic Evaluation of the Potential Yield of NdFeB Magnet Recycling. *Environ Sci Technol* **2013**, *47* (18), 10129–10136. https://doi.org/10.1021/ES305007W.

(32) Cui, H.; Zhang, X.; Chen, J.; Qian, X.; Zhong, Y.; Ma, C.; Zhang, H.; Liu, K. The Construction of a Microbial Synthesis System for Rare Earth Enrichment and Material Applications. *Advanced Materials* **2023**, *35* (33), 2303457. https://doi.org/10.1002/ADMA.202303457.

(33) Zheng, X.; Liu, E.; Zhang, F.; Yan, Y.; Pan, J. Efficient Adsorption and Separation of Dysprosium from NdFeB Magnets in an Acidic System by Ion Imprinted Mesoporous Silica Sealed

in a Dialysis Bag. *Green Chemistry* **2016**, *18* (18), 5031–5040. https://doi.org/10.1039/C6GC01426G.

(34) Zhang, E.; Wu, Y. C.; Shao, H.; Klimavicius, V.; Zhang, H.; Taberna, P. L.; Grothe, J.; Buntkowsky, G.; Xu, F.; Simon, P.; Kaskel, S. Unraveling the Capacitive Charge Storage Mechanism of Nitrogen-Doped Porous Carbons by EQCM and SsNMR. *J Am Chem Soc* **2022**, *144* (31), 14217–14225. https://doi.org/10.1021/JACS.2C04841.

(35) Beladi-Mousavi, S. M.; Khezri, B.; Matějková, S.; Sofer, Z.; Pumera, M. Supercapacitors in Motion: Autonomous Microswimmers for Natural-Resource Recovery. *Angewandte Chemie International Edition* **2019**, *58* (38), 13340–13344. https://doi.org/10.1002/ANIE.201906642.

(36) Chen, M. Y.; Klunk, M. D.; Diep, V. M.; Sailor, M. J. Electric-Field-Assisted Protein Transport, Capture, and Interferometric Sensing in Carbonized Porous Silicon Films. *Advanced Materials* **2011**, *23* (39), 4537–4542. https://doi.org/10.1002/ADMA.201102090.

(37) Korenblit, Y.; Kajdos, A.; West, W. C.; Smart, M. C.; Brandon, E. J.; Kvit, A.; Jagiello, J.; Yushin, G. In Situ Studies of Ion Transport in Microporous Supercapacitor Electrodes at Ultralow Temperatures. *Adv Funct Mater* **2012**, *22* (8), 1655–1662. https://doi.org/10.1002/ADFM.201102573.

(38) Sun, M.; Staykov, A.; Yamauchi, M. Understanding the Roles of Hydroxide in CO_2 Electroreduction on a Cu Electrode for Achieving Variable Selectivity. *ACS Catal* **2022**, *12* (24), 14856–14863. https://doi.org/10.1021/ACSCATAL.2C03650.

(39) Byers, C. P.; Hoener, B. S.; Chang, W. S.; Link, S.; Landes, C. F. Single-Particle Plasmon Voltammetry (SpPV) for Detecting Anion Adsorption. *Nano Lett* **2016**, *16* (4), 2314–2321. https://doi.org/10.1021/ACS.NANOLETT.5B04990.

(40) Macías, C.; Rasines, G.; Lavela, P.; Zafra, M. C.; Tirado, J. L.; Ania, C. Mn-Containing N-Doped Monolithic Carbon Aerogels with Enhanced Macroporosity as Electrodes for Capacitive Deionization. *ACS Sustain Chem Eng* **2016**, *4* (5), 2487–2494. https://doi.org/10.1021/ACSSUSCHEMENG.5B01444.

(41) Lu, J.; Kumar Mishra, P.; Hunter, T. N.; Yang, F.; Lu, Z.; Harbottle, D.; Xu, Z. Functionalization of Mesoporous Carbons Derived from Pomelo Peel as Capacitive Electrodes for Preferential Removal/Recovery of Copper and Lead from Contaminated Water. *Chemical Engineering Journal* **2022**, *433*, 134508. https://doi.org/10.1016/J.CEJ.2022.134508.

(42) Efome, J. E.; Rana, D.; Matsuura, T.; Lan, C. Q. Metal–Organic Frameworks Supported on Nanofibers to Remove Heavy Metals. *J Mater Chem A Mater* **2018**, *6* (10), 4550–4555. https://doi.org/10.1039/C7TA10428F.

(43) Macías-García, A.; Carrasco-Amador, J. P.; Encinas-Sánchez, V.; Díaz-Díez, M. A.; Torrejón-Martín, D. Preparation of Activated Carbon from Kenaf by Activation with H_3PO_4. Kinetic Study of the Adsorption/Electroadsorption Using a System of Supports Designed in 3D, for Environmental Applications. *J Environ Chem Eng* **2019**, *7* (4), 103196. https://doi.org/10.1016/J.JECE.2019.103196.

(44) Aburabie, J.; Mohammed, S.; Kumaran, A.; Hashaikeh, R. From Waste to Wealth: Chelating Polymeric Membranes for Precious Palladium Recovery from Wastewater. *J Mater Chem A Mater* **2023**, *11* (42), 22845–22858. https://doi.org/10.1039/D3TA04931K.

(45) Huang, C. C.; He, J. C. Electrosorptive Removal of Copper Ions from Wastewater by Using Ordered Mesoporous Carbon Electrodes. *Chemical Engineering Journal* **2013**, *221*, 469–475. https://doi.org/10.1016/J.CEJ.2013.02.028.

(46) Li, P.; Gui, Y.; Blackwood, D. J. Development of a Nanostructured α-MnO_2/Carbon Paper Composite for Removal of Ni^{2+}/Mn^{2+} Ions by Electrosorption. *ACS Appl Mater Interfaces* **2018**, *10* (23), 19615–19625. https://doi.org/10.1021/ACSAMI.8B02471.

(47) Wang, H.; Yan, T.; Shen, J.; Zhang, J.; Shi, L.; Zhang, D. Efficient Removal of Metal Ions by Capacitive Deionization with Straw Waste Derived Graphitic Porous Carbon Nanosheets. *Environ Sci Nano* **2020**, *7* (1), 317–326. https://doi.org/10.1039/C9EN01233H.

(48) Chao, H. P.; Chen, S. H. Adsorption Characteristics of Both Cationic and Oxyanionic Metal Ions on Hexadecyltrimethylammonium Bromide-Modified NaY Zeolite. *Chemical Engineering Journal* **2012**, *193–194*, 283–289. https://doi.org/10.1016/J.CEJ.2012.04.059.

(49) Valverde, A.; de Fernandez-de Luis, R.; Salazar, H.; Gonçalves, B. F.; King, S.; Almásy, L.; Kriechbaum, M.; Laza, J. M.; Vilas-Vilela, J. L.; Martins, P. M.; Lanceros-Mendez, S.; Porro, J. M.; Petrenko, V. I. On The Multiscale Structure and Morphology of PVDF-HFP@MOF Membranes in The Scope of Water Remediation Applications. *Adv Mater Interfaces* **2023**, *10* (31), 2300424. https://doi.org/10.1002/ADMI.202300424.

(50) Elabbas, S.; Ouazzani, N.; Mandi, L.; Berrekhis, F.; Perdicakis, M.; Pontvianne, S.; Pons, M. N.; Lapicque, F.; Leclerc, J. P. Treatment of Highly Concentrated Tannery Wastewater Using Electrocoagulation: Influence of the Quality of Aluminium Used for the Electrode. *J Hazard Mater* **2016**, *319*, 69–77. https://doi.org/10.1016/J.JHAZMAT.2015.12.067.

(51) Shang, M.; Ma, B.; Hu, X.; Liu, L.; Wang, J.; Zhang, X. Biomimetic Core-Shell-Structured Nanofiber Membranes for Rapid and Portable Water Purification. *ACS Appl Mater Interfaces* **2022**, *14* (39), 44849–44858. https://doi.org/10.1021/ACSAMI.2C12537.

(52) Mao, M.; Yan, T.; Shen, J.; Zhang, J.; Zhang, D. Selective Capacitive Removal of Heavy Metal Ions from Wastewater over Lewis Base Sites of S-Doped Fe-N-C Cathodes via an Electro-Adsorption Process. *Environ Sci Technol* **2021**, *55* (11), 7665–7673. https://doi.org/10.1021/ACS.EST.1C01483.

(53) Zhan, W.; Yuan, Y.; Zhang, X.; Liang, Y.; Song, S.; de Jesús Martínez-López, M.; Arauz-Lara, J. L.; Jia, F. Efficient and Selective Lead(II) Removal within a Wide Concentration Range through Chemisorption and Electrosorption Coupling Process via Defective MoS_2 Electrode. *Sep Purif Technol* **2024**, *329*, 125183. https://doi.org/10.1016/J.SEPPUR.2023.125183.

(54) Chen, Y.; Huang, S.; Ji, X.; Adepalli, K.; Yin, K.; Ling, X.; Wang, X.; Xue, J.; Dresselhaus, M.; Kong, J.; Yildiz, B. Tuning Electronic Structure of Single Layer MoS_2 through Defect and Interface Engineering. *ACS Nano* **2018**, *12* (3), 2569–2579. https://doi.org/10.1021/ACSNANO.7B08418.

Chapter V. Rare and precious metals recovery at a low concentration by carbon-based electrodes

5.1. Introduction

Due to the special properties of rare earth elements (REEs) and precious metals, they still played an important role in the transition toward green energy, for example, electric batteries[1–3], wind and solar energy[4,5], catalysis[6,7], semiconductors[8,9], luminescence[10,11]. The recovery of REEs and precious metals from ores[12–14] and waste materials[15–17] was necessary for green development. Thus, many researches[18–20] have recently been proposed for developing processes and materials for the recovery of REEs and precious metals in aqueous solutions from low-grade resources, for instance, mining processing wastewater, refining wastewater, seawater, etc.

Various methods, such as, solvent extraction[21–23], ion exchange[24–26], chemical precipitation[27–30], and sorption[31–33] have been largely used in separating and recovering REEs and precious metals. However, these approaches were hard for actual application due to large consumption of reagents[34], or high cost, or poor recovery[35]. In addition, most current methods focused on the recovery in high concentration[36–38], while rare researches were related with low concentration. There are still challenges to effectively recover REEs and precious metals within low concentration range from aqueous solutions.

Electro-adsorption was a kind of promising way to adsorb low-concentration target ions in solution since the target ions were induced to overcome the electrostatic repulsion and towards the adsorbent under the electric field[39]. Materials as the working electrode are vital for the interaction between electrolyte and electrode[40]. The target ions are captured *via* physical interaction into the pores formed in EDL. According to the ion storage equation in EDL capacitance, $C = \frac{\varepsilon A}{d}$, capacitance is related with surface area[41]. As a result, porous electrode was beneficial for the recovery of low-concentration REEs.

Carbon materials, for instance, activated carbon (AC), graphite, graphene, carbon nanotubes, with their super porous structure, low cost, and high specific surface area properties have been found as common adsorbents for metal ions adsorption[42,43]. Few previous works[44,45] demonstrated that activated carbon electrode could bind with REEs and precious metals, but focusing on the modification of AC and interaction with metals.

During the electro-adsorption process, the function of pores is indispensable. The adsorption process of metals and role of pores on carbon electrode need to be further investigated. To our best knowledge, no studies extending electro-assisted sorption *via* carbon-based electrodes for low-concentration REEs and precious metals recovery and related self-properties have been researched.

As a typical precious metal, gold(Au) was chosen to study the application of carbon-based electrodes on gold recovery. Among the leaching methods, thiosulfate leaching was the most promising green way for gold extraction from gold ores instead of cyanide leaching in industries[46]. However, the bottleneck for applying thiosulfate leaching is Au(I) recovery from thiosulfate leaching solutions.

Herein, a facile device for electro-assisted recovery of low-concentration REEs and Au(I) from aqueous solutions using porous carbon materials was developed. AC, graphene, and graphite were selected as typical carbon materials. As for the representative light, middle and heavy REEs, La(III), Gd(III) and Y(III) were chosen for studying recovery, respectively. The aim is to provide the insights into recovering low-concentration REEs and Au(I) with porous carbon-based electrode in environmental application. The study was firstly carried out to deeply evaluate the recovery of low-concentration REEs and Au(I) in the EDL capacitance by porous structure of carbon-based electrodes.

5.2. Materials and methods

5.2.1. Materials

AC was provided as commercial resources from the Sinopharm Chemical Reagent Company. Graphene is obtained from Xiamen Knano Graphene Technology Co., Ltd. Graphite powder is purchased from shanghai Macklin Biochemical Co., Ltd. Conductive carbon black was obtained from the Cabot Corporation. Lanthanum nitrate hexahydrate ($LaN_3O_9 \cdot 6H_2O$), gadolinium nitrate hexahydrate ($GdN_3O_9 \cdot 6H_2O$), yttrium nitrate hexahydrate ($YN_3O_9 \cdot 6H_2O$) and arsenazo III were purchased from Aladdin Co., China, while others (polytetrafluoroethylene ($(C_2F_4)n$), sodium hydroxide (NaOH), nitric acid (HNO_3), potassium chloride (KCl), sodium chloride (NaCl), magnesium chloride ($MgCl_2$), calcium chloride ($CaCl_2$), lead chloride ($PbCl_2$), copper chloride ($CuCl_2$), nickel chloride ($CaCl_2$), manganese chloride ($MnCl_2$), aluminum chloride hexahydrate ($AlCl_3 \cdot 6H_2O$), iron chloride ($FeCl_3$), ammonium thiosulfate ($H_8N_2O_3S_2$), and iron chloride ($FeCl_3$)) were supplied by Sinopharm Chemical Reagent Company.

Standard chloroauric acid ($HAuCl_4$) was purchased from Well Group Scientific Ltd., USA. The deionized water used in this work was produced by Millipore Milli-Q Direct 8/16 water purification system.

5.2.2. Fabrication of carbon-based electrodes

Carbon materials (AC, graphene, graphite), conductive carbon black and polyvinylidene fluoride (dissolved in the DMA, 12.5 $mg \cdot mL^{-1}$), in an 8:1:1 mass ratio was mixed, and then the mixture was coated on titanium plate. Afterwards, the electrodes were heated at 60°C for 3 h to remove the residual organic solvent. The prepared electrodes were immerged in the deionized water for 24 h to keep shape. Finally, after drying in 60°C for 1 h, the electrodes were used in the REEs and Au(I) recovery.

5.2.3. Electro-assisted REEs and Au(I) recovery

A self-made cell with an external power was applied for carrying out REEs recovery experiments. The solution cycle was realized by a peristaltic pump at a rate of 45 rpm. At a certain time, 2.5 mL solution was extracted and filtered using 0.22 μm filter membrane. Following, the concentration of REEs filtrate was detected by a UV-vis spectrophotometer (Lambda 750S), while gold element was tested by atomic adsorption spectrophotometer (Agilent 280FS AA, America). The adsorption capacity (Q) and recovery (R) for REEs and Au(I) were calculated by the following formula. The equation difference for Au(I) adsorption capacity was without surface area of electrode because of the little influence.

$$\mathrm{Q} = (C_0 - C_t) \times \frac{(V_0 - V_t)}{\mathrm{A} \cdot \mathrm{m}} \qquad (1)$$

$$\mathrm{R} = (C_0 - C_t) \times \frac{1}{C_0} \qquad (2)$$

Where C_0 and C_t were the concentration at the initial and a certain moment, respectively, mg/L; V_0 and V_t meant the volume of reaction solution at the initial and a certain moment, respectively, L; A displayed the effective surface area of AC electrode, dm^2; m exhibited the mass used in the electrode, mg.

5.2.4. Desorption and regeneration tests

After the recovery of REEs, the carbon-based electrode was immersed in a 100 mL solution of HCl (1 M) or NH_4Cl (1 M) without an external power to desorb REEs.

2 mL solution was extracted and filtered at a certain time. The desorption capacity and efficiency were calculated by the following formula:

$$D = C_d \times \frac{1}{C_0} \times 100\% \qquad (3)$$

In which C_d was the concentration of REEs at a certain moment in the desorption experiment, mg/L.

5.2.5. Characterization

X-ray diffraction (XRD) with Cu-Kα radiation was applied on detecting the crystal structure of AC, D8 Advance, Bruker AXS, Germany. Transmission electron microscopy (TEM) was used to observe the morphology and microstructure of AC, JEM-F200 microscope, Japan. SEM was applied for investigating the morphologies of graphite and graphene, Phenom ProX G6, Netherlands. Raman was provided for studying the atomic bond structure of samples, INVIA Renishaw, England. Elemental state information was gained through X-ray photoelectron spectroscopy (XPS, Thermo Scientific K-Alpha, America). X-ray photoelectron spectroscopy was performed on the analysis of elemental composition, Thermo Scientific K-alpha, America. Distribution of pore structure was studied by the Brunauer-Emmett-Teller (BET), V-Sorb X800, China. Electrochemical characteristic of titanium plate and AC electrode including cyclic voltammetry (CV) and electrochemical impedance spectroscopy (EIS) was researched using VersaSTAT-450, PAR, America.

5.2.6. Electrochemical measurements

Electrochemical characteristic of titanium plate, AC, graphene, and graphic electrode including cyclic voltammetry (CV) and electrochemical impedance spectroscopy (EIS) was researched using VersaSTAT-450, PAR, America. A conventional three-electrode cell was applied on determining the electrochemical characteristics of titanium plate and AC electrode including cyclic voltammetry (CV) and electrochemical impedance spectroscopy (EIS) in a 1 M Na_2SO_4 or 5 ppm $Au(S_2O_3)_2^{3-}$ solutions. The three electrodes were platinum electrode (counter electrode), standard calomel electrode (reference electrode) and the titanium / AC electrode (working electrode).

5.2.7. REEs determination

The concentration of sorption was determined by UV-vis spectrophotometer.

Calibration curves were obtained as the following procedure. Firstly, a certain amount of REEs was dissolved in a 100 mL volumetric flask to obtain 2000 mg/L standard solution. After, various concentrations of REEs solution with 2 mL arsenazo III was obtained in a 25 mL colorimetric tube. The absorbance of La(III), Gd(III) and Y(III) was measured at 655 nm, 651 nm, 651 nm respectively. The calibration curves were obtained with the concentration of rare earth in the horizontal coordinate and the absorbance in the vertical coordinate.

5.3. Results and discussion

5.3.1. Characterization of carbon-based materials

Crystal structure of carbon materials, AC, graphite, and graphene was analyzed by XRD (Figure 5-1a). The peak at around 25° in AC was detected, being caused by an almost amorphous structure in graphene[47]. As for graphite and graphene, typical characteristics of two sharp peaks located at about 26.5° and 54.5°, which derived from (002) and (004) planes of graphitic structure[48,49]. Chemical bond information in carbon materials was measured based on FTIR test, as shown in Figure 5-1b. The adsorption peak at ~3440 cm^{-1} was due to the vibration (O-H) in hydroxyl groups[50]. Typical bands between 1700 and 1400 cm^{-1} were identified as characteristic of groups C=O stretching vibration in AC[51]. A situated band at 1152 cm^{-1} in AC was attributed to the C-O stretching vibration[52], and the radiation adsorption of the groups C-C=O in-plane bending vibration was present. Peaks at ~1096 and 1017 cm^{-1} demonstrated the presence of C-O functional groups[53]. In view of the provided XRD and FTIR results, the carbon materials were pure, while with hydroxyl groups.

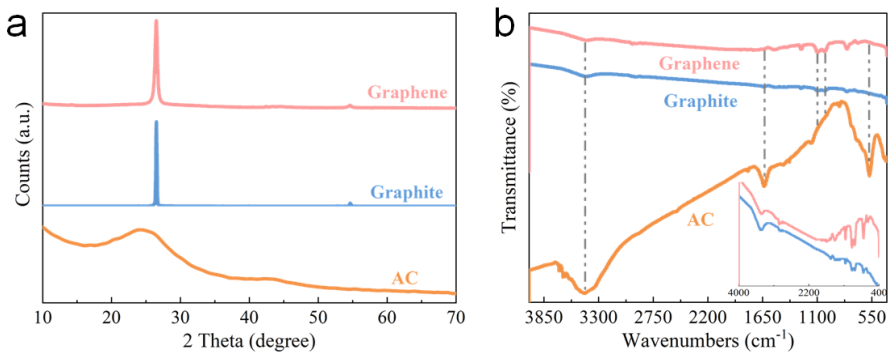

Figure 5-1. (a) XRD patterns and FTIR spectra of carbon-based materials.

The porous structure of carbon materials was evaluated from the adsorption-desorption isotherms of nitrogen by BET (Figure 5-2a). When the relative pressure was

during low value, the adsorption increased quickly, while there was hysteresis loop between 0.4 and 1.0 in the relative high pressure. The phenomenon demonstrated that coexistence of micropores and mesopores in carbon materials[54]. Enclosed area of AC was largest among the carbon materials, revealing that it had richest porous structure. For further investigating the pore structure of carbon materials, the meso- and macroporous pore size cumulation and distribution were exhibited in Figure 5-2b and 5-2c, respectively. AC possessed richest pores, and it might be very suitable for ions storage. Regarding the mesopores, most pores distribution of carbon materials was located within 50 nm, which was beneficial for the formation of porous EDL and ions storage. As for microporous structure (Figure 5-2d), the cumulative pore distribution sharply increased at the pore width between 0.75 to 1.00 nm and then slowly upper to 2.75 nm, demonstrating many micropores in AC, also the result could be directly seen through the distribution pore size (mainly located in the size range below 2 nm)[54].

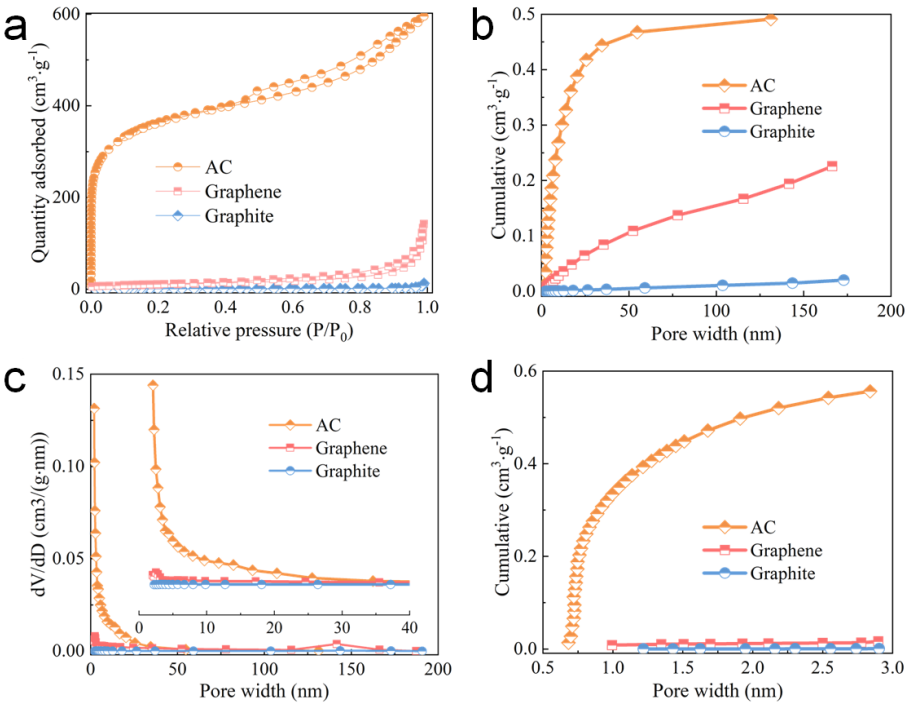

Figure 5-2. (a) Nitrogen adsorption-desorption isotherms, (b) mesopores, macropores cumulation and (c) mesopores, macropores cumulation distribution, and (d) micropores cumulation of carbon-based materials.

Morphologies and structures of carbon materials were characterized according to SEM and TEM. Graphite (Figure 5-3a) showed a scale-like and flat surface, while graphene (Figure 5-3b) displayed a rippled and crumpled structure, resulting in more reaction sites in graphene. According to the TEM image (Figure 5-3c), AC exhibited rough morphology with highly interconnected pores (yellow dotted boxes). As shown

in Figure 5-3d, pores in AC could be clearly distinguished (green dotted boxes). The selected area electron diffraction (SAED) pattern in the inset picture suggested a certain crystallinity degree of AC, which was accordant with the consequence of XRD. Furthermore, the arranged lattice fringes with spacing of 0.349 nm (Figure 5-3e) was originated from the (002) plane of graphite structure[55], which indicated the formation of graphite crystallites. Notably, a highly disordered structure (white dotted boxes) with micropores and pseudo-graphic structures in the formation of graphite crystallite (orange dotted boxes) were proved in Figure 5-3e and 5-3f[56]. Therefore, AC could be ascribed to porous graphitic carbon, and the abundant pores formed the EDL capacity for ion storage.

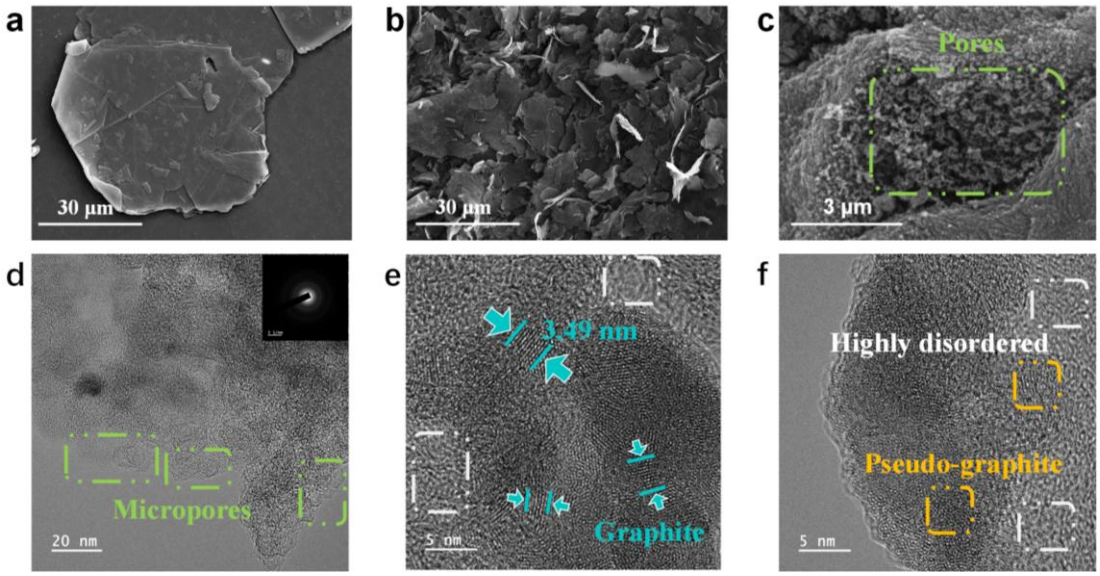

Figure 5-3. SEM images of (a) graphite, (b) graphene, and (c) AC. (d) TEM images and SAED pattern (as inset picture), (e, f) HRTEM images of AC.

XPS was performed to investigate the chemical states of carbon materials. There were strong absorption peaks in the survey spectra (Figure 5-4a), belonging to the absorption peaks of C KL1, O 1s, and C 1s, respectively, which indicates that carbon materials were mainly composed of C and O elements. Figure 5-4b revealed XPS O 1s spectra of carbon materials, and the binding energy peaks at ~531 and 533 eV were typical O 1s absorption peaks of C-O and C=O bonds, respectively. XPS C 1s spectra in Figure 5-4c showed the existence of carbon groups on the surface. Binding energy peaks at ~284, 286, 288, and 290 eV were respectively corresponded to the C–C, C-O-C, COOR, and Π-Π bond. The above results exhibited that various carbon materials possessed different functional groups on the surface.

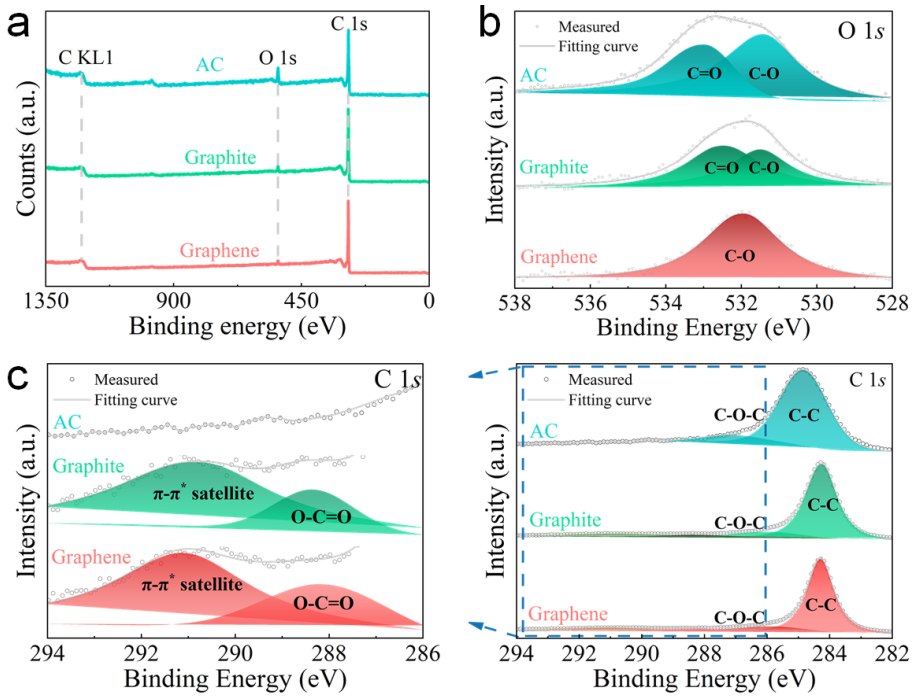

Figure 5-4. XPS (a) survey, (b) O 1*s*, and (c) C 1*s* spectra of carbon materials.

5.3.2. La(III) sorption performance evaluation

Electro-assisted La(III) sorption activity was performed on porous carbon materials, as shown in Figure 5-5a and 5-5b. Adsorption capacity and related recovery of La(III) on carbon-based electrodes increased as time elapsed. Among all the carbon-based electrodes, AC electrode owned best La(III) recovery might originate from richest pores. Also, the recovery on graphene electrode was better than that on graphite electrode. As time passed, the La(III) adsorption on AC electrode tended to balance owing to the saturation of reaction sites, while growing tendency happened on graphene and graphite electrode because of rich macropores for slow ions transfer. The maximum adsorption capacity according to simulation could achieve 342.38 mg/(g·dm^2), and corresponding recovery was ~87%. To compare with previous works, the adsorption capacity was adjusted to unified unit. From Table 5-1, the work showed great improvement in low-concentration REEs recovery. Apart from this, pseudo-first-order (Eq. 4) and pseudo-second-order kinetic model (Eq. 5)[57,58] were applied for investigating the recovery process (Table 5-2).

$$q_t = q_e \times [1 - \exp(-k_1 t)] \quad (4)$$

$$q_t = \frac{t}{(t/q_e) + (1/k_2 q_e^2)} \quad (5)$$

where q_e and q_t were the adsorbed REEs at equilibrium time and t moment (min), respectively, mg/g; k_1 and k_2 were the first- and second-order rate constants,

respectively, min^{-1}.

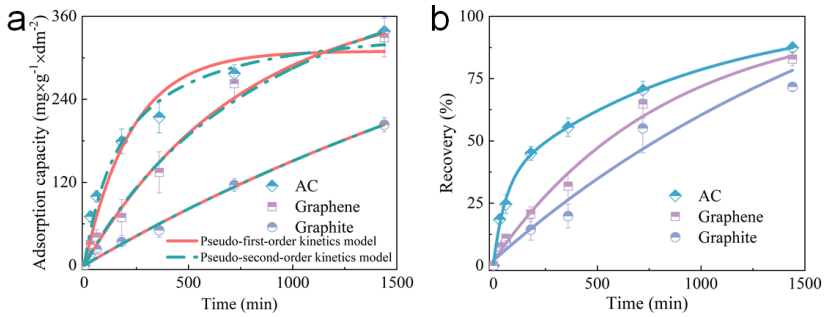

Figure 5-5. REEs recovery performance by carbon-based electrode over time: (a) adsorption capacity and (b) recovery.

Table 5-1. Comparison of La(III) adsorption capacity in the work with other literatures.

Adsorbents	Initial concentration (mg/L)	Adsorption capacity (mg/g)	Reference
carbon nanotube	100	23.23	[60]
PA-MNPs	100	18.4	[61]
Activated carbon functionalized	50	10.14	[62]
Ca−Alginate Beads	25	6.37	[63]
Carboxylated cellulose filter	28	33.7	[64]
Ca−Alginate Beads	25	6.37	[65]
Fe_3O_4/GNPs	10	3.84	[66]
AC electrodes	9.84	61.63	This work

Table 5-2. Kinetic parameters for simulating La(III) recovery by carbon-based electrodes.

	Pseudo-first-order kinetic model		Pseudo-second-order kinetic model	
	q_e (mg/(g·dm^2)	R^2	q_e (mg/(g·dm^2)	R^2
AC	309.6591	0.9512	360.0251	0.9816
Graphene	393.8837	0.9872	585.0042	0.9847
Graphite	546.2353	0.9883	986.7876	0.9883

Adsorption process on AC electrode was more inclined to pseudo-second-order

kinetic model, and it revealed chemical interaction dominated (interacted O-REEs bond) during adsorption process, resulting from rich oxygen-containing groups. Regarding graphene and graphite electrode, the situation was highly consistent with two models, exhibiting the existence of physical and chemical interactions. The effect of initial concentration on the La(III) recovery using AC electrode was investigated (Figure 5-6). With the increasing initial concentration, the adsorption capacity increased and then tended to balance due to the saturation of reaction sites. As a result, when the initial concentration was lower than 5 mg/L, the recovery reached ~100%. Following, the recovery declined as the saturation of adsorption sites. Whatever, the CEC method by AC electrode obtained more than 85% recovery as initial concentration bellowing 10 mg/L.

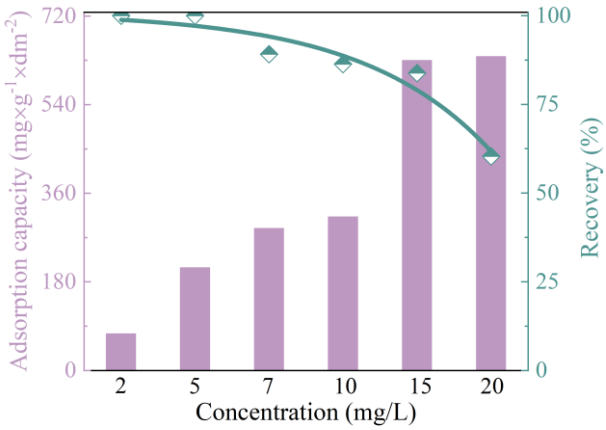

Figure 5-6. Recovery performance under various concentration by carbon-based electrode.

In Figure 5-7a and 5-7b, adsorption capacity and corresponding recovery with both and only one AC electrode (cathode or anode), and without AC electrode were showed (Table 5-3). Adsorption capacity and recovery using both AC electrodes was higher than that by only one AC electrode, which could be ascribed to the rapid and mostly planar interelectrode diffusion within the trench, rapid diffusion of analyte into the trench, and improved specificity from two applied electrode potentials. AC electrode as cathode reached better La(III) recovery performance than that as anode, because of the stronger electrostatic interaction in cathode. Without AC electrode, the adsorption capacity and recovery of La(III) via titanium plate was almost zero, indicating that there wasn't reaction between La(III) and titanium plate. When AC electrode was only used as cathode, the recovery was dominated by physical interaction, while contrast in the use of two AC electrodes, which demonstrated the existence of strong electrostatic interaction in cathode.

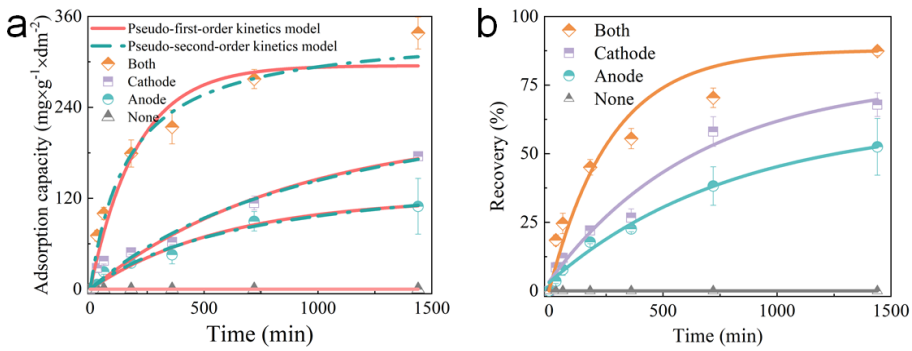

Figure 5-7. (a) Adsorption capacity and (b) recovery on both and only one carbon-based electrode (cathode or anode), and without carbon-based electrode.

Table 5-3. Kinetic parameters for simulating recovery of La(III) on both and only one carbon-based electrode (cathode or anode), and without carbon-based electrode.

	Pseudo-first-order kinetic model		Pseudo-second-order kinetic model	
AC	q_e (mg/(g·dm^2))	R^2	q_e (mg/(g·dm^2))	R^2
Both	309.6591	0.9512	360.0251	0.9816
Cathode	213.8804	0.9435	222.1278	0.9475
Anode	120.7560	0.9751	166.1236	0.9753

To unravel the interaction between La(III) and reaction sites of carbon-based electrodes, FTIR was performed after the La(III) recovery, as shown in Figure 5-8. The peaks for stretching vibration of O-H, C=O and C-O shifted after the La(III) recovery compared with the result before adsorption[59], for instance, the C-O stretching vibration was 1152 cm^{-1} after adsorption, exhibiting the interaction between La(III) and oxygen-containing groups. Because of the existence of chemical interaction of La(III) and oxygen-containing groups, AC anode would adsorb a certain amount of La(III) as well when applying both AC electrodes for recovery.

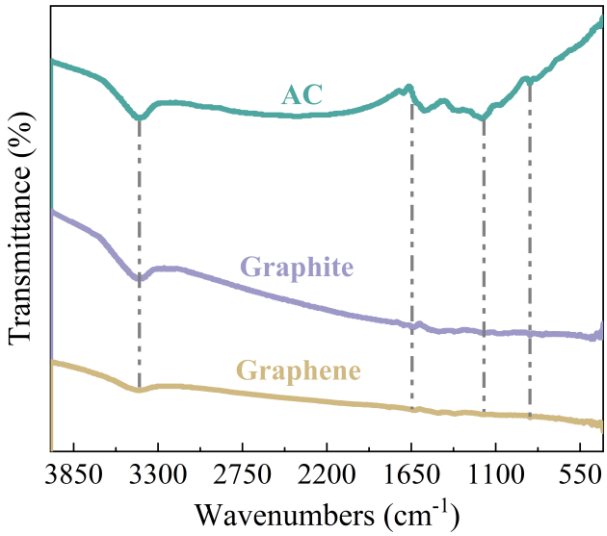

Figure 5-8. FTIR spectrum of carbon-based electrodes after La(III) recovery.

5.3.3. Interaction between La(III) and carbon-based electrodes

XPS was carried out for investigating the interaction role of oxygen species with REEs, a case of La(III), was carried out. From the survey spectra (Figure 5-9a), the peaks for La appeared on both carbon-based cathode and carbon-based anode, indicating the adsorption of La(III). The existed interaction between La(III) and carbon-based materials and flu of solution led to the happen of adsorption on anode as well. For the high resolution La 3*d* spectra (Figure 5-9b), there are four fitted peaks at ~835.45, ~838.86, ~852.38 and ~855.58 eV, corresponding to the presence of La-N and La-O coordination bond[59]. Intensity of peaks in anode was weaker than that in cathode, showing that the La(III) adsorption mainly occurred in cathode On the basis of the above reported results, the recovery of La(III) on electrode *via* physical and chemical interaction was demonstrated.

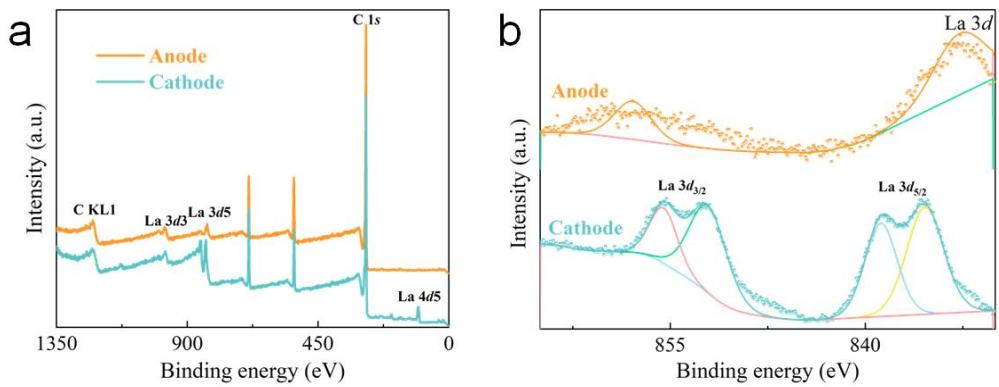

Figure 5-9. XPS (a) survey, (b) La 3*d* spectra of AC anode and cathode after La(III) recovery.

5.3.4. Extending recovery performances of Gd(III) and Y(III)

To evaluate the actual application of REEs recovery, carbon-based electrodes were applied in the recovery of medium and heavy REEs, Gd(III) and Y(III), in various concentrations. As shown in Figure 5-10a and 5-10b, adsorption capacity and recovery of Gd(III) using AC electrode was highest among carbon-based electrodes, following as graphene electrode, graphite electrode. The difference might be owing to various electrochemical properties. AC electrode could reach ~100% under initial concentration of 7 mg/L, and adsorption capacity was up to 305.87 mg/(g·dm^2). The higher concentration led to declined recovery due to saturated EDL capacity and active sites. According to SEM (Figure 5-10c) and related EDS mapping (Figure 5-10d) results, Gd(III) was recovered on carbon-based electrodes.

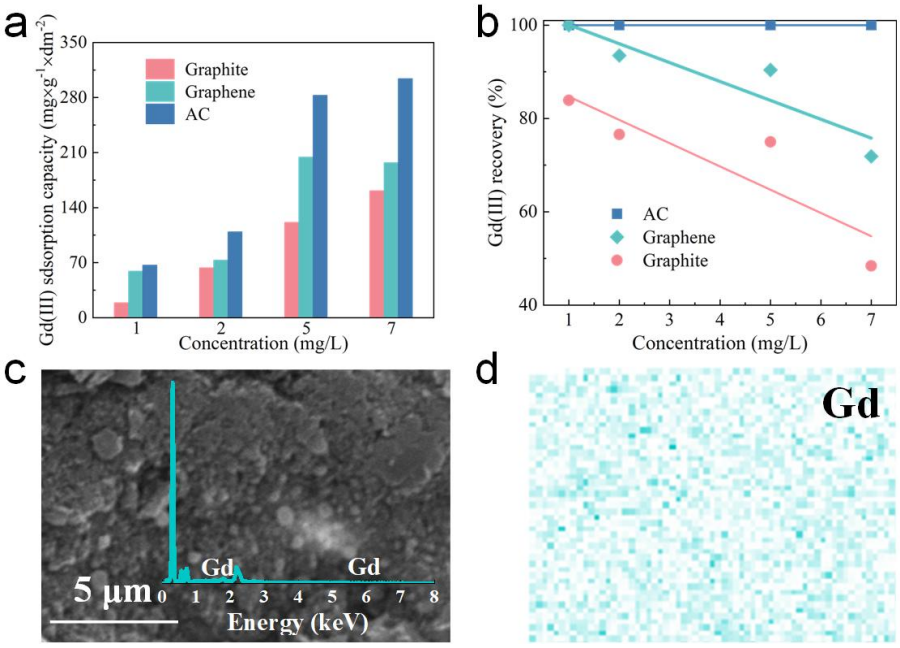

Figure 5-10. (a) Adsorption capacity and (b) recovery of low-concentration Gd(III) on carbon-based electrodes. (c) SEM morphology and (d) corresponding EDS mapping of carbon-based electrode after Gd(III) sorption.

As for Y(III), sorption ability, including adsorption capacity and recovery in Figure 5-11a and 5-11b revealed the same tendency using carbon-based electrodes, in order of AC electrode, graphene electrode and graphite electrode. Since similar physical and chemical properties of REEs, they behaved similar tendency on various carbon-based electrodes. Besides, recovery was 100% using AC electrode when the initial concentration below 2 mg/L, with 100.32 mg/(g·dm^2). After recovery, carbon-based electrode was characterized by SEM-EDS, as shown in Figure 5-11c and 5-11d. The results exhibited that the well-distributed and existence of Y elements. In all, comparing

sorption ability of La(III), Gd(III) and Y(III) using carbon-based materials, AC electrode had best sorption ability, and then graphene electrode, graphite electrode, which was related with their different electrochemical behaviors. As for various REEs sorption on same carbon-based electrode, sorption capacity and recovery from big to small were La(III), Gd(III) and Y(III), which was owing to various configuration of extra-nuclear electron and solvent ion size.

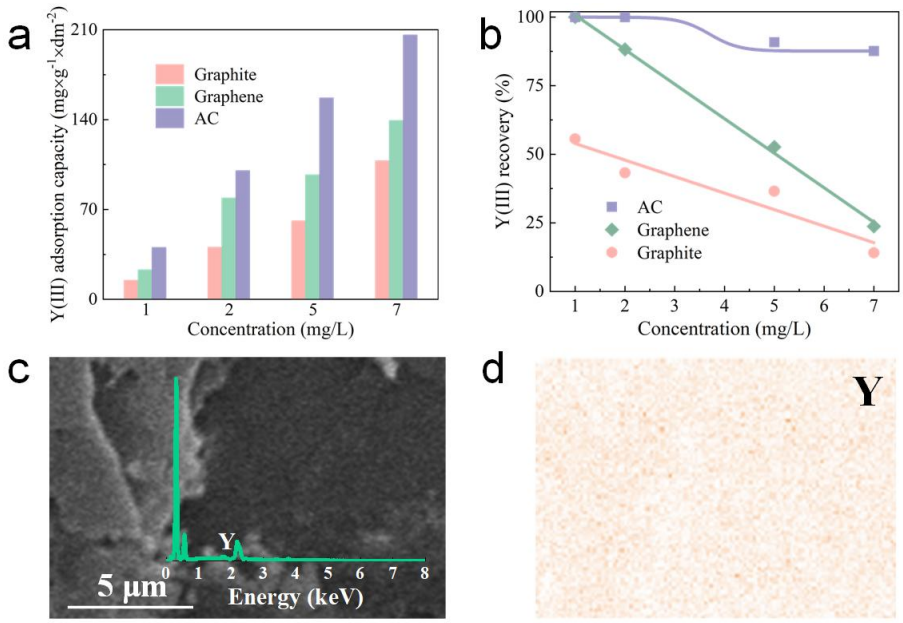

Figure 5-11. (a) Adsorption capacity and (b) recovery of low-concentration Y(III) on carbon-based electrodes. (c) SEM morphology and (d) corresponding EDS mapping of carbon-based electrode after Y(III) sorption.

5.3.5. Desorption and reuse of electrodes

Desorption studies were important for the reusability of electrode, as well as the recovery of targeted ions. Here, HCl and NH_4Cl were applied to investigate desorption ability of La(III) from carbon-based electrode. The desorption efficiency using HCl enhanced sharply and reached higher than 90% within 20 min (Figure 5-12a). As for desorption by NH_4Cl solution (Figure 5-12c), the rate for desorption was slower than that using HCl, while the desorption reached almost 100% within 120 min. In both ways for desorption, the desorbed La(III) concentration from cathode was higher than that from anode (also proved in the different color as insert picture of Fig. 8c, demonstrating that the La(III) adsorption mainly happened on cathode. The reusability of AC electrode by NH_4Cl (Figure 5-12b) was stronger than that using HCl (Figure 5-12d), because the instability of AC electrode in acid solution. After four circles, the adsorption capacity

and recovery were still at a high level compared with the initial one when NH_4Cl was applied for reusing the AC electrode. In the desorption mechanism, REE ions were relatively easily and selectively desorbed by the monovalent ions and then transferred into solution as soluble chlorides (Eq. 6-7).

$$C\text{-}La+3\ HCl=C\text{-}H_3+LaCl_3 \qquad (6)$$

$$C\text{-}La+3\ NH_4Cl=C\text{-}(NH_4)_3+LaCl_3 \qquad (7)$$

The above results presented a method for the regenerated application of CEC method by AC electrode.

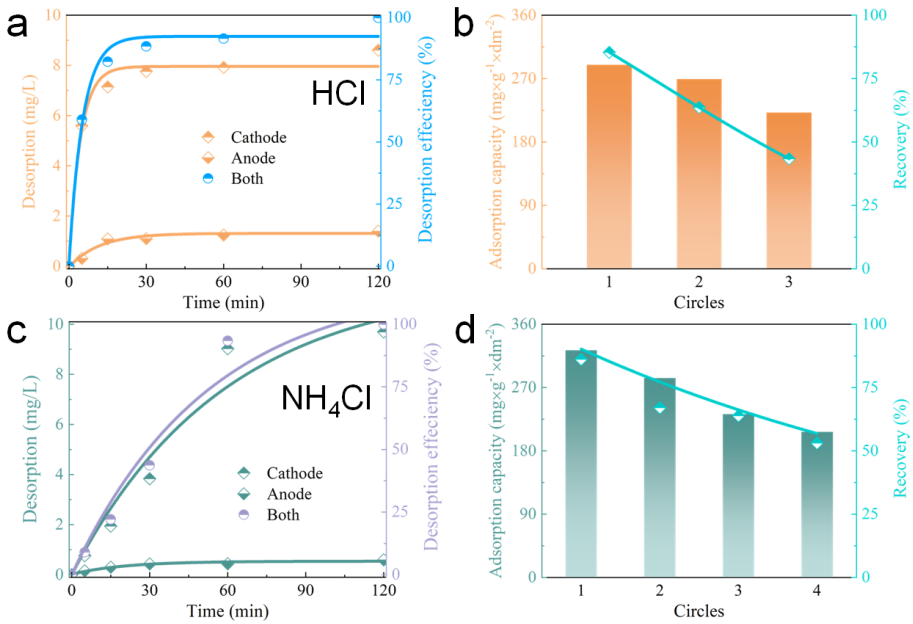

Figure 5-12. The desorption efficiency of La(III) from AC electrode using (a) HCl and (c) NH_4Cl. The reusability of AC electrode by the desorption of (b) HCl and (d) NH_4Cl.

5.3.6. Au(I) recovery from thiosulfate solutions

Application of carbon-based electrodes on Au(I) recovery from thiosulfate solutions was evaluated shown in Figure 5-13a. AC showed the biggest adsorption capacity and corresponding recovery among carbon-based electrodes, being followed by graphene and graphite electrodes. Except this, to further evaluate the application of carbon-based electrodes on Au(I) recovery, adsorption capacity and recovery were tested in a binary mixed solution (Figure 5-13b). As could be found, the adsorption capacity and recovery were minimally affected. In any event, the adsorption capacity and recovery remained at a high level.

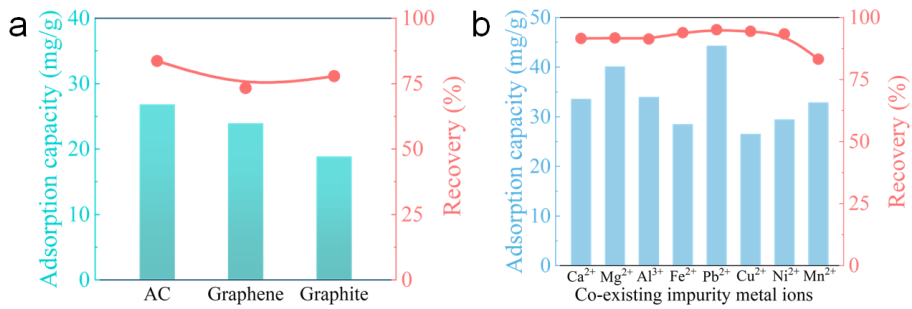

Figure 5-13. (a) Adsorption capacity and recovery of Au(I) from thiosulfate solutions by carbon-based electrodes. (b) Adsorption capacity and recovery of Au(I) from thiosulfate solutions in the presence of interferential ions.

5.3.7. Au state after recovery

XPS was carried out to study the substance after Au(I) recovery. There existed Au peaks on XPS survey (Figure 5-14a) revealed Au(I) recovery from thiosulfate solutions. No obvious changes occurred in peaks of C 1s (Figure 5-14b) and O 1s (Figure 5-14c) spectra, which demonstrated nonexistence of chemical reaction. The peaks in Au 4f spectra (Figure 5-14d) were ascribed to gold particles, indicating that the recovery state of Au(I) from thiosulfate solutions was gold metal[67]. Therefore, the above results confirmed the reduction and recovery of Au(I) from thiosulfate solutions on carbon-based electrodes.

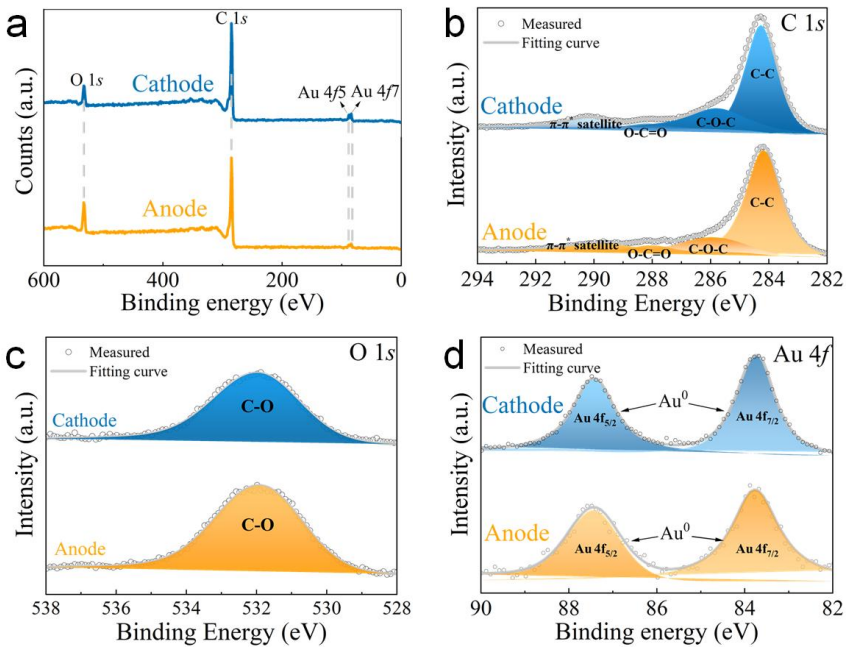

Figure 5-14. XPS (a) survey, (b) C 1*s*, (c) O 1*s*, and (d) Au 4*f* spectra of both AC electrodes after Au(I) recovery.

5.3.8. Electrochemical behaviors of carbon-based electrodes

With the aim of revealing electrochemical behaviors of carbon-based electrodes, EDLC ability was conducted. Specific capacity collected at scan rates from 5 to 100 $mV \cdot s^{-1}$ was calculated in Figure 5-15a. Note that the best capacity of carbon-based electrodes was AC, and then graphene. It can be inferred that the EDLC was closely related to pores. Sorption ability was no only related with storage, also the ion transfer originating from attraction. Ion diffusion was another non-negligible impactor in electro-assisted sorption process, and EIS was used to evaluate (Figure 5-15b). The smaller diameter of semicircle meant the lower charge transfer resistance. AC electrode had relatively lowest resistance, resulting in a best electrochemical performance for the transfer of REEs and Au(I). With richer pores, the transfer resistance was lower. Cyclic voltammetry (CV) curves of carbon-based electrodes in Au(I) solution (Figure 5-15c) were performed to find the reduction reaction and ion storage. An evident peak at negative voltage region suggests the happen of Au(I) reduction. The enclosed area is highly related with the ability ion storage and chemical reaction. As seen, AC electrode possessed the best ion capacity ability and most drastic Au(I) reduction reaction among carbon-based electrodes, and graphene electrode took second place. As well, smallest charge transfer happened on AC electrode in Au(I) recovery process (Figure 5-15d).

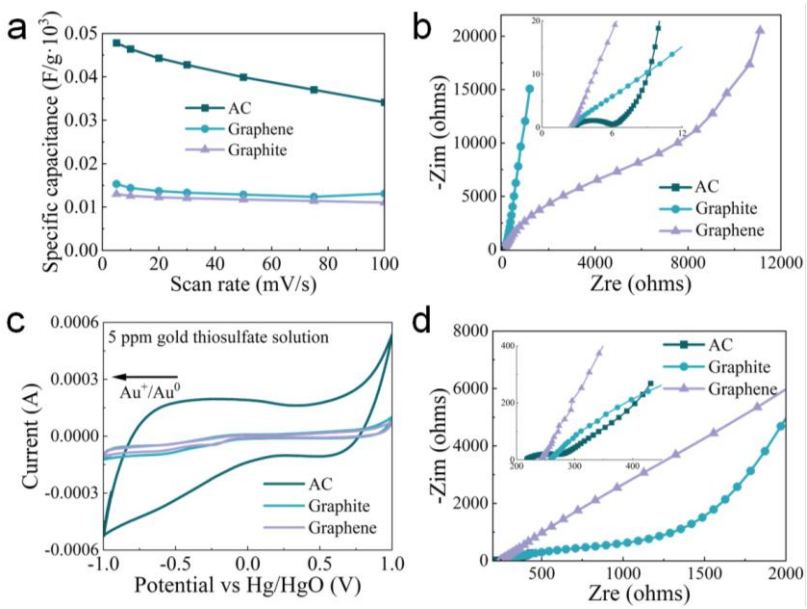

Figure 5-15. Electrochemical performances: CV curves at different scan rate for (a) AC electrode, (b) graphene electrode and (c) graphite electrode. (e) Illustration for ions storage. (d) CV curves scanned at 10 mV/s and (f) EIS for carbon-based electrodes and titanium electrode.

5.4. Conclusions

Electro-assisted recovery of REEs and Au(I) by carbon-based materials had a great potential in low concentration range. All the carbon-based materials with porous structure showed efficient recovery of REEs and Au(I). In the initial concentration of less than 5 mg/L, the recovery of La(III) was up to 100%. The adsorption capacity of La(III) for AC electrode reached 368.20 mg/(g·dm^2). Gd(III) and Y(III) recovery using AC electrode obtained ~100% under initial concentration of 7 and 2 mg/L, respectively, and the related adsorption capacity was 305.87 and 100.32 mg/(g·dm^2). Au(I) recovery approached almost 90%. The excellent recovery of REEs and Au(I) was resulted from strong EDLC and electrostatic interaction from applied voltage and chemisorption from oxygen-containing groups. Higher applied voltage and lower distance between electrodes were beneficial for the recovery. Recovery performance was highly related with pores content and oxygen-containing group. Richer pores were better for ions storage in EDL and transfer in aqueous solution. HCl and NH_4Cl were applied for desorbing REEs from carbon-based electrodes, respectively. High desorption efficiency (more than 90%) within 20 min was obtained using HCl. Total desorption was realized by NH_4Cl solution, and the structure of carbon-based electrode was almost the same. After four cycles, the adsorption capacity and recovery declined owing to the dropped materials. Interestingly, Au(I) as gold metal form was recovered on the surface of electrode. The work provided a new insight for the recovery of low-concentration REEs and Au(I) based on carbon-based electrodes.

5.5. References

(1) Hirsh, H. S.; Li, Y.; Tan, D. H. S.; Zhang, M.; Zhao, E.; Meng, Y. S. Sodium-Ion Batteries Paving the Way for Grid Energy Storage. *Adv Energy Mater* **2020**, *10* (32), 2001274. https://doi.org/10.1002/aenm.202001274.

(2) Bombelli, P.; Savanth, A.; Scarampi, A.; Rowden, S. J. L.; Green, D. H.; Erbe, A.; Årstøl, E.; Jevremovic, I.; Hohmann-Marriott, M. F.; Trasatti, S. P.; Ozer, E.; Howe, C. J. Powering a Microprocessor by Photosynthesis. *Energy Environ Sci* **2022**, *15* (6), 2529–2536. https://doi.org/10.1039/D2EE00233G.

(3) Guo, X.; Zhang, G.; Li, Q.; Xue, H.; Pang, H. Non-Noble Metal-Transition Metal Oxide Materials for Electrochemical Energy Storage. *Energy Storage Mater* **2018**, *15*, 171–201. https://doi.org/10.1016/j.ensm.2018.04.002.

(4) Ji, S. F.; Qu, Y.; Wang, T.; Chen, Y. J.; Wang, G. F.; Li, X.; Dong, J. C.; Chen, Q. Y.; Zhang, W.

Y.; Zhang, Z. D.; Liang, S. Y.; Yu, R.; Wang, Y.; Wang, D. S.; Li, Y. D. Rare-Earth Single Erbium Atoms for Enhanced Photocatalytic CO_2 Reduction. *Angewandte Chemie International Edition* **2020**, *59* (26), 10651–10657. https://doi.org/10.1002/anie.202003623.

(5) Zheng, B. Z.; Fan, J. Y.; Chen, B.; Qin, X.; Wang, J.; Wang, F.; Deng, R. R.; Liu, X. G. Rare-Earth Doping in Nanostructured Inorganic Materials. *Chem Rev* **2022**, *122* (6), 5519–5603. https://doi.org/10.1021/acs.chemrev.1c00644.

(6) Ryoo, R.; Kim, J.; Jo, C.; Han, S. W.; Kim, J.-C.; Park, H.; Han, J.; Shin, H. S.; Shin, J. W. Rare-Earth–Platinum Alloy Nanoparticles in Mesoporous Zeolite for Catalysis. *Nature* **2020**, *585* (7824), 221–224. https://doi.org/10.1038/s41586-020-2671-4.

(7) Chen, Z.; Yang, W.; Wu, Y.; Zhang, C.; Luo, J.; Chen, C.; Li, Y. Atomic Iron on Mesoporous N-Doped Carbon to Achieve Dehydrogenation Reaction at Room Temperature. *Nano Res* **2020**, *13* (11), 3075–3081. https://doi.org/10.1007/s12274-020-2975-6.

(8) Ran, J.; Gao, G.; Li, F.-T.; Ma, T.-Y.; Du, A.; Qiao, S.-Z. Ti_3C_2 MXene Co-Catalyst on Metal Sulfide Photo-Absorbers for Enhanced Visible-Light Photocatalytic Hydrogen Production. *Nat Commun* **2017**, *8* (1), 13907. https://doi.org/10.1038/ncomms13907.

(9) Wang, D.; Li, X.; Li, H.; Li, L.; Hong, X.; Peng, Q.; Li, Y. Semiconductor–Noble Metal Hybrid Nanomaterials with Controlled Structures. *J. Mater. Chem. A* **2013**, *1* (5), 1587–1590. https://doi.org/10.1039/C2TA00765G.

(10) Zhong, Y.; Ma, Z.; Zhu, S.; Yue, J.; Zhang, M.; Antaris, A. L.; Yuan, J.; Cui, R.; Wan, H.; Zhou, Y.; Wang, W.; Huang, N. F.; Luo, J.; Hu, Z.; Dai, H. Boosting the Down-Shifting Luminescence of Rare-Earth Nanocrystals for Biological Imaging beyond 1500 Nm. *Nat Commun* **2017**, *8* (1), 737. https://doi.org/10.1038/s41467-017-00917-6.

(11) Lin, R.; Li, F.; Liu, S.; Qi, X.; Zhang, J.; Chen, X. A Noble-Metal-Free Porous Coordination Framework with Exceptional Sensing Efficiency for Oxygen. *Angewandte Chemie International Edition* **2013**, *52* (50), 13429–13433. https://doi.org/10.1002/anie.201307217.

(12) Borst, A. M.; Smith, M. P.; Finch, A. A.; Estrade, G.; Villanova-de-Benavent, C.; Nason, P.; Marquis, E.; Horsburgh, N. J.; Goodenough, K. M.; Xu, C.; Kynický, J.; Geraki, K. Adsorption of Rare Earth Elements in Regolith-Hosted Clay Deposits. *Nat Commun* **2020**, *11* (1), 4386. https://doi.org/10.1038/s41467-020-17801-5.

(13) Pan, J.; Zhou, C.; Tang, M.; Cao, S.; Liu, C.; Zhang, N.; Wen, M.; Luo, Y.; Hu, T.; Ji, W. Study on the Modes of Occurrence of Rare Earth Elements in Coal Fly Ash by Statistics and a Sequential Chemical Extraction Procedure. *Fuel* **2019**, *237*, 555–565. https://doi.org/10.1016/j.fuel.2018.09.139.

(14) Whitehead, J. A.; Lawrance, G. A.; McCluskey, A. 'Green' Leaching: Recyclable and Selective Leaching of Gold-Bearing Ore in an Ionic Liquid. *Green Chemistry* **2004**, *6* (7), 313–315.

https://doi.org/10.1039/B406148A.

(15) Kegl, T.; Kosak, A.; Lobnik, A.; Novak, Z.; Kralj, A. K.; Ban, I. Adsorption of Rare Earth Metals from Wastewater by Nanomaterials: A Review. *J Hazard Mater* **2020**, *386*. https://doi.org/10.1016/j.jhazmat.2019.121632.

(16) Lie, J.; Liu, J.-C. Selective Recovery of Rare Earth Elements (REEs) from Spent NiMH Batteries by Two-Stage Acid Leaching. *J Environ Chem Eng* **2021**, *9* (5), 106084. https://doi.org/10.1016/j.jece.2021.106084.

(17) Meng, Q.; Yan, X.; Li, G. Eco-Friendly and Reagent Recyclable Gold Extraction by Iodination Leaching-Electrodeposition Recovery. *J Clean Prod* **2021**, *323*, 129115. https://doi.org/10.1016/J.JCLEPRO.2021.129115.

(18) Ramasamy, D. L.; Porada, S.; Sillanpää, M. Marine Algae: A Promising Resource for the Selective Recovery of Scandium and Rare Earth Elements from Aqueous Systems. *Chemical Engineering Journal* **2019**, *371*, 759–768. https://doi.org/10.1016/J.CEJ.2019.04.106.

(19) Omodara, L.; Pitkäaho, S.; Turpeinen, E. M.; Saavalainen, P.; Oravisjärvi, K.; Keiski, R. L. Recycling and Substitution of Light Rare Earth Elements, Cerium, Lanthanum, Neodymium, and Praseodymium from End-of-Life Applications - A Review. *J Clean Prod* **2019**, *236*, 117573. https://doi.org/10.1016/J.JCLEPRO.2019.07.048.

(20) Zhang, W.; Honaker, R. Characterization and Recovery of Rare Earth Elements and Other Critical Metals (Co, Cr, Li, Mn, Sr, and V) from the Calcination Products of a Coal Refuse Sample. *Fuel* **2020**, *267*, 117236. https://doi.org/10.1016/j.fuel.2020.117236.

(21) Zhang, M.; Peng, X.; Su, J.; Yang, Z.; Zeb, S.; Li, L.; Xu, C.; Zhao, Y.; Sun, G.; Cui, Y. Highly Efficient Extraction Separation of La^{3+} and Ce^{3+} with N, N, N′, N′-Tetraisobutyl-3-Oxadiglycolamide from Mixed REEs. *Sep Purif Technol* **2021**, *258*, 118012. https://doi.org/10.1016/j.seppur.2020.118012.

(22) Mu, R.; Chen, J.; Zou, D.; Li, K.; Li, D. Liquid-Liquid Extraction and Recovery of Cerium(IV) and Phosphorus from Sulfuric Acid Solution Using Cyanex 923. *Sep Purif Technol* **2019**, *209*, 351–358. https://doi.org/10.1016/j.seppur.2018.07.008.

(23) Lu, Y.; Song, Q.; Xu, Z. Integrated Technology for Recovering Au from Waste Memory Module by Chlorination Process: Selective Leaching, Extraction, and Distillation. *J Clean Prod* **2017**, *161*, 30–39. https://doi.org/10.1016/j.jclepro.2017.05.033.

(24) El Ouardi, Y.; Virolainen, S.; Massima Mouele, E. S.; Laatikainen, M.; Repo, E.; Laatikainen, K. The Recent Progress of Ion Exchange for the Separation of Rare Earths from Secondary Resources – A Review. *Hydrometallurgy* **2023**, *218*, 106047. https://doi.org/10.1016/j.hydromet.2023.106047.

(25) Hermassi, M.; Granados, M.; Valderrama, C.; Ayora, C.; Cortina, J. L. Recovery of Rare Earth

Elements from Acidic Mine Waters: An Unknown Secondary Resource. *Science of The Total Environment* **2022**, *810*, 152258. https://doi.org/10.1016/j.scitotenv.2021.152258.

(26) Naushad, M.; Mittal, A.; Rathore, M.; Gupta, V. Ion-Exchange Kinetic Studies for Cd(II), Co(II), Cu(II), and Pb(II) Metal Ions over a Composite Cation Exchanger. *Desalination Water Treat* **2015**, *54* (10), 2883–2890. https://doi.org/10.1080/19443994.2014.904823.

(27) Liu, Z. S.; Zhou, H. P.; Li, W. Q.; Luo, X. P.; Wang, J. L.; Liu, F. P. Separation and Coextraction of REEs and Fe from NdFeB Sludge by Co-Leaching and Stepwise Precipitation. *Sep Purif Technol* **2022**, *282*. https://doi.org/10.1016/j.seppur.2021.119795.

(28) Binnemans, K.; Jones, P. T.; Blanpain, B.; Van Gerven, T.; Yang, Y.; Walton, A.; Buchert, M. Recycling of Rare Earths: A Critical Review. *J Clean Prod* **2013**, *51*, 1–22. https://doi.org/https://doi.org/10.1016/j.jclepro.2012.12.037.

(29) Trinh, H. B.; Lee, J.; Kim, S.; Kim, J. Recovery of Cerium from Spent Autocatalyst by Sulfatizing–Leaching–Precipitation Process. *ACS Sustain Chem Eng* **2020**, *8* (41), 15630–15639. https://doi.org/10.1021/acssuschemeng.0c05136.

(30) Li, D. Development Course of Separating Rare Earths with Acid Phosphorus Extractants: A Critical Review. *Journal of Rare Earths* **2019**, *37* (5), 468–486. https://doi.org/https://doi.org/10.1016/j.jre.2018.07.016.

(31) Yang, X.; Debeli, D. K.; Shan, G.; Pan, P. Selective Adsorption and High Recovery of La3+ Using Graphene Oxide/Poly (N-Isopropyl Acrylamide-Maleic Acid) Cryogel. *Chemical Engineering Journal* **2020**, *379*, 122335. https://doi.org/10.1016/j.cej.2019.122335.

(32) Liu, T.; Chen, J. Extraction and Separation of Heavy Rare Earth Elements: A Review. *Sep Purif Technol* **2021**, *276*, 119263. https://doi.org/10.1016/j.seppur.2021.119263.

(33) Senanayake, G. A Surface Adsorption/Reaction Mechanism for Gold Oxidation by Copper(II) in Ammoniacal Thiosulfate Solutions. *J Colloid Interface Sci* **2005**, *286* (1), 253–257. https://doi.org/10.1016/j.jcis.2004.12.041.

(34) Jeffrey, M. I.; Hewitt, D. M.; Dai, X.; Brunt, S. D. Ion Exchange Adsorption and Elution for Recovering Gold Thiosulfate from Leach Solutions. *Hydrometallurgy* **2010**, *100* (3–4), 136–143. https://doi.org/10.1016/j.hydromet.2009.11.003.

(35) Hamza, M. F.; Abdellah, W. M.; Zaki, D. I.; Wei, Y. Z.; Althumayri, K.; Brostow, W.; Hamad, N. A. A Phosphonic Functionalized Biopolymer for the Sorption of Lanthanum (III) and Application in the Recovery of Rare Earth Elements. *Sustainability* **2023**, *15* (3). https://doi.org/10.3390/su15032843.

(36) Su, J.; Guo, X.; Gao, Y.; Wu, S.; Xu, R.; Sun, X. Recovery of Thorium and Rare Earths from Leachate of Ion-Absorbed Rare Earth Radioactive Residues with N1923 and Cyanex® 572. *Journal of Rare Earths* **2021**, *39* (10), 1273–1281. https://doi.org/10.1016/j.jre.2020.09.005.

(37) Modi, P.; Jamal, A.; Varshney, R.; Rahi, I. C.; Siddiqui, M. A. Rare Earth Elements Mobility, Leaching and Recovery by Different Chemicals Treatment on Coal Samples and Calcined Samples of Sohagpur Coalfield, Madhya Pradesh, India. *International Journal of Coal Preparation and Utilization* **2023**, *43* (1), 148–168. https://doi.org/10.1080/19392699.2022.2031171.

(38) Zhan, W.; Yuan, Y.; Yang, B.; Jia, F.; Song, S. Construction of MoS_2 Nano-Heterojunction via ZnS Doping for Enhancing in-Situ Photocatalytic Reduction of Gold Thiosulfate Complex. *Chemical Engineering Journal* **2020**, *394*, 124866. https://doi.org/10.1016/j.cej.2020.124866.

(39) Mao, M. L.; Yan, T. T.; Shen, J. J.; Zhang, J. P.; Zhang, D. S. Capacitive Removal of Heavy Metal Ions from Wastewater via an Electro-Adsorption and Electro-Reaction Coupling Process. *Environ Sci Technol* **2021**, *55* (5), 3333–3340. https://doi.org/10.1021/acs.est.0c07849.

(40) Zhan, W.; Yuan, Y.; Zhang, X.; Liang, Y.; Song, S.; de Jesús Martínez-López, M.; Arauz-Lara, J. L.; Jia, F. Efficient and Selective Lead(II) Removal within a Wide Concentration Range through Chemisorption and Electrosorption Coupling Process via Defective MoS2 Electrode. *Sep Purif Technol* **2024**, *329*, 125183. https://doi.org/10.1016/j.seppur.2023.125183.

(41) Liu, Y.; Deng, Y.-Y.; Zhang, Q.; Liu, H. Overview of Recent Developments of Resource Recovery from Wastewater via Electrochemistry-Based Technologies. *Science of The Total Environment* **2021**, *757*, 143901. https://doi.org/10.1016/j.scitotenv.2020.143901.

(42) Campeau, D.; Rayo, D. F. L.; Mansour, A.; Muratov, K.; Gagosz, F. Gold-Catalyzed Reactions of Specially Activated Alkynes, Allenes, and Alkenes. *Chem Rev* **2021**, *121* (14), 8756–8867. https://doi.org/10.1021/acs.chemrev.0c00788.

(43) Chaisiwamongkhol, K.; Batchelor-McAuley, C.; Sokolov, S. V.; Holter, J.; Young, N. P.; Compton, R. G. Optimising Carbon Electrode Materials for Adsorptive Stripping Voltammetry. *Appl Mater Today* **2017**, *7*, 60–66. https://doi.org/10.1016/j.apmt.2017.02.003.

(44) Zhao, F.; Chen, S.; Xiang, H.; Gao, T.; Wang, D.; Wei, D.; Sillanpää, M.; Ke, Y.; Tang, C.-J. Selectively Capacitive Recovery of Rare Earth Elements from Aqueous Solution onto Lewis Base Sites of Pyrrolic-N Doped Activated Carbon Electrodes. *Carbon N Y* **2022**, *197*, 282–291. https://doi.org/10.1016/j.carbon.2022.06.033.

(45) Wang, L.; Gao, Y.; Chai, Y.; Sun, X. Recovery of Rare Earth by Electro-Sorption with Sodium Diphenylamine Sulfonate Modified Activated Carbon Electrode. *Sep Purif Technol* **2022**, *292*, 121005. https://doi.org/10.1016/j.seppur.2022.121005.

(46) Sun, K.; Mao, S.; Zhan, W.; Liu, C.; Jia, F.; Song, S. In-Situ Reduction of $Au(S_2O_3)_2^{3-}$ for Efficient Recovery of Gold with Magnetically Separable Shell-Core Structured $MoS_2@Fe_3O_4$ Composite. *Hydrometallurgy* **2020**, *19*, 105514. https://doi.org/10.1016/j.hydromet.2020.105514.

(47) Iannicelli-Zubiani, E. M.; Stampino, P. G.; Cristiani, C.; Dotelli, G. Enhanced Lanthanum Adsorption by Amine Modified Activated Carbon. *Chemical Engineering* **2018**, *341*, 75–82.

https://doi.org/10.1016/j.cej.2018.01.154.

(48) Liu, D.; Yang, Z.; Li, W.; Qiu, S.; Luo, Y. Electrochemical Intercalation of Potassium into Graphite in KF Melt. *Electrochim Acta* **2010**, *55* (3), 1013–1018. https://doi.org/10.1016/j.electacta.2009.09.072.

(49) Guo, J.; Chen, Z.; El-Bahy, Z. M.; Liu, H.; Abo-Dief, H. M.; Abdul, W.; Abualnaja, K. M.; Alanazi, A. K.; Zhang, P.; Huang, M.; Hu, G.; Zhu, J. Tunable Negative Dielectric Properties of Magnetic $CoFe_2O_4$/Graphite-Polypyrrole Metacomposites. *Adv Compos Hybrid Mater* **2022**, *5* (2), 899–906. https://doi.org/10.1007/s42114-022-00485-4.

(50) Macias-Garcia, A.; Corzo, M. G.; Dominguez, M. A.; Franco, M. A.; Naharro, J. M. Study of the Adsorption and Electroadsorption Process of Cu (II) Ions within Thermally and Chemically Modified Activated Carbon. *J Hazard Mater* **2017**, *328*, 46–55. https://doi.org/10.1016/j.jhazmat.2016.11.036.

(51) Bleda-Martinez, M. J.; Macia-Agullo, J. A.; Lozano-Castello, D.; Morallon, E.; Cazorla-Amoros, D.; Linares-Solano, A. Role of Surface Chemistry on Electric Double Layer Capacitance of Carbon Materials. *Carbon N Y* **2005**, *43* (13), 2677–2684. https://doi.org/10.1016/j.carbon.2005.05.027.

(52) Chen, Q. Study on the Adsorption of Lanthanum(III) from Aqueous Solution by Bamboo Charcoal. *Journal of Rare Earths* **2010**, *28*, 125–131. https://doi.org/10.1016/S1002-0721(10)60272-4.

(53) Pingale, A. D.; Owhal, A.; Katarkar, A. S.; Belgamwar, S. U.; Rathore, J. S. Facile Synthesis of Graphene by Ultrasonic-Assisted Electrochemical Exfoliation of Graphite. *Mater Today Proc* **2021**, *44*, 467–472. https://doi.org/10.1016/j.matpr.2020.10.045.

(54) Yao, Y. H.; Huang, G. X.; Liu, Y. B.; Liu, Y.; Li, Y. Y.; Han, G. X.; Xing, B. L.; Liu, Q. R.; Jia, J. B.; Zhang, C. X. Facile Synthesis of B/N Co-Doped Porous Carbon Nanosheets with High Heteroatom Content and Electrical Conductivity for Excellent-Performance Supercapacitors. *Appl Surf Sci* **2022**, *580*. https://doi.org/10.1016/j.apsusc.2021.152236.

(55) Yao, Y. H.; Huang, G. X.; Liu, Y.; Li, Y. Y.; Han, G. X.; Kang, W. W.; Xing, B. L.; Liu, Q. R.; Jia, J. B.; Zhang, C. X. Microstructure Modification of Porous Carbon Induced by Low-Dosage Manganese Nitrate for High-Performance Supercapacitor Electrode. *Electrochim Acta* **2022**, *408*. https://doi.org/10.1016/j.electacta.2022.139928.

(56) Liu, Y. B.; Huang, G. X.; Li, Y. Y.; Yao, Y. H.; Liu, Q. R.; Xing, B. L.; Jia, J. B.; Zhang, C. X. Structural Evolution of Porous Graphitic Carbon Nanosheets Based on Quinonyl Decomposition for Supercapacitor Electrodes. *Appl Surf Sci* **2021**, *537*. https://doi.org/10.1016/j.apsusc.2020.147824.

(57) Zhan, W.; Jia, F.; Yuan, Y.; Liu, C.; Sun, K.; Yang, B.; Song, S. Controllable Incorporation of

Oxygen in MoS_2 for Efficient Adsorption of Hg^{2+} in Aqueous Solutions. *J Hazard Mater* **2020**, *384*, 121382. https://doi.org/10.1016/j.jhazmat.2019.121382.

(58) Jia, F.; Wang, Q.; Wu, J.; Li, Y.; Song, S. Two-Dimensional Molybdenum Disulfide as a Superb Adsorbent for Removing Hg^{2+} from Water. *ACS Sustain Chem Eng* **2017**, *5* (8), 7410–7419. https://doi.org/10.1021/acssuschemeng.7b01880.

(59) Zhao, F. P.; Repo, E.; Song, Y.; Yin, D. L.; Ben Hammouda, S.; Chen, L.; Kalliola, S.; Tang, J. T.; Tam, K. C.; Sillanpaa, M. Polyethylenimine-Cross-Linked Cellulose Nanocrystals for Highly Efficient Recovery of Rare Earth Elements from Water and a Mechanism Study. *Green Chemistry* **2017**, *19* (20), 4816–4828. https://doi.org/10.1039/c7gc01770g.

(60) Huang, L.; Liu, L.; Huang, W.; Zhao, B.; Shen, Z.; Bao, Y.; Znad, H. Recovery of Lanthanum Cations by Functionalized Magnetic Multi-Walled Carbon Nanotube Bundles. *RSC Adv* **2021**, *11* (8), 4751–4759. https://doi.org/10.1039/D0RA09902C.

(61) Gaete, J.; Molina, L.; Valenzuela, F.; Basualto, C. Recovery of Lanthanum, Praseodymium and Samarium by Adsorption Using Magnetic Nanoparticles Functionalized with a Phosphonic Group. *Hydrometallurgy* **2021**, *203*, 105698. https://doi.org/10.1016/j.hydromet.2021.105698.

(62) Awwad, N. S.; Gad, H. M. H.; Ahmad, M. I.; Aly, H. F. Sorption of Lanthanum and Erbium from Aqueous Solution by Activated Carbon Prepared from Rice Husk. *Colloids Surf B Biointerfaces* **2010**, *81* (2), 593–599. https://doi.org/10.1016/j.colsurfb.2010.08.002.

(63) Song, D.; Park, S.-J.; Kang, H. W.; Park, S. Bin; Han, J.-I. Recovery of Lithium(I), Strontium(II), and Lanthanum(III) Using Ca–Alginate Beads. *J Chem Eng Data* **2013**, *58* (9), 2455–2464. https://doi.org/10.1021/je400317v.

(64) Li, C.; Ma, H.; Venkateswaran, S.; Hsiao, B. S. Sustainable Carboxylated Cellulose Filters for Efficient Removal and Recovery of Lanthanum. *Environ Res* **2020**, *188*, 109685. https://doi.org/10.1016/j.envres.2020.109685.

(65) Afonso, E. L.; Carvalho, L.; Fateixa, S.; Amorim, C. O.; Amaral, V. S.; Vale, C.; Pereira, E.; Silva, C. M.; Trindade, T.; Lopes, C. B. Can Contaminated Waters or Wastewater Be Alternative Sources for Technology-Critical Elements? The Case of Removal and Recovery of Lanthanides. *J Hazard Mater* **2019**, *380*. https://doi.org/10.1016/J.JHAZMAT.2019.120845.

(66) Song, D.; Park, S. J.; Kang, H. W.; Park, S. Bin; Han, J. I. Recovery of Lithium(I), Strontium(II), and Lanthanum(III) Using Ca-Alginate Beads. *J Chem Eng Data* **2013**, *58* (9), 2455–2464. https://doi.org/10.1021/JE400317V.

(67) Zhan, W.; Yuan, Y.; Yao, X.; Yang, B.; Jia, F.; Lin, C.; Arauz-Lara, J. L.; Song, S. Efficient Recovery of Gold(I) from Thiosulfate Solutions through Photocatalytic Reduction with Mn(II)-Doped MoS_2. *ACS Sustain Chem Eng* **2021**, *9* (35), 11681–11690. https://doi.org/10.1021/acssuschemeng.1c02160.

Chapter VI. Efficient electroreduction recovery of low-concentration $Au(S_2O_3)_2^{3-}$ via walnut shell charcoal electrodes

6.1. Introduction

As a valuable metal, gold has wide applications with enormous significance in economy[1], electronics[2], automobiles[3], and currecy[4]. Cyanide leaching is a well-established method for extracting gold from ores[5,6], which occupies a dominant position in industry[7]. Over time, there has been an evolution in the processes used for extracting gold as world develops[8,9], with a focus on economic efficiency and environmental sustainability[10,11]. Besides, grown as continuous exploitation of rich gold ores, most existing gold deposits have low-grade characteristics[12]. The classical cyanide leaching method hardly extracts gold from refractory ore, such as gold ore containing carbon[13]. Moreover, this cyanide leaching strategy has other drawbacks, such as high toxicity[14] and high energy consumption[15], which would damage the environment[16]. Thus, developing an alternative to cyanide leaching for actual applications is urgently needed.

Thiosulfate leaching is one of the most promising methods for industrial applications among cyanide-free leaching methods, including the halogen leaching method[17], thiourea leaching method[18,19], and thiocyanate leaching method[20,21]. Due to its environmental friendliness and great selectivity in gold extraction[22–24], thiosulfate is an effective complexing agent that enhances the solubility and recovery of metals because of its high selectivity and ability to resist interference from impurity ions; thus, it has potential in leaching gold mines with low-grade characteristics, especially gold ores containing carbon[25,26]. Moreover, because of the inorganic salt property of thiosulfate, the environmental impact of using thiosulfate leaching is minimal[27,28]. Nevertheless, the application of the thiosulfate leaching method for low-concentration gold thiosulfate complex ($Au(S_2O_3)_2^{3-}$) recovery from leaching solutions is difficult.

Currently, methods for $Au(S_2O_3)_2^{3-}$ recovery from leaching solutions are precipitation[29], solvent extraction[30], adsorption[31], and electrodeposition[32]. The product obtained via the displacement precipitation process contains impurities and has a low grade. Solvent extraction is an expensive process that requires a significant number of organic solvents and strict control over the reaction conditions, resulting in increased manufacturing costs[33]. The adsorption method is a simple and cost-effective technique that facilitates the interaction between ions and materials[34]. However, the process of

adsorption may encounter issues such as inadequate or excessive adsorption, which can lead to a reduction in the amount of recovered gold[35]. The electrodeposition method allows the migration and reduction of ions in solution, but the recovery of $Au(S_2O_3)_2^{3-}$, particularly at low concentrations, is inadequate[36], possibly owing to insufficient force.

Considering that enhanced interaction between electrode and $Au(S_2O_3)_2^{3-}$ could be improved through applying materials, combining the advantages of adsorption and electrodeposition could be adopted for realizing efficient recovery of $Au(S_2O_3)_2^{3-}$ as well as reduction[37,38]. When the material is introduced, the attractive force between targeted ions and material would be greatly enhanced[39], thus strengthening the migration of $Au(S_2O_3)_2^{3-}$ in solutions and the reaction of $Au(S_2O_3)_2^{3-}$ on the electrode. Electroreduction is achieved by coating materials on traditional titanium (Ti) plates to recover low-concentration $Au(S_2O_3)_2^{3-}$ from aqueous solutions. The electroreduction method has been applied in metal ion recovery40, such as Cr(VI)[41], Bi(III)[42], and Zn(II)[43], achieving simultaneous recovery and reduction. Herein, this approach could solve the problem of low-concentration $Au(S_2O_3)_2^{3-}$ recovery.

Charcoal has the merits of a large specific surface area and rich oxygen-containing functional groups, which provide sufficient reactive sites with $Au(S_2O_3)_2^{3-}$[44,45]. Walnut shells could be converted into biochar with high adsorption properties through a specific preparation process[46]. They are widely available and cost-effective, providing a rich source of raw materials for biochar production, especially in Chin[47]. Walnut shell charcoal (WSC) has been proven that it can be utilized not only for adsorbing metal ions but also as a catalyst carrier or electrode material[48]. A titanium (Ti) plate with high conductivity[49] and good stability[50] can be applied as the substrate for coating charcoal materials to prepare the electrodes. In addition, Activation is a common way to tune micropore structure of WSC. Thus, we proposed activation method to enrich micropore structure of WSC for efficient electro reduction-recovery of low-concentration $Au(S_2O_3)_2^{3-}$. In this work, electroreduction using the WSC electrode is proposed to achieve simultaneous efficient recovery of low-concentration $Au(S_2O_3)_2^{3-}$ and reduction.

6.2. Materials and methods

6.2.1. Materials

Walnuts were bought from Zhiyin Store, Wuhan Province, China. Standard chloroauric acid ($HAuCl_4$, 1000 $mg \cdot L^{-1}$) was purchased from Well Group Scientific

Ltd., USA. Ammonium thiosulfate (98wt%) was obtained from Sigma-Aldrich (Shanghai, China). Potassium hydroxide (KOH), sodium hydroxide (NaOH), sodium sulfate (Na_2SO_4), and dimethylacetamide (DMA) (12.5 mg·mL^{-1}) were obtained from Sinopharm Chemical Reagent Co., Ltd. (Shanghai, China). Vinylidene fluoride was procured from Alfa Aesar (China) Chemicals Co., Ltd. Ammonium thiosulfate ($(NH_4)_2S_2O_3$) was purchased from Aladdin Co., China. Conductive carbon black was obtained from American Cabot, while carbon black was acquired from Suzhou Sinero Technology Co., Ltd. (China). Deionized water was produced by Millipore SAS (France) with 18.2 MΩ·cm.

6.2.2. Preparation of WSC

Walnut shells were crushed into powder using a crusher and screened with a 200-mesh sieve (about 0.075 mm) as the original materials. Then, the powder was placed in a porcelain boat and heated in a tube furnace at certain carbonization temperatures (400°C, 500°C, 600°C, 700°C, and 800°C) in a nitrogen atmosphere for 60 min. After cooling down to room temperature, the obtained black samples were washed with ethanol and deionized water with mass ratios of deionized water and ethanol to samples of about 1:900 and 1:100, respectively, to purify the product. Through freeze-drying at −20°C in vacuum, the WSC was finally obtained. WSC is denoted as WSC-X, where X is the carbonization temperature.

6.2.3. Preparation of multi-porous WSC

Based on the original WSC-400 materials, multi-porous AC was synthesized by activation method. WSC-400 and KOH in a mass ratio of 1:3 were mixed and grinded, and then the mixture was heated at a certain temperature under nitrogen atmosphere for 2 h. After cooling to room temperature, the obtained products were washed with HCl and deionized water. Finally, through freeze-drying, multi-porous AC samples were prepared. According to the synthesis temperature, 500ºC, 600ºC, 700ºC, and 800ºC, samples were named as multi-WSC500, multi-WSC600, multi-WSC700, and multi-WSC800, respectively.

6.2.4. Fabrication of WSC and multi-porous WSC electrodes

Samples, conductive carbon black, and polyvinylidene fluoride were mixed evenly at a mass ratio of 8:1:1 in a mortar and dissolved in DMA. Then, with approximately

30 mg ± 5 mg of the mixture, using the flat part on the back of the spoon, it was evenly coated on the Ti plate. Next, the electrode was heated at 60°C for at least 1 h to remove the residual organic solvent. Finally, the prepared electrode was immersed in deionized water to form and dried before use.

6.2.5. $Au(S_2O_3)_2^{3-}$ recovery by electroreduction

Briefly, a certain molar ratio (Au to $S_2O_3^{2-}$ as 1 to 4) of ammonium thiosulfate was mixed with deionized water, and an appropriate amount of sodium hydroxide was added to control the pH to 10. Afterward, chloroauric acid and sodium hydroxide were added dropwise in turn. During the process, the pH of the solution should be maintained at 10. After all the required chloroauric acid had been added, the volume of the solution was adjusted to 200 mL.

Two electrodes coated with samples with a specific voltage were put at a certain distance into the electrolytic cell that contained the solution. The electrolytic cell was connected to a peristaltic pump, and the solution was cycled at a speed of 50 rpm. At a certain time, 2.5 mL of solution was extracted and filtered using a 0.22 μm filter membrane. The concentration of filtrate was determined using an atomic absorption spectrometer. The following formulas were used to calculate the adsorption capacity and recovery:

$$\mathrm{Q} = \frac{(C_0 - C_t) \times (V_0 - V_t)}{\mathrm{m}} \qquad (1)$$

$$\mathrm{R} = \frac{(C_0 - C_t)}{C_0} \qquad (2)$$

Where C_0 and C_t are the concentrations of Au at the initial and a certain moment, respectively, mg·L^{-1}; V_0 and V_t are the volumes of reaction solution at the initial and a certain moment, respectively, L; and m is the material mass used in the electrode, mg.

6.2.6. Characterization

The pyrolysis was analyzed using a synchronous thermal analyzer (Nechi, STA449F3Jupiter, Germany) in a high-purity nitrogen atmosphere at a heating rate of 10°C·min^{-1}. The internal structure and morphology of materials were analyzed by X-ray diffraction (XRD, D8 Advance, Bruker AXS, Germany) using Cu-Kα radiation. Raman spectra were collected using an INVIA Raman microscope with an Ar laser (Renishaw, England). Surface functional groups were analyzed using an American

Nexus Fourier transform infrared spectrometer in the wavenumber range of 4000–400 cm^{-1}. Pore structure distribution, adsorption and desorption isotherms were studied by the Brunauer–Emmett–Teller method (BET, V-Sorb X800, China). Microstructures and corresponding energy dispersive spectra (EDS) were collected on a scanning electron microscope (SEM, Phenom ProX G6, Netherlands) and transmission electron microscope (TEM, FEI Tecnai G2 F20, America). The chemical element state was determined by X-ray photoelectron spectroscopy (XPS, Thermo Scientific K-Alpha, America). The gold concentration of the solution was determined using an Agilent 280FS AA Spectrometer (G8434A, America).

6.2.7. Electrochemical measurements

Cyclic voltammetry (CV) and electrochemical impedance spectroscopy (EIS) were applied. Both experiments were measured in 50 mL of 1 $mol \cdot L^{-1}$ Na_2SO_4 and 5 $mg \cdot L^{-1}$ $Au(S_2O_3)_2^{3-}$ via a three-electrode system (VersaSTAT-450, PAR, USA). The working electrode operated in this experiment with about 1 cm^2 was made of the same material as the electrode in the Au removal process. A Pt plate and a Hg/HgO 1M KOH electrode were the counter electrode and reference electrode, respectively. The frequency range of the EIS test was 0.01–10000 Hz. The specific capacitance (C, $F \cdot g^{-1}$) of electrodes according to CV curves was calculated by the following equation:

$$C = \frac{\int I \mathrm{d}V}{2mv\Delta V} \qquad (3)$$

Where I was the current density, A; m was the mass of materials, g; v was the scan rate in CV experiment, $mV \cdot s^{-1}$; ΔV was the operating voltage difference, V.

6.3. Results and discussion

6.3.1. Synthesis of WSC and multi-porous WSC

WSC was obtained from walnut shells by the carbonization method, and it could be divided into three stages according to the thermogravimetry analysis (TG) (Figure 6-1a). The first stage was the dehydration drying stage in the temperature range of 40°C–120°C. Free water and molecular-bound water on the surface and inside of the sample were removed[51], and the mass loss was 2.64%. The second stage was pyrolysis in the temperature range of 120°C–500°C. During the process at this temperature range, at first, the TG curve was almost linear, with only a small amount of mass loss (0.35%) due to the depolymerization reaction. Afterward, the TG curve decreased sharply, and

most of the weight loss (63.71%) of the samples occurred in pyrolysis of cellulose and hemicellulose. Small molecular gases (such as CO, CO_2, and CH_4) and condensable macromolecule volatiles[52] were produced to generate pores. Meanwhile, an obvious weight loss peak could be seen in the corresponding DTG curve, and the weight loss rate reached the maximum at 333.3°C, that is, the peak of the DTG curve, which was a main weight loss stage. The third stage was the slow decomposition stage of the residue in the temperature range of 500°C–800°C. The weight loss ratio was 4.49%, and the weight loss process was relatively slow, mainly by lignin pyrolysis. At this time, the change of the DTG curve was slow, and the decomposition rate was slow[53–55]. Here, the WSC samples with various carbonization temperatures, from 400°C to 800°C, were synthesized to investigate the effect of carbonization temperature on electroreduction $Au(S_2O_3)_2^{3-}$ performances. According to the below equation, the yield was calculated.

$$Y = \frac{M_{bc}}{M_{bs}} \times 100\% \qquad (4)$$

Where M_{bc} and M_{bs} are the quality of biochar after and before pyrolysis, respectively, and Y is the yield. The final yield is 28.8%.

In all carbonization processes, different gases were produced, causing the pore size to increase with temperature and gradually reach saturation in the third stage.

TG-DSC analysis of WSC was obtained in Figure 6-1b to understand the possible reaction during activation process. It was obvious that there were three significant mass variation stage. The first stage with 2.60% mass reduction from normal temperature to 120ºC was due to the dehydration drying. Next step arising at temperature between 120ºC and 380ºC with 5.34% mass loss involved the breakdown of cellulose, lignin, and hemicellulose. Meanwhile, amounts of gases, such as CO, CO_2, and CH_4, were produced and released to create pores in AC. The third stage with 19.40% mass loss from 380ºC to 700ºC was resulted from the pyrolysis of lignin with a relatively slow rate. The last stage from 700ºC to 1000ºC with just 3.61% mass loss was a slow decomposition stage, demonstrating that the sample was hardly variable during this stage. Therefore, most multi-porous AC samples were prepared at the temperature of third stage to gain more micropores.

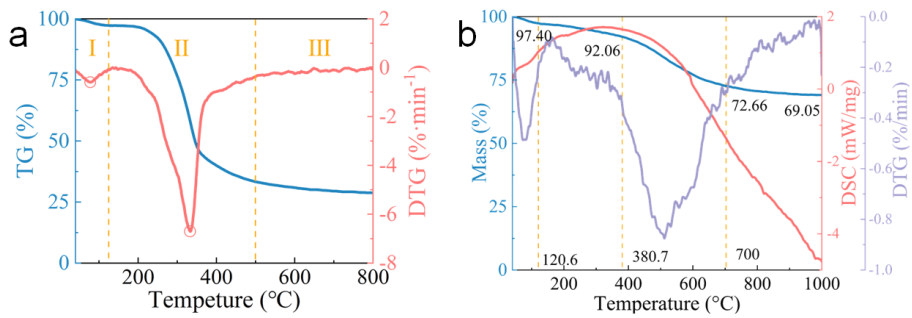

Figure 6-1. (a) TG spectra of walnut shell powder. (b) Mass loss, DTG, and DSC of WSC.

6.3.2. Structure characterization

Crystal structure of samples was detected by XRD tests (Figure 6-2). There were two clear broad peaks at about 22° and 44°, corresponding to the diffraction peaks of graphite carbon, which indicated that WSC and multi-porous WSC belonged to typical amorphous carbon[56]. Upward warping at a low diffraction angle in WSC was ascribed to high porosity. A wide diffraction peak from 15° to 30° originated from the so-called graphite structure (002) crystal plane. The intensity of the (002) crystal plane diffraction peak was weaker, and the width was wider at the same time, which meant that the graphitization degree of WSC and multi-porous WSC was relatively low. Higher activation temperature, more structural collapse was intensified and less graphitic structure remained. Moreover, the graphitization degree and order degree of WSC multi-porous WSC increased with the increase in carbonization and activation temperature, respectively[57,58].

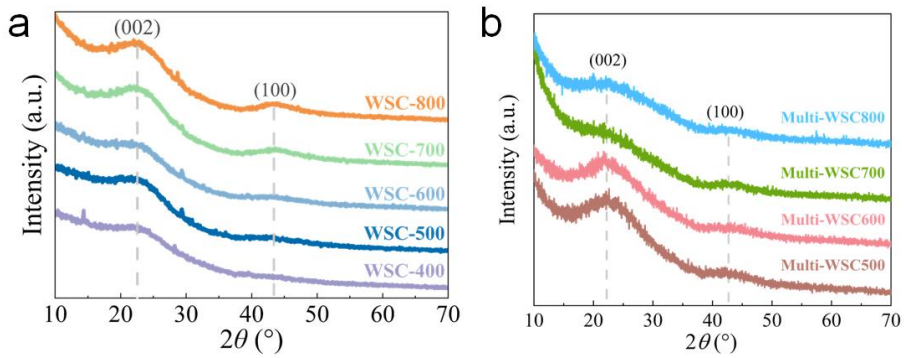

Figure 6-2. XRD pattern of (a) WSC and (b) multi-porous WSC under various synthesis temperature.

The molecular vibration and rotation of functional groups of WSC and multi-porous WSC were tested by Raman (Figure 6-3). The characteristic peak at 1350 cm^{-1} originated from the vibration of the graphite carbon crystal edge, called the

D band, representing the defect of the C atomic lattice. The characteristic peak at 1580 cm^{-1} was a typical Raman peak of bulk crystalline graphite, called the G-band, representing the in-plane stretching vibration of the C atom sp^2 hybrid and the degree of carbonization of the material. This peak was the basic vibration mode of the graphite crystal, and its intensity was related to crystal size. The intensity ratio of D-band and G-band (I_D/I_G) was an evaluation of defective degrees in carbon structure. It was notable that multi-porous WSC had a rather low I_D/I_G ratio, endorsing their partially graphitic structures. The intensity ratio of multi-porous AC was higher than that of WSC, being ascribed to the structural collapse and erosion by KOH activation.

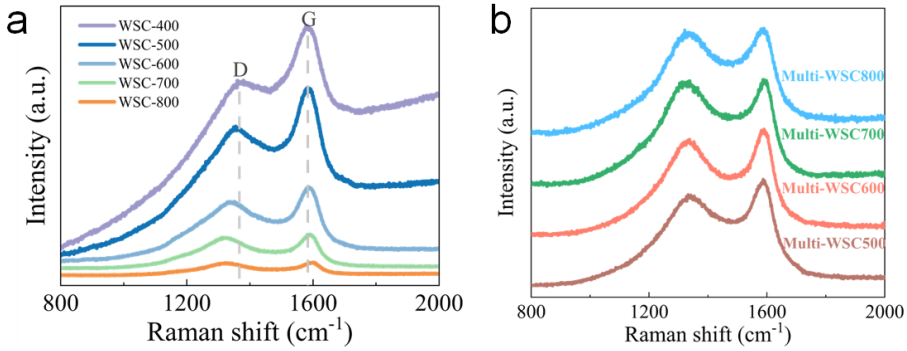

Figure 6-3. Raman spectra of (a) WSC and (b) multi-porous WSC under various synthesis temperature.

XPS was performed to investigate the chemical states of elements in WSC and multi-porous WSC (Figure 6-4). There were strong absorption peaks at binding energies of ~1223, ~532, and ~284 eV in the survey spectrum (Figure 6-4a and 6-4d), belonging to the absorption peaks of C KL1, O 1*s*, and C 1*s*, respectively, which indicated that WSC and multi-porous WSC were mainly composed of C and O elements. Figure 6-4b and 6-4e showed the C 1*s* XPS spectrum of WSC and multi-porous WSC, revealing the carbon atoms of three groups on the surface. Binding energy peaks at ~284, ~286, ~288, and ~290 eV corresponded to the C–C, C-O, COOR, and Π−Π* groups respectively[59]. The O 1*s* spectra in Figure 6-4c and 6-4f showed two fitted peaks located at ~532 and ~533 eV, corresponding to C=O and C-O oxygen-containing functional group respectively, which may improve the wettability of WSC electrode and provide active sites for reaction.

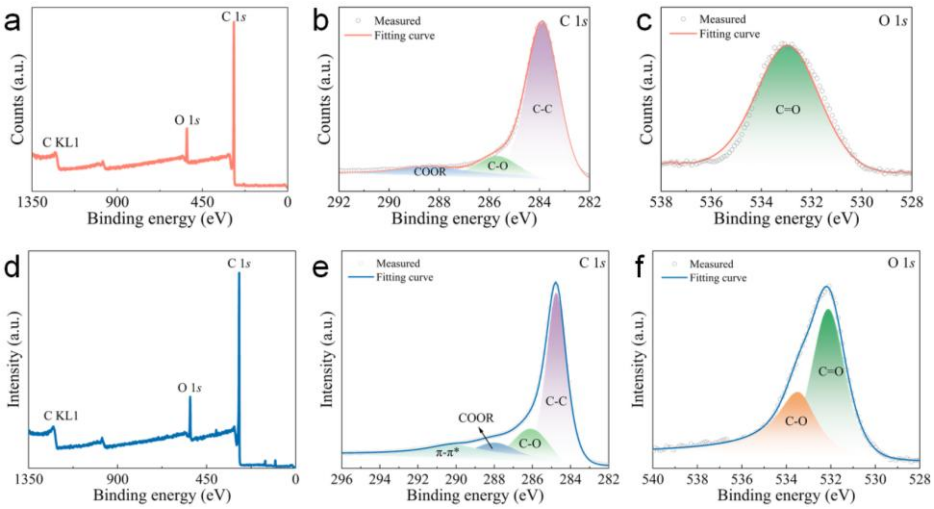

Figure 6-4. XPS survey of (a) WSC and (d) multi-porous WSC, C 1*s* of (b) WSC and (e) multi-porous WSC, O 1*s* of (c) WSC and (f) multi-porous WSC.

6.3.3. Morphology and pore characteristics

The morphology of all samples was characterized by SEM and TEM. In Figure 6-5a, 6-5b, 6-5c, 6-5d and 6-5e, all WSC samples had similar blocky morphology but various pores. It could be seen that all WSC possessed irregular holes, as revealed in white circles, corresponding to the results of cumulative pore volume curves. As the carbonization temperature increased, the amounts of pores increased while the size of the WSC decreased, which may be due to the gradual pyrolysis of lignin. Overall, the higher the carbonization temperature, the richer the pore size. In addition, the distorted areas in Figure 6-5f resulted from amorphous carbon.

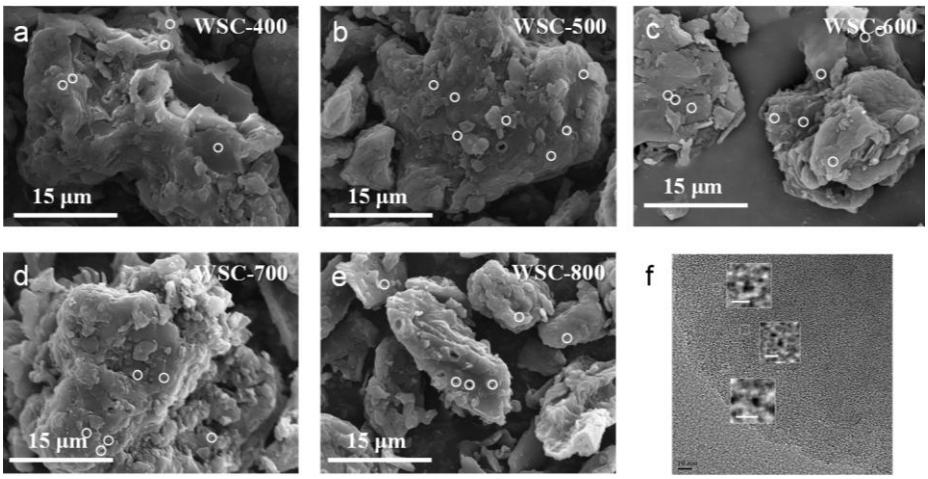

Figure 6-5. (a-e) SEM images of WSC under various synthesis temperature and (f) TEM image of WSC.

Surface became rough (Figure 6-6) after activation, corroborating the activator's

pore-creating outcome. By the close views, it revealed that the surface is abundant with slit-shaped and wedge-shaped pore structure, which would be desirable for absorption. These different multi-porous WSC samples exhibited diverse dimensions of pores. With the rising of the activation temperature, a widespread porous web created due to the etching of KOH and gas release. The hierarchical porous structure with large amount of mesopores and micropores co-reside on the wall of a macropores appeared on multi-WSC700, which revealed WSC activated at 700°C most benefit for the generation of multi-porous structure.

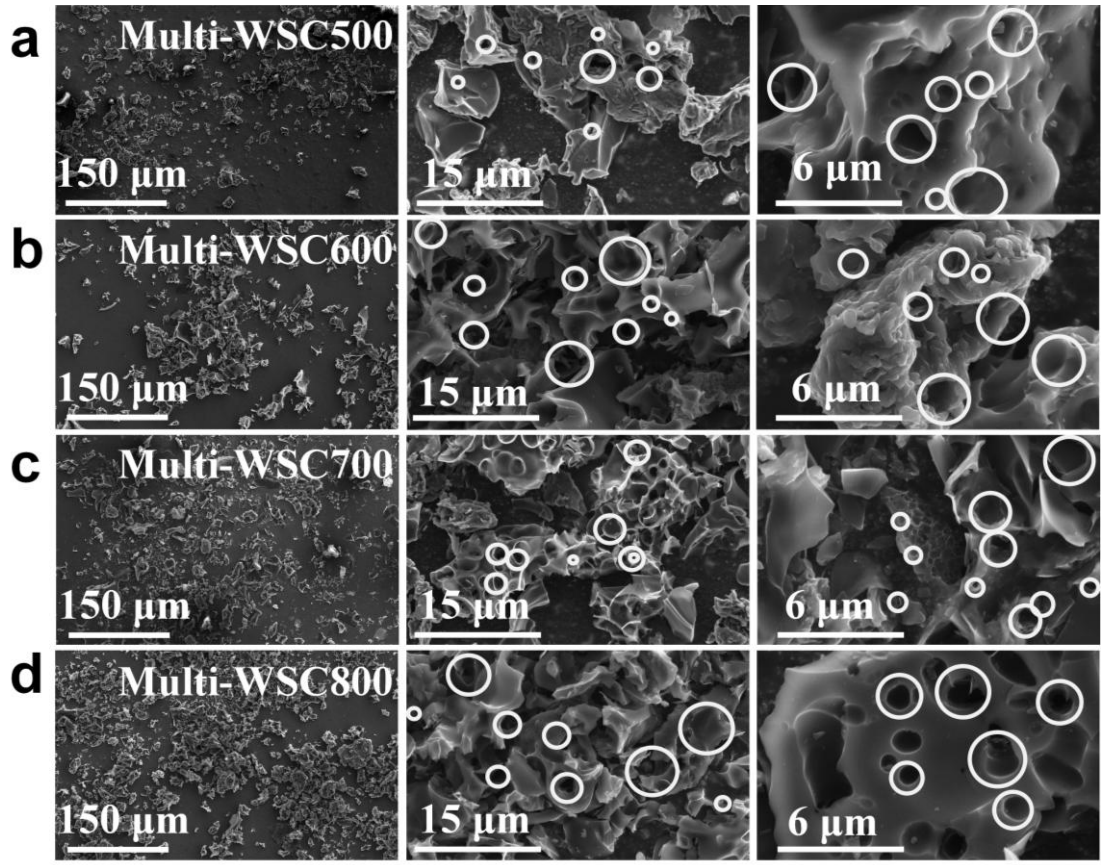

Figure 6-6. SEM images of multi-porous WSC under various synthesis temperature.

Pore characteristics were explored using BET test. The N_2 adsorption–desorption curves of WSC and multi-porous WSC in Figure 6-7a and 6-7d belonged to the type IV curve, and there were adsorption hysteresis loops in the middle, corresponding to the capillary condensation system of porous adsorbents. All the curves were an intermediate types IV isotherms behavior with H4 hysteresis loops, verifying that the samples have both micropores and mesopores. Based on the curves, the specific surface areas of the WSC and multi-porous WSC samples were given in Figure 6-7c and 6-7f. The specific surface area increased with the increase in carbonization temperature, reached the maximum at a certain carbonization temperature, and then decreased. A

large surface area was beneficial for providing more active sites. After activation, the surface area was obviously improved, especially multi-WSC700 had the highest specific surface area of 2783.3 m^2/g.

Different pore size worked in various ways during the absorption process. The presence of macropores and large mesopores facilitated ion diffusion, whilst small mesopores and micropores increased ion-accessible surface area and significantly contributed to adsorption capacity. The pores structure of WSC and multi-porous WSC was obtained, and the cumulative pore volume curves and pore diameter distributions were shown in Figure 6-7b and 6-7e, respectively. It could be concluded that there were more pores when increasing the carbonization temperature. At higher than 700°C, the pore channel collapsed, resulting in decreased pores and specific surface areas. increasing activation temperature enhanced the mesopores and micropores volume of WSC, especially micropores. When the size of the micropores was comparable to the ion size, the micropores made maximum contribution to the EDLC due to high electro absorption originated from the strong interaction of ions with the pore in wall.

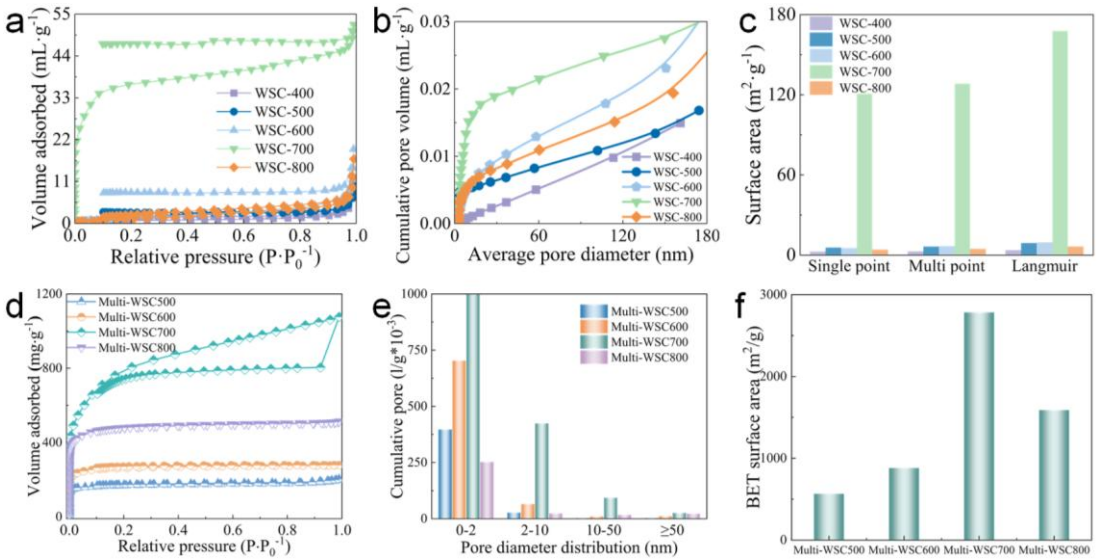

Figure 6-7. (a) Nitrogen adsorption-desorption isotherms, (b) cumulative pore volume curves, and (c) surface area of WSC under various synthesis temperature. (d) Nitrogen adsorption-desorption isotherms, (e) pore diameter distributions, and (f) BET surface area of multi-porous WSC.

6.3.4. $Au(S_2O_3)_2^{3-}$ recovery performances by electroreduction

$Au(S_2O_3)_2^{3-}$ recovery performances by the WSC electrode were evaluated. Figure 6-8 showed the adsorption capacity and corresponding recovery of different WSC

electrodes. WSC electrodes showed excellent recovery of $Au(S_2O_3)_2^{3-}$ (highest recovery of 95%), with WSC-400 having the lowest adsorption capacity. With the increase in carbonatization temperature, recovery improved and then plateaued after dropping a little. The dropped recovery, as observed for the WSC-800 electrode, may originate from a less functional group and a corresponding smaller electric double layer for ion storage.

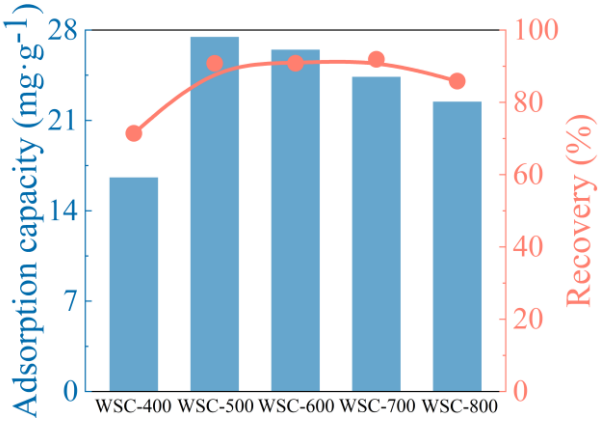

Figure 6-8. Adsorption capacity and recovery performances of $Au(S_2O_3)_2^{3-}$ on WSC electrodes.

Low-concentration $Au(S_2O_3)_2^{3-}$ recovery performances through electroreduction via multi-porous AC was studied as shown in Figure 6-9a and 6-9b. The adsorption capacity and recovery were improved by activation. Grown the activation temperature, the adsorption capacity and recovery clearly enhanced, while little decrease in multi-WSC800 was due to the collapse of the pores. To gain the insight of adsorption process, "Webber-Morris" dynamics model (Eq. 5) was applied to study the kinetics ion diffusion processes in electro reduction-recovery, and corresponding fitting data were exhibited in Table 6-1.

$$q_t = k_i t^{1/2} + C \qquad (5)$$

Where t was the reaction time, min; q_t was the adsorbed Au at t moment, mg/g; k_i was the rate constants, min^{-1}; C was the constant.

After being fitted, the adsorption process was divided into three steps, surface contact, diffusion, and balance. The fitting curve didn't pass through the origin data, revealing that the adsorption process was controlled by the internal diffusion and other adsorption stages. For the first step, $Au(S_2O_3)_2^{3-}$ diffused rapidly to the surface of electrodes under the synergistic forces of electric field force, concentration gradient driving force, and attraction force from electrode. k_1 of multi-WSC700 electrodes was highest, being resulted from strong interaction between multi-AC4 and $Au(S_2O_3)_2^{3-}$. As for k_2 of multi-WSC700, it decreased but still reached a high place, that was the reason

that macroporous and mesoporous structures provided efficient ion transport paths. The third step was the balance due to the increase of mass transfer resistance. Smallest slope of multi-WSC700 exhibited the best recovery performance. The results showed that the mesopores and macropores paved a way for ion diffusion, and micropores provided abundant active sites for $Au(S_2O_3)_2^{3-}$ adsorption. Compared with other works using similar materials in Table 6-2, this work achieved efficient and high recovery of $Au(S_2O_3)_2^{3-}$.

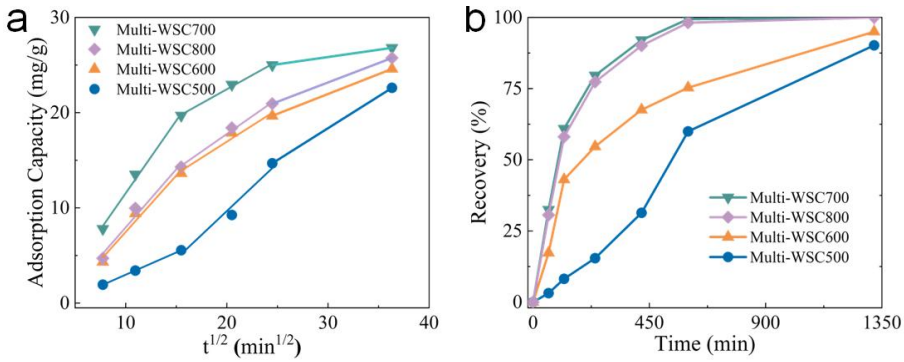

Figure 6-9. (a) Adsorption capacity of $Au(S_2O_3)_2^{3-}$ on multi-porous WSC electrodes, being fitted by "Webber-Morris" dynamics model. (b) Recovery of $Au(S_2O_3)_2^{3-}$ on multi-porous WSC electrodes.

Table 6-1. Fitting parameters of $Au(S_2O_3)_2^{3-}$ electroreduction recovery steps on multi-porous WSC electrodes descripted by "Webber-Morris" dynamics model.

Materials	Diffusion			Internal diffusion		
	k_1	C_1	R_1^2	k_2	C_2	R_2^2
AC1	0.289	-1.592	0.988	0.432	-3.796	0.997
AC2	0.467	-1.690	1	1.003	-10.395	0.985
AC3	1.184	-4.373	0.988	0.677	3.414	0.986
AC4	1.525	-3.712	0.997	0.592	10.623	0.998
AC5	1.220	-4.246	0.988	0.741	2.943	0.997

Table 6-2. Comparing recovery capacities of WSC, multi-porous WSC with other materials.

Material	Concentration (mg/g)	Recovery capacity (mg/g)	Recovery (%)	References
Cupric ferrocyanide-impregnated activated carbon	100	1.474	75	[60]
AgFC-impregnated activated carbon	100	1.212	70	[61]
MMT-impregnated activated carbon	10	1.9	93.7	[62]
SCN-AC	150	11.86	79	[63]
WSC	10	42.9	95.2	This work
Multi-porous WSC	5	36.33	100	This work

6.3.5. Gold element state after $Au(S_2O_3)_2^{3-}$ recovery

After being applied as an electrode for $Au(S_2O_3)_2^{3-}$ electroreduction, the gold state on electrode was explored by SEM-EDS and XPS. The SEM images (Figure 6-10a) showed a similar morphology to before, with the corresponding EDS elemental distribution. Figure 6-10b indicated the good distribution of Au on the surface of the electrode.

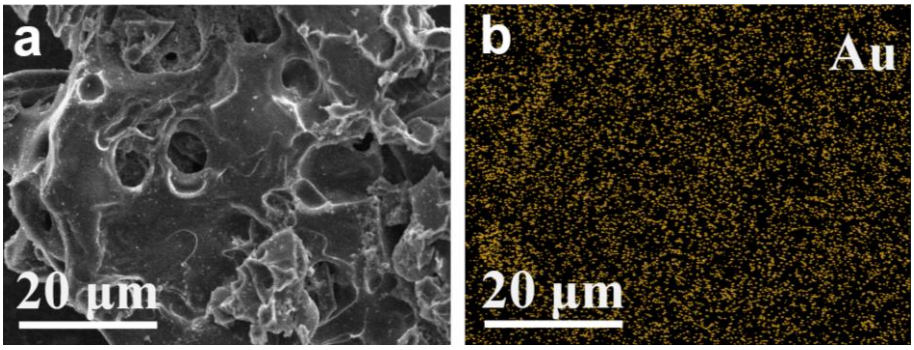

Figure 6-10. (a) SEM image and (b) corresponding Au EDS mapping of electrode after $Au(S_2O_3)_2^{3-}$ recovery.

Furthermore, XPS was conducted to study the gold element state and interaction. From the XPS survey spectrum (Figure 6-11a), Au, C, and O elements were observed on the electrode after $Au(S_2O_3)_2^{3-}$ recovery, confirming the successful gold recovery experiment. To further study the state of the gold, the Au 4f XPS spectrum was collected and is displayed in Figure 6-11d. The binding energy peaks at ~84 and ~88 eV were associated with the Au 4*f*7/2 and Au 4*f*5/2 peaks, respectively, indicating the presence

of the gold element (Au^0) after the recovery experiment. As for the other element spectra, such as C (Figure 6-11b) and O (Figure 6-11c), they showed the same functional groups as before recovery. The above results demonstrated that $Au(S_2O_3)_2^{3-}$ was successfully recovered in the form of gold particles by the electrode.

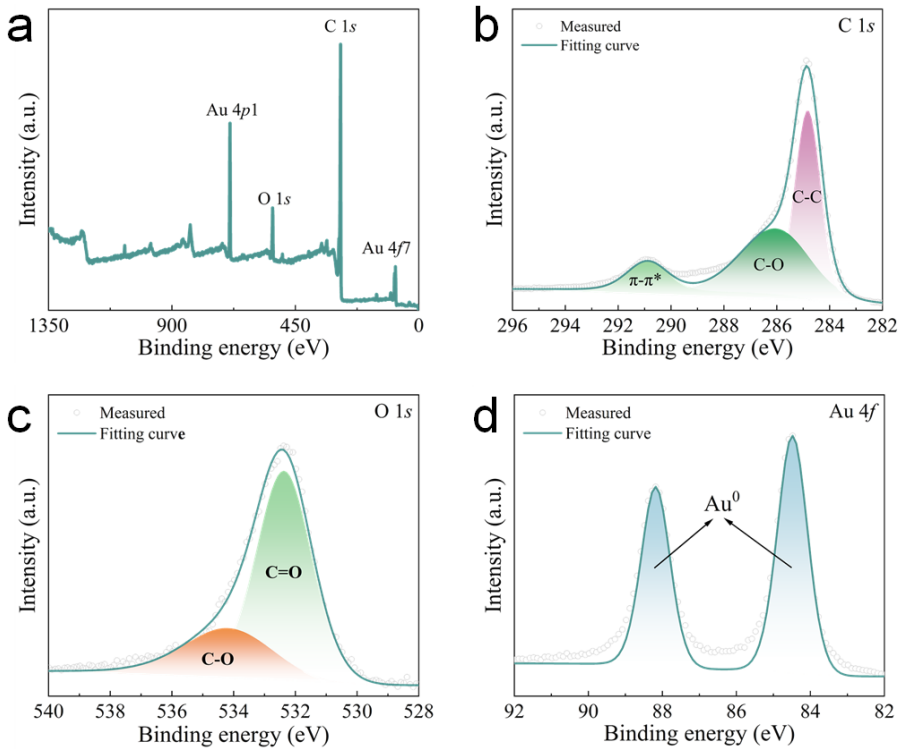

Figure 6-11. XPS (a) survey, (b) C 1s, (c) O 1s, and (d) Au 4f of electrode after $Au(S_2O_3)_2^{3-}$ recovery.

6.3.6. Electrochemical behaviors

To explore the electrochemical behaviors of WSC and multi-porous WSC, CV, and EIS were conducted in Na_2SO_4 and $Au(S_2O_3)_2^{3-}$ solutions. To investigate the reaction process, the CV curves revealed that in $Au(S_2O_3)_2^{3-}$ solution (Figure 6-12), gold depletion occurred in the range of −0.2 to −0.8 V, demonstrating a reduction reaction. The area under the CV curve first increased and then decreased, with WSC-700 having the highest capacitance, which was beneficial for the reaction of $Au(S_2O_3)_2^{3-}$.

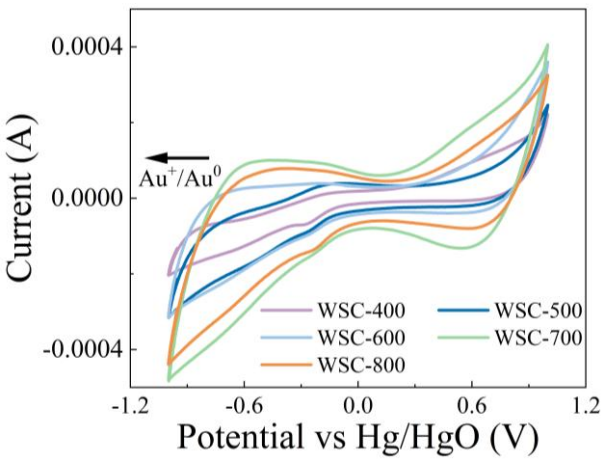

Figure 6-12. CV curves of WSC under various synthesis temperature in $Au(S_2O_3)_2^{3-}$ solution.

The recovery performances would be related to mesoporous structure (Figure 6-13a) because they usually served as the reactive sites. The better recoveries of WSC-500 and WSC-600 than WSC-800 were due to more oxygen functional groups interacting with $Au(S_2O_3)_2^{3-}$. The EIS curves in Na_2SO_4 (Figure 6-13b) showed a small semicircle arc, with WSC-400 showing the largest impedance. With lower charge transfer and reactive sites, WSC-400 had the poorest recovery ability of $Au(S_2O_3)_2^{3-}$. Therefore, the $Au(S_2O_3)_2^{3-}$ recovery ability depends on both reaction ability and charge transfer.

Multi-WSC700 performed the largest calculated specific capacitance which was controlled by the micropore volume but independent of the mesopores volume, showing the highest capacitance for ion storage (Figure 6-13c). Ion diffusion was tested by EIS (Figure 6-13d), the smaller diameter of semicircle meant the lower charge transfer resistance in EIS. With more micropores and mesopores, the reactive sites were richer and the transfer resistance was lower, and multi-WSC700 possessed relatively smallest impedance and lowest resistance, resulting in a best performance for Au(I) ions transfer and recovery.

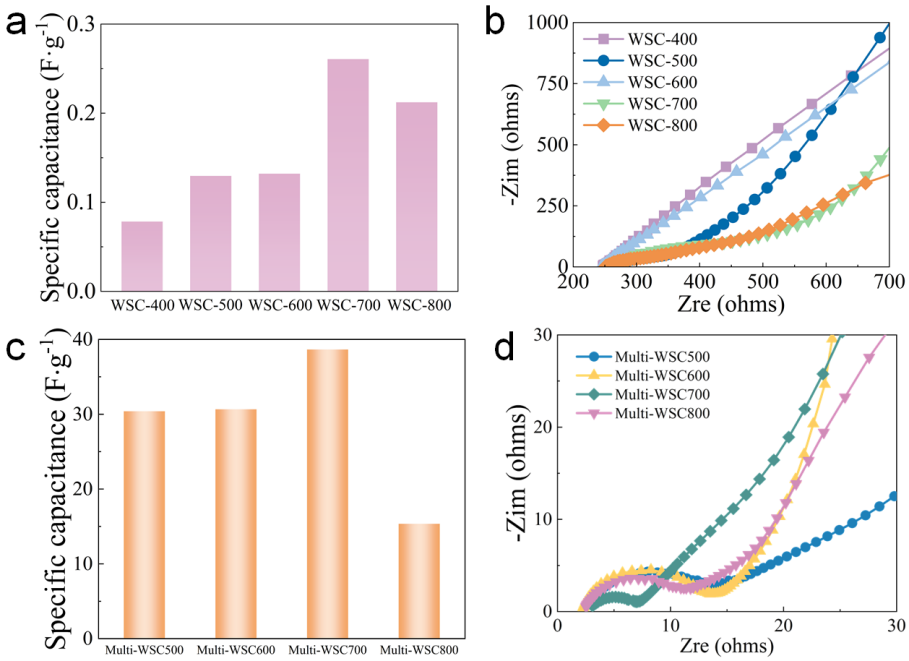

Figure 6-13. Specific capacitance of (a) WSC and (c) multi-porous WSC. EIS curves of (b) WSC and (d) multi-porous WSC.

6.4. Conclusions

The biochar electrodes based on WSC and multi-porous WSC were successfully prepared to achieve the efficient recovery of gold at low concentrations. Various porous WSC materials with tailored pore structures through adjustment of activation temperatures was synthesized and the electroreduction performance for $Au(S_2O_3)_2^{3-}$ recovery was systematically investigated. Applying WSC electrode, at an initial low concentration condition, the recovery rate for gold was over 85%, with the highest recovery of 95%, corresponding to a reduction of 42.9 $mg \cdot g^{-1}$. The $Au(S_2O_3)_2^{3-}$ recovery reached ~100% from low concentration gold thiosulfate solution and the adsorption capacity of $Au(S_2O_3)_2^{3-}$ achieved to 36.33 mg/g when using multi-WSC700, exhibiting significantly enhanced adsorption capacity and $Au(S_2O_3)_2^{3-}$ recovery efficiency compared to non-activated counterparts due to the porous structure facilitating efficient ion adsorption and storage. The recovery performance of $Au(S_2O_3)_2^{3-}$ in the electroreduction method was linked to the pore size and number of functional groups of the electrode material. The greater the number of functional groups and pore size active sites, the better the recovery effect. This work offers new insights into the electrochemical recovery of low-concentration gold elements from solutions by electroreduction.

6.5. References

(1) Wang, C.; Lin, G.; Zhao, J.; Wang, S.; Zhang, L.; Xi, Y.; Li, X.; Ying, Y. Highly Selective Recovery of Au(III) from Wastewater by Thioctic Acid Modified Zr-MOF: Experiment and DFT Calculation. *Chemical Engineering Journal* **2020**, *380*, 122511. https://doi.org/10.1016/J.CEJ.2019.122511.

(2) Lu, Z.; Li, T.; Mudshinge, S. R.; Xu, B.; Hammond, G. B. Optimization of Catalysts and Conditions in Gold(I) Catalysis - Counterion and Additive Effects. *Chemical Reviews* **2021**, *121* (14), 8452–8477. https://doi.org/10.1021/ACS.CHEMREV.0C00713.

(3) Choi, S.; Han, S. I.; Jung, D.; Hwang, H. J.; Lim, C.; Bae, S.; Park, O. K.; Tschabrunn, C. M.; Lee, M.; Bae, S. Y.; Yu, J. W.; Ryu, J. H.; Lee, S. W.; Park, K.; Kang, P. M.; Lee, W. B.; Nezafat, R.; Hyeon, T.; Kim, D. H. Highly Conductive, Stretchable and Biocompatible Ag–Au Core–Sheath Nanowire Composite for Wearable and Implantable Bioelectronics. *Nature Nanotechnology* **2018**, *13* (11), 1048–1056. https://doi.org/10.1038/s41565-018-0226-8.

(4) Qian, H. L.; Meng, F. L.; Yang, C. X.; Yan, X. P. Irreversible Amide-Linked Covalent Organic Framework for Selective and Ultrafast Gold Recovery. *Angewandte Chemie International Edition* **2020**, *59* (40), 17607–17613. https://doi.org/10.1002/ANIE.202006535.

(5) Dang, X. E.; Ke, W. S.; Tang, C.; Lv, J.; Zhou, X.; Liu, C. P. Increasing Leaching Rate of Gold Cyanide of Two-Stage Calcination Generated from Refractory Ore Containing Arsenopyrite and Pyrrhotite. *Rare Metals* **2016**, *35* (10), 804–810. https://doi.org/10.1007/s12598-015-0470-0.

(6) Xia, J.; Marthi, R.; Twinney, J.; Ghahreman, A. A Review on Adsorption Mechanism of Gold Cyanide Complex onto Activation Carbon. *Journal of Industrial and Engineering Chemistry* **2022**, *111*, 35–42. https://doi.org/10.1016/j.jiec.2022.04.014.

(7) Niu, H.; Yang, H.; Tong, L. Research on Gold Leaching of Carbonaceous Pressure-Oxidized Gold Ore via a Highly Effective, Green and Low Toxic Agent Trichloroisocyanuric Acid. *Journal of Cleaner Production* **2023**, *419*, 138062. https://doi.org/10.1016/J.JCLEPRO.2023.138062.

(8) Konyratbekova, S. S.; Baikonurova, A.; Akcil, A. Non-Cyanide Leaching Processes in Gold Hydrometallurgy and Iodine-Iodide Applications: A Review. *Mineral Processing and Extractive Metallurgy Review* **2015**, *36* (3), 198–212. https://doi.org/10.1080/08827508.2014.942813.

(9) Sun, C. bao; Zhang, X. liang; Kou, J.; Xing, Y. A Review of Gold Extraction Using Noncyanide Lixiviants: Fundamentals, Advancements, and Challenges toward Alkaline Sulfur-Containing Leaching Agents. *International Journal of Minerals, Metallurgy and Materials* **2020**, *27* (4), 417–431. https://doi.org/10.1007/s12613-019-1955-x.

(10) Liao, L.; Song, Y.; Zhang, P.; Li, Y.; Bao, J.; Zhou, J. Treatment of Actual Cyanide Gold Extraction Wastewater by Persulfate Oxidation and Its Reaction Mechanism. *Research on Chemical Intermediates* **2023**, *49* (8), 3705–3721. https://doi.org/10.1007/s11164-022-04928-x.

(11) Zhou, S.; Li, W.; Liu, W.; Zhai, J. Removal of Metal Ions from Cyanide Gold Extraction Wastewater by Alkaline Ion-Exchange Fibers. *Hydrometallurgy* **2023**, *215*, 105992. https://doi.org/10.1016/j.hydromet.2022.105992.

(12) Birloaga, I.; De Michelis, I.; Ferella, F.; Buzatu, M.; Vegliò, F. Study on the Influence of Various Factors in the Hydrometallurgical Processing of Waste Printed Circuit Boards for Copper and Gold Recovery. *Waste Management* **2013**, *33* (4), 935–941. https://doi.org/10.1016/J.WASMAN.2013.01.003.

(13) Yang, Y.; Xie, Z.; Xu, B.; Li, Q.; Jiang, T. Gold Extraction from a High Carbon Low-Grade Refractory Gold Ore by Flotation-Roasting-Leaching Process. *Rare Metal Technology 2015* **2015**, 63–70. https://doi.org/10.1007/978-3-319-48188-3_8.

(14) Zhang, L.; Jiang, T.; Guo, X. yi; Tian, Q. hua; Zhong, S. ping; Dong, L.; Qin, H.; Liu, Z. wei; Makuza, B. Sustainable Processing of Gold Cyanide Tailings: Reduction Roasting, Mechanical Activation, Non-Cyanide Leaching, and Magnetic Separation. *Hydrometallurgy* **2023**, *217*, 106028. https://doi.org/10.1016/J.HYDROMET.2023.106028.

(15) Jones, L.; Hackl, R. P. Sources of High Cyanide Consumption for a Biooxidized Refractory Gold Concentrate. *Process Metallurgy* **1999**, *9*, 337–346. https://doi.org/10.1016/S1572-4409(99)80034-0.

(16) Zhan, W.; Yuan, Y.; Yao, X.; Yang, B.; Jia, F.; Lin, C.; Arauz-Lara, J. L.; Song, S. Efficient Recovery of Gold(I) from Thiosulfate Solutions through Photocatalytic Reduction with Mn(II)-Doped MoS_2. *ACS Sustainable Chemistry and Engineering* **2021**, *9* (35), 11681–11690. https://doi.org/10.1021/acssuschemeng.1c02160.

(17) Filcenco Olteanu, A.; Dobre, T.; Panturu, E.; Radu, A. D.; Akcil, A. Experimental Process Analysis and Mathematical Modeling for Selective Gold Leaching from Slag through Wet Chlorination. *Hydrometallurgy* **2014**, *144–145*, 170–185. https://doi.org/10.1016/J.HYDROMET.2014.02.011.

(18) Li, K.; Li, Q.; Zhang, Y.; Liu, X.; Yang, Y.; Jiang, T. Improved Thiourea Leaching of Gold from a Gold Ore Using Additives. *Hydrometallurgy* **2023**, *222*, 106204. https://doi.org/10.1016/J.HYDROMET.2023.106204.

(19) Ahmed, M. R.; Mohammed, H. S.; El-Feky, M. G.; Abdel-Monem, Y. K. Gold Leaching Using Thiourea from Uranium Tailing Material, Gabal El-Missikat, Central Eastern Desert, Egypt. *Journal of Sustainable Metallurgy* **2020**, *6* (4), 599–611. https://doi.org/10.1007/S40831-020-00295-2.

(20) Le, G.; Li, W. J.; Song, K.; Song, Y. S.; Chen, Y.; Bai, A. P.; Cheng, Y. Electrochemical Dissolution Behavior of Gold and Its Main Coexistent Sulfide Minerals in Acid Thiocyanate Solutions. *Rare Metals* **2022**, *41* (1), 254–261. https://doi.org/10.1007/S12598-020-01614-Y.

(21) Wu, H.; Feng, Y.; Huang, W.; Li, H.; Liao, S. The Role of Glycine in the Ammonium

Thiocyanate Leaching of Gold. *Hydrometallurgy* **2019**, *185*, 111–116. https://doi.org/10.1016/J.HYDROMET.2019.01.019.

(22) Xu, B.; Kong, W.; Li, Q.; Yang, Y.; Jiang, T.; Liu, X. A Review of Thiosulfate Leaching of Gold: Focus on Thiosulfate Consumption and Gold Recovery from Pregnant Solution. *Metals* **2017**, *7* (6). https://doi.org/10.3390/met7060222.

(23) Xiang, P.; Zhang, Y.; Liu, Q. Gold Leaching from Printed Circuit Board Scrap with Thiosulfate. *IOP Conference Series: Materials Science and Engineering* **2018**, *394* (2). https://doi.org/10.1088/1757-899X/394/2/022001.

(24) Ubaldini, S.; Guglietta, D.; Vegliò, F.; Giuliano, V. Valorization of Mining Waste by Application of Innovative Thiosulphate Leaching for Gold Recovery. *Metals* **2019**, *9* (3), 1–12. https://doi.org/10.3390/met9030274.

(25) Lin, Y.; Hu, X.; Zi, F.; Chen, Y.; Chen, S.; Li, X.; Zhao, L.; Li, Y. Synergistical Thiourea and Thiosulfate Leaching Gold from a Gold Concentrate Calcine with Copper-Ammonia Catalysis. *Separation and Purification Technology* **2023**, *327*, 124928. https://doi.org/10.1016/J.SEPPUR.2023.124928.

(26) Zhang, Y.; Li, Q.; Liu, X.; Jiang, T. A Thermodynamic Analysis on Thiosulfate Leaching of Gold under the Catalysis of Fe^{3+}/Fe^{2+} Complexes. *Minerals Engineering* **2022**, *180*, 107511. https://doi.org/10.1016/J.MINENG.2022.107511.

(27) Ou, Y.; Yang, Y.; Li, K.; Gao, W.; Wang, L.; Li, Q.; Jiang, T. Eco-Friendly and Low-Energy Innovative Scheme of Self-Generated Thiosulfate by Atmospheric Oxidation for Green Gold Extraction. *Journal of Cleaner Production* **2023**, *387*, 135818. https://doi.org/10.1016/J.JCLEPRO.2022.135818.

(28) Wang, Q.; Hu, X.; Zi, F.; Yang, P.; Chen, Y.; Chen, S. Environmentally Friendly Extraction of Gold from Refractory Concentrate Using a Copper – Ethylenediamine – Thiosulfate Solution. *Journal of Cleaner Production* **2019**, *214*, 860–872. https://doi.org/10.1016/J.JCLEPRO.2019.01.007.

(29) Behnamfard, A.; Salarirad, M. M.; Veglio, F. Process Development for Recovery of Copper and Precious Metals from Waste Printed Circuit Boards with Emphasize on Palladium and Gold Leaching and Precipitation. *Waste Management* **2013**, *33* (11), 2354–2363. https://doi.org/10.1016/J.WASMAN.2013.07.017.

(30) Li, X.; Zhao, L.; Chen, S.; Lin, Y.; Hu, X.; Zi, F. Highly Efficient and Selective Extraction of Au(I) from Thiosulfate Gold-Leaching Solution Using Diphenylphosphine. *Journal of Environmental Chemical Engineering* **2024**, *12* (1), 111750. https://doi.org/10.1016/J.JECE.2023.111750.

(31) XIE, F.; CHEN, J. nan; ZHANG, X. zhen; XU, B.; WANG, W. Adsorption Mechanism of

Copper and Gold Thiosulfates onto Activated Carbon. *Transactions of Nonferrous Metals Society of China* **2023**, *33* (10), 3210–3221. https://doi.org/10.1016/S1003-6326(23)66328-9.

(32) Dong, Z.; Jiang, T.; Xu, B.; Wu, J.; Li, Q.; Yang, Y. A Comparative Study of Electrodeposition and Sodium Dithionite Reduction for Recovering Gold in Gold-Rich Solution from the Adsorption of Thiosulfate Solution by Ion Exchange Resin. *Separation and Purification Technology* **2024**, *328*, 125053. https://doi.org/10.1016/J.SEPPUR.2023.125053.

(33) Raiguel, S.; Gijsemans, L.; Van Den Bossche, A.; Onghena, B.; Binnemans, K. Solvent Extraction of Gold(III) with Diethyl Carbonate. *ACS Sustainable Chemistry and Engineering* **2020**, *8* (36), 13713–13723. https://doi.org/10.1021/acssuschemeng.0c04008.

(34) Zhao, L.; Zhou, Q.; Yang, Y.; Zhang, Y.; Qiu, Y.; Chen, Y.; Jin, X.; Yang, X.; Wang, S. Ultra-High Adsorption Capacity and Selectivity of Photo-Enhanced Sulfur-Rich M_2S_3 (MBi and Sb) for Gold Recovery from Electronic Wastewater. *Journal of Water Process Engineering* **2024**, *57*, 104572. https://doi.org/10.1016/J.JWPE.2023.104572.

(35) Xiang, Y.; Cheng, C.-Y.; Liu, M.-H.; Bai, W.-C.; Zang, Z.-X.; Xu, L.; Yu, Y.; Liu, G.-J. Efficient Recovery of Gold Using Macroporous Metal-Organic Framework Prepared by the "MOF in MOF" Method. *Separation and Purification Technology* **2024**, *335*, 126131. https://doi.org/10.1016/J.SEPPUR.2023.126131.

(36) Dong, Z.; Jiang, T.; Xu, B.; Yang, Y.; Li, Q. An Eco-Friendly and Efficient Process of Low Potential Thiosulfate Leaching-Resin Adsorption Recovery for Extracting Gold from a Roasted Gold Concentrate. *Journal of Cleaner Production* **2019**, *229*, 387–398. https://doi.org/10.1016/j.jclepro.2019.05.033.

(37) Ouchi, T.; Wu, S.; Okabe, T. H. Recycling of Gold Using Anodic Electrochemical Deposition from Molten Salt Electrolyte. *Journal of The Electrochemical Society* **2020**, *167* (12), 123501. https://doi.org/10.1149/1945-7111/aba6c5.

(38) Matsumiya, M.; Kinoshita, R.; Sasaki, Y. Recovery of Gold by Solvent Extraction and Direct Electrodeposition Using Phosphonium-Based Ionic Liquids. *Journal of The Electrochemical Society* **2022**, *169* (8), 082513. https://doi.org/10.1149/1945-7111/ac876d.

(39) Hou, D.; Bai, F.; Dong, P.; Chen, J.; Zhang, Y.; Meng, F.; Zhang, Z.; Zhang, C.; Zhang, Y.; Hu, J. Recent Development of Low Temperature Plasma Technology for Lithium-Ion Battery Materials. *Journal of Power Sources* **2023**, *584*, 233599. https://doi.org/10.1016/J.JPOWSOUR.2023.233599.

(40) Sun, K.; Tebyetekerwa, M.; Wang, C.; Wang, X.; Zhang, X.; Zhao, X. S. Electrocapacitive Deionization: Mechanisms, Electrodes, and Cell Designs. *Adv Funct Mater* **2023**, *33* (18). https://doi.org/10.1002/adfm.202213578.

(41) Sall, M. L.; Diaw, A. K. D.; Gningue-Sall, D.; Chevillot-Biraud, A.; Oturan, N.; Oturan, M. A.; Aaron, J. J. Removal of Cr(VI) from Aqueous Solution Using Electrosynthesized 4-Amino-3-

Hydroxynaphthalene-1-Sulfonic Acid Doped Polypyrrole as Adsorbent. *ENVIRONMENTAL SCIENCE AND POLLUTION RESEARCH* **2017**, *24* (26), 21111–21127. https://doi.org/10.1007/s11356-017-9713-y.

(42) Nosal-Wiercińska, A.; Martyna, M.; Wiśniewska, M. Influence of Mixed 2-Thiocytosine–Ionic Surfactants Adsorption Layers on Kinetics and Mechanism of Bi(III) Ions Electro Reduction: Use of the Nanostructured R-AgLAFE. *Applied Nanoscience (Switzerland)* **2023**, *13* (7), 4737–4745. https://doi.org/10.1007/S13204-022-02605-4.

(43) Yin, Y. Y.; Peng, Y. G.; Zhou, M.; Zhang, P.; Cheng, Y. Y.; Chen, P.; Xing, X. Q.; Ma, X. X.; Zhu, Q. G.; Sun, X. F.; Qian, Q. L.; Kang, X. C.; Han, B. X. Highly Efficient Zinc Electrode Prepared by Electro-Deposition in a Salt-Induced Pre-Phase Separation Region Solution. *SCIENCE BULLETIN* **2023**, *68* (20), 2362–2369. https://doi.org/10.1016/j.scib.2023.08.042.

(44) Hu, Z.; Wu, R.; Pang, X.; Yu, C.; Jian, X. Adsorption of Phosphorus in Water by Metal-Modified Large-Size Biochar: Realizing the Recovery and Recycling of Phosphorus. *Sustainable Chemistry and Pharmacy* **2023**, *36*, 101279. https://doi.org/10.1016/j.scp.2023.101279.

(45) Alimohammadi, Z.; Younesi, H.; Bahramifar, N. Desorption of Reactive Red 198 from Activated Carbon Prepared from Walnut Shells: Effects of Temperature, Sodium Carbonate Concentration and Organic Solvent Dose. *Advances in Environmental Technology* **2016**, *2* (3), 137–141. https://doi.org/10.22104/AET.2017.432.

(46) Mansoor, A.; Anjum, S.; Mustafa, Z.; Khurram, R.; Sattar, M.; Ilayas, T. Erbium Substituted Baddeleyites ($Er_xZr_{(1-x)}O_2$): Structural, Ferroelectric, Magnetic and Electrochemical Analysis for Supercapacitors Electrodes Using Walnut Shells Charcoal. *Ceramics International* **2023**, *49* (24), 39825–39842. https://doi.org/10.1016/J.CERAMINT.2023.09.027.

(47) Zhu, K.; Ma, J.; Cong, J.; Zhang, T.; Lei, H.; Xu, H.; Li, M. The Road to Reuse of Walnut By-Products: A Comprehensive Review of Bioactive Compounds, Extraction and Identification Methods, Biomedical and Industrial Applications. *Trends in Food Science & Technology* **2024**, *143*, 104264. https://doi.org/10.1016/J.TIFS.2023.104264.

(48) Lu, L.; Shan, R.; Shi, Y.; Wang, S.; Yuan, H. A Novel TiO_2/Biochar Composite Catalysts for Photocatalytic Degradation of Methyl Orange. *Chemosphere* **2019**, *222*, 391–398. https://doi.org/10.1016/J.CHEMOSPHERE.2019.01.132.

(49) Terzi, F.; Dossi, N. Ti as an Electrode Material. How to Make the Future Better than the Present. *Analytical and Bioanalytical Chemistry* **2015**, *407* (24). https://doi.org/10.1007/S00216-015-8919-4.

(50) Zhan, W.; Zhang, X.; Yuan, Y.; Weng, Q.; Song, S.; Martínez-López, M. de J.; Arauz-Lara, J. L.; Jia, F. Regulating Chemisorption and Electrosorption Activity for Efficient Uptake of Rare Earth Elements in Low Concentration on Oxygen-Doped Molybdenum Disulfide. *ACS Nano* **2024**.

https://doi.org/10.1021/ACSNANO.4C00691.

(51) Zeriouh, A.; Belkbir, L. Thermal Decomposition of a Moroccan Wood under a Nitrogen Atmosphere. *Thermochimica Acta* **1995**, *258* (C), 243–248. https://doi.org/10.1016/0040-6031(94)02246-K.

(52) Energy, A.; Biomass, C. 05/00194 Characterization of Chars from Pyrolysis of Lignin. *Fuel and Energy Abstracts* **2005**, *46* (1), 27. https://doi.org/10.1016/s0140-6701(05)80195-x.

(53) Chen, D.; Cen, K.; Zhuang, X.; Gan, Z.; Zhou, J.; Zhang, Y.; Zhang, H. Insight into Biomass Pyrolysis Mechanism Based on Cellulose, Hemicellulose, and Lignin: Evolution of Volatiles and Kinetics, Elucidation of Reaction Pathways, and Characterization of Gas, Biochar and Bio-oil. *Combustion and Flame* **2022**, *242*. https://doi.org/10.1016/j.combustflame.2022.112142.

(54) Tenimu, A. A. Thermogravimetric and Dfferential Thermal Investigation of Rice Husk Cellulose. *Bayero Journal of Pure and Applied Sciences* **2020**, *12* (1), 6–11. https://doi.org/10.4314/bajopas.v12i1.2.

(55) Tao, Y.; Li, S.; Li, P.; Wu, Q. Thermogravimetric Analyses (TGA) of Lignins Isolated from the Residue of Corn Stover Bioethanol (CSB) Production. *Holzforschung* **2016**, *70* (12), 1175–1182. https://doi.org/10.1515/hf-2016-0022.

(56) Dou, Y.; Bai, Q.; Guo, W.; Wang, H.; Chen, S.; Wang, T. Study on the Adsorption Characteristics of Organic Contaminants on Alumina Surface Coated with Clean Graphene and the Influence of Amorphous Carbon on Wetting Behavior. *Applied Surface Science* **2024**, *643*, 158658. https://doi.org/10.1016/J.APSUSC.2023.158658.

(57) Popov, K. M.; Arkhipov, V. E.; Kurenya, A. G.; Fedorovskaya, E. O.; Kovalenko, K. A.; Okotrub, A. V.; Bulusheva, L. G. Supercapacitor Performance of Binder-Free Buckypapers from Multiwall Carbon Nanotubes Synthesized at Different Temperatures. *Physica Status Solidi (B) Basic Research* **2016**, *253* (12), 2406–2412. https://doi.org/10.1002/pssb.201600240.

(58) Kesavan, T.; Sasidharan, M. Palm Spathe Derived N-Doped Carbon Nanosheets as a High Performance Electrode for Li-Ion Batteries and Supercapacitors. *ACS Sustainable Chemistry and Engineering* **2019**, *7* (14), 12160–12169. https://doi.org/10.1021/acssuschemeng.9b01261.

(59) Tang, B.; Zheng, L.; Dai, X.; Chen, H. Nitrogen/Oxygen Co-Doped Porous Carbons Derived from a Facilely-Synthesized Schiff-Base Polymer for High-Performance Supercapacitor. *Journal of Energy Storage* **2019**, *26* (September), 100961. https://doi.org/10.1016/j.est.2019.100961.

(60) Yu, H.; Zi, F.; Hu, X.; Nie, Y.; Xiang, P.; Xu, J.; Chi, H. Adsorption of the Gold-Thiosulfate Complex Ion onto Cupric Ferrocyanide (CuFC)-Impregnated Activated Carbon in Aqueous Solutions. *Hydrometallurgy* **2015**, *154*, 111–117. https://doi.org/10.1016/J.HYDROMET.2015.04.009.

(61) Yu, H.; Zi, F.; Hu, X.; Nie, Y.; Chen, Y.; Cheng, H. Adsorption of Gold from Thiosulfate

Solutions with Chemically Modified Activated Carbon. *Adsorption Science and Technology* **2018**, *36* (1–2), 408–428. https://doi.org/10.1177/0263617417698864.

(62) Chen, Y.; Zi, F.; Hu, X.; Lin, Y.; Du, H.; Hu, J.; Yang, P.; Zhang, Y.; Yang, B. The First Effective Utilization of Activated Carbon in Gold Thiosulfate System: A More Eco-Friendly, Easier Method for Gold Recovery and Material Regeneration. *Minerals Engineering* **2020**, *155*. https://doi.org/10.1016/J.MINENG.2020.106441.

(63) Wang, C.; Chen, S.; Chen, Y.; Zi, F.; Hu, X.; Qin, X.; Zhang, Y.; Yang, P.; He, Y.; He, P.; Lin, Y.; Zhang, G. Modification of Activated Carbon by Chemical Vapour Deposition through Thermal Decomposition of Thiourea for Enhanced Adsorption of Gold Thiosulfate Complex. *Separation and Purification Technology* **2020**, *241*. https://doi.org/10.1016/J.SEPPUR.2020.116632.

Chapter VII.

7.1. Introduction

7.2.

7.2.1.

7.2.2.

7.2.3

7.2.4.

7.2.5.

7.2.6.

7.2.7.

7.2.8.

7.2.9.

7.2.10.

7.2.11.

7.2.12.

Figure 7-1.

Figure 7-2.

7.3.

7.3.1.

Figure 7-3.

Figure 7-4.

Figure 7-5.

Figure 7-6.

Figure 7-7.

7.3.2.

Figure 7-8.

Figure 7-9.

Table 7-1.

Figure 7-10.

Figure 7-11.

Figure 7-12.

Figure 7-13.

7.3.3.

Figure 7-14.

Figure 7-15.

7.3.4.

Figure 7-16.

Figure 7-17.

Figure 7-18.

Figure 7-19.

7.3.5.

Figure 7-20.

Figure 7-21.

Figure 7-22.

7.4.

7.5.

Chapter VIII. Conclusions

Low-concentration REEs and Au(I) recovery from solutions is very important to the fields of hydrometallurgy, water treatment, and energy. Traditional approaches like adsorption, chemical precipitate, electro deposition, and ion exchange were hardly used in industrial applications because of their high-cost, or complex operations. This work combined traditional electro deposition and adsorption, named as CEC process, to realize highly efficient recovery of REEs and Au(I) from various leaching solutions. The conclusions are listed as following:

1) Low-concentration REEs was totally recovered on the surface of oxygen-doped MoS_2 through adjusting the interaction between REEs and sulfur or oxygen atoms.

2) Trace Gd(III) was efficient separated and recovered from REEs with similar properties by inducing defects on MoS_2 electrode according to various interaction of extra-nuclear electrons of REEs and unsaturated sulfur atoms.

3) Forecast based on simulation, La(III) can be separated and recovered by inducing unsaturated Mo atoms on MoS_2 electrode.

4) Total desorption from MoS_2 based electrodes was achieved within 120 minutes, and MoS_2 based electrodes kept good reuse ability.

5) Low-cost carbon-based electrodes achieved efficient REEs recovery with ~100%, and different recovery performances were highly related with their functional groups and pore distributions.

6) Tight interaction of REEs with the surface of electrode promoted the recovery.

7) Strong EDLC, and small charge transfer resistance enhanced REEs recovery and storage.

8) Quick desorption of REEs within 20 minutes from carbon-based electrodes was obtained.

9) Au(I) in thiosulfate solutions was recovered as the state of gold metal (90% recovery) using carbon-based electrodes, which would shorten the traditional recovery procedures.

10) To reduce the cost of electrodes, walnut shell powders as raw materials was used to successfully prepare charcoal electrodes via carbonization and excitation methods.

11) Rich functional groups were beneficial for interaction with REEs and Au(I), more pores facilitated the storage ability of target ions.

12) Compared with non-activated counterparts, multi-porous WSC electrodes possessed the better Au(I) recovery with ~100% due to the porous structure.

13) ……
…….
14) ……
…….
15) ……
……..
16) ……
…….
17) Au(I) recovery from thiosulfate leaching e-waste and gold ores solutions reached 100% in the existence of interfering ions.

Chapter IX. Perspective

Here, the work presented a new method for REEs and gold recovery through regulating chemisorption and electrosorption based on transition metal sulfide and porous materials electrodes. Although the excellent recovery of REEs and gold under low concentration condition was obtained, the actual component in leaching solutions is complex. Therefore, in the future works, studying the REEs recovery from actual leaching solutions and purifying gold particles from electrodes are two necessary works to further promote the application of this method.

Publications in studies

(*indicates corresponding author.)

1) **Weiquan Zhan**, Yuan Yuan, Qizheng Weng, Yanan Pan, Shaoxian Song, José Luis Arauz-Lara, Feifei Jia, Wencai Zhang. "Enhanced trace gadolinium(III) extraction via tailored chemisorption on defect-engineered molybdenum disulfide electrodes". ***Chemical Engineering Journal***, 2025, 512, 162632. DOI: 10.1016/j.cej.2025.162632. IF: **13.2**, Q1.

2) **Weiquan Zhan**, Xuan Zhang, Yuan Yuan, Qizheng Weng, Shaoxian Song, María de Jesuś Martínez-López, José Luis Arauz-Lara, Feifei Jia. "Regulating Chemisorption and Electrosorption Activity for Efficient Uptake of Rare Earth Elements in Low Concentration on Oxygen-Doped Molybdenum Disulfide", ***ACS Nano***, 2024, 18, 7298-7310. DOI: 10.1021/acsnano.4c00691. IF: **16**, Q1.

3) **Weiquan Zhan**, Yuan Yuan, Xuan Zhang, Yumeng Liang, Shaoxian Song, María de Jesús Martínez-Lopez, Jose Luis Arauz-Lara, Feifei Jia. "Efficient and selective Lead(II) removal within a wide concentration range through chemisorption and electrosorption coupling process via defective MoS_2 electrode", ***Separation and Purification Technology***, 2024, 329, 125183. DOI: 10.1016/j.seppur.2023.125183. IF: **9**, Q1.

4) **Weiquan Zhan**, Siyuan Yang, Shenxu Bao, Liuyi Ren, Cheng Liu. "A novel insight of interaction mechanism of carboxymethyl cellulose with talc surface: A combined molecular dynamic simulation and DFT investigation", ***Applied Clay Science***, 2024, 247, 197201. DOI: 10.1016/j.clay.2023.107201. IF: **5.8**, Q1.

5) **Weiquan Zhan**, Yuan Yuan, Chang Liu, Peng Chen, Yumeng Liang, Yu Wang, José Luis Arauz-Lara, Feifei Jia. "Preparation and application of 0D, 2D and 3D molybdenite: a review". ***Minerals and Mineral Materials***, 2022, 1, 5. DOI: 10.20517/mmm.2022.04.

6) **Weiquan Zhan**, Yuan Yuan, Xin Yao, Bingqiao Yang, Feifei Jia, Changsheng Lin, José Luis Arauz-Lara, Shaoxian Song. "Efficient Recovery of Gold(I) from Thiosulfate Solutions through Photocatalytic Reduction with Mn(II)-Doped MoS_2". ***ACS Sustainable Chemistry & Engineering***, 2021, 9, 11681-11590. DOI: 10.1021/acssuschemeng.1c02160. IF: **7.3**, Q1.

7) Qizheng Weng, **Weiquan Zhan***, Xuan Zhang, Shaoxian Song, Zhenlong Zeng, Hnin May Lwin, José Luis Arauz-Lara, Feifei Jia. "Electrochemical reduction and recovery of trace gold(I) from environmentally friendly thiosulfate leaching solutions using carbon electrodes". ***Carbon***, 2025, 232, 119799. DOI: 10.1016/j.carbon.2024.119799. IF: **11.6**, Q1.

8) Yanan Pan, **Weiquan Zhan***, Wencai Zhang. "Sustainable lithium extraction from produced water: Integrating membrane pretreatment and next-generation adsorbents". ***Journal of Environmental Management***, 2025, 382, 125343. DOI: 10.1016/j.jenvman.2025.125343. IF: **8.4**, Q1.

9) Xuan Zhang, **Weiquan Zhan***, Qizheng Weng, Sheng Wang, Shaoxian Song, José Luis Arauz-Lara, Feifei Jia. "Electro Reduction-Recovery of $Au(S_2O_3)_2^{3-}$ within A Low Concentration Range via Multi-Porous Activated Carbon Electrodes". ***Separation and Purification Technology***, 2025, 354, 129134. DOI: 10.1016/j.seppur.2024.129134. IF: **9**, Q1.

10) Yanan Pan, **Weiquan Zhan***, Wencai Zhang. "Advanced computational strategies for lithium chemical and electrochemical adsorption: A comprehensive state-of-the-art review". ***Desalination***, 2025, 600, 118524. DOI: 10.1016/j.desal.2024.118524. IF: **9.8**, Q1.

11) Hassan H.A. Younes, Lei Qin, Abdelaal S.A. Ahmed, Feifei Jia, Shaoxian Song, **Weiquan Zhan***. "Exploring phosphorus dissociation kinetics in HCl-leached moderate-grate phosphate ores: Towards high-quality dicalcium phosphate production". ***Minerals Engineering***, 2025, 231, 109480. DOI: 10.1016/j.mineng.2025.109480. IF: **5**, Q1.

12) Xuan Zhang, **Weiquan Zhan***, Qizheng Weng, Shaoxian Song, José Luis Arauz-Lara, Feifei Jia. "Electro-assisted sorption behavior and mechanism of low-concentration rare earth elements on carbon based materials". ***Applied Surface Science***, 2024, 664, 160224. DOI: 10.1016/j.apsusc.2024.160224. **IF: 6.9**, Q1.

13) Jiabei Gao, **Weiquan Zhan***, Xuan Zhang, Shaoxian Song, José Luis Arauz-Lara, Feifei Jia. "Facet Engineering in Cadmium Sulfide for Efficient Reduction-Recovery of Low-Concentration Gold(I) from Thiosulfate Solutions". ***Journal of Molecular Liquids***, 2024, 413, 126018. DOI: 10.1016/j.molliq.2024.126018. IF: **5.2**, Q1.

14) Qizheng Weng, Shaoxian Song, **Weiquan Zhan***, Xuan Zhang, Ziwei Xiang, Jiabei Gao, Feifei Jia. "Novel recovery of a low-concentration gold thiosulfate complex through electroreduction via a walnut shell charcoal electrode". ***Green and Smart Mining Engineering***, 2024, 1, 58-66. DOI: doi.org/10.1016/j.gsme.2024.03.004.

15) Yumeng Liang, **Weiquan Zhan***, Yuan Yuan, Noe Zamora-Romero, Feifei Jia, Bingqiao Yang, Zamoniddin Nasrddinov, Jose Luis Arauz-Lara, Shaoxian Song. "Manganese and oxygen dual-doping MoS_2 boosts reduction and adsorption activity toward efficient recovery of gold(I) from thiosulfate solutions". ***Journal of Alloys and Compounds***, 2022, 928, 167185. DOI: 10.1016/j.jallcom.2022.167185. IF: **6.3**, Q1.

16) Yuan Yuan, **Weiquan Zhan**, Yang Tian, Alejandro López-Valdivieso, Hao Yi, Shaoxian Song, Luis A. Cisternas, Feifei Jia. "Novel strategy for improved sylvite flotation through controlled crystallization". ***Minerals Engineering***, 2024, 211, 108695. DOI: 10.1016/j.mineng.2024.108695. IF: **5**, Q1.

17) Yuan Yuan, **Weiquan Zhan**, Feifei Jia, Shaoxian Song, Alejandro López-Valdivieso. "The reduction mechanism of $HAuCl_4$ on the surface of edge-rich molybdenum disulfide". ***Surfaces and Interfaces***, 2022, 33, 102199. DOI: 10.1016/j.surfn.2022.102199. IF: **6.3**, Q1.

18) Yuan Yuan, **Weiquan Zhan**, Alejandro Lopéz Valdivieso, Songliang Ma, Yang Tian, Hao Yi, Guangfeng Dong, Shaoxian Song, Luis A. Cisternas, Feifei Jia. "Novel insights into Sylvite flotation modulated by exposing facets". ***Powder Technology***, 2024, 119969. DOI: 10.1016/j.powtec.2024.119969. IF: **4.6**, Q1.

Submission

1) **Weiquan Zhan**, Frieder Scheiba, Chun Zhan, Shaoxian Song, José Luis Arauz-Lara, Feifei Jia. "Manipulating Porous Structure of Electrode for Electro Reduction-recovery of Gold", submitted.

2) **Weiquan Zhan**, Qizheng Weng, Peng Chen, Feifei Jia, Shaoxian Song. "Boosting Electrochemical Reduction-Recovery of Trace Gold(I) with Ferric-Modified Walnut Shell Charcoal", submitted.

Patents in studies

1) Feifei Jia, **Weiquan Zhan**, Xuan Zhang, Qizheng Weng, Shaoxian Song. A method for recovering precious metals based on porous materials combined with electrochemical reduction method, Chinese patent, CN118345449A.

2) Feifei Jia, Xuan Zhang, **Weiquan Zhan**, Qizheng Weng, Shaoxian Song. A method for recovering precious metals from thiosulfate leaching solutions based on fixed pore materials, Chinese patent, CN118345450A.

3) Feifei Jia, Qizheng Weng, **Weiquan Zhan**, Xuan Zhang, Shaoxian Song. A method for recovering gold thiosulfate complex by electrochemical reduction, Chinese patent, CN118345448A.

Conferences

1) November 6-9, 2024, 2024 Central Regional Meeting, Pennsylvania, USA. **Oral presentation**

2) March 29-31, 2024, The 8th International Forum for Young Scholars, Wuhan, China. **Oral presentation**

3) October 8-12, 2024. XXI Encuentro Sobre Procesamiento De Minerales, San Luis Potosi, Mexico. **Poster**

4) December 1-3, 2023, The Foundation of Mineral Processing & Extractive Metallurgy, Anhui, China. **Oral presentation**

5) July 21-23, 2023, The International Young Scholars Forums of Institute of Zhejiang University-Quzhou, Quzhou, China, **Oral presentation**

6) August 21-25, 2022, ACS Fall 2022 Sustainability in A Changing World, Chicago, IL, USA. **Oral presentation**

7) August 15-20, 2021, XXIX International Materials Research Congress, Cancun, Mexico. **Oral presentation**

8) December 3-5, 2020, The Second Non-metallic Mineral Materials Innovation Technology and Industry Development Forum, Wuhan, China. **Poster**

Permission

1) **Weiquan Zhan**, Yuan Yuan, Qizheng Weng, Yanan Pan, Shaoxian Song, José Luis Arauz-Lara, Feifei Jia, Wencai Zhang. "Enhanced trace gadolinium(III) extraction via tailored chemisorption on defect-engineered molybdenum disulfide electrodes". *Chemical Engineering Journal*, 2025, 512, 162632. DOI: 10.1016/j.cej.2025.162632.

Enhanced trace gadolinium(III) extraction via tailored chemisorption on defect-engineered molybdenum disulfide electrodes

Author: Weiquan Zhan,Yuan Yuan,Qizheng Weng,Yanan Pan,Shaoxian Song,José Luis Arauz-Lara,Feifei Jia,Wencai Zhang
Publication: Chemical Engineering Journal
Publisher: Elsevier
Date: 15 May 2025

2) Qizheng Weng, **Weiquan Zhan***, Xuan Zhang, Shaoxian Song, Zhenlong Zeng, Hnin May Lwin, José Luis Arauz-Lara, Feifei Jia. "Electrochemical reduction and recovery of trace gold(I) from environmentally friendly thiosulfate leaching solutions using carbon electrodes". *Carbon*, 2025, 232, 119799. DOI: 10.1016/j.carbon.2024.119799.

Electrochemical reduction and recovery of trace gold(I) from environmentally friendly thiosulfate leaching solutions using carbon electrodes

Author: Qizheng Weng,Weiquan Zhan,Xuan Zhang,Shaoxian Song,Zhenlong Zeng,Hnin May Lwin,José Luis Arauz-Lara,Feifei Jia
Publication: Carbon
Publisher: Elsevier
Date: 15 January 2025

© 2024 Elsevier Ltd. All rights are reserved, including those for text and data mining, AI training, and similar technologies.

Journal Author Rights

Please note that, as the author of this Elsevier article, you retain the right to include it in a thesis or dissertation, provided it is not published commercially. Permission is not required, but please ensure that you reference the journal as the original source. For more information on this and on your other retained rights, please visit: https://www.elsevier.com/about/our-business/policies/copyright#Author-rights

3) Xuan Zhang, **Weiquan Zhan***, Qizheng Weng, Sheng Wang, Shaoxian Song, José Luis Arauz-Lara, Feifei Jia. "Electro Reduction-Recovery of $Au(S_2O_3)_2^{3-}$ within A Low Concentration Range via Multi-Porous Activated Carbon Electrodes". *Separation and Purification Technology*, 2025, 354, 129134. DOI: 10.1016/j.seppur.2024.129134.

Electro reduction-recovery of Au(S2O3)2 3– within a low concentration range via multi-porous activated carbon electrodes

Author: Xuan Zhang,Weiquan Zhan,Qizheng Weng,Sheng Wang,Shaoxian Song,José Luis Arauz-Lara,Feifei Jia
Publication: Separation and Purification Technology
Publisher: Elsevier
Date: 19 February 2025

© 2024 Elsevier B.V. All rights are reserved, including those for text and data mining, AI training, and similar technologies.

Journal Author Rights

Please note that, as the author of this Elsevier article, you retain the right to include it in a thesis or dissertation, provided it is not published commercially. Permission is not required, but please ensure that you reference the journal as the original source. For more information on this and on your other retained rights, please visit: https://www.elsevier.com/about/our-business/policies/copyright#Author-rights

4) **Weiquan Zhan**, Xuan Zhang, Yuan Yuan, Qizheng Weng, Shaoxian Song, María de Jesuś Martínez-López, José Luis Arauz-Lara, Feifei Jia. "Regulating Chemisorption and Electrosorption Activity for Efficient Uptake of Rare Earth Elements in Low Concentration on Oxygen-Doped Molybdenum Disulfide", *ACS Nano*, 2024, 18, 7298-7310. DOI: org/10.1021/acsnano.4c00691.

ACS Publications
Most Trusted. Most Cited. Most Read.

Regulating Chemisorption and Electrosorption Activity for Efficient Uptake of Rare Earth Elements in Low Concentration on Oxygen-Doped Molybdenum Disulfide

Author: Weiquan Zhan, Xuan Zhang, Yuan Yuan, et al
Publication: ACS Nano
Publisher: American Chemical Society
Date: Mar 1, 2024

Copyright © 2024, American Chemical Society

PERMISSION/LICENSE IS GRANTED FOR YOUR ORDER AT NO CHARGE

This type of permission/license, instead of the standard Terms and Conditions, is sent to you because no fee is being charged for your order. Please note the following:

- Permission is granted for your request in both print and electronic formats, and translations.
- If figures and/or tables were requested, they may be adapted or used in part.
- Please print this page for your records and send a copy of it to your publisher/graduate school.
- Appropriate credit for the requested material should be given as follows: "Reprinted (adapted) with permission from {COMPLETE REFERENCE CITATION}. Copyright {YEAR} American Chemical Society." Insert appropriate information in place of the capitalized words.
- One-time permission is granted only for the use specified in your RightsLink request. No additional uses are granted (such as derivative works or other editions). For any uses, please submit a new request.

If credit is given to another source for the material you requested from RightsLink, permission must be obtained from that source.

BACK CLOSE WINDOW

5) Qizheng Weng, Shaoxian Song, **Weiquan Zhan***, Xuan Zhang, Ziwei Xiang, Jiabei Gao, Feifei Jia. “Novel recovery of a low-concentration gold thiosulfate complex through electroreduction via a walnut shell charcoal electrode”. *Green and Smart Mining Engineering*, 2024, 1, 58-66. DOI: doi.org/10.1016/j.gsme.2024.03.004.

This is an open-access journal, so no permission is required, and the content can be used directly.

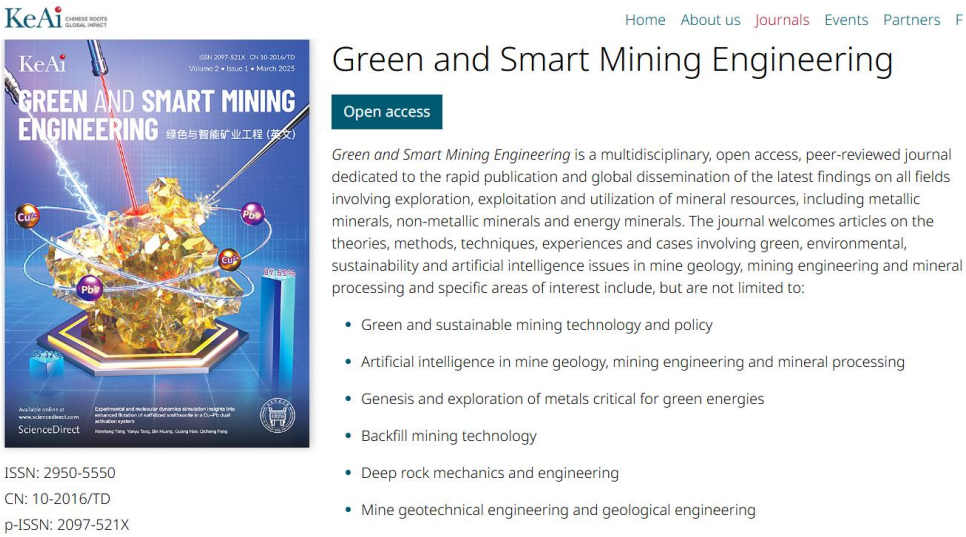

6) **Weiquan Zhan**, Yuan Yuan, Chang Liu, Peng Chen, Yumeng Liang, Yu Wang, José Luis Arauz-Lara, Feifei Jia. “Preparation and application of 0D, 2D and 3D molybdenite: a review”. *Minerals and Mineral Materials*, 2022, 1, 5. DOI: 10.20517/mmm.2022.04.

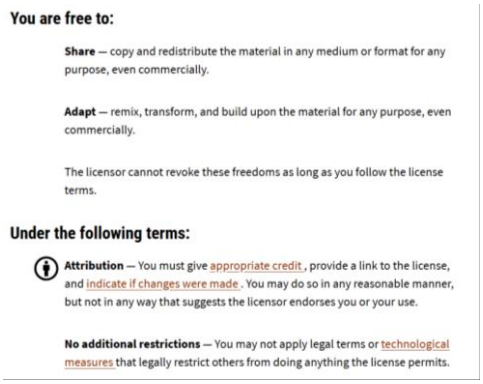

7) Xuan Zhang, **Weiquan Zhan***, Qizheng Weng, Shaoxian Song, José Luis Arauz-Lara, Feifei Jia. “Electro-assisted sorption behavior and mechanism of low-concentration rare earth elements on carbon based materials”. *Applied Surface Science*, 2024, 664, 160224. DOI: 10.1016/j.apsusc.2024.160224.

Electro-assisted sorption behavior and mechanism of low-concentration rare earth elements on carbon based materials

Author: Xuan Zhang,Weiquan Zhan,Qizheng Weng,Shaoxian Song,José Luis Arauz-Lara,Feifei Jia

Publication: Applied Surface Science

Publisher: Elsevier

Date: 15 August 2024